Gas Mixture Dynamics in Pipeline Networks with a Focus on Linearization and Optimal Control

by

Luke S. Baker

A Dissertation Presented in Partial Fulfillment
of the Requirement for the Degree
Doctor of Philosophy

Approved April 2023 by the
Graduate Supervisory Committee:

Dieter Armbruster, Chair
Anatoly Zlotnik
Rodrigo B. Platte
Michael Herty
Fabio Milner

ARIZONA STATE UNIVERSITY

May 2023

ABSTRACT

Balancing temporal shortages of renewable energy with natural gas for the generation of electricity is a challenge for dispatchers. This is compounded by the recent proposal of blending cleanly-produced hydrogen into natural gas networks. To introduce the concepts of gas flow, this thesis begins by linearizing the partial differential equations (PDEs) that govern the flow of natural gas in a single pipe. The solution of the linearized PDEs is used to investigate wave attenuation and characterize critical operating regions where linearization is applicable. The nonlinear PDEs for a single gas are extended to mixtures of gases with the addition of a PDE that governs the conservation of composition. The gas mixture formulation is developed for general gas networks that can inject or withdraw arbitrary time-varying mixtures of gases into or from the network at arbitrarily specified nodes, while being influenced by time-varying control actions of compressor units. The PDE formulation is discretized in space to form a nonlinear control system of ordinary differential equations (ODEs), which is used to prove that homogeneous mixtures are well-behaved and heterogeneous mixtures may be ill-behaved in the sense of monotone-ordering of solutions. Numerical simulations are performed to compute interfaces that delimit monotone and periodic system responses. The ODE system is used as the constraints of an optimal control problem (OCP) to minimize the expended energy of compressors. Moreover, the ODE system for the natural gas network is linearized and used as the constraints of a linear OCP. The OCPs are digitally implemented as optimization problems following the discretization of the time domain. The optimization problems are applied to pipelines and small test networks. Some qualitative and computational applications, including linearization error analysis and transient responses, are also investigated.

I dedicate this dissertation to my mom, Donna, and my brothers, Fulton and Johnny.

ACKNOWLEDGEMENTS

I would like to express my deepest gratitude to my advisors, Prof. Dieter Armbruster from Arizona State University (ASU) and Dr. Anatoly Zlotnik from Los Alamos National Laboratory, for their continuous support and direction of my thesis. Their expertise and words of wisdom have greatly inspired my thesis and the direction of my early career. My sincere thanks are extended to ASU, the School of Mathematical and Statistical Sciences, and Los Alamos National Laboratory for the many professional development opportunities that they have provided. I am deeply grateful to Prof. Rodrigo Platte from ASU for his willingness to provide technical support and advice throughout the duration of my graduate studies. I am thankful to Profs. Michael Herty from RWTH Aachen University, Fabio Milner from ASU, and Anna Scaglione from Cornell University for their insightful conversations that have further influenced the direction of my thesis. Additionally, I would like to thank Prof. Ulrich Zurcher from Cleveland State University for his mentoring during my undergraduate studies. His training and demonstration of prolonged patience greatly prepared me for graduate school. Lastly, this thesis was considerably influenced by the love and support from my parents, siblings, friends, and other loved ones that were with me every step of the way. Thank you all for your support.

TABLE OF CONTENTS

Page

LIST OF FIGURES vi

CHAPTER

1 INTRODUCTION 1

2 BACKGROUND 8

3 NATURAL GAS PIPELINE ANALYSIS 14

3.1 Flow Equations 14

3.2 Linear Flow Equations 16

3.3 Laplace Domain Solution 17

3.4 Transfer Matrix Representation 21

3.5 Wave Attenuation 21

4 NATURAL GAS PIPELINE APPLICATIONS 24

4.1 Reliable Operating Region 24

4.2 Flow Reversal 27

4.2.1 Flow Reversal Critical Curves 28

4.2.2 Null Points 28

4.3 Linearization Error Analysis 31

4.4 Examples 33

5 GAS MIXTURE DYNAMICS IN NETWORKS 35

5.1 Flow Equations 35

5.2 Spatial Discretization 42

5.3 Equivalent Systems 47

6 MONOTONIC AND PERIODIC OPERATING REGIONS 51

CHAPTER Page

6.1 Monotonicity 51

6.1.1 Homogeneous Concentration 52

6.1.2 Heterogeneous Concentration 55

6.2 Network Example 56

6.3 Phase Interfaces 60

6.3.1 Monotonic Interface 61

6.3.2 Periodic Interface 62

7 OPTIMAL CONTROL OF HETEROGENEOUS MIXTURES 68

7.1 Formulation 68

7.2 Implementation 70

7.3 Example 73

8 LINEAR CONTROL SYSTEM 76

8.1 System Reduction to Natural Gas 76

8.2 Linear System and Linear OCP 78

8.3 Transient Response 82

8.4 Network Example 85

8.5 Linearization Error Analysis 86

9 CONCLUSION 92

REFERENCES 96

APPENDIX

A PUBLISHED WORKS 103

LIST OF FIGURES

Figure Page

1.1 U.S. Natural Gas Transportation Infrastructure (Energy Information Administration, Office of Oil & Gas, Natural Gas Division, Natural Gas Transportation Information System (U.S. Energy Information Administration (2008))). The EIA Has Determined That the Informational Map Displays Here Do Not Raise Security Concerns, Based on the Application of the Federal Geographic Data Committee's *Guidelines for Providing Appropriate Access to Geospatial Data in Response to Security Concerns.* 2

3.1 Electric Circuit Representation of a Section of Pipeline. 18

4.1 Top: (Left) Boundary of ROR_1. (Right) Boundary of ROR_2. Bottom: Minimum between the boundary of the ROR and the flow reversal critical curve (defined in Section 4.2). 26

4.2 Left: Inlet-generated Null Point ξ_1. Right: Outlet-generated Null Point ξ_2 for Various Amplitude Factors. 29

4.3 **(Left)** Top: Color Map of the Error in (4.2) as a Function of (f_1, κ_1). Bottom: Color Map of the Error as a Function of (f_2, κ_2). The Curve on the Top Is the Value $\min(\kappa_{\mathrm{FRCC}_1}, \kappa_{\mathrm{ROR}_1})$ That Was Depicted on the Bottom of Figure 4.1 for $\overline{\varphi} = 200$, Which We Label Here as $\mathrm{ROR}_1 \cap \mathrm{FRCC}$ for Simplicity, and Similarly for the Bottom Curve. **(Right)** Top: Error in (4.2) Plotted as a Function of (f_1, κ_1), Where $\kappa_1 = \min(r\kappa_{\mathrm{FRCC}_1}, \kappa_{\mathrm{ROR}_1})$ for $r = 1, .75, .5$. Bottom: Error as a Function of (f_2, κ_2), Where $\kappa_2 = \min(\kappa_{\mathrm{FRCC}_2}, r\kappa_{\mathrm{ROR}_2})$ for $r = 1, .75, .5$. 32

4.4 Simulation of Solutions on the Nontrivial FRCC. 33

4.5 Simulation of Null Points. Only the Nonlinear Solution Is Plotted. 34

Figure Page

5.1 Configuration of the Boundary Conditions. (Left) a Single Pipeline $k : i \mapsto j$ with $i \in \mathcal{V}_s$ and $j \in \mathcal{V}_w$. (Right) A Small Network Defined by $j \in \mathcal{V}_w$, $k_1 : i_1 \mapsto j$ with $i_1 \in \mathcal{V}_s$, and $k_2 : i_2 \mapsto j$ with $i_2 \in \mathcal{V}_q$. 41

6.1 Network Configuration (Not to Scale). The Triangles Represent Compressor Stations. Pipeline Dimensions Between Nodes: Blue to Black (20 Km), Black to Green (70 Km), Green to Maroon (10 Km), Black to Maroon (60 Km), and Maroon to Cyan (80 Km). The Pipelines Have Uniform Diameter (.9144 M) and Friction Factor (.01), Except for the Black to Maroon Pipeline That Has Diameter (.635 M) and Friction Factor (.015). 57

6.2 **(Left)** Two Solutions (Solid Lines Vs. Dots) at the Color-coordinated Network Nodes in Figure 6.1. The Boundary Conditions for Both Solutions Are $(\boldsymbol{p}_s)_{\text{blue}} = 5$ MPa, $\boldsymbol{\alpha}^{(2)}_{\text{blue}}(t) = 0.01(1 + \sin(4\pi t/T))$, $\boldsymbol{\beta}^{(2)}_{\text{green}}(t) = 0.125(1 + \sin(12\pi t/T))$, $\boldsymbol{q}_{\text{green}}(t) = 3$ (kg/s), $\boldsymbol{w}_{\text{black}}(t) = 60(1-\sin(6\pi t/T))$ (kg/s), $\mu_{\text{red}} = 1.0678$, $\underline{\mu}_{\text{yellow}} = 1.0140$, and $\underline{\mu}_{\text{purple}} = 1.0734$, Where $T = 60$ (hr). The Boundary Condition That Differs Between the Two Solutions Is $\boldsymbol{w}_{\text{cyan}}(t) = 110$ (kg/s) (Solid Lines) and $\boldsymbol{w}_{\text{cyan}}(t) = 130$ (kg/s) (Dots). **(Right)** Same Boundary Conditions Except For $(\boldsymbol{p}_s)_{\text{blue}} = 10$ (MPa). 58

Figure Page

6.3 **(Left)** The Boundary Conditions for the Two Solutions Are $(\boldsymbol{p}_s)_{\text{blue}} = 5$ (MPa), $\boldsymbol{\alpha}^{(2)}_{\text{blue}}(t) = 0$, $\boldsymbol{\beta}^{(2)}_{\text{green}}(t) = 1$, $\boldsymbol{q}_{\text{green}}(t) = 9(1 + \sin(6\pi t/T))$ (kg/s), $\boldsymbol{w}_{\text{black}}(t) = 100(1 - \sin(6\pi t/T))$ (kg/s), $\mu_{\text{red}} = 1.1096$, $\underline{\mu}_{\text{yellow}} = 1.0057$, and $\underline{\mu}_{\text{purple}} = 1.1301$, Where $T = 80$ (hr). The Other Boundary Condition Is $\boldsymbol{w}_{\text{cyan}}(t) = 130$ (kg/s) (Solid Lines) and $\boldsymbol{w}_{\text{cyan}}(t) = 150$ (kg/s) (dots). **(Right)** Same Boundary Conditions Except For $(\boldsymbol{p}_s)_{\text{blue}} = 10$ (MPa). 59

6.4 Monotonic Interfaces. 62

6.5 Pipeline Solution With Boundary Conditions $\boldsymbol{w}_2(t) = 75\pi(D/2)^2$ (kg/s). **(Left)** $\omega_* = 0.25$ and $\kappa = 1.0$ With $\mathcal{P} = 0.12$. **(Middle)** $\omega_* = 0.1$ and $\kappa = 0.98$ With $\mathcal{P} = 0.1$. **(Right)** $\omega_* = 0.6$ and $\kappa = 0.9$ With $\mathcal{P} = 1.49$. 64

6.6 **(Left)** Color Map of the Power Spectrum $\mathcal{P}$ in (6.13) as a Function of (ω_*, κ) In (6.8). The Boundary Conditions Are $\alpha_1 = 0.2$ and $\boldsymbol{w}_2(t) = 75$. The Coloring Depicts the Minimum Between 1 and $\mathcal{P}$ In (6.13). **(Right)** Phase Operating Regions That Separate Periodic and Monotonic ($P\&M$), Periodic and Not Monotonic ($P\&\neg M$), and Neither Periodic nor Monotonic ($\neg P\&\neg M$). 66

Figure Page

7.1 **(Left)** Top: Configuration of the Network. Pipeline Dimensions: Blue to Purple = 50 km, Purple to Cyan = 30 km, Purple to Green = 20 km, and Green to Cyan Is 30 km. Bottom: Withdrawal Flow Profiles, Color-coded to Correspond to Associated Nodes. The Network Has Two Compressors, Indicated by Triangles, Located at the Start and End of the Pipe Directed from Blue to Purple. **(Right)** Left Column: Hydrogen Concentration Profiles at the Supply Node. Right Column: Corresponding Optimal Compressor Responses. 72

Figure Page

7.2 **(Left)** Left Column: Optimized Pressure at Refined Withdrawal Nodes Driven by the Respective Concentration Profiles from Figure 7.1. Right Column: Simulated Pressure at Refined Withdrawal Nodes Driven by Inlet Concentration and Optimal Compression Profiles from Figure 7.1. The Average l^2 Norm of the Relative Difference in Pressures, Using the Metric (7.6), Are Approximately .769%, .770%, And .769% for the Top, Middle, and Bottom Rows. The Maximum Relative Difference in Pressures, Using the Metric (7.7), Are Approximately 2.154%, 2.038%, and 1.971% for the Top, Middle, and Bottom Rows. The Combined Computational times for Optimization and Simulation Are Approximately 10.0 S, 8.0 S, and 7.7 S for the Top, Middle, and Bottom Rows, Respectively. **(Right)** Left Column: Optimized Mass Flux in Refined Edges Driven by the Respective Concentration Profiles from Figure 7.1. Right Column: Simulated Mass Flux in Refined Edges Driven by Inlet Concentration and Optimal Compression Profiles from Figure 7.1. The l^2 Relative Difference Metric Values Using (7.6) Are Approximately 3.994%, 4.608%, and 5.258% for the Top, Middle, and Bottom Rows. The Maximum Relative Difference Values Using Metric (7.7) Are Approximately 12.967%, 16.713%, and 21.509%, Respectively. 74

8.1 Computational time of the NLP as a function of the number of refined nodes of a single pipeline. The parameters are $\ell = 100$ (km), $D = 1$ (m), $\lambda = 0.01$, and $\sigma = 377$ (m/s). 81

Figure Page

8.2 Eigenvalues ($*$) of A and Poles ($\circ$) of $G(s)$ for a Single Pipeline with 30 Refined Edges. The Pipeline Parameters Are $\ell = 100$ (km), $D = 0.75$ (m), $\lambda = 0.01$, and $\sigma = 377$ (m/s). 82

8.3 **(Left)** Top: Network Configuration. Bottom Left: Mass Outflow Profiles at the Color-coordinated Nodes. Bottom Right: Eigenvalues of the State Matrix A Associated With the Network. **(Right)** Optimal Nodal Pressures, Mass Flows at the Inlets of the Edges, and the Compressor Actions. Pressure and Compressor Actions Are Color-coordinated With the Nodes and Compressor Stations of the Network to the Left. Solid Lines Represent the Nonlinear Solution and Marker Symbols Represent the Linearized Solution. 87

8.4 Percent Relative Error (as in (8.17)) as a Function of Percent Flow Variation (100κ) as Defined in (8.22) 91

Chapter 1

INTRODUCTION

Natural gas pipeline systems are designed to transport natural gas hundreds and even thousands of miles within and across the border lines of the United States from production plants to customers. Natural gas is a fossil fuel composed mostly of methane that is extracted from basins deep beneath the surface of the earth. There are over two million miles of pipelines in the United States that transport trillions of cubic feet of natural gas every year (see Figure 1.1 for an illustration). Friction between flowing gas and pipeline walls causes the pressure of the gas to decrease in the direction of transportation. As their name suggests, compressor stations are integrated into the network to boost the pressure of the gas back to satisfactory quality required for transportation and customer use. Compressor stations are large mechanical facilities that consist of one or several compressor units depending on the needs of the adjacent pipeline. There are over one thousand active compressor stations in the United States gas network (Figure 1.1). Natural gas infrastructures consist of other critical components such as regulators, valves, and sensor equipment. These components primarily serve to ensure the safety of the operation. Regulators may be turned on to reduce the pressure of the received gas, valves may be closed to redirect gas from one pipeline to another, and sensing meters provide system operators with recurrent pressure readings.

Natural gas is purchased primarily through daily contracts between the supplier and the customer. Up until recent years, natural gas was almost entirely purchased by local distribution companies (LDCs) for subsequent delivery to residences and businesses. LDCs have their own sets of distribution pipelines that distribute much

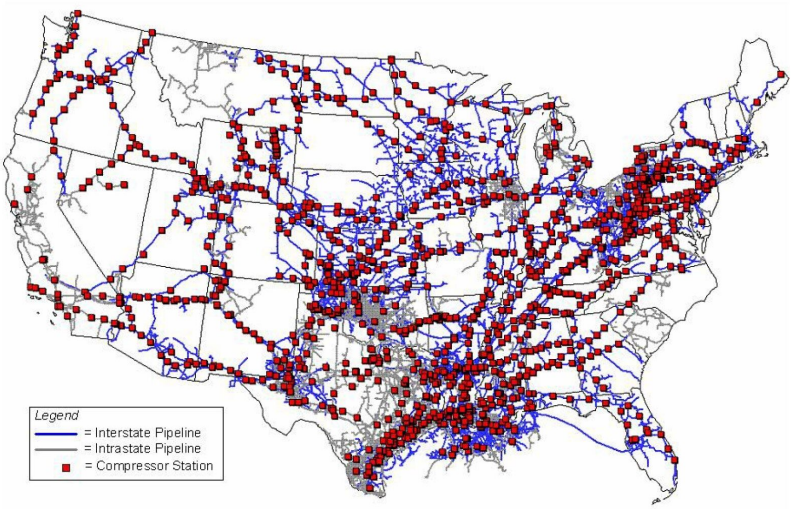

Figure 1.1: U.S. natural gas transportation infrastructure (Energy Information Administration, Office of Oil & Gas, Natural Gas Division, Natural Gas Transportation Information System (U.S. Energy Information Administration (2008))). The EIA has determined that the informational map displays here do not raise security concerns, based on the application of the federal geographic data committee's *Guidelines for Providing Appropriate Access to Geospatial Data in Response to Security Concerns*.

smaller volumes of natural gas over shorter distances and at much lower pressures than transmission pipelines. Regulators may be used in transitioning natural gas from transmission pipelines to distribution pipelines. During these early years, natural gas was steadily withdrawn from the network with a predictable volume each day. Under steady supply and withdrawal rates, the operation is independent of time and may be modeled mathematically using simple algebraic equations. This is known as the steady-state operation.

In the last 20 to 30 years, new emissions restrictions, along with the increased supply of natural gas in the United States, have further expanded the application of natural gas. In addition to LDCs, natural gas is now the primary source of energy used to generate electricity. According to the U.S. Energy Information Administration, natural gas currently accounts for 36% of total electric generation and is projected to increase to 39% by the year 2050. Electric power generators withdraw natural gas

from the network as a reliable energy source that balances temporary fluctuations of unreliable sources such as wind and solar. Although wind and solar are sustainable and renewable energy resources that are relatively cheaper than natural gas, they are generally unpredictable and highly variable throughout the course of a day. Natural gas is used for electric generation during time periods of shortages of these renewable energy sources. Time-varying fluctuations in withdrawal caused by renewable energy shortages induce time-varying flows in the natural gas transportation system, which poses great challenges to system operators, existing technology, and the research community. Mathematically, time-varying operations must be modeled with a system of nonlinear partial differential equations (PDEs) in each pipeline with independent variables being time and location along the pipe. The sets of PDEs for each pipe are coupled together with nodal conservation laws to form the network operation, which results in a large-scale system of nonlinear PDEs. This is known as the transient operation; it is considerably more challenging than the steady-state case of algebraic equations with algebraic coupling constraints.

The challenge of time-varying withdrawal is compounded with the transportation of not only natural gas but rather with heterogeneous mixtures of natural gas and hydrogen. One of the benefits of hydrogen is that it reacts with oxygen during combustion to form energy and release only water vapor if the hydrogen is cleanly produced from low-carbon energy sources such as biomass, solar, wind, nuclear, or fossil resources with carbon capture and storage. Studies indicate that mixtures of natural gas containing 20% hydrogen by molar fraction may be safely transported in natural gas pipelines and that these percentages of mixtures do not appear to damage end-user appliances or compromise their performance (see e.g. Melaina *et al.* (2013)). Thus, hydrogen could be transported through the existing infrastructure and then separated, or the mixture could be used directly as an end-use fuel. How-

ever, the unforeseen challenge of blending hydrogen with natural gas stems from their significantly different physical and chemical properties. The density of natural gas (primarily methane) is eight times as large as the density of hydrogen at room temperature and atmospheric pressure. This implies that the velocity of hydrogen is larger than that of natural gas at consistent flux rates. From a mathematical perspective, the effect of blending hydrogen into natural gas pipelines requires an additional PDE for each pipe to model the conservation of composition. This results in twice as many density variables than the case of just pure natural gas.

In both the steady-state and transient operation, the operational expenses of compressor units are so large that even a small improvement in their performance could save a significant amount of money. Therefore, the actions of the compressor units should be controlled according to the delivery requirements to minimize the expenditure of compressor energy. This is mathematically formulated as a PDE-constrained optimization problem. The objective is to minimize the amount of gas that compressor energy, while being subjected to satisfying withdrawal contracts, pressure limitations, and the physics of transporting mixtures of gases through the network. Figure 1.1 suggests that the optimal operation of the entire U.S. natural gas network is a task so great that the model requires simplification. The challenge, then, is to develop a model that is capable of handling large networks, while demonstrating the ability to accurately describe typical transient dynamics that occur in practice. The development of a relatively simple and relatively accurate model is one of the intentions of this thesis.

The remainder of this thesis is organized in detail as follows. A review of some of the background on modeling natural gas systems, with a focus on theory and computation, is presented in Chapter 2. In Chapter 3, we present the PDEs that are commonly used to model the flow of natural gas in a transmission pipeline. In

addition, this chapter details the linearization of these equations and derives the solution of the linearized PDEs. This development is well-known in the field. Our contribution involves the attenuation of waves propagating through the pipe. The wave attenuation analysis leads to the characterization of critical curves in Chapter 4 that partition the boundary condition parameters (frequency and amplitude of waves) into reliable and non-reliable operating regions. In addition, this chapter characterizes another set of critical curves that partition the boundary condition parameters into flow reversal and non-reversal regions. The minimum between the values of these two critical curves may be used to represent a more practical operating region. In particular, also in Chapter 4, we show that the level curves of the error between the linear and nonlinear solutions over the space of boundary parameters (frequency and amplitude of waves) are similar in geometrical shape to the practical critical curves. Therefore, the critical curves can be used to estimate the maximal region where linearization error is within a specified tolerance. To the best of the author's knowledge, the work presented in Chapter 4 has not been done before.

Chapter 5 introduces a simplified system of PDEs that govern sufficiently slow dynamics of mixtures of gases in networks. This chapter extends a popular spatial discretization scheme, originally developed for natural gas networks (Grundel *et al.* (2013, 2014)), to discretize the gas mixture PDEs and obtain an ODE control system. The development follows the approach taken in (Zlotnik *et al.* (2015a)) for pure natural gas. Chapter 5 also investigates transformations of flow variables to transform one ODE system into equivalent ODE systems. Chapter 6 proves that the equivalent ODE systems are monotone-ordered over the entire state and input space if the concentration of hydrogen is homogeneous everywhere in the network. Moreover, it is also proved that the ODE systems are not monotone-ordered, in general, over the entire state and input space if the concentration is heterogeneous. The first result is

an extension of the work done in (Zlotnik *et al.* (2016a); Misra *et al.* (2020)), where they proved that the simplified pure natural gas ODE systems are monotone-ordered (which would correspond to zero hydrogen concentration in our model). By the continuity of solutions with respect to inputs and initial conditions, we expect there to be a nontrivial interface that partitions the input space (concentration frequency and amplitude boundary conditions) into monotonic and non-monotonic regions (for each fixed set of plant parameters, such as network topology, pipe lengths, etc). This interface is investigated numerically in Chapter 6 for a pipeline with a specific set of plant parameters. In addition, Chapter 6 uses numerical simulations to demonstrate that certain pairs of frequencies and amplitudes of the sinusoidal concentration forcing may generate a non-periodic solution of the ODE system.

The ODE system of the gas mixture is used in Chapter 7 as the constraints of an optimal control problem that is developed to minimize the the amount of gas that compressors consume during operation. This problem has received significant attention for pure natural gas flows. However, to the author's knowledge, there are no results on the optimal control of transient flows of heterogeneous mixtures of gases in pipelines or networks of pipelines. We derive a nonlinear optimization program (NLP) by discretizing the time domain and using Euler's approximation for the time-derivative of the ODE system constraints. We apply the NLP for a mixture of gases in a small test network in Chapter 7 to demonstrate that small changes in gas concentration may create large changes in compressor activity and pressure gradients. In addition, the optimal compressor solution is interpolated in time and supplied to the ODE system to simulate the optimal trajectories of the ODE system. The optimal simulation is compared to the much coarser discretized optimization solution. Chapter 8 studies the optimization of transient flows of natural gas in networks. This chapter focuses on the development of a linear time-invariant

control system that may be used as the constraints of a linear optimization problem. An analytical bound on the error between the solutions of the linear and nonlinear systems is derived and verified computationally by plotting the error against the size of the flow variation around the steady-state. Moreover, Chapter 8 investigates the eigenvalues of the linear control system and compares them to the poles of the transfer matrix that was derived in Chapter 3 for the attenuation of waves. The approximation of the eigenvalues in a pipeline using the poles of the transfer matrix may be reasonably accurate for single pipelines with certain parameters. To the best of the author's knowledge, this comparison has not been done before for ODE systems that represent discretized PDEs of gas systems.

Chapter 9 presents some concluding remarks. Throughout this thesis, we try to point out separations between our contributions and contributions from the works of others. We also try to point out open questions resulting from our contributions.

Chapter 2

BACKGROUND

The set of Euler equations is the most commonly used model to describe the flow of natural gas in a transportation pipeline. The Euler equations consist of three nonlinear PDEs that represent the conservation of mass, momentum, and energy (Olds and Sage (1951); Stoner (1969); Issa and Spalding (1972); Wylie *et al.* (1974); Fincham and Goldwater (1979); van Deen and Reintsema (1983)). The flow variables are pressure, density, velocity, and temperature of the gas. This requires an equation of state to achieve a closed system. An equation of state is an algebraic relation between pressure, density, and temperature that enables the determination of any one of these three variables from knowledge of the other two. The Euler equations, coupled with the equation of state, collectively represent a closed system. There are many equations of state that vary in accuracy and operational ranges in which they apply (Modisette (2000)). The sensitivity of the equation of state to different operating regions is investigated in (Chaczykowski (2009)).

The energy equation can be neglected when the flow is characterized to be isothermal. The thermal and isothermal models are compared in (Osiadacz and Chaczykowski (2001)). It was demonstrated that a 50% variation in flow may introduce a 1% difference in the solutions of the two models when the temperature changes by 30° Celsius. When the flow is determined to be sufficiently slow, the inertia and kinetic energy terms in the momentum equation may be neglected (Osiadacz and GburzyĹska (2022); Herrán-González *et al.* (2009); Brouwer *et al.* (2011)). These simplifications, one at a time, lead to a hyperbolic system and a parabolic system of semilinear PDEs. In the latter case, the conservation of mass and momentum can be combined into a

single nonlinear diffusion equation expressed in terms of pressure. The above simplified models are used to reduce computational effort and provide insight into the qualitative behavior of flow. Some analytical investigations arising from the simplified PDEs include pressure sensitivity to time-varying withdrawal rates (Chertkov *et al.* (2015)) and approximate solutions (Herty *et al.* (2010)).

The solution of the isothermal Euler equations has been shown to exist uniquely in steady-state (Gugat *et al.* (2018); Ríos-Mercado *et al.* (2002)). A few specific solutions were proven to be unique in (Gugat and Wintergerst (2018); Gugat and Ulbrich (2017)). Additionally, the simplified parabolic system has been shown to satisfy certain physically intuitive and conceptually valuable monotonicity properties (Misra *et al.* (2020)), which imply uniqueness (assuming existence). Assuming existence of the solution of the isothermal Euler equations, a Lyapunov function was used in (Gugat *et al.* (2011); Gugat and Herty (2011)) to investigate exact controllability and feedback stabilization. For sufficiently small flow variations, existence and uniqueness of compressor actuation located midway between the inlet and outlet of a pipeline is proven in (Gugat *et al.* (2011)). The actuation is defined by a feedback controller that achieves, in finite time, a constant flux of gas through the compressor, while remaining sufficiently close to the specified profiles of supply and withdrawal.

The Euler equations may have closed-form solutions for very specific initial and boundary conditions. However, for general initial and boundary conditions, these equations do not admit a closed form solution and are usually solved numerically with the method of characteristics or finite volume and difference methods, including Euler, Crank-Nicolson, and Lax-Wendroff (Poloni *et al.* (1987); Bender (1979); Heath and Blunt (1968); Abbaspour and Chapman (2008)). The review in (Thorley and Tiley (1987)) compares some of these methods and discusses experimental validation. We refer the reader to (Zlotnik *et al.* (2017)) for a more recent validation

experiment. A method using Riemann invariants is developed in (Grundel and Herty (2020)) and compared to other finite volume methods that use midpoint and endpoint approximations. There, the authors report a reduction of unphysical oscillations with the Riemann invariants in comparison to the midpoint and endpoint methods. The reader is referred to (Qiu *et al.* (2020)) for details on the finite volume method and to (Stolwijk and Mehrmann (2018); Himpe *et al.* (2021)) for the midpoint and endpoint methods.

Assuming that a solution exists for a given set of compressor control inputs, it is nontrivial, even in steady-state, to design the control actions of compressors to minimize the amount of fuel that they consume during operation. After discretizing the pipelines in space, the resulting steady-state optimization problem is nonlinear, nonconvex, and was first solved in (Wong and Larson (1968a)) for a cascade connection pipes and quickly extended to tree networks in (Wong and Larson (1968b)). Since then, the optimization of compressor actuation in steady-state received significant attention (Percell and Ryan (1987); Ríos-Mercado *et al.* (2002); Carter (1998); De Wolf and Smeers (2000); Rachford and Carter (2000); Misra *et al.* (2015)). A model reduction method is employed in (Ríos-Mercado *et al.* (2002)) to improve the convergence properties of the optimization problem. The number of unknown variables in the reduced optimization problem is usually between 2% and 20% of the original number of unknown variables. It is shown in (Ríos-Mercado *et al.* (2002)) that this percentage, for their reduction method, is at most $2m/(l+n+m)\times 100\%$, where m, n, and l are the numbers of compressor stations, original network nodes, and pipelines, respectively. We refer the reader to (Grundel *et al.* (2014)) for other methods of model reduction. In (De Wolf and Smeers (2000)), the steady-state network optimization problem is split into two subroutines. In the first routine, an approximate convex optimization problem is obtained using piecewise linear connections. This approximation is shown

to satisfy all of the optimization constraints except for one. The optimal solution from the first routine is then used as a starting point for the full optimization problem. In (Correa-Posada and Sanchez-Martin (2014)), a mixed-integer linear program (LP) is developed for integrated optimization of electric power and natural gas networks operating in steady-state.

The transient optimization problem in natural gas networks is considerably more challenging than the associated steady-state problem, since the control actions of compressors and flow variables may no longer be assumed to be constant values in time. The number of optimization variables for the transient problem is N times larger than the associated steady-state problem, where N is the number of samples of the discretized time domain. As in the steady-state case, the goal is to design control actions of compressors to minimize their fuel consumption or maximize the economic value (Zlotnik *et al.* (2019)). As mentioned though, the optimal control action will vary in time if the withdrawal profiles vary in time, so the steady-state and transient optimization problems cannot be treated in the same way. Some of the early studies regarding transient optimization can be found in (Ehrhardt and Steinbach (2005); Steinbach (2007); Domschke *et al.* (2011)) and references therein. In these works, the Euler equations are discretized in space and time using first order finite differences. A first-order finite difference method is used in (Liu *et al.* (2011)) for optimal coordinated scheduling of electric and natural gas networks. An alternative to finite differences is the pseudospectral method (Ruths *et al.* (2011)). It was first derived for transient optimization in single pipelines (Zlotnik *et al.* (2015b)) and, shortly after, extended to networks (Zlotnik *et al.* (2015a)). In these works, the space domain is discretized using a finite volume method with a midpoint approximation (Grundel *et al.* (2013)). The pseudospectral transient optimization model has been subsequently used by its developers in a number of applications, including the opti-

mal coordination of natural gas and electric power networks and the estimation of parameters (Zlotnik *et al.* (2016b); Sundar and Zlotnik (2018)). An adaptive transient optimization model that switches between the isothermal Euler equations, the simplified hyperbolic semilinear PDEs, and the steady-state equations is developed in (Bales *et al.* (2009)). A review of some of the existing work in the optimization of natural gas networks may be found in (Ríos-Mercado and Borraz-Sánchez (2015)). More details on modeling and optimization formulations may be found in (Herty (2007); Benner *et al.* (2018); Herty (2008)).

Linearization of the Euler equations and its simplifications has been applied in a number of studies. For details on linearizing Euler's equations, the reader is referred to (Hall *et al.* (1994); Hall and Crawley (1989)). Some benefits and limitations of linearization are outlined in (Hennings (2018)). The nonlinear and linearized PDEs are simulated in (Luongo (1986)) using finite differences, where a 25% reduction in simulation time is reported. The accuracy of linearization is compared in (Wang *et al.* (2015)) between four different, yet equivalent, representations of the PDEs, e.g. using mass flux and density or using velocity and pressure, etc. Green's functions are used in (Beylin *et al.* (2020)) to form a linear optimization program, which is applied on a gas network to demonstrate a reduction of optimization time by two orders of magnitude in comparison to the nonlinear optimization program. A mixed-integer linear programming approach based on piecewise linearization of the nonlinear terms was developed in (Domschke *et al.* (2011)) for the optimal control of transient flows. A similar linearization approach for the coupled gas network and electric power grid is presented in (Sirvent *et al.* (2017)) for the case of steady-state gas flow. Piecewise linearization requires the addition of discretization points to accurately interpolate the nonlinear terms with linear segments, which could significantly increase the size of the network.

The dominant eigenmodes of the linearized equations are determined in (Behbahani-Nejad and Shekari (2010)) and used to construct a reduced model. Linearization of the Euler equations leads to a linear system of PDEs that may be solved in the Laplace domain (Zecchin *et al.* (2009)) and written in terms of a transfer function that maps specified inputs (boundary conditions/control actions) to outputs. The transfer function was used to detect the location of leaks in (Reddy *et al.* (2011)) and to investigate the attenuation of waves in (Baker *et al.* (2021)). The transfer function and some of its simplifications are analyzed in (Králik *et al.* (1984); Reddy *et al.* (2006)). In (Alamian *et al.* (2012)), the transfer function is approximated in the Laplace domain to first order in frequency and the approximate transfer function is inverted into a state-space realization. Another state-space representation is developed in (Aalto (2008)), where dominant Hankel singular values are used to reduce the transfer function and invert it back to state-space. We refer the reader to (Chen (1984)) for more details of state-space representations of linear systems.

The background of modeling and computing natural gas transport operations, as presented in this chapter, is far from complete, and does not begin to touch upon the surface of many excellent contributions to the field. For more details, we refer the reader to the references within the material mentioned here.

Chapter 3

NATURAL GAS PIPELINE ANALYSIS

This chapter investigates sinusoidal operations in natural gas pipelines using a transfer matrix. The flow equations for natural gas are presented in Section 3.1 and the linearized equations are derived in Section 3.2. The linear equations are solved in the frequency domain in Section 3.3. The transfer matrix that maps input variables to output variables is derived in Section 3.4. Section 3.5 studies the attenuation and amplification of waves. Much of this work, except for the results in Section 3.5, may be found in other sources (see, e.g. Králik *et al.* (1984); Reddy *et al.* (2006); Zecchin *et al.* (2009)). We refer the reader to our publication (Baker *et al.* (2021)) for more details.

3.1 Flow Equations

Isothermal flow of natural gas through a horizontal transmission pipeline is modeled with the one-dimensional isothermal Euler equations (Osiadacz (1984); Thorley and Tiley (1987)),

$$\partial_t \rho + \partial_x(\rho u) = 0, \tag{3.1a}$$

$$\partial_t(\rho u) + \partial_x(p + \rho u^2) = -\frac{\lambda}{2D}\rho u|u|, \tag{3.1b}$$

where $u(t,x)$, $p(t,x)$, and $\rho(t,x)$ are the velocity, pressure, and density variables of the gas, respectively. Here, $t \in [0,T]$ and $x \in [0,\ell]$, where T denotes the time horizon and ℓ denotes the length of the pipe. The above PDE system describes mass conservation (3.1a) and momentum conservation (3.1b). The dominant term in the momentum equation (3.1b) is the phenomenological Darcy-Weisbach term that

models momentum loss caused by turbulent friction, and is scaled by a dimensionless parameter λ called the friction factor. The remaining parameters are the internal pipe diameter D and the wave (sound) speed $\sigma = \sqrt{ZR\mathbf{T}}$, where Z, R, and $\mathbf{T}$ are the gas compressibility factor, specific gas constant, and absolute temperature, respectively. We assume that gas pressure p and gas density ρ satisfy the ideal gas equation of state $p = \sigma^2\rho$ with constant wave speed σ. While non-ideal modeling is necessary in practice to correctly quantify flows at pressures used in large gas transport pipelines (Srinivasan *et al.* (2022)), ideal gas modeling still qualitatively captures the flow phenomenology. Extension to non-ideal gas modeling can be made by applying appropriate nonlinear transforms (Gyrya and Zlotnik (2019)).

It is standard to use the per area mass flux $\varphi = \rho u$. For slowly-varying boundary conditions, the kinetic energy term $\partial_x(\rho u^2)$ and the inertia term $\partial_t(\rho u)$ in equation (3.1b) may be omitted (Osiadacz (1984)). In this case, the flow equations in (3.1) may be reduced to either a hyperbolic system or a parabolic system. In this chapter, we consider the hyperbolic equation

$$\partial_t\rho + \partial_x\varphi = 0, \tag{3.2}$$

$$\partial_t\varphi + \sigma^2\partial_x\rho = -\frac{\lambda}{2D}\frac{\varphi|\varphi|}{\rho}. \tag{3.3}$$

The initial and boundary conditions associated with (3.2)-(3.3) are given by

$$\rho(0,x) = \varrho(x), \qquad \varphi(0,x) = \phi(x), \qquad x \in [0,\ell], \tag{3.4}$$

$$\rho(t,0) = \rho_1(t), \qquad \varphi(t,0) = \varphi_1(t), \qquad t \in [0,T], \tag{3.5}$$

where ρ_1 and φ_1 dictate the rates of density and mass flux at inlet of the pipeline (node 1). The initial condition in (3.4) is assumed to be the steady-state solution defined by

$$\phi(x) = \overline{\varphi}, \qquad \varrho^2(x) = \overline{\rho}^2 - \frac{\lambda\overline{\varphi}|\overline{\varphi}|}{\sigma^2 D}x, \tag{3.6}$$

where $\overline{\rho} = \rho_1(0)$ and $\overline{\varphi} = \varphi_1(0)$ are constants. We assume standard conditions for well-posedness (Gugat *et al.* (2012)), and specifically that the boundary conditions are smooth, slowly-varying, bounded in their respective domains, and compatible with the initial conditions to ensure the existence of a smooth, slowly-varying, bounded solution (Gugat and Herty (2011)).

3.2 Linear Flow Equations

It is convenient in the analysis of linearization to write density and flux as a summation of steady-state and variation terms of the form

$$\begin{aligned} \rho(t,x) &= \varrho(x) + \rho_e(t,x), \\ \varphi(t,x) &= \phi(x) + \varphi_e(t,x). \end{aligned} \tag{3.7}$$

We substitute (3.7) into (3.2)-(3.3) to get the governing equations of the variation variables, where the nonlinearity on the right hand side of (3.3) becomes

$$f(\rho_e, \varphi_e) = \frac{\lambda}{2D}\left(\frac{\phi|\phi|}{\varrho} - \frac{(\phi+\varphi_e)|\phi+\varphi_e|}{\varrho+\rho_e}\right). \tag{3.8}$$

Making the following two approximations: i) the function f in (3.8) is approximated with its linearization around the origin and ii) the coefficients of the linearization are approximated using $1/\varrho(x) \simeq 1/\overline{\rho}$, we obtain the constant coefficient linear system

$$\partial_t \rho_e + \partial_x \varphi_e = 0, \tag{3.9}$$

$$\partial_t \varphi_e + \sigma^2 \partial_x \rho_e = \alpha \rho_e + \beta \varphi_e, \tag{3.10}$$

with initial and boundary conditions

$$\begin{aligned} \rho_e(0,x) &= 0, & x &\in [0,\ell], \\ \varphi_e(0,x) &= 0, & x &\in [0,\ell], \\ \rho_e(t,0) &= \rho_1(t) - \overline{\rho}, & t &\in [0,T], \\ \varphi_e(t,0) &= \varphi_1(t) - \overline{\varphi}, & t &\in [0,T], \end{aligned} \tag{3.11}$$

where α and β are constant coefficients given by

$$\alpha = \frac{\lambda\overline{\varphi}|\overline{\varphi}|}{2D\overline{\rho}^2}, \qquad \beta = -\frac{\lambda|\overline{\varphi}|}{D\overline{\rho}}. \tag{3.12}$$

Here, we label the linearized variables with the same symbols as the nonlinear variables. From here onward, these symbols will always represent the flow variations of the linear system. Therefore, we have the approximation

$$\begin{aligned} \rho(t,x) &\simeq \varrho(x) + \rho_e(t,x), \\ \varphi(t,x) &\simeq \phi(x) + \varphi_e(t,x). \end{aligned} \tag{3.13}$$

The class of linear systems in (3.9)-(3.11) is called *amplified* if α in (3.10) is defined by (3.12). It is called *unamplified* if α in (3.10) is defined to be zero.

3.3 Laplace Domain Solution

The continuous-time Laplace transform of a function $\psi(t,x)$ is defined by

$$\Psi(s,x) = \int_0^\infty \psi(t,x)e^{-st}dt,$$

where $s = r + \mathbf{j}\omega$ is the Laplace frequency and $\mathbf{j} = \sqrt{-1}$ is the imaginary unit. Occasionally, we use the operator notation $\Psi(s,x) = (\mathfrak{L}\psi)(s,x)$ to denote the Laplace transform of the function ψ.

The Laplace transforms of the variation variables are defined by $P(s,x) = (\mathfrak{L}\rho_e)(s,x)$ and $\Phi(s,x) = (\mathfrak{L}\varphi_e)(s,x)$. In this definition, the time interval $[0,T]$ is extended to the nonnegative real numbers and the variation variables are extended with compact support or with periodic extension with period T, depending upon the sought application. Applying the Laplace transform to (3.9)-(3.10), we obtain the following set of equations

$$\begin{aligned} sP + \partial_x\Phi &= 0, \\ s\Phi + \sigma^2\partial_x P &= \alpha P + \beta\Phi. \end{aligned} \tag{3.14}$$

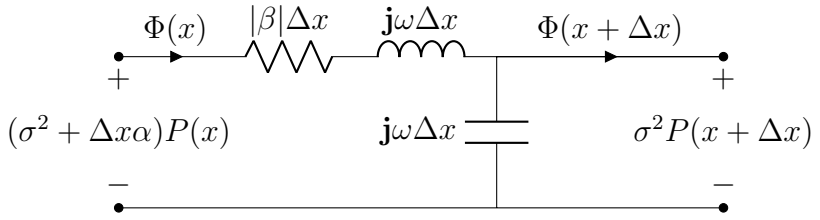

Figure 3.1: Electric Circuit Representation of a Section of Pipeline.

The boundary conditions associated with (3.14) are given by

$$P(s,0) = P_1(s), \qquad \Phi(s,0) = \Phi_1(s), \tag{3.15}$$

where $P_1(s) = \mathfrak{L}(\rho_1(t) - \overline{\rho})(s)$ and $\Phi_1(s) = \mathfrak{L}(\varphi_1(t) - \overline{\varphi})(s)$. The equations in (3.14)-(3.15) characterize the transient and sinusoidal responses in the Laplace domain. Since the coefficients in (3.14) are constant, we can derive a solution analytically. We first consider the following example.

Example. Suppose that a small section of pipe with a length of Δx is represented by the two-port network shown in Figure 3.1. The equations in (3.14) are obtained by applying Kirchhoff's circuit laws. The drop in density along the pipeline is considered to be comparable to the voltage drop induced by the impedance of the circuit. The conservation of current through a node in a power system is identical to the conservation of flux through a node in a gas system. In this way, voltage and current in electric transmission lines are thought to play similar roles to density and mass flux in natural gas pipelines. It is seen in Figure 3.1 that $|\beta|$ represents *resistance* and α represents *amplification* of density. The amplification of density explains the previous terminology. □

Similar to an electric line, define series impedance and characteristic impedance for the gas pipeline, respectively, by

$$z(s) = s - \beta, \qquad z_c(s) = \sqrt{\frac{s-\beta}{s}}. \tag{3.16}$$

It is relevant to note that both of these terms depend on β, but neither depend on α.

The equations in (3.14) are weakly coupled and can be decoupled by introducing second-order derivatives

$$\begin{aligned} \sigma^2 \partial_{xx} P - \alpha \partial_x P - szP &= 0, \\ \sigma^2 \partial_{xx} \Phi - \alpha \partial_x \Phi - sz\Phi &= 0. \end{aligned} \tag{3.17}$$

A solution of (3.17) is given by

$$P(s,x) = \Psi_+ e^{\mu_+ x} + \Psi_- e^{\mu_- x}, \tag{3.18}$$

$$\Phi(s,x) = \frac{\sigma^2}{z} \left(\mu_- \Psi_+ e^{\mu_+ x} + \mu_+ \Psi_- e^{\mu_- x} \right), \tag{3.19}$$

where $\mu_\pm = \alpha/(2\sigma^2) \pm \mu/\sigma^2$ and $\mu = \sqrt{\alpha^2/4 + \sigma^2 sz}$. The complex exponential terms $e^{\mu_\pm x}$ represent traveling waves that propagate in opposite directions along the length of the pipe. The waves travel along the pipe with attenuation depending upon $\mu_\pm$ and the set of frequencies with which P_1 and Φ_1 in (3.15) are composed. Both of the traveling waves $e^{\mu_\pm x}$ are physically relevant since the pipe has finite length and, therefore, the waves are bounded. In general, it follows that Ψ_+ and Ψ_- are both nonzero.

The coefficients $\Psi_\pm$ are uniquely determined by the boundary conditions. Evaluating (3.18)-(3.19) at $x = 0$ and using (3.15) we obtain

$$\Psi_\pm = \pm \frac{\mu_\pm}{\mu_+ - \mu_-} P_1 \mp \frac{z\sigma^{-2}}{\mu_+ - \mu_-} \Phi_1.$$

Substituting these coefficients into (3.18)-(3.19) gives an expression for P and Φ explicitly in terms of P_1 and Φ_1 of the form

$$P = \frac{\mu_+ e^{\mu_+ x} - \mu_- e^{\mu_- x}}{\mu_+ - \mu_-} P_1 - \frac{z}{\sigma^2} \frac{e^{\mu_+ x} - e^{\mu_- x}}{\mu_+ - \mu_-} \Phi_1, \tag{3.20}$$

$$\Phi = -s \frac{e^{\mu_+ x} - e^{\mu_- x}}{\mu_+ - \mu_-} P_1 - \frac{\mu_- e^{\mu_+ x} - \mu_+ e^{\mu_- x}}{\mu_+ - \mu_-} \Phi_1. \tag{3.21}$$

These expressions define the solution of (3.14) for each $x \in [0, \ell]$.

Example. We consider periodic solutions with $s = \mathbf{j}\omega$. Suppose that the boundary condition profiles in (3.11) are periodic with period T. Expanding into Fourier series representations gives the expressions

$$\rho_e(t,0) = \sum_{k=-\infty}^{\infty} \overline{\rho}_k e^{\mathbf{j}\omega_k t}, \quad \varphi_e(t,0) = \sum_{k=-\infty}^{\infty} \overline{\varphi}_k e^{\mathbf{j}\omega_k t}, \tag{3.22}$$

where $\omega_k = 2\pi k/T$ for each integer k. The Fourier coefficients are constants defined in the usual way. Let $\delta(\omega)$ be the impulse at $\omega = 0$. The Fourier transforms of the representations in (3.22) are the trains of impulses

$$P_1(\omega) = \sum_{k=-\infty}^{\infty} 2\pi\overline{\rho}_k \delta(\omega - \omega_k), \tag{3.23}$$

$$\Phi_1(\omega) = \sum_{k=-\infty}^{\infty} 2\pi\overline{\varphi}_k \delta(\omega - \omega_k), \tag{3.24}$$

where the areas of the impulses are proportional to the Fourier series coefficients of the boundary conditions. Define

$$a(\omega,x) = \frac{\mu_+ e^{\mu_+ x} - \mu_- e^{\mu_- x}}{\mu_+ - \mu_-}, \qquad b(\omega,x) = -\frac{z}{\sigma^2}\frac{e^{\mu_+ x} - e^{\mu_- x}}{\mu_+ - \mu_-}, \tag{3.25}$$

$$c(\omega,x) = -y\frac{e^{\mu_+ x} - e^{\mu_- x}}{\mu_+ - \mu_-}, \qquad d(\omega,x) = -\frac{\mu_- e^{\mu_+ x} - \mu_+ e^{\mu_- x}}{\mu_+ - \mu_-}. \tag{3.26}$$

Taking inverse Fourier transforms in (3.20)-(3.21) and using the definition of the impulse, we obtain the solution expression in the time domain given by

$$\begin{aligned} \rho_e(t,x) &= \textstyle\sum_{k=-\infty}^{\infty} [a(\omega_k,x)\overline{\rho}_k + b(\omega_k,x)\overline{\varphi}_k] e^{\mathbf{j}\omega_k t}, \\ \varphi_e(t,x) &= \textstyle\sum_{k=-\infty}^{\infty} [c(\omega_k,x)\overline{\rho}_k + d(\omega_k,x)\overline{\varphi}_k] e^{\mathbf{j}\omega_k t}. \end{aligned} \tag{3.27}$$

The coefficients of the solution are weighted sums of the Fourier series coefficients in (3.22), where the weights are equal to the samples of the coefficients in (3.20)-(3.21) at equally spaced frequencies $\omega = \omega_k$.

The harmonic component $e^{\mathbf{j}\omega_n t}$ is present in (3.27) if and only if it is present in at least one of the Fourier series representations in (3.22). This is the principle of

superposition in linear systems. We interpret this result as follows. A given frequency component is present in density and mass flux along the entire pipe if and only if it is present in either density or mass flux at the boundary of the pipe. It is evident from (3.27) that the magnitude of the harmonic component $e^{\mathrm{j}\omega_n t}$ is altered according to the magnitudes of the coefficients a, b, c, and d evaluated at the frequency ω_n. This is called wave attenuation. $\square$

3.4 Transfer Matrix Representation

The transfer matrix maps input variables to output variables. The natural input for a gas pipeline is the density at the inlet and the mass flux at the outlet of the pipeline. Rearranging (3.20)-(3.21) for an unamplified pipeline, we obtain the spatially-dependent transfer matrix representation

$$\begin{bmatrix} P \\ \Phi \end{bmatrix} = \begin{bmatrix} \frac{\cosh\left(\frac{\gamma}{\sigma}(\ell-x)\right)}{\cosh\left(\frac{\gamma}{\sigma}\ell\right)} & -\frac{z_c}{\sigma}\frac{\sinh\left(\frac{\gamma}{\sigma}x\right)}{\cosh\left(\frac{\gamma}{\sigma}\ell\right)} \\ \frac{\sigma}{z_c}\frac{\sinh\left(\frac{\gamma}{\sigma}(\ell-x)\right)}{\cosh\left(\frac{\gamma}{\sigma}\ell\right)} & \frac{\cosh\left(\frac{\gamma}{\sigma}x\right)}{\cosh\left(\frac{\gamma}{\sigma}\ell\right)} \end{bmatrix} \begin{bmatrix} P_1 \\ \Phi_2 \end{bmatrix}, \tag{3.28}$$

where $P_1(s) = P(s,0)$ and $\Phi_2(s) = \Phi(s,\ell)$. Evaluating the top equation of (3.28) at $x = \ell$ and the bottom equation at $x = 0$ leads to the nodal transfer matrix representation

$$\begin{bmatrix} P_2 \\ \Phi_1 \end{bmatrix} = \begin{bmatrix} \operatorname{sech}\left(\gamma\frac{\ell}{\sigma}\right) & -\frac{z_c}{\sigma}\tanh\left(\gamma\frac{\ell}{\sigma}\right) \\ \frac{\sigma}{z_c}\tanh\left(\gamma\frac{\ell}{\sigma}\right) & \operatorname{sech}\left(\gamma\frac{\ell}{\sigma}\right) \end{bmatrix} \begin{bmatrix} P_1 \\ \Phi_2 \end{bmatrix}, \tag{3.29}$$

where $P_2(s) = P(s,\ell)$ and $\Phi_1(s) = \Phi(s,0)$.

3.5 Wave Attenuation

As illustrated in the last example in Section 3.3, the attenuation of a wave in a gas pipeline describes how the amplitude of the wave changes as the wave propagates through the pipe. By the superposition principle of linear systems, the attenuation

of each sinusoidal component of the wave is determined by the amplitude of its coefficient within the solution, as in (3.27). Therefore, for the remainder of this chapter, we assume that the boundary conditions are periodic and consider each harmonic component separately. The boundary conditions are given by

$$\rho_e(t,0) = \kappa_1 \overline{\rho} \sin(\omega_1 t), \quad \varphi_e(t,\ell) = \kappa_2 \overline{\varphi} \sin(\omega_2 t), \tag{3.30}$$

where ω_k are frequencies in radians per hour and κ_k are amplitude factors for $k = 1, 2$.

Example. The most natural operation of a gas pipeline is specified by constant pressure or density at the inlet and variable mass flow at the outlet of the pipeline, i.e. ω_1 is zero and ω_2 is a free parameter in (3.30). The Fourier transforms of the boundary conditions in (3.30) are given by

$$P_1 = 0, \qquad \Phi_2 = \kappa_2 \overline{\varphi} \frac{\pi}{\mathbf{j}} \left(\delta(\omega - \omega_2) - \delta(\omega + \omega_2) \right).$$

Substituting these expressions into (3.29) results in

$$P_2 = -\frac{z_c}{\sigma} \tanh(\gamma \tfrac{\ell}{\sigma})] \Phi_2, \qquad \Phi_1 = \operatorname{sech}(\gamma \tfrac{\ell}{\sigma}) \Phi_2. \tag{3.31}$$

The limits of the magnitudes of these expressions, as $\omega_2 \to \infty$, are given by (Baker *et al.* (2021))

$$|P_2| \to \frac{1}{\sigma} |\Phi_2|, \qquad |\Phi_1| \to O(e^{-|\beta|\ell/(2\sigma)}) \approx 0. \tag{3.32}$$

The limiting expressions in (3.32) show that, as the frequency of flux at the outlet increases, the amplitude of the flux at the inlet approaches zero, while the amplitude of density at the outlet approaches the amplitude of flux at the outlet divided by the speed of sound σ. We conclude that if mass flux withdrawal is characterized by high frequency oscillation, the resulting oscillatory wave at the inlet will be damped out. In pipeline operations, this is an important feature. In particular, high frequency

demand oscillations are averaged out and there is no need to adjust supply rates at the sending end of the pipe to match them. □

Example. An alternate mode of operation is specified by varying inlet density and holding outlet mass flow constant. Intuitively, in networks of pipelines this operation corresponds, e.g. to the spectral decomposition of pressure variations caused by varying withdrawal in neighboring pipelines. In this case, ω_1 is a free parameter and ω_2 is zero in (3.30). Following the calculations that lead to (3.31) we arrive at

$$P_2 = \operatorname{sech}(\gamma \tfrac{\ell}{\sigma}) P_1, \qquad \Phi_1 = \frac{\sigma}{z_c} \tanh(\gamma \tfrac{\ell}{\sigma})] P_1. \tag{3.33}$$

Taking the high frequency limits, we find

$$|P_2| \to O(e^{-|\beta|\ell/(2\sigma)}) \approx 0, \qquad |\Phi_1| \to \sigma |P_1|. \tag{3.34}$$

The limiting expressions in (3.34) show that as the frequency of inlet density increases, the amplitude of outlet density approaches zero and the amplitude of the resulting oscillation in the inlet flux approaches an amplitude of being σ times as large as the amplitude of the inlet density. Therefore, at high frequency, the resulting flux oscillations have amplitudes large enough to drive gas into the negative flow direction, as the factor $\sigma \in (300, 500)$ in (3.34) is large. □

Chapter 4

NATURAL GAS PIPELINE APPLICATIONS

We use the results on wave attenuation from the previous chapter to investigate several applications of natural gas flows in a pipeline. To the best of the author's knowledge, these applications of the transfer matrix have not been explored before in natural gas pipelines. A reliable operating region is defined and derived in Section 4.1 and flow reversal waves is defined and derived in Section 4.2. The error resulting from linearization is analyzed as a function of frequency and amplitude of the boundary conditions in Section 4.3. The key result in this error analysis is that the level curves of the error plot are similar in geometrical shape to the boundary of the reliable operating region that avoids flow reversal. Therefore, the scaled boundary curves can be used to estimate the maximal regions where linearization is applicable. Section 4.4 demonstrates the results using numerical simulations.

4.1 Reliable Operating Region

The solution of (3.2)-(3.5) is said to be *reliable* if the amplitude of $\rho(t,\ell)$ does not exceed $0.1\overline{\rho}$. From Parseval's theorem (Oppenheim *et al.* (1997)), the "boundary" of this criterion is defined in the frequency domain by $|P(\mathbf{j}\omega,\ell)| = 0.1\overline{\rho}$. Suppose $\overline{\rho}$ and $\overline{\varphi}$ are positive in such a way that the steady-state in (3.6) is well-defined for all $x \in [0,\ell]$. We assume that the boundary conditions (of the linear and nonlinear PDEs of variation variables) are periodic and consider each harmonic component separately. As in (3.30), the boundary conditions are given by

$$\rho_e(t,0) = \kappa_1\overline{\rho}\sin(\omega_1 t), \quad \varphi_e(t,\ell) = \kappa_2\overline{\varphi}\sin(\omega_2 t),$$

where ω_k are frequencies in radians per hour and κ_k are amplitude factors for $k = 1, 2$. We consider the following reliability question concerning the frequency ω_2 and amplitude factor κ_2, corresponding to varying flux at the outlet of the pipe.

> *If density is constant at the inlet of the pipe ($\omega_1 = 0$ or $\kappa_1 = 0$) and mass flux varies at the outlet with frequency $\omega_2 = 2\pi f_2$, what is the maximum value of κ_2 for which the amplitude of $\rho(t, \ell)$ is less than $0.1\overline{\rho}$?*

Using (3.29) with $|P_1| = 0$, $|P_2| = 0.1\overline{\rho}$, and $|\Phi_2| = \kappa_2\overline{\varphi}$, the solution of this problem is given by

$$\kappa_2 = \kappa_{\mathrm{ROR}_2} := \frac{0.1\overline{\rho}\sigma}{\overline{\varphi}|z_c(\omega_2)|}|\coth(\gamma(\omega_2)\ell/\sigma)|. \tag{4.1}$$

Since κ_{ROR_2} is determined from the boundary of all such reliable solutions, it follows that the pair ω_2 and κ_2 generates a reliable solution for all κ_2 with $0 \le \kappa_2 \le \kappa_{\mathrm{ROR}_2}$. We define the reliable operating region by

$$\mathrm{ROR}_2 = \{(\omega_2, \kappa_2) : 0 \le \omega_2 < \infty \ \& \ 0 \le \kappa_2 \le \kappa_{\mathrm{ROR}_2}\},$$

where κ_{ROR_2}, defined in (4.1), is a function of ω_2 and the flow parameters.

The top right side of Figure 4.1 depicts κ_{ROR_2} as a function of ω_2 for various values of $\overline{\varphi}$. The other parameter values are $\ell = 100$ (km), $D = 0.5$ (m), $\lambda = 0.011$, $\sigma = 338.23$ (m/s), and $\overline{\rho} = 56.817$ (kg/m^3) (Gyrya and Zlotnik (2019)). These parameters are used for the remaining computations presented in this chapter. It is evident from Figure 4.1 that the flux at the outlet may vary around its mean by more than 100% (i.e., $\kappa_2 > 1$ in (3.30)) and still satisfy the condition of being a reliable solution (i.e., $\kappa_2 \le \kappa_{\mathrm{ROR}_2}$). For $\kappa_2 > 1$, we assume that the pipeline is bidirectional with the capability of delivering gas in both directions. In this case, there are time intervals corresponding to the valleys of the sinusoid in (3.30) during which mass flux is negative at the outlet, i.e. gas is injected back into the pipeline at the outlet.

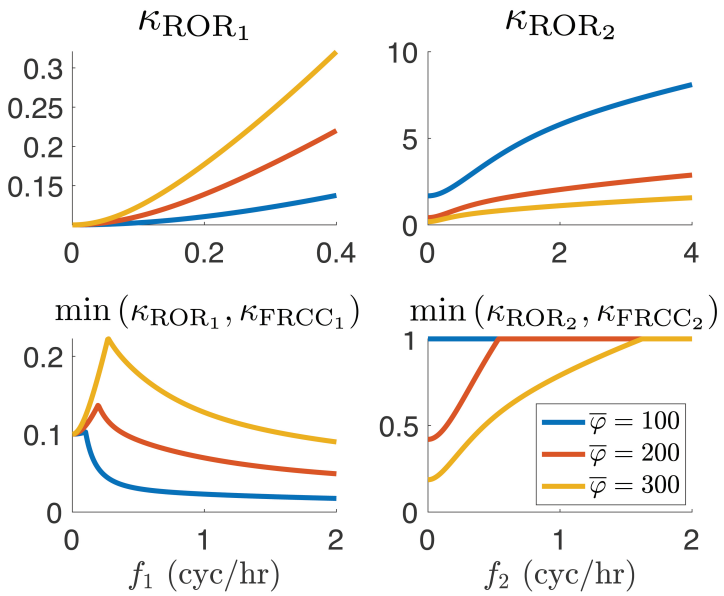

Figure 4.1: Top: (Left) Boundary of ROR_1. (Right) Boundary of ROR_2. Bottom: Minimum between the boundary of the ROR and the flow reversal critical curve (defined in Section 4.2).

A similar reliability question exists for variations in density at the inlet and constant mass flux at the outlet. In particular, if flux is constant at the outlet of the pipe and density varies at the inlet with frequency $\omega_1 = 2\pi f_1$, what is the maximum value of κ_1, denoted by κ_{ROR_1}, with which the amplitude of $\rho(t, \ell)$ is less than $0.1\overline{\rho}$? The hyperbolic expressions in (3.29) can be used to show that κ_{ROR_1} increases exponentially with increasing ω_1. This is a consequence of high frequency wave attenuation. It is clear that the linear system approximation is not applicable for such large amplitude variations in density. However, for low frequencies, we may derive a solution in a similar way as we did for κ_{ROR_2}. In doing so, we define the reliable operating region by

$$\mathrm{ROR}_1 = \{(\omega_1, \kappa_1) : 0 \leq \omega_2 < \infty \ \& \ 0 \leq \kappa_1 \leq \kappa_{\mathrm{ROR}_1}\},$$

where $\kappa_{\mathrm{ROR}_1} = \min\{0.1|\cosh(\gamma(\omega_1)\ell/\sigma)|, \kappa_1^{\max}\}$ and $\kappa_1^{\max} = 0.3$ is a judicious bound. In practice, the amplitude of pressure should be as close to zero as possible, so $\kappa_1^{\max} = 0.3$ is reasonable for our purpose. The top left-hand side of Figure 4.1 depicts κ_{ROR_1}

as a function of low frequency ω_1 for various values of $\overline{\varphi}$.

Although the curves on the top of Figure 4.1 represent the boundaries of the RORs, the curves on the bottom are more feasible. The curves on the bottom of Figure 4.1 start to trace along the ROR curves for small frequencies until they reach a point after which they trace what we call the flow reversal critical curves (FRCCs) (see Section 4.2). An FRCC represents the boundary of a region that limits the solution to flow in only one direction, i.e., the flux varies by less than 100% of its mean. The key takeaways between the tops and bottoms of Figure 4.1 are summarized as follows. First, the bottom left figure significantly damps the exponential growth of κ_{ROR_1}. We, therefore, expect the bottom region to be more appropriate for linearization than the top region. Second, the curves on the bottom right figure increase as the frequency increases, but they are bounded by unity for all $\overline{\varphi}$, as expected by the definition of the FRCC. The boundary curves of the bottom figures provide more appropriate regions for linearization than the top figures since the flow variation is now limited to at most 100% of its mean.

4.2 Flow Reversal

There are many frequency and amplitude pairs in both regions ROR_1 and ROR_2 that can create flow reversal waves. A flow reversal occurs in sinusoidal operation if the amplitude of $\varphi(t_*, x_*)$, for some $t_* \in [0, T]$ and $x_* \in [0, \ell]$, is greater than the steady-state mean value $\overline{\varphi}$ around which $\varphi(t, x)$ oscillates. Using Parseval's theorem, we say that flow reverses direction at position $x \in [0, \ell]$ with frequency ω if $|\Phi(\omega, x)| > \overline{\varphi}$. If flow reverses direction with frequency ω, then the null point $\xi \in [0, \ell]$ is defined by $|\Phi(\omega, \xi)| = \overline{\varphi}$ (assuming it exists). If no solution ξ exists, then one of two things happen: either flow does not reverse direction or the flow reversal wave propagates the entire length of the pipe approximately unattenuated.

4.2.1 Flow Reversal Critical Curves

The FRCCs are defined to be the interfaces (in the (ω, κ) plane) above which the corresponding flow solution reverses direction and below which it does not. Clearly, if density is constant at the inlet and mass flux varies at the outlet according to the boundary condition in (3.30), then the maximum value of the amplitude factor κ_2 that avoids flow reversal must be $\kappa_{\mathrm{FRCC}_2} = 1$ for all frequencies. That is, the pair (ω_2, κ_2) generates a solution that does not change direction if $0 \leq \kappa_2 \leq \kappa_{\mathrm{FRCC}_2} = 1$. This is the trivial FRCC that provides the upper bound of unity on the bottom right side of Figure 4.1. The nontrivial FRCC is posed as follows.

> *If flux is constant at the outlet and density varies at the inlet with frequency* $\omega_1 = 2\pi f_1$, *which value of* κ_1 *with* $(\omega_1, \kappa_1) \in \mathrm{ROR}_1$ *satisfies* $|\Phi(\omega_1, 0)| = \overline{\varphi}$?

The solution is given by $\kappa_1 = \kappa_{\mathrm{FRCC}_1} = \overline{\varphi}|z_c||\coth(\gamma(\omega_1)\ell/\sigma)|/(\sigma\overline{\rho})$. For each value of ω_1, any value of $\kappa_1 < \kappa_{\mathrm{FRCC}_1}$ with $(\omega_1, \kappa_1) \in \mathrm{ROR}_1$ will result in a reliable operation that avoids flow reversal at the inlet, i.e. *pullback*, and any value of $\kappa_1 > \kappa_{\mathrm{FRCC}_1}$ with $(\omega_1, \kappa_1) \in \mathrm{ROR}_1$ will result in a reliable pullback operation. Thus, for a given set of pipeline parameters, the pair $(\omega_1, \kappa_{\mathrm{FRCC}_1})$ defines the FRCC. The minimum value, $\min(\kappa_{\mathrm{FRCC}_1}, \kappa_{\mathrm{ROR}_1})$, is plotted as a function of ω_1 on the bottom left-hand side of Figure 4.1. The FRCC improves the judicious choice of limiting $\kappa_1^{\max} \leq 0.3$ for high frequencies in the definition of ROR_1.

4.2.2 Null Points

If flow reversal exists, we may investigate the existence and location of the null point. We consider the following question.

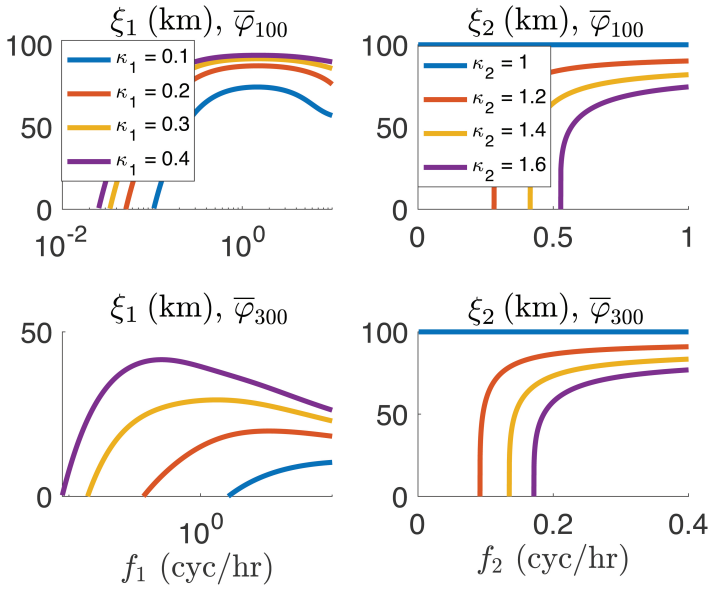

Figure 4.2: Left: Inlet-generated null point ξ_1. Right: Outlet-generated null point ξ_2 for various amplitude factors.

> *If density is constant at the inlet and flux varies at the outlet with frequency* $\omega_2 = 2\pi f_2$ *and amplitude factor* $\kappa_2 \geq 1$ *with* $(\omega_2, \kappa_2) \in \mathrm{ROR}_2$, *which value of* $\xi_2 \in [0, \ell]$ *satisfies* $|\Phi(\omega_2, \xi_2)| = \overline{\varphi}$*?*

The null point ξ_2 is plotted on the right-hand side of Figure 4.2 as a function of f_2 for various values of κ_2. Figure 4.2 shows that there is essentially a jump in the location of the null point near $f_2 = 0.5$ for $\overline{\varphi} = 100$ and near $f_2 = 0.2$ for $\overline{\varphi} = 300$. In general, the faster that flux oscillates at the outlet, the closer the null point is to the outlet. This result is a consequence of the attenuation of high frequency waves. For $\overline{\varphi} = 100$, the null point ξ_2 will be located within 20 km from the outlet of the 100 km pipeline if $f_2 > 5$. For $\overline{\varphi} = 300$, the null point will be located within 20 km from the outlet if $f_2 > 1$. This suggests that smaller means of flux require higher frequencies than larger means to have null points within 20 km from the outlet.

The behavior of the null point for low and high frequencies can be investigated with asymptotic expansions. Taking magnitudes of the bottom equation in (3.28),

applying the boundary conditions $|P_1|$=0 and $\Phi_2 = \kappa_2\overline{\varphi}$, and using the definition of the null point $|\Phi| = \overline{\varphi}$, we obtain the description of the null point as a function of ω_2, κ_2, and the other pipeline parameters as

$$\frac{|\cosh(\gamma\ell/\sigma)|}{\kappa_2} = |\cosh(\gamma\xi_2/\sigma)|.$$

For large ω_2, this equation can be approximated with $|\exp(\gamma\xi_2/\sigma)| = |\exp(\gamma\ell/\sigma)|/\kappa_2$, from which we obtain $\xi_2 = [\ell - \sigma\ln(\kappa_2)/|\gamma|]$. For $\kappa_2 = 1$, we recover the constant blue curve $\xi_2 = \ell = 100$ km in Figure 4.2 described by the trivial FRCC. The lack of attenuation of low frequency waves suggests that, for small ω_2, the reversal wave will propagate from the outlet to almost the inlet of the pipe, i.e., the null point ξ_2, if it exists, should be close to zero for low frequency excitation. Therefore, for small ω_2, we use a second order Taylor series expansion around $\xi_2 = 0$ to obtain the approximate representation $1 + |\gamma\xi_2/\sigma|^2/2 = |\cosh(\gamma\ell/\sigma)|/\kappa_2$, from which it follows that $\xi_2 = \sigma\left(2|\cosh(\gamma\ell/\sigma)|/\kappa_2 - 2\right)^{1/2}/|\gamma|$. The resulting square-root approximation indicates that the null point of a flow reversal wave does not exist if ω_2 and $\kappa_2 > 1$ are such that $|\cosh(\gamma(j\omega_2)\ell/\sigma)| < \kappa_2$ with $(\omega_2, \kappa_2) \in \mathrm{ROR}_2$. This conclusion is evident from the right-hand-side of Figure 4.2, where the values $\xi_2(\omega_2)$ do not exist for sufficiently small ω_2. We conclude that for sufficiently small frequency, the flow reversal wave will propagate through the entire pipe practically unattenuated and flow reversal at the outlet will reach the inlet, so long as the operation is reliable. As a final observation of asymptotic analysis, since $|\cosh(\gamma(j\omega_2)\ell/\sigma)| \to 1$ as $\ell \to 0$, it follows that flow reversal waves propagate the entire length of a sufficiently small pipe, as expected.

We now present the contrasting problem of pullback.

If flux is constant at the outlet and density varies at the inlet with frequency $\omega_1 = 2\pi f_1$ *and amplitude factor* κ_1 *such that* $|\Phi(\omega_1, 0)| > \overline{\varphi}$ *and* $(\omega_1, \kappa_1) \in$

ROR_1, *which value of* $\xi_1 \in [0, \ell]$ *satisfies* $|\Phi(\omega_1, \xi_1)| = \overline{\varphi}$*?*

The null point ξ_1 is plotted as a function of f_1 on the left-hand side of Figure 4.2 for various values of κ_1. The curves indicate that flow reversal waves generated at the inlet may propagate to nearly 10 km from the outlet. Recalling that the outlet flux is constant, it is clear that a pullback wave cannot propagate along the entire length of the pipeline, in contrast to above *pushback* waves.

4.3 Linearization Error Analysis

Define $\rho_{\text{lin}}(t, x)$ and $\varphi_{\text{lin}}(t, x)$ to be the solutions of the linear equations that come from linearizing (3.2)-(3.3) around the steady-state solution (Baker *et al.* (2021)). The error of linearization is measured with the metric

$$\max\left(\max_{t,x}\left|\frac{\rho(t,x)-\rho_{\text{lin}}(t,x)}{\overline{\rho}}\right|, \max_{t,x}\left|\frac{\varphi(t,x)-\varphi_{\text{lin}}(t,x)}{\overline{\varphi}}\right|\right). \tag{4.2}$$

The error is shown as a color map on the left side of Figure 4.3 as a function of frequency and amplitude of the sinusoidal boundary condition. The top left side of Figure 4.3 is the error resulting from varying density at the inlet and the bottom left side of Figure 4.3 is the error resulting form varying flux at the outlet. The figure also displays the critical curves that were investigated in Figure 4.1 (for the same pipeline parameters, particularly $\overline{\varphi} = 200$). These error plots indicate that the level curves of the error plots trace along parts of the critical curves. This leads us to conclude that the critical curves can be scaled in a meaningful way to reduce the linearization error and obtain an estimate on the maximal operating region where linearization is applicable.

Instead of scaling the entire critical curves to reduce the error, the left side of Figure 4.3 suggests that only parts of each of these curves need to be scaled. The top right side of Figure 4.3 plots the linearization error as a function of (f_1, κ_1), where

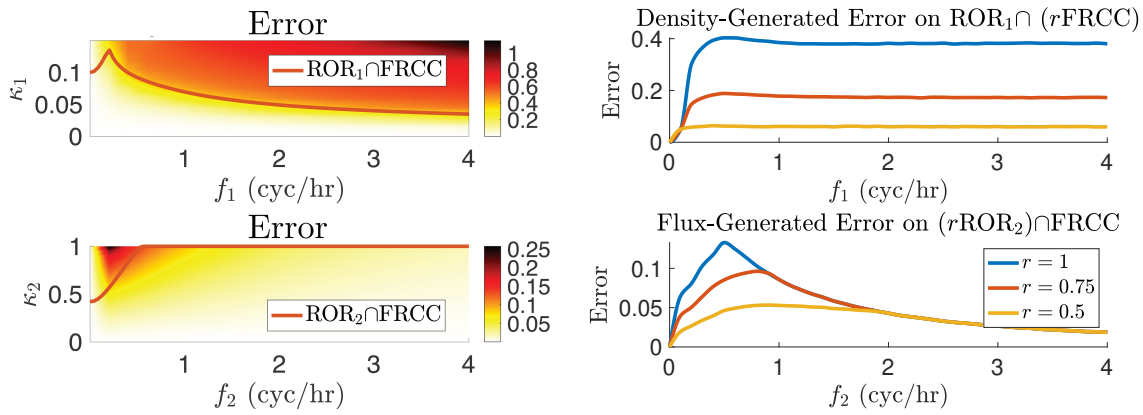

Figure 4.3: (Left) Top: Color map of the error in (4.2) as a function of (f_1, κ_1). Bottom: Color map of the error as a function of (f_2, κ_2). The curve on the top is the value $\min(\kappa_{\text{FRCC}_1}, \kappa_{\text{ROR}_1})$ that was depicted on the bottom of Figure 4.1 for $\overline{\varphi} = 200$, which we label here as $\text{ROR}_1 \cap \text{FRCC}$ for simplicity, and similarly for the bottom curve. **(Right)** Top: Error in (4.2) plotted as a function of (f_1, κ_1), where $\kappa_1 = \min(r\kappa_{\text{FRCC}_1}, \kappa_{\text{ROR}_1})$ for $r = 1, .75, .5$. Bottom: Error as a function of (f_2, κ_2), where $\kappa_2 = \min(\kappa_{\text{FRCC}_2}, r\kappa_{\text{ROR}_2})$ for $r = 1, .75, .5$.

$\kappa_1 = \min(\kappa_{\text{ROR}_1}, r\kappa_{\text{FRCC}_1})$ for $r = 1$, 0.75, and 0.5. In this case, we scale only the FRCC part of the critical curve by a factor of r. What does this mean physically? The value $r = 1$ limits the flux to vary by no more than 100% of its mean and the value $r = 0.5$ limits flux to vary by no more than 50%. Since r did not scale the ROR part of the critical curve, the density at the outlet is still allowed to vary by up to 10% of $\overline{\rho}$, as defined in ROR_1. The bottom right side of Figure 4.3 plots the linearization error as a function of (f_2, κ_2), where $\kappa_2 = \min(r\kappa_{\text{ROR}_2}, \kappa_{\text{FRCC}_2})$ for $r = 1$, 0.75, and 0.5. In this case, we scale only the ROR part of the critical curve. The value $\kappa_2 = r\kappa_{\text{ROR}_2}$ means that the density wave at the outlet varies by at most $10r\%$ of $\overline{\rho}$, while the flux can still vary by up to 100% of its mean. These scales can be used to obtain an estimate of the maximal region where linearization has an error of less than a specified percentage of the steady-state values. For example, if we need the error to be within 5%, Figure 4.3 suggests that we should limit the flow variations to

within 50% of the steady-state solution.

4.4 Examples

We present a few examples to illustrate the applications of RORs, FRCCs, and null points. Our first example illustrates operations on the nontrivial FRCC. Suppose that flux at the outlet is constant and equal to $\overline{\varphi} = 100$ and density at the inlet varies with frequency $f_1 = 0.1$ (cyc/hr). The value of κ_1 on the ROR_1 curve for this frequency is $\kappa_{\text{ROR}_1} = 0.1376$. The value of κ_1 on the FRCC curve for this frequency is $\kappa_{\text{FRCC}_1} = 0.1034$.

Since $\kappa_{\text{FRCC}_1} \leq \kappa_{\text{ROR}_1}$, the pair (0.1, 0.1034) represents a reliable operation. The top of Figure 4.4 simulates the operation (0.1, 0.1034) for $T = 10$ hr. As designed, the left-hand-side shows that flow reversal at the inlet is just avoided, while the right-hand-side shows that density fluctuates by no more than 10% of $\overline{\rho} = 56.817$, confirming reliability. As expected for small frequency, the error between the solutions of the nonlinear and linearized flow equations is relatively small, even for this 100% variation of flux at the inlet.

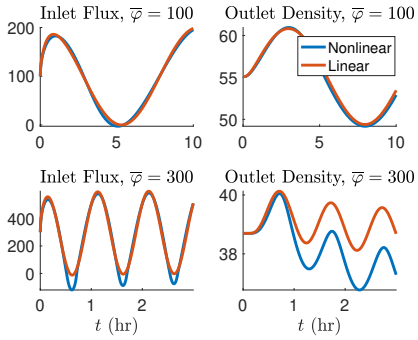

Figure 4.4: Simulation of solutions on the nontrivial FRCC.

The bottom of Figure 4.4 simulates an operation for $T = 3$ hr with $\overline{\varphi} = 300$ and $f_1 = 1$ (cyc/hr). The amplitude factor on the nontrivial FRCC for this frequency is $\kappa_{\text{FRCC}_1} = 0.1282$. The pair (1, 0.1282) is beneath the yellow curve on the top left-hand side of Figure 4.1, so our results suggest that this operation is reliable. The bottom left-hand side of Figure 4.4 shows that the linear solution avoids pullback, as expected, but the nonlinear solution does have some pullback. This discrepancy is a consequence of the larger error for high frequency waves with large amplitudes. The steady-state

profile of density in (3.6) decreases downstream to the value $\varrho(\ell) = 38.6967$. Although linearization is less appropriate for this operation, we still see that the variations in density at the outlet are within 10% of $\overline{\rho} = 56.817$ for both the linear and nonlinear solutions, again confirming the reliability. This example illustrates the importance to scale the critical curves to reduce the error to within a smaller percentage.

The next example demonstrates the null points ξ_1 and ξ_2 for two reliable flow reversals. We first consider the outlet-generated flow reversal null point ξ_2, for which density at the inlet is constant and flux at the outlet varies with a frequency of ω_2 and amplitude factor κ_2. The top left-hand-side of Figure 4.5 simulates an operation for $T = 4$ hr with $\overline{\varphi} = 100$, $f_2 = 0.25$, and $\kappa_2 = 1.2$. Since $\kappa_2 > 1$, flow reversal exists at the outlet.

The operation is reliable since the pair $(0.25, 1.2)$ is beneath the blue curve on the top right-hand side of Figure 4.1. Note also that the frequency $f_2 = 0.25$ is to the left of the red curve on the top right-hand side of Figure 4.2, indicating that the null point does not exist. The top of Figure 4.5 indeed shows that the reversed flow at the outlet propagates the entire length of the pipeline. We now consider ξ_1, for which flux at the outlet is constant and density at the inlet varies with a frequency of ω_1 and amplitude factor κ_1. The bottom of Figure 4.5 simulates an operation for $T = 1$ hr with $\overline{\varphi} = 100$, $f_1 = 1$, and $\kappa_1 = 0.2$. The top left-hand side of Figure 4.2 suggests that the null point exists and equals $\xi_1 = 86.89$.

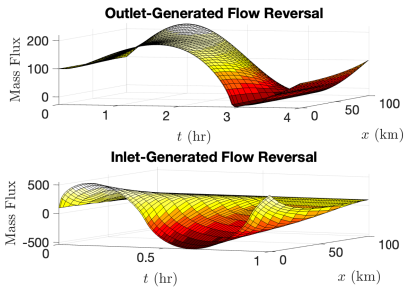

Figure 4.5: Simulation of null points. Only the nonlinear solution is plotted.

Chapter 5

GAS MIXTURE DYNAMICS IN NETWORKS

This chapter presents a mathematical formulation to model the transportation of mixtures of gases through pipeline networks. The PDEs that govern heterogeneous mixtures of hydrogen and natural gas are presented in Section 5.1. In Section 5.2, the PDE system is discretized with a finite volume method in space to obtain a nonlinear control system of ODEs. Section 5.3 presents a derivation of equivalent ODE systems in terms of other state variables of interest. The discretization method presented here has received significant attention by others for the case of natural gas flows in networks (Grundel *et al.* (2013); Stolwijk and Mehrmann (2018); Himpe *et al.* (2021)). Our advancement is the extension of the discretization method from pure natural gas systems to gas mixture systems.

5.1 Flow Equations

Graph-theoretic notation will be used to define flows throughout a network of pipelines. A gas transport network is modeled as a connected and directed graph $(\mathcal{E}, \mathcal{V})$ consisting of edges $\mathcal{E} = \{1, \ldots, E\}$ and nodes $\mathcal{V} = \{1, \ldots, V\}$, where E and V denote the numbers of edges and nodes, respectively. It is assumed that the elements of these sets are ordered according to their integer labels. The edges represent pipelines and the nodes represent junctions or stations where gas can be injected into or withdrawn from the network. From here onward, we use the terms edge and pipeline interchangeably. The symbol k is reserved for identifying edges in $\mathcal{E}$ and the symbols i and j are reserved for identifying nodes in $\mathcal{V}$. The graph is directed by assigning a positive flow direction along each edge. It is assumed that gas phys-

ically flows in only the direction of positive flow, so that the mass flow and velocity values of the gas are positive quantities everywhere in the network. The notation $k : i \mapsto j$ means that edge $k \in \mathcal{E}$ is directed from node $i \in \mathcal{V}$ to node $j \in \mathcal{V}$. For each node $j \in \mathcal{V}$, we define (potentially empty) incoming and outgoing sets of pipelines by $_{\mapsto}j = \{k \in \mathcal{E} | k : i \mapsto j\}$ and $j_{\mapsto} = \{k \in \mathcal{E} | k : j \mapsto i\}$, respectively.

Natural gas is mostly composed of methane (75-99% molar fraction), ethane (1-15%), propane (1-10%), n-butane (0-2%), and isobutene (0-1%). The molecular weight and density of methane at room temperature and atmospheric pressure is 16.04 (g/mol) and 0.657 (kg/m^3). The ratio of the molecular weights of ethane to the primary component methane is 1.874. The ratio of the molecular weights of the components of natural gas is as large as 3.623. However, the ratio of the molecular weight of methane to hydrogen is 15.915 (an even larger for the other components of natural gas). Therefore, although natural gas is already a mixture of several gases, the properties of these constituent gases are relatively similar to allow for the approximation of natural gas dynamics. However, if a significant amount of hydrogen is blended into the network, there needs to be an additional dynamic equation that models the composition of natural gas and hydrogen. Although we focus primarily on blending two gases in a network of pipelines, the following derivation can be extended to mixtures of more than two gases.

There are several approaches to define the flow of a mixture of gases (see, e.g., Chaczykowski *et al.* (2018); Subani *et al.* (2015); Kazi *et al.* (2022)). We follow the approach taken in (Chaczykowski *et al.* (2018)). The key advancement in our presentation is the development of a control system model that includes time-varying activity of compressor control actions to account for time-varying injections and withdrawals of constituent gases. For each pipe $k \in \mathcal{E}$, we define partial pressures $p_k^{(1)}$ and $p_k^{(2)}$; partial densities $\rho_k^{(1)}$ and $\rho_k^{(2)}$; partial mass fluxes $\varphi_k^{(1)}$ and $\varphi_k^{(2)}$; and mass

fractions $\eta_k^{(1)}$ and $\eta_k^{(2)}$, where

$$\eta_k^{(m)} = \frac{\rho_k^{(m)}}{\rho_k^{(1)} + \rho_k^{(2)}} = \frac{\varphi_k^{(m)}}{\varphi_k^{(1)} + \varphi_k^{(2)}}. \tag{5.1}$$

We assume that total density ρ_k and total flux φ_k are related to their constituent counterparts by the mass fraction given by

$$\rho_k^{(m)} = \eta_k^{(m)} \rho_k, \qquad \varphi_k^{(m)} = \eta_k^{(m)} \varphi_k. \tag{5.2}$$

Since $(\eta_k^{(1)} + \eta_k^{(2)}) = 1$, it follows from the above definitions that $\rho_k = (\rho_k^{(1)} + \rho_k^{(2)})$ and $\varphi_k = (\varphi_k^{(1)} + \varphi_k^{(2)})$. From here onward, superscripts "(1)" and "(2)" will always be used to identify the correspondence of variables to natural gas and hydrogen, respectively. In general, all of the above variables depend on time $t \in [0, T]$ and axial location $x \in [0, \ell_k]$, where T is the time horizon and ℓ_k is the length of the pipe $k \in \mathcal{E}$. We assume that the equation of state is ideal for both gases, i.e., partial pressure is ideally related to partial density by the relation $p_k^{(m)} = \sigma_m^2 \rho_k^{(m)}$, where σ_1 and σ_2 are the sound speeds of natural gas and hydrogen, respectively. The total pressure of the mixture is defined to be the summation of partial pressures given by

$$p_k = p_k^{(1)} + p_k^{(2)} = \sigma_1^2 \rho_k^{(1)} + \sigma_2^2 \rho_k^{(2)} = \left(\sigma_1^2 \eta_k^{(1)} + \sigma_2^2 \eta_k^{(2)} \right) \rho_k = \sigma^2 \rho_k.$$

The outcomes from this relation deserve attention. First, the ideal gas law for the constituent gases demonstrates that the local wave speed σ of the mixture depends on the local concentration of the gases according to $\sigma(t, x; k) = \sqrt{\sigma_1^2 \eta_k^{(1)}(t, x) + \sigma_2^2 \eta_k^{(2)}(t, x)}$. Second, it follows that the total and partial pressure variables are not related by simple scaling with the mass fraction, in contrast to total density and total flux that are related by (5.2), since, in general, $p_k^{(m)} = \sigma_m^2 \rho_k^{(m)} = \eta_k^{(m)} \sigma_m^2 \rho_k \neq \eta_k^{(m)} \sigma^2 \rho_k = \eta_k^{(m)} p_k$. The pressure variables are related to one another through the volumetric concentration defined by

$$\nu_k^{(m)} = \frac{\sigma_m^2 \rho_k^{(m)}}{\sigma_1^2 \rho_k^{(1)} + \sigma_2^2 \rho_k^{(2)}} = \frac{\sigma_m^2 \eta_k^{(m)}}{\sigma_1^2 \eta_k^{(1)} + \sigma_2^2 \eta_k^{(2)}}.$$

In particular, $p_k^{(m)} = \nu_k^{(m)} p_k$. From here onward, we use the terms mass fraction and concentration interchangeably. We specifically refer to volumetric concentration where that quantity is examined.

The propagation of either concentration quantity $\eta_k^{(m)}$ can be modeled by the convection-diffusion equation in which the diffusion terms can be omitted (Chaczykowski *et al.* (2018)). Similarly to (Chaczykowski *et al.* (2018)), we extend the Euler equations in (3.1a)-(3.1b) to include concentration tracking. Doing this for each $k \in \mathcal{E}$ leads to the system

$$\begin{aligned} \partial_t \eta_k^{(m)} + \left(\frac{\varphi_k}{\rho_k}\right) \partial_x \eta_k^{(m)} &= 0, && (5.3) \\ \partial_t \rho_k + \partial_x \varphi_k &= 0, && (5.4) \\ \partial_t \varphi_k + \partial_x \left(p_k + \frac{\varphi_k |\varphi_k|}{\rho_k}\right) &= -\frac{\lambda_k}{2D_k} \frac{\varphi_k |\varphi_k|}{\rho_k}. && (5.5) \end{aligned}$$

Here, D_k and λ_k are the diameter and friction factor of the pipeline. In this formulation, (5.3) is defined for either $m = 1$ or $m = 2$. Since $\eta_k^{(1)} = (1 - \eta_k^{(2)})$, it follows that both $\eta_k^{(1)}$ and $\eta_k^{(2)}$ satisfy (5.3) if and only if one of these variables do. In (5.3)-(5.5), we are explicitly governing total pressure, total density, total mass flux, and concentration of the mixture, under the assumption of the ideal equation of state. For convenience, we reformulate (5.3)-(5.4) into an equivalent system that has a symmetrical appearance. For $m = 1$ and $m = 2$, we compute

$$\begin{aligned} \partial_t \rho_k^{(m)} + \partial_x \varphi_k^{(m)} &= \partial_t \left(\eta_k^{(m)} \rho_k\right) + \partial_x \left(\eta_k^{(m)} \varphi_k\right) \\ &= \left(\rho_k \partial_t \eta_k^{(m)} + \varphi_k \partial_x \eta_k^{(m)}\right) + \eta_k^{(m)} \left(\partial_t \rho_k + \partial_x \varphi_k\right). \end{aligned}$$

If the two equations in (5.3)-(5.4) for either $m = 1$ or $m = 2$ are satisfied, then the above sequence of equations shows that $(\partial_t \rho_k^{(m)} + \partial_x \varphi_k^{(m)}) = 0$ for both $m = 1$ and $m = 2$. Conversely, suppose that $(\partial_t \rho_k^{(m)} + \partial_x \varphi_k^{(m)}) = 0$ for both $m = 1$ and $m = 2$. Adding these two equations and using the relation $(\eta_k^{(1)} + \eta_k^{(2)}) = 1$ with the definition

(5.2) shows that $(\partial_t \rho_k + \partial_x \varphi_k) = 0$. Thus, the above sequence of equations reduces to (5.3). Using (5.1)-(5.2) and the equation of state $p_k(t,x) = (\sigma(t,x;k))^2 \rho_k(t,x)$, we obtain the equivalent system of equations

$$\partial_t \rho_k^{(m)} + \partial_x \left(\frac{\rho_k^{(m)}}{\rho_k^{(1)} + \rho_k^{(2)}} \varphi_k \right) = 0, \tag{5.6}$$

$$\partial_t \varphi_k + \partial_x \left(\sigma_1^2 \rho_k^{(1)} + \sigma_2^2 \rho_k^{(2)} + \frac{\varphi_k^2}{\rho_k^{(1)} + \rho_k^{(2)}} \right) = -\frac{\lambda_k}{2D_k} \frac{\varphi_k |\varphi_k|}{\rho_k^{(1)} + \rho_k^{(2)}}, \tag{5.7}$$

where (5.6) is defined for both $m = 1$ and $m = 2$. We assume, for simplicity of exposition, that the boundary conditions are sufficiently slowly time-varying so that the inertia and kinetic energy terms may be removed from the momentum equation (Sundar and Zlotnik (2018); Misra *et al.* (2020)). Moving forward, for each $k \in \mathcal{E}$, we assume that the dynamics of the mixture are governed by

$$\partial_t \rho_k^{(m)} + \partial_x \left(\frac{\rho_k^{(m)}}{\rho_k^{(1)} + \rho_k^{(2)}} \varphi_k \right) = 0, \tag{5.8}$$

$$\partial_x \left(\sigma_1^2 \rho_k^{(1)} + \sigma_2^2 \rho_k^{(2)} \right) = -\frac{\lambda_k}{2D_k} \frac{\varphi_k |\varphi_k|}{\rho_k^{(1)} + \rho_k^{(2)}}. \tag{5.9}$$

Compressor and regulator stations are critical components that actuate the flow of gas throughout the network and reduce pressure in the direction of flow, respectively. For convenience, we assume that a compressor is located at the inlet and a regulator is located at the outlet of each pipeline, where inlet and outlet are defined with respect to the oriented positive flow direction. For each pipeline $k \in \mathcal{E}$, compression and regulation are modeled with multiplicative control variables $\underline{\mu}_k(t) \geq 1$ and $\overline{\mu}_k(t) \geq 1$, respectively. For example, the pressure of gas leaving a compressor unit is $\underline{\mu}_k(t)$ times larger than the pressure of gas entering the unit.

The boundary conditions for a mixture of gases allow for more degrees of freedom than those for a single gas, and are formulated here to enable definition of a range of potential scenarios. All of the flow quantities defined in this paragraph are,

in general, time-varying, but we omit time-dependence for readability. The network nodes are partitioned into slack nodes $\mathcal{V}_s \subset \mathcal{V}$ and non-slack nodes $\mathcal{V}_d \subset \mathcal{V}$. Slack nodes are assumed to be ordered in $\mathcal{V}$ before non-slack nodes, so that $i < j$ for all $i \in \mathcal{V}_s$ and $j \in \mathcal{V}_d$. A mixture of gas is injected into the network at each slack node $i \in \mathcal{V}_s$. The boundary conditions at the slack nodes $i \in \mathcal{V}_s$ are defined by specifying individual densities $\boldsymbol{s}_i^{(1)}$ and $\boldsymbol{s}_i^{(2)}$. Alternatively, pressure $(\boldsymbol{p}_s)_i$ and concentration $\boldsymbol{\alpha}_i^{(m)}$ may be specified at slack nodes $i \in \mathcal{V}_s$. The relations $(\boldsymbol{p}_s)_i = (\sigma_1^2 \boldsymbol{s}_i^{(1)} + \sigma_2^2 \boldsymbol{s}_i^{(2)})$ and $\boldsymbol{\alpha}_i^{(m)} = \boldsymbol{s}_i^{(m)}/(\boldsymbol{s}_i^{(1)} + \boldsymbol{s}_i^{(2)})$ can then be used to determine the corresponding densities that will achieve the specified pressures and concentrations. Non-slack nodes are partitioned into injection nodes $\mathcal{V}_q \subset \mathcal{V}_d$ and withdrawal nodes $\mathcal{V}_w \subset \mathcal{V}_d$. We order the non-slack nodes $\mathcal{V}_d$ with injection nodes enumerated before withdrawal nodes, so that $i < j$ for all $i \in \mathcal{V}_q$ and $j \in \mathcal{V}_w$. A mixture is withdrawn from the network at each withdrawal node $j \in \mathcal{V}_w$ with boundary conditions specified by mass outflow $\boldsymbol{w}_j \geq 0$. At each injection node $j \in \mathcal{V}_q$, a mixture is injected into the network with boundary conditions specified by both the mass inflow $\boldsymbol{q}_j$, with $\boldsymbol{q}_j \geq 0$, and the concentration $\boldsymbol{\beta}_j^{(m)}$. Although a mass inflow is specified at each injection node $j \in \mathcal{V}_q$ with concentration $\boldsymbol{\beta}_j^{(m)}$, this does not, in general, imply that the concentration flowing from node j into outgoing edges is equal to $\boldsymbol{\beta}_j^{(m)}$, because the nodal concentration is a mixture of flows entering node j either by injection or from incoming pipelines. Boundary condition designations are illustrated using each of the two alternative specifications at the slack node for a single pipeline and small example network in Figure 5.1.

Individual density and concentration variables are unknown at non-slack nodes and are denoted by $\boldsymbol{\rho}_j^{(m)}$ and $\boldsymbol{\eta}_j^{(m)} = \boldsymbol{\rho}_j^{(m)}/(\boldsymbol{\rho}_j^{(1)} + \boldsymbol{\rho}_j^{(2)})$, respectively, for each $j \in \mathcal{V}_d$. All of the nodal quantities in this study are identified with bold symbols. Inlet and outlet edge variables are defined by attaching underlines below and overlines above the associated edge variables, respectively. For example, $\underline{\varphi}_k(t) = \varphi_k(t, 0)$ and

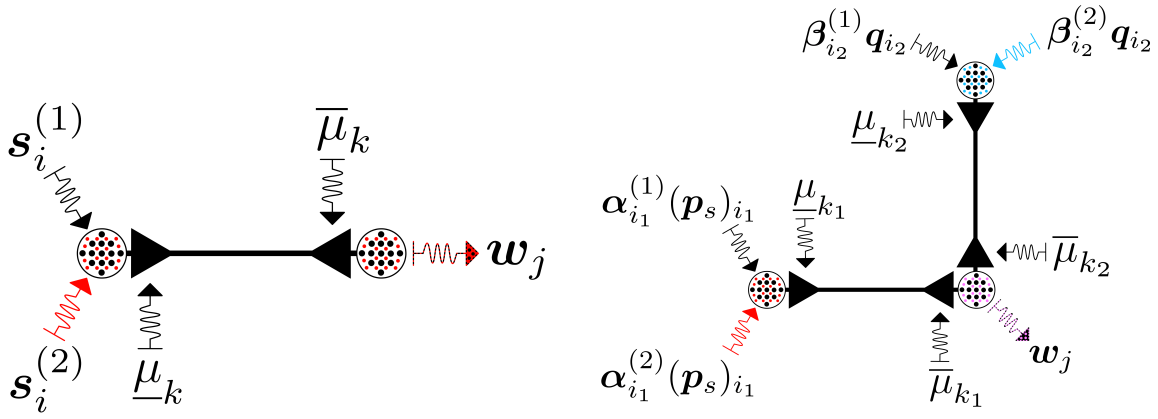

Figure 5.1: Configuration of the boundary conditions. (Left) A single pipeline $k : i \mapsto j$ with $i \in \mathcal{V}_s$ and $j \in \mathcal{V}_w$. (Right) A small network defined by $j \in \mathcal{V}_w$, $k_1 : i_1 \mapsto j$ with $i_1 \in \mathcal{V}_s$, and $k_2 : i_2 \mapsto j$ with $i_2 \in \mathcal{V}_q$.

$\overline{\varphi}_k(t) = \varphi_k(t, \ell_k)$. Define the cross-sectional area of edge $k \in \mathcal{E}$ by $\chi_k = \pi D_k^2/4$. The boundary conditions for the flow of the mixture are defined for $m = 1$ and $m = 2$ by

$$\underline{\rho}_k^{(m)} = \underline{\mu}_k \boldsymbol{s}_i^{(m)}, \qquad \overline{\rho}_k^{(m)} = \overline{\mu}_k \boldsymbol{\rho}_j^{(m)}, \tag{5.10}$$

$$\underline{\rho}_k^{(m)} = \underline{\mu}_k \boldsymbol{\rho}_i^{(m)}, \qquad \overline{\rho}_k^{(m)} = \overline{\mu}_k \boldsymbol{\rho}_j^{(m)}, \tag{5.11}$$

$$\boldsymbol{\gamma}_j^{(m)} \boldsymbol{d}_j = \sum_{k \in \mapsto j} \chi_k \overline{\eta}_k^{(m)} \overline{\varphi}_k - \sum_{k \in j \mapsto} \chi_k \underline{\eta}_k^{(m)} \underline{\varphi}_k, \tag{5.12}$$

where (5.10) is defined for $k : i \mapsto j$ with $i \in \mathcal{V}_s$, (5.11) is defined for $k : i \mapsto j$ with $i, j \in \mathcal{V}_d$, and (5.12) is defined for $j \in \mathcal{V}_d$ with the condition that $\boldsymbol{\gamma}_j^{(m)} \boldsymbol{d}_j = \boldsymbol{\eta}_j^{(m)} \boldsymbol{w}_j$ if $j \in \mathcal{V}_w$ and $\boldsymbol{\gamma}_j^{(m)} \boldsymbol{d}_j = -\boldsymbol{\beta}_j^{(m)} \boldsymbol{q}_j$ if $j \in \mathcal{V}_q$. The initial condition of partial density is assumed to be a steady-state solution given for all $k \in \mathcal{E}$ and $x \in [0, \ell_k]$ by

$$\rho_k^{(m)}(0, x) = \varrho_k^{(m)}(x). \tag{5.13}$$

The steady-state solution is defined to be the time-invariant solution of the system in (5.8)-(5.12) when the boundary condition profiles are time-invariant (i.e. equal to the initial values of the time-varying boundary profiles). More details on the initial condition for the discretized system are provided in the following section. Mass flux is

not initially specified because it is uniquely determined from partial densities due to the simplifying assumption that momentum is dominated by friction. Alternatively, we may also consider periodic temporal constraints defined by

$$\rho_k^{(m)}(0,x) = \rho_k^{(m)}(T,x). \tag{5.14}$$

Periodicity in time requires the parameters $\boldsymbol{s}^{(m)}(t)$, $\boldsymbol{w}(t)$, $\boldsymbol{q}$, $\underline{\mu}_k(t)$, and $\overline{\mu}_k(t)$ to be periodic with period T. The flow of the mixture of gases in the network is defined by the initial-boundary value system of PDEs (5.8)-(5.12) with (5.13) or with (5.14).

5.2 Spatial Discretization

To analyze the initial boundary value system of PDEs (5.8)-(5.13) on the graph $(\mathcal{E},\mathcal{V})$, we have developed a process of discretization, which includes a *refinement* of the graph, *approximation* of the PDE system by an ODE system using a finite volume approach, and a *reformulation* in terms of variable vectors and parameter matrices. The vectors include variables that represent the states and boundary parameters, and the matrices incorporate network model parameters, the incidence structure of the graph, and the values of the control variables.

A refinement $(\hat{\mathcal{E}},\hat{\mathcal{V}})$ of the graph $(\mathcal{E},\mathcal{V})$ is created by adding auxiliary nodes to $\mathcal{V}$ in order to subdivide the edges of $\mathcal{E}$ so that $\ell_k \leq \ell$ for all $k \in \hat{\mathcal{E}}$, where $\ell \leq 10$ (km) is sufficiently small (Grundel *et al.* (2013)). The refined graph inherits the prescribed orientation of the parent graph. Assuming sufficiently fine network refinement, the relative difference of the density variables of adjacent nodes in the solution to the IBVP (5.8)-(5.13) can be made arbitrarily small in magnitude because of continuity of the solution to the system given well-posed conditions (Gugat *et al.* (2012)). We assume for all $k \in \hat{\mathcal{E}}$ that

$$\frac{\left|\overline{\rho}_k^{(m)} - \underline{\rho}_k^{(m)}\right|}{\underline{\rho}_k^{(m)}} < \epsilon, \qquad \frac{\left|\overline{\rho}_k^{(m)} - \underline{\rho}_k^{(m)}\right|}{\overline{\rho}_k^{(m)}} < \epsilon, \tag{5.15}$$

where $0 \leq \epsilon \ll 1$. The proofs on monotone-ordering in the next chapter only require $\epsilon \leq 1$. We assume that the graph has been sufficiently refined to satisfy (5.15) and that the hats may be omitted moving forward.

The approximation of the PDE system with an ODE system is obtained by applying a finite volume approximation method on each refined pipeline segment that was originally developed in (Grundel *et al.* (2014)) for natural gas systems. We extend this approximation method in this work to account for the mixture of gases. The system of ODEs is obtained by integrating the dynamic equations in (5.8)-(5.9) along the length of each refined pipeline segment so that

$$\int_0^\ell \partial_t \rho^{(m)} dx = -\int_0^\ell \partial_x \left(\frac{\rho^{(m)}}{\rho^{(1)} + \rho^{(2)}} \varphi \right) dx,$$
$$\int_0^\ell \partial_x \left(\sigma_1^2 \rho^{(1)} + \sigma_2^2 \rho^{(2)} \right) dx = -\frac{\lambda}{2D} \int_0^\ell \frac{\varphi |\varphi|}{\rho^{(1)} + \rho^{(2)}} dx,$$

where edge subscripts have been removed for readability. The above integrals of space derivatives are evaluated using the fundamental theorem of calculus. The remaining integrals may be approximated using various methods. Two such methods used for natural gas networks are the midpoint and endpoint approximations (Stolwijk and Mehrmann (2018); Himpe *et al.* (2021)). We adopt the endpoint method to approximate pipeline density with outlet density and pipeline flux with inlet flux. These approximations are independent of the spatial variable and may be factored out of the above integrals. The integral equations become

$$\ell \dot{\overline{\rho}}^{(m)} = \underline{\eta}^{(m)} \underline{\varphi} - \overline{\eta}^{(m)} \overline{\varphi}, \tag{5.16}$$
$$\sum_{n=1}^{2} \sigma_n^2 \left(\overline{\rho}^{(n)} - \underline{\rho}^{(n)} \right) = -\frac{\lambda \ell}{2D} \frac{\underline{\varphi} \left| \underline{\varphi} \right|}{\overline{\rho}^{(1)} + \overline{\rho}^{(2)}}, \tag{5.17}$$

where a dot above a variable represents the time-derivative of the variable.

We now write the discretized system in matrix-vector form. Although our approach is similar to the one in (Zlotnik *et al.* (2015b)), the extension to a mixture of

gases is nontrivial. Define $E \times E$ diagonal matrices L and X with diagonal entries $L_{kk} = \ell_k$ and $X_{kk} = \chi_k$. Define the time-varying (transposed) incidence matrix M of size $E \times V$ componentwise by

$$M_{kj} = \begin{cases} \overline{\mu}_k(t), & \text{edge } k \in_{\mapsto} j \text{ enters node } j, \\ -\underline{\mu}_k(t), & \text{edge } k \in j_{\mapsto} \text{ leaves node } j, \\ 0, & \text{else.} \end{cases} \tag{5.18}$$

Define the $E \times V_s$ submatrix M_s of M by the removal of columns $i \in \mathcal{V}_d$, the $E \times (V - V_s)$ submatrix M_d of M by the removal of columns $i \in \mathcal{V}_s$, and the positive and negative parts of M_d by $\overline{M}_d$ and $\underline{M}_d$ so that $M_d = (\overline{M}_d + \underline{M}_d)/2$ and $|M_d| = (\overline{M}_d - \underline{M}_d)/2$, where V_s denotes the number of slack nodes and $|A|$ denotes the componentwise absolute value of a matrix A. Define the signed matrices Q_d =sign(M_d), $\overline{Q}_d$ =sign$(\overline{M}_d)$, $\underline{Q}_d$ =sign$(\underline{M}_d)$, and similarly for M_s. These signed matrices are well-defined by the lower-bound constraints on compression and regulation. Define the $V_d \times V_d$ identity matrix I, the $V_d \times V_q$ submatrix I_q of I by the removal of columns $j \in \mathcal{V}_w$, and the $V_d \times V_d$ matrix I_w by replacing columns $j \in \mathcal{V}_q$ of I with the zero vector. Here, V_d and V_q denote the numbers of non-slack nodes and non-slack injection nodes, respectively.

Define inlet and outlet edge mass flux vectors by $\underline{\varphi} = (\underline{\varphi}_1, \ldots, \underline{\varphi}_E)^T$ and $\overline{\varphi} = (\overline{\varphi}_1, \ldots, \overline{\varphi}_E)^T$, and similarly for inlet and outlet edge concentrations $\underline{\eta}$ and $\overline{\eta}$. Moreover, define the vectors $\boldsymbol{\rho}^{(m)} = (\boldsymbol{\rho}^{(m)}_{V_s+1}, \ldots, \boldsymbol{\rho}^{(m)}_{V_d})^T$, $\boldsymbol{\alpha}^{(m)} = (\boldsymbol{\alpha}^{(m)}_1, \ldots, \boldsymbol{\alpha}^{(m)}_{V_s})^T$, and $\boldsymbol{\beta}^{(m)} = (\boldsymbol{\beta}^{(m)}_{V_s+1}, \ldots, \boldsymbol{\beta}^{(m)}_{V_q})^T$, where the subscripts of the vector components are indexed according to the node labels in $\mathcal{V}$. Similarly, define the vectors $\boldsymbol{\eta}^{(m)} = (\boldsymbol{\eta}^{(m)}_{V_s+1}, \ldots, \boldsymbol{\eta}^{(m)}_{V_d})^T$ and $\boldsymbol{d} = (\boldsymbol{d}_{V_s+1}, \ldots, \boldsymbol{d}_{V_d})^T$. Recall that the components of $\boldsymbol{d}$ are positive for those corresponding to non-slack withdrawal nodes and negative for non-slack injection nodes.

Define the function $f : \mathbb{R}^E \times \mathbb{R}^E \to \mathbb{R}^E$ component-wise for $k \in \mathcal{E}$ by

$$f_k(y, z) = -\text{sign}(z_k)\Lambda_k \left| y_k z_k \right|^{1/2}, \tag{5.19}$$

where $\Lambda_k = \sqrt{2D_k/(\lambda_k \ell_k)}$. This function is used to express $\underline{\varphi}$ in (5.17) in terms of density and its spatial derivative so that we may eliminate flux from the dynamic equations. Using the function in (5.19), the discretized flow in (5.16)-(5.17) together with the boundary conditions in (5.10)-(5.12) may be expressed in matrix-vector form as

$$L\overline{M}_d \dot{\boldsymbol{\rho}}^{(m)} = \underline{\eta}^{(m)} \odot F - \overline{\eta}^{(m)} \odot \overline{\varphi}, \tag{5.20}$$

$$\boldsymbol{\gamma}^{(m)} \odot \boldsymbol{d} = \overline{Q}_d^T X \left(\overline{\eta}^{(m)} \odot \overline{\varphi} \right) + \underline{Q}_d^T X \left(\underline{\eta}^{(m)} \odot F \right), \tag{5.21}$$

where $\odot$ is the Hadamard product and

$$F = f\left(\overline{M}_d \left(\boldsymbol{\rho}^{(1)} + \boldsymbol{\rho}^{(2)} \right), \sum_m \sigma_m^2 \left(M_s \boldsymbol{s}^{(m)} + M_d \boldsymbol{\rho}^{(m)} \right) \right). \tag{5.22}$$

The Hadamard product of two vectors $x \in \mathbb{R}^N$ and $y \in \mathbb{R}^N$ is defined to be the vector $(a \odot b) \in \mathbb{R}^N$ with components $(a \odot b)_n = a_n b_n$ for $n = 1, \ldots, N$. In the above derivation, we assume that regulators vary slowly so that the time derivative of $\overline{M}_d$ is insignificant, justifying its removal from (5.20). The discretized system in (5.20)-(5.21) is a set of ordinary differential algebraic equations (DAEs) (Griepentrog and März (1986)). The tractability index (Himpe *et al.* (2021)) of the DAE quantifies the complexity of transforming it to an ODE. It is shown in (Banagaaya *et al.* (2022)) that the tractability index of (5.20)-(5.21) is equal to one if every pipeline incident to a slack node is directed away from the slack node. Let us now write the DAE as an ODE. Multiplying both sides of (5.20) on the left by $\overline{Q}_d^T X$ and using (5.21), we may combine (5.20) and (5.21) to form the equation $\overline{Q}_d^T X L \overline{M}_d \dot{\boldsymbol{\rho}}^{(m)} = [Q_d^T X (\underline{\eta}^{(m)} \odot F) - \boldsymbol{\gamma}^{(m)} \odot \boldsymbol{d}]$, where we have used $Q_d = (\underline{Q}_d + \overline{Q}_d)$. By writing edge concentrations in terms of

nodal concentrations, and nodal concentrations in terms of concentrations of flows into the nodes, the system in (5.20)-(5.21) may be written for $m = 1, 2$ as

$$R\dot{\boldsymbol{\rho}}^{(m)} \;=\; Q_d^T X \left(\left(|\underline{Q}_s| \boldsymbol{\alpha}^{(m)} + |\underline{Q}_d| \boldsymbol{\eta}^{(m)} \right) \odot F \right) - \left(I_q \boldsymbol{\beta}^{(m)} + I_w \boldsymbol{\eta}^{(m)} \right) \odot \boldsymbol{d}, \quad (5.23)$$

where $R = \overline{Q}_d^T X L \overline{M}_d$. The system in (5.23) will be called the partial density system of ODEs. Each row k of $\overline{M}_d$ contains exactly one nonzero component given by $\overline{M}_{kj} = \overline{\mu}_k$ for $k \in_{\mapsto} j$. Using the additional fact that X and L are diagonal, it can be shown that the mass matrix R on the left-hand-side of (5.23) is diagonal with positive diagonal components given by $\boldsymbol{r}_j = \sum_{k \in_{\mapsto} j} \chi_k \ell_k \overline{\mu}_k$ for $j \in \mathcal{V}_d$. Therefore, the matrix R may readily be inverted to obtain a nonlinear control system in the usual, although complicated, ODE form. The initial condition in (5.13), sampled at the refined nodes of the network, denoted by $\boldsymbol{\varrho}^{(m)}$, is the time-invariant solution of the system in (5.23) with $\boldsymbol{d} = \boldsymbol{d}(0)$, $\boldsymbol{\alpha}^{(m)} = \boldsymbol{\alpha}^{(m)}(0)$, and $\boldsymbol{\beta}^{(m)} = \boldsymbol{\beta}^{(m)}(0)$. Depending on which temporal conditions we consider, the initial condition of (5.23) is defined by either

$$\boldsymbol{\rho}^{(m)}(0) = \boldsymbol{\varrho}^{(m)} \quad \text{or} \quad \boldsymbol{\rho}^{(m)}(0) = \boldsymbol{\rho}^{(m)}(T). \quad (5.24)$$

We now present a result on the discretization method. Proposition 1 below shows that the discretized system in (5.23) approaches the continuous system in (5.8)-(5.9) in a single pipeline as the distance between adjacent nodes of the refined pipeline approaches zero.

Proposition 1. Consider a single pipeline of length ℓ, and refine its graph as a chain connection of E segments of uniform length $\Delta\ell = \ell/E$, diameter D, and friction factor λ. Suppose the gas mixture is supplied to the pipeline at only the inlet $\mathcal{V}_s = \{1\}$ with boundary conditions as in (5.10)-(5.12) and withdrawn from only the outlet so that $\boldsymbol{w}_j = 0$ for $j \neq E + 1$. Suppose for simplicity that there are no compressors or regulators. Then the resulting system in (5.23) is a consistent spatial discretization of (5.8)-(5.12).

Proof. The matrix $\overline{M}_d$ is the $E \times E$ identity matrix, $\underline{M}_d$ is the $E \times E$ lower off-diagonal matrix with nonzero entries $(\underline{M}_d)_{n+1,n} = -1$, and $\underline{Q}_s$ is an $E \times 1$ unit vector with one nonzero entry given by $(\underline{Q}_s)_1 = -1$. For the intermediate segment $n : n \mapsto (n+1)$ with $2 \leq n \leq E-1$, the associated dynamics in (5.23) are given by

$$\begin{aligned} \dot{\boldsymbol{\rho}}_{n+1}^{(m)} + \frac{1}{\Delta\ell}\left(\boldsymbol{\eta}_{n+1}^{(m)}\underline{\varphi}_{n+1} - \boldsymbol{\eta}_{n}^{(m)}\underline{\varphi}_{n}\right) &= 0 \\ \frac{1}{\Delta\ell}\sum_{m=1}^{2}\sigma_m^2\left(\boldsymbol{\rho}_{n+1}^{(m)} - \boldsymbol{\rho}_{n}^{(m)}\right) &= -\frac{\lambda}{2D}\frac{\underline{\varphi}_n|\underline{\varphi}_n|}{\boldsymbol{\rho}_{n+1}^{(1)} + \boldsymbol{\rho}_{n+1}^{(2)}}. \end{aligned}$$

Taking the limit $\Delta\ell \to 0$, the above equations approach the dynamics in (5.8)-(5.9). Similarly, as $\Delta\ell \to 0$, it can be shown that the first and last segments of the pipe reduce to the dynamics (5.8)-(5.9) with boundary conditions (5.10)-(5.12). □

5.3 Equivalent Systems

The system in (5.23) is expressed in terms of partial densities at non-slack nodes. Equivalent systems expressed in terms of other variables of interest may be derived from (5.23) using appropriate transformations. This should come with no surprise since we have already performed a transformation in the continuous case going from (5.3)-(5.5) to (5.6)-(5.7). In fact, such transformations exist even for pure natural gas equations. For example, the equations of natural gas flow may be expressed in terms of pressure and velocity, in terms of density and mass flux, or in terms of their dimensionless quantities, ect. Define vectors $\boldsymbol{\rho}$, $\boldsymbol{p}$, $\boldsymbol{\nu}^{(m)}$, and $\boldsymbol{E}$ of nodal values for density, pressure, volumetric concentration, and energy, respectively, at non-slack

nodes by

$$\begin{aligned}
\boldsymbol{\rho} &= \boldsymbol{\rho}^{(1)} + \boldsymbol{\rho}^{(2)}, && (5.25)\\
\boldsymbol{p} &= \sigma_1^2\boldsymbol{\rho}^{(1)} + \sigma_2^2\boldsymbol{\rho}^{(2)}, && (5.26)\\
\boldsymbol{\nu}^{(m)} &= \frac{\sigma_m^2\boldsymbol{\rho}^{(m)}}{\sigma_1^2\boldsymbol{\rho}^{(1)} + \sigma_2^2\boldsymbol{\rho}^{(2)}}, && (5.27)\\
\boldsymbol{E} &= (|\overline{Q}_d^T|X_{\underline{\varphi}}) \odot \left(r^{(1)}\boldsymbol{\eta}^{(1)} + r^{(2)}\boldsymbol{\eta}^{(2)}\right), && (5.28)
\end{aligned}$$

where $r^{(1)} = 44.2$ (MJ/kg) and $r^{(2)} = 141.8$ (MJ/kg) are calorific values of natural gas and hydrogen, respectively. Equivalent systems may be expressed in terms of any two vector variables from the set $\{\boldsymbol{\rho}^{(m)}, \boldsymbol{\eta}^{(m)}, \boldsymbol{\nu}^{(m)}, \boldsymbol{\rho}, \boldsymbol{p}, \boldsymbol{E}\}$, excluding pairs from the subset $\{\boldsymbol{\eta}^{(1)}, \boldsymbol{\eta}^{(2)}, \boldsymbol{\nu}^{(1)}, \boldsymbol{\nu}^{(2)}\}$ because variables in the latter subset would reduce to constant vectors in the case of homogeneous mixtures. The choice of which equivalent system to use may depend on the sought application, although some systems have better conditioning with fewer nonlinear operations than others. Define localized sound speed vectors $\boldsymbol{a} = (\sigma_1^2\boldsymbol{\alpha}^{(1)} + \sigma_2^2\boldsymbol{\alpha}^{(2)})^{1/2}$ and $\boldsymbol{b} = (\sigma_1^2\boldsymbol{\beta}^{(1)} + \sigma_2^2\boldsymbol{\beta}^{(2)})^{1/2}$, where the square-root is applied component-wise. In general, these may be time-varying speeds. The transformation from partial densities to *total density and pressure* is obtained by superimposing (5.23) for $m = 1, 2$ to obtain an equation for $\dot{\boldsymbol{\rho}}$ and linearly combining (5.23) for $m = 1, 2$ with coefficients σ_1^2 and σ_2^2 to obtain an equation for $\dot{\boldsymbol{p}}$. In the first case, we have

$$\begin{aligned}
R\left(\dot{\boldsymbol{\rho}}^{(1)} + \dot{\boldsymbol{\rho}}^{(2)}\right) &= Q_d^T X \left(\left(|\underline{Q}_s|\left(\boldsymbol{\alpha}^{(1)} + \boldsymbol{\alpha}^{(2)}\right) + |\underline{Q}_d|\left(\boldsymbol{\eta}^{(1)} + \boldsymbol{\eta}^{(2)}\right)\right) \odot F\right)\\
&\quad - \left(I_q\left(\boldsymbol{\beta}^{(1)} + \boldsymbol{\beta}^{(2)}\right) + I_w\left(\boldsymbol{\eta}^{(1)} + \boldsymbol{\eta}^{(2)}\right)\right) \odot \boldsymbol{d}.
\end{aligned}$$

The above summations of concentration vectors are equal to vectors of ones of the appropriate dimensions. The matrix $[|\underline{Q}_s|\,|\underline{Q}_d|]$ is the "outgoing submatrix" of the incidence matrix, where each row of $[|\underline{Q}_s|\,|\underline{Q}_d|]$ is a standard unit vector in Euclidean space. Therefore, the products $|\underline{Q}_s|(\boldsymbol{\alpha}^{(1)} + \boldsymbol{\alpha}^{(2)})$ and $|\underline{Q}_d|(\boldsymbol{\eta}^{(1)} + \boldsymbol{\eta}^{(2)})$ are also vectors

of ones of appropriate dimensions. Likewise, the vector in the Hadamard product with $\boldsymbol{d}$ is also a vector of ones. In the second case, we have

$$\begin{aligned} & R\left(\sigma_1^2\dot{\boldsymbol{\rho}}^{(1)}+\sigma_2^2\dot{\boldsymbol{\rho}}^{(2)}\right) \\ & \quad = Q_d^T X\left(\left(|\underline{Q}_s|\left(\sigma_1^2\boldsymbol{\alpha}^{(1)}+\sigma_2^2\boldsymbol{\alpha}^{(2)}\right)+|\underline{Q}_d|\left(\sigma_1^2\boldsymbol{\eta}^{(1)}+\sigma_2^2\boldsymbol{\eta}^{(2)}\right)\right)\odot F\right) \\ & \qquad -\left(I_q\left(\sigma_1^2\boldsymbol{\beta}^{(1)}+\sigma_2^2\boldsymbol{\beta}^{(2)}\right)+I_w\left(\sigma_1^2\boldsymbol{\eta}^{(1)}+\sigma_2^2\boldsymbol{\eta}^{(2)}\right)\right)\odot\boldsymbol{d}. \end{aligned}$$

Since $\boldsymbol{p}=\boldsymbol{c}^2\odot\boldsymbol{\rho}$, where $\boldsymbol{c}=(\sigma_1^2\boldsymbol{\eta}^{(1)}+\sigma_2^2\boldsymbol{\eta}^{(2)})^{1/2}$, it follows that the vector $(\sigma_1^2\boldsymbol{\eta}^{(1)}+\sigma_2^2\boldsymbol{\eta}^{(2)})$ is equal to the componentwise vector division $\boldsymbol{p}/\boldsymbol{\rho}$. Using the above definitions, we obtain the equivalent system

$$\begin{aligned} R\dot{\boldsymbol{\rho}} &= Q_d^T X F-\boldsymbol{d}, && (5.29)\\ R\dot{\boldsymbol{p}} &= Q_d^T X\left(\left(|\underline{Q}_s|\boldsymbol{a}^2+|\underline{Q}_d|\frac{\boldsymbol{p}}{\boldsymbol{\rho}}\right)\odot F\right)-\left(I_q\boldsymbol{b}^2+I_w\frac{\boldsymbol{p}}{\boldsymbol{\rho}}\right)\odot\boldsymbol{d}, && (5.30)\end{aligned}$$

where $F=f(\overline{M}_d\boldsymbol{\rho},M_s\boldsymbol{p}_s+M_d\boldsymbol{p})$. The system in (5.29)-(5.30) will be called the total density and pressure system of ODEs. We do not derive other equivalent systems. Instead, we compute the solution of the partial density system of ODEs numerically, and, thereafter, obtain the other variables of interest by subsequently applying the appropriate transformations.

The coupled systems split into isolated subsystems when the mixture is homogeneous. Suppose that $\boldsymbol{\eta}^{(m)}$, hence $\boldsymbol{c}$, are constant vectors. Using the relation $\boldsymbol{p}=\boldsymbol{c}^2\odot\boldsymbol{\rho}$, the above system of total density and pressure decouples into the two isolated subsystems

$$R\dot{\boldsymbol{\rho}} = Q_d^T X f\left(\overline{M}_d\boldsymbol{\rho},M_s\left(\boldsymbol{a}^2\odot\boldsymbol{\rho}_s\right)+M_d\left(\boldsymbol{c}^2\odot\boldsymbol{\rho}\right)\right)-\boldsymbol{d} \qquad (5.31)$$

and

$$\begin{aligned} R\dot{\boldsymbol{p}} &= Q_d^T X\left(\left(|\underline{Q}_s|\boldsymbol{a}^2+|\underline{Q}_d|\boldsymbol{c}^2\right)\odot f\left(\overline{M}_d\frac{\boldsymbol{p}}{\boldsymbol{c}^2},M_s\boldsymbol{p}_s+M_d\boldsymbol{p}\right)\right) \\ &\quad -\left(I_q\boldsymbol{b}^2+I_w\boldsymbol{c}^2\right)\odot\boldsymbol{d}, && (5.32)\end{aligned}$$

where $\boldsymbol{\rho}_s$ is the nodal density vector at the supply nodes (boundary condition profile) defined by $\boldsymbol{p}_s = \boldsymbol{a}^2 \odot \boldsymbol{\rho}_s$. The system in (5.31) is called the isolated total density system of ODEs and the system in (5.32) is called the isolated total pressure system. These two isolated systems ought to be equivalent to one another through the transformation $\boldsymbol{p} = \boldsymbol{c}^2 \odot \boldsymbol{\rho}$. This is to say that the solution $\boldsymbol{\rho}$ of (5.31) and the solution $\boldsymbol{p}$ of (5.32) must be linearly related by $\boldsymbol{p} = \boldsymbol{c}^2 \odot \boldsymbol{\rho}$ for constant vector $\boldsymbol{c}^2$. We do not present rigorous definitions and proofs of conditions on $\boldsymbol{\alpha}^{(m)}$, $\boldsymbol{\beta}^{(m)}$, $\boldsymbol{q}$, $\boldsymbol{w}$, and network topology that would result in $\boldsymbol{\eta}^{(m)}$ being constant and the two isolated subsystems being equivalent.

Chapter 6

MONOTONIC AND PERIODIC OPERATING REGIONS

This chapter investigates system properties that may lead to monotonicity and periodicity of solutions. Section 6.1 presents definitions and a theorem concerning monotone-ordering of solutions. Section 6.1.1 contains a proof that each of the equivalent systems from the previous chapter have monotonic solutions if the concentration is constant. In Section 6.1.2, we prove that the solutions are, in general, non-monotonic if the concentration is heterogeneous. Section 6.2 illustrates the non-monotonic results using numerical simulations of flows through a small network. Moreover, that section illustrates that certain types of equivalent systems may have more desirable monotone system behavior than others in certain operating regimes. Sections 6.3.1 and 6.3.2 numerically compute the monotonic and periodic interfaces for flow in a single pipeline with certain pipeline parameters.

6.1 Monotonicity

The monotonicity of solutions to flows of a homogeneous gas through an actuated transport network was examined as a means to reduce the complexity of optimization and optimal control of natural gas networks in the presence of uncertainty (Misra *et al.* (2020)). Here, we examine how such concepts can be extended to the transport of inhomogeneous gas mixtures, and specifically to characterize the extent and variability of hydrogen blending into a natural gas pipeline that is acceptable in the sense of maintaining monotone-ordering of solutions. We first present some analytical results before proceeding with numerical simulations in the next section.

A nonlinear input-to-state initial-value system of ODEs may be generally ex-

pressed as

$$\dot{x} = g(x, u, d), \qquad x(0) = y, \tag{6.1}$$

where $x(t) \in \mathcal{X} \subset \mathbb{R}^n$ is the state vector, $u(t) \in \mathcal{U} \subset \mathbb{R}^m$ is the control input vector, and $d(t) \in \mathcal{D} \subset \mathbb{R}^r$ is the parameter input vector defined for $t \in [0, T]$. It is assumed that the subsets $\mathcal{X}, \mathcal{U}$, and $\mathcal{D}$ are compact and convex and that the function $g : \mathcal{X} \times \mathcal{U} \times \mathcal{D} \to \mathcal{X}$ is Lipschitz in $\mathcal{X} \times \mathcal{U} \times \mathcal{D}$.

Definitions: For a given piecewise-continuous control input $u(t) \subset \mathcal{U}$, suppose that two independent state solutions $\{x_1(t), x_2(t)\} \subset \mathcal{X}$ exist (and are thus unique because g is Lipschitz) with corresponding initial conditions $\{y_1, y_2\} \subset \mathcal{X}$ and piecewise-continuous parameter inputs $\{d_1(t), d_2(t)\} \subset \mathcal{D}$ for $t \in [0, T]$. For the given control input $u(t)$, the system (6.1) is said to be *monotone-ordered* with respect to $d(t)$ if $x_1(t) \leq x_2(t)$ for $t \in [0, T]$ whenever $y_1 \leq y_2$ and $d_1(t) \leq d_2(t)$, where inequalities for vectors are taken componentwise. In this case, the solution states x_1 and x_2 are said to be *monotone-ordered*. For simplicity, we say that a monotone-ordered system and a set of monotone-ordered solutions are *monotone*, *monotonic*, and have the property of *monotonicity*. An $n \times n$ matrix A is called *Metzler* if all of its off-diagonal elements are non-negative, i.e. $A_{ij} \geq 0$ for all $i \neq j$. An $n \times m$ matrix is called *non-negative* if all of its entries are non-negative.

Theorem 1 (Monotonicity) (Angeli and Sontag (2003); Hirsch and Smith (2006)): The nonlinear system in (6.1) is monotone if and only if the Jacobian matrices $\partial g/\partial x$ and $\partial g/\partial d$ are, respectively, Metzler and non-negative almost everywhere in $\mathcal{X} \times \mathcal{U} \times \mathcal{D}$.

6.1.1 Homogeneous Concentration

In this subsection, our goal is to prove that the solutions of the equivalent systems in Section 5.3 are monotone-ordered if the concentration is constant. We first

reformulate the systems in terms of the definitions of monotonicity presented above. In steady-state (Misra *et al.* (2020)), the pressure $\boldsymbol{p}$ increases componentwise with *decreasing* withdrawal $\boldsymbol{w} \geq 0$ and with *increasing* injection $-\boldsymbol{q} \leq 0$. In reference to (6.1), we assume that all non-slack nodes are injection nodes and define the input parameter $d \in \mathcal{D}$ by $d = (\boldsymbol{p}_s, \boldsymbol{d}) = (\boldsymbol{p}_s, -\boldsymbol{q})$. Moreover, we assume that the flow is always in the positive orientation of the directed graph and that the concentration vector is constant in such a way that the coupled system in (5.29)-(5.30) reduces to the isolated systems in (5.31)-(5.32). Before we state our result, let us first recall some definitions.

Recall that X is diagonal with components $X_{kk} = \chi_k$ for $k \in \mathcal{E}$; that R is diagonal with components $R_{jj} = \boldsymbol{r}_j = \sum_{k \in \mapsto j} \chi_k \ell_k \overline{\mu}_k$ for $j \in \mathcal{V}_d$; that Q_d^T maps edge vectors $\psi \in \mathbb{R}^E$ to non-slack node vectors by $(Q_d^T \psi)_j = (\sum_{k:i \mapsto j} \psi_k - \sum_{k:j \mapsto i} \psi_k)$ for $j \in \mathcal{V}_d$; and that $f_k(y,z) = -\text{sign}(z_k)\Lambda_k \sqrt{|y_k z_k|}$. The system dynamics in (5.32) are rewritten here for simplicity:

$$R\dot{\boldsymbol{p}} \;=\; Q_d^T X \left(\left(|\underline{Q}_s| \boldsymbol{a}^2 + |\underline{Q}_d| \boldsymbol{c}^2 \right) \odot f\left(\overline{M}_d \frac{\boldsymbol{p}}{\boldsymbol{c}^2}, M_s \boldsymbol{p}_s + M_d \boldsymbol{p} \right) \right) + \boldsymbol{b}^2 \odot \boldsymbol{q}.$$

The k-th component of $(\overline{M}_d \boldsymbol{p}/\boldsymbol{c}^2)$ with $k : i \mapsto j$ is given by $(\overline{M}_d \boldsymbol{p}/\boldsymbol{c}^2)_k = \overline{\mu}_k \boldsymbol{p}_j / \boldsymbol{c}_j^2$. The k-th component of $(M_s \boldsymbol{p}_s + M_d \boldsymbol{p})$ with $k : i \mapsto j$ is given by $(M_s \boldsymbol{p}_s + M_d \boldsymbol{p})_k = (\overline{\mu}_k \boldsymbol{p}_j - \underline{\mu}_k \boldsymbol{p}_i)$. Since the flow is in the positive direction, it follows from (5.9) that $\overline{\mu}_k \boldsymbol{p}_j(t) < \underline{\mu}_k \boldsymbol{p}_i(t)$ for all $t \in [0,T]$ and $i, j \in \mathcal{V}$ with $k : i \mapsto j$. Thus, the sign and absolute value operations in the definition of the components of f are unnecessary. It follows that the j-th state dynamics in (5.32) for $j \in \mathcal{V}_d$ may be written as

$$\boldsymbol{r}_j \dot{\boldsymbol{p}}_j = \sum_{k:i \mapsto j} \frac{\boldsymbol{\sigma}_i^2 \chi_k \Lambda_k}{\boldsymbol{c}_j} \left(\overline{\mu}_k \boldsymbol{p}_j \left(\underline{\mu}_k \boldsymbol{p}_i - \overline{\mu}_k \boldsymbol{p}_j \right) \right)^{1/2} \tag{6.2}$$

$$- \sum_{k:j \mapsto i} \frac{\boldsymbol{c}_j^2 \chi_k \Lambda_k}{\boldsymbol{c}_i} \left(\overline{\mu}_k \boldsymbol{p}_i \left(\underline{\mu}_k \boldsymbol{p}_j - \overline{\mu}_k \boldsymbol{p}_i \right) \right)^{1/2} + \boldsymbol{b}_j^2 \boldsymbol{q}_j, \tag{6.3}$$

where $\boldsymbol{p}_i = (\boldsymbol{p}_s)_i$ and $\boldsymbol{\sigma}_i^2 = \boldsymbol{a}_i^2$ if $i \in \mathcal{V}_s$, whereas $\boldsymbol{\sigma}_i^2 = \boldsymbol{c}_i^2$ if $i \in \mathcal{V}_d$. It is clear from this expanded form that the function on the right-hand-side of (5.32) is continuously differentiable (hence Lipschitz) in the state and input variables over the domain of positive flow and pressure.

Proposition 2 (Monotonicity of Total Pressure and Density): Assume that i) all non-slack nodes are injection nodes; ii) gas flows only in the positive direction through each edge according to its orientation in the network graph; iii) pressure is positive in each node; and iv) (5.15) is satisfied. Suppose that the concentration vector $\boldsymbol{\eta}^{(2)}$ is constant, that the isolated subsystems in (5.31)-(5.32) are equivalent, and that there exist two state solutions $\boldsymbol{p}_1$, $\boldsymbol{p}_2$ of the system in (5.32) with respective initial conditions $\boldsymbol{\pi}_1$, $\boldsymbol{\pi}_2$, slack pressures $(\boldsymbol{p}_s)_1$, $(\boldsymbol{p}_s)_2$, and non-slack injection flows $\boldsymbol{q}_1$, $\boldsymbol{q}_2$ for a given fixed set of control inputs $\{\underline{\mu}, \overline{\mu}\}$. Here, the vector subscripts denote the first and second solutions and not the refined nodes. If $\boldsymbol{\pi}_1 \leq \boldsymbol{\pi}_2$, $(\boldsymbol{p}_s)_1(t) \leq (\boldsymbol{p}_s)_2(t)$, and $\boldsymbol{q}_1(t) \geq \boldsymbol{q}_2(t)$ componentwise for all $t \in [0, T]$, then $\boldsymbol{p}_1(t) \leq \boldsymbol{p}_2(t)$. Consequently, $\boldsymbol{\rho}_1(t) \leq \boldsymbol{\rho}_2(t)$, where $\boldsymbol{\rho}_1$ and $\boldsymbol{\rho}_2$ are the corresponding total density solutions.

Proof: Throughout this proof, the state and input subscripts correspond to the nodes of the refined graph. In reference to Theorem 1, we first show that the state Jacobian matrix is Metzler, i.e., $\partial \dot{\boldsymbol{p}}_j / \partial \boldsymbol{p}_i$ is non-negative for all i, $j \in \mathcal{V}_d$ with $i \neq j$. If i and j are non-adjacent with $i \neq j$, then clearly $\partial \dot{\boldsymbol{p}}_j / \partial \boldsymbol{p}_i = 0$. Suppose that i and j are adjacent with $k : j \mapsto i$. Substituting (5.10)-(5.11) into (5.15) and using the relation between pressure and partial densities, it can be shown that $(\overline{\mu}_k \boldsymbol{p}_i - \underline{\mu}_k \boldsymbol{p}_j) > -\overline{\mu}_k \boldsymbol{p}_i$. Thus, the Jacobian component

$$\frac{\partial \dot{\boldsymbol{p}}_j}{\partial \boldsymbol{p}_i} = \frac{\boldsymbol{c}_j^2 \chi_k \Lambda_k \overline{\mu}_k (2\overline{\mu}_k \boldsymbol{p}_i - \underline{\mu}_k \boldsymbol{p}_j)}{2\boldsymbol{r}_j \boldsymbol{c}_i (\overline{\mu}_k \boldsymbol{p}_i (\underline{\mu}_k \boldsymbol{p}_j - \overline{\mu}_k \boldsymbol{p}_i))^{1/2}} \tag{6.4}$$

is positive. Suppose that i and j are adjacent with $k : i \mapsto j$. Then

$$\frac{\partial \dot{\boldsymbol{p}}_j}{\partial \boldsymbol{p}_i} = \frac{\boldsymbol{\sigma}_i^2 \chi_k \Lambda_k \underline{\mu}_k \overline{\mu}_k \boldsymbol{p}_j}{2\boldsymbol{r}_j \boldsymbol{c}_j (\overline{\mu}_k \boldsymbol{p}_j (\underline{\mu}_k \boldsymbol{p}_i - \overline{\mu}_k \boldsymbol{p}_j))^{1/2}} > 0. \tag{6.5}$$

Because $j \in \mathcal{V}_d$ is arbitrary, it follows that the state Jacobian matrix is Metzler. We now show that the parameter Jacobian matrix is non-negative. The above computation can be extended to show that $\partial \dot{\boldsymbol{p}}_j / \partial (\boldsymbol{p}_s)_i$ is non-negative for $i \in \mathcal{V}_s$. With respect to mass inflow parameters, the Jacobian components $\partial \dot{\boldsymbol{p}}_j / \partial \boldsymbol{q}_i = \boldsymbol{b}_j^2 / \boldsymbol{r}_j \delta_{i,j}$ are non-negative ($\delta_{i,j}$ is the Kronecker delta). We conclude from Theorem 1 that the system in (5.32) is monotone. Because $\boldsymbol{p}_j = \boldsymbol{c}_j^2 \boldsymbol{\rho}_j$ for $j \in \mathcal{V}_d$, it follows that the isolated total density system is monotone as well. $\square$

Corollary (Monotonicity of Equivalent Systems): Assume that the conditions hold from Proposition 2. Then $\boldsymbol{\rho}_1^{(m)}(t) \leq \boldsymbol{\rho}_2^{(m)}(t)$ componentwise for all $t \in [0, T]$, where $\boldsymbol{\rho}_1^{(m)}$ and $\boldsymbol{\rho}_2^{(m)}$ are the partial densities of the two solutions.

Proof: By Proposition 2, we have $\boldsymbol{\rho}_1^{(m)} = \boldsymbol{\eta}^{(m)} \odot \boldsymbol{\rho}_1 \leq \boldsymbol{\eta}^{(m)} \odot \boldsymbol{\rho}_2 = \boldsymbol{\rho}_2^{(m)}$. $\square$

6.1.2 Heterogeneous Concentration

In the case of general heterogeneous mixtures, the concentration input vectors $\boldsymbol{\alpha}^{(m)}$ and $\boldsymbol{\beta}^{(m)}$ may be time-varying. Therefore, the parameter input space $\mathcal{D}$ must be extended to include vectors of the form $d = (\boldsymbol{p}_s, -\boldsymbol{q}, \boldsymbol{\alpha}^{(m)}, \boldsymbol{\beta}^{(m)})$. We have the following result.

Proposition 3 (Non-Monotonicity of Total Pressure and Density): Assume that i) all non-slack nodes are injection nodes; ii) gas flows only in the positive direction through each edge according to its orientation in the network graph; and iii) pressure and density are positive in each node. Suppose that, for a given fixed set of control inputs $\{\underline{\mu}, \overline{\mu}\}$, there exist two state solutions $(\boldsymbol{\rho}, \boldsymbol{p})_1$, $(\boldsymbol{\rho}, \boldsymbol{p})_2$ of the system in (5.29)-(5.30) with respective initial conditions $(\boldsymbol{\varrho}, \boldsymbol{\pi})_1$, $(\boldsymbol{\varrho}, \boldsymbol{\pi})_2$, slack inputs $(\boldsymbol{\rho}_s, \boldsymbol{p}_s)_1$, $(\boldsymbol{\rho}_s, \boldsymbol{p}_s)_2$, and non-slack mass inflows $\boldsymbol{q}_1$, $\boldsymbol{q}_2$ that satisfy $(\boldsymbol{\varrho}, \boldsymbol{\pi})_1 \leq (\boldsymbol{\varrho}, \boldsymbol{\pi})_2$, $(\boldsymbol{\rho}_s(t), \boldsymbol{p}_s(t))_1 \leq (\boldsymbol{\rho}_s(t), \boldsymbol{p}_s(t))_2$, and $\boldsymbol{q}_1(t) \geq \boldsymbol{q}_2(t)$ componentwise for all $t \in [0, T]$. If $\boldsymbol{\eta}^{(m)}(t)$ is time-varying, then, in general, $(\boldsymbol{\rho}(t), \boldsymbol{p}(t))_1 \not\leq (\boldsymbol{\rho}(t), \boldsymbol{p}(t))_2$ component-wise

for all $t \in [0, T]$.

Proof: Throughout this proof, the state and input subscripts correspond to the nodes of the refined graph. From Theorem 1, it suffices to show that one component of the state Jacobian matrix is negative. The j-th nodal pressure dynamics in (5.30) may be written as

$$\boldsymbol{r}_j \dot{\boldsymbol{p}}_j = \sum_{k:i \mapsto j} \boldsymbol{\sigma}_i^2 \chi_k \Lambda_k \left(\overline{\mu}_k \boldsymbol{\rho}_j \left(\underline{\mu}_k \boldsymbol{p}_i - \overline{\mu}_k \boldsymbol{p}_j \right) \right)^{1/2} \tag{6.6}$$

$$- \sum_{k:j \mapsto i} \frac{\boldsymbol{p}_j}{\boldsymbol{\rho}_j} \chi_k \Lambda_k \left(\overline{\mu}_k \boldsymbol{\rho}_i \left(\underline{\mu}_k \boldsymbol{p}_j - \overline{\mu}_k \boldsymbol{p}_i \right) \right)^{1/2} + \boldsymbol{b}_j^2 \boldsymbol{q}_j, \tag{6.7}$$

where $\boldsymbol{p}_i = (\boldsymbol{p}_s)_i$, $\boldsymbol{\rho}_i = (\boldsymbol{\rho}_s)_i$, and $\boldsymbol{\sigma}_i^2 = \boldsymbol{a}_i^2$ if $i \in \mathcal{V}_s$, and $\boldsymbol{\sigma}_i^2 = \boldsymbol{p}_i / \boldsymbol{\rho}_i$ if $i \in \mathcal{V}_d$. By adding a refined edge to the graph if necessary, we assume that there is an edge $k' : i' \mapsto j$ with $i' \in \mathcal{V}_d$. The Jacobian component corresponding to $\boldsymbol{\rho}_{i'}$ is given by

$$\frac{\partial \dot{\boldsymbol{p}}_j}{\partial \boldsymbol{\rho}_{i'}} = -\frac{\chi_{k'} \Lambda_{k'}}{\boldsymbol{r}_j} \frac{\boldsymbol{p}_{i'}}{\boldsymbol{\rho}_{i'}^2} \left(\overline{\mu}_{k'} \boldsymbol{\rho}_j \left(\underline{\mu}_{k'} \boldsymbol{p}_{i'} - \overline{\mu}_{k'} \boldsymbol{p}_j \right) \right)^{1/2},$$

which is negative. It follows from Theorem 1 that the system in (5.29)-(5.30) is not monotone, regardless of (5.15). □

6.2 Network Example

We use numerical simulations to examine how time-varying heterogeneity of a transported mixture affects flow dynamics throughout a network and compare equivalent system variables. The simulations are performed for a test network that was used in a previous study (Gyrya and Zlotnik (2019)), in which the authors presented a staggered grid discretization method for the numerical solution of homogeneous natural gas pipeline flow. The configuration and dimensions of the network are shown in Figure 6.1. The dark blue node is a slack node at which pressure and concentration are specified, the black, maroon, and cyan nodes are non-slack withdrawal nodes, and the green node is a non-slack injection node. The sound speeds are chosen to be $\sigma_1 = 377$

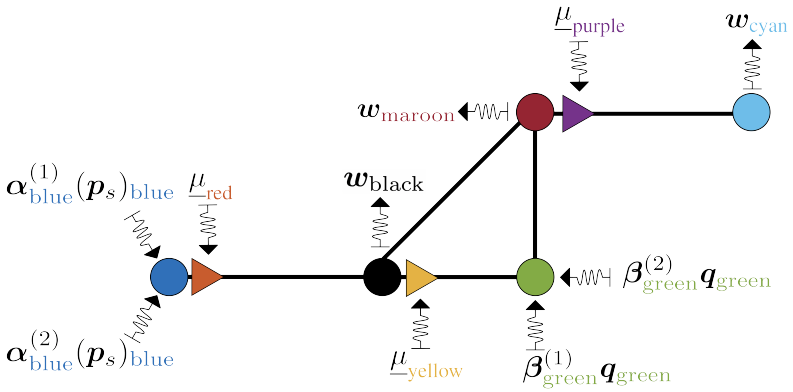

Figure 6.1: Network configuration (not to scale). The triangles represent compressor stations. Pipeline dimensions between nodes: blue to black (20 Km), black to green (70 Km), green to maroon (10 Km), black to maroon (60 Km), and maroon to cyan (80 Km). The pipelines have uniform diameter (.9144 M) and friction factor (.01), except for the black to maroon pipeline that has diameter (.635 M) and friction factor (.015).

(m/s) and $\sigma_2 = 2.8\sigma_1$. We simulate several examples to illustrate that some physical quantities exhibit fewer crossings than others in certain operating regimes, given ordered boundary parameters. These examples provide insight into which equivalent system may be more useful for a particular operating regime. Figures 6.2-6.3 show the solutions of four different examples. Two solutions corresponding to monotone-ordered boundary conditions are simulated for each example. We now describe the results of each simulation.

On the left side of Figure 6.2, total pressure, density, and energy solutions at the non-slack nodes do not overlap, but the mass and volumetric concentrations do overlap. The solutions on the right side of Figure 6.2 have the same boundary conditions as those on the left except for the supply pressure. By doubling the supply pressure, the total density now overlaps at each non-slack node but the pressure and energy still do not overlap. In Figure 6.3, the blue node injects pure natural gas and the green node injects pure hydrogen with a varying mass inflow profile. As seen on the left side of Figure 6.3, the pressure and energy solutions at each node do not

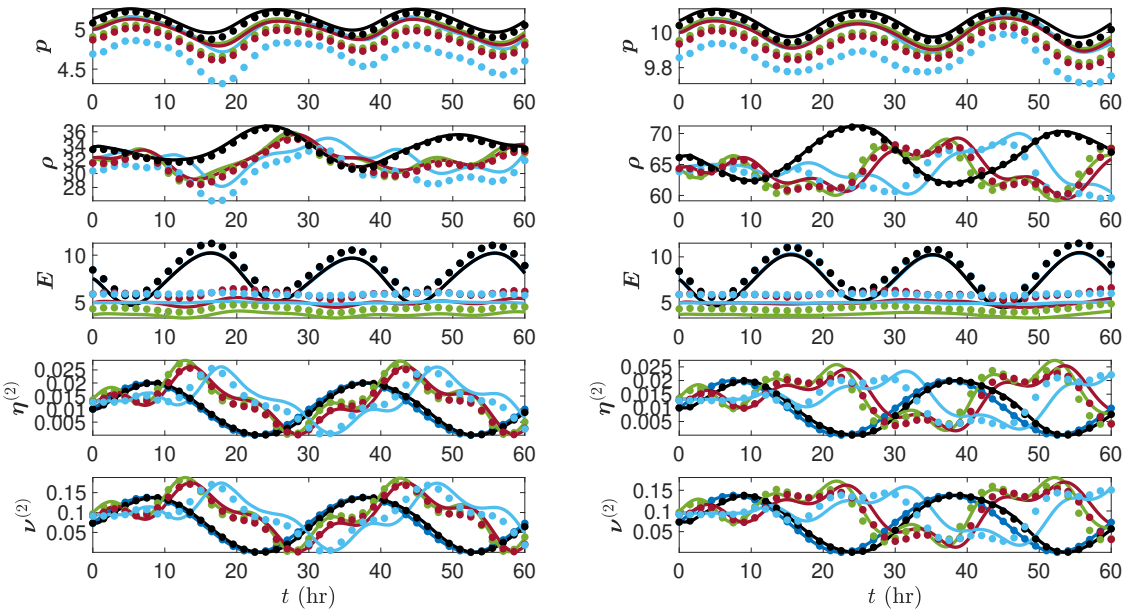

Figure 6.2: (Left) Two solutions (solid lines vs. dots) at the color-coordinated network nodes in Figure 6.1. The boundary conditions for both solutions are $(\boldsymbol{p}_s)_{\text{blue}} = 5$ MPa, $\boldsymbol{\alpha}^{(2)}_{\text{blue}}(t) = 0.01(1+\sin(4\pi t/T))$, $\boldsymbol{\beta}^{(2)}_{\text{green}}(t) = 0.125(1+\sin(12\pi t/T))$, $\boldsymbol{q}_{\text{green}}(t) = 3$ (kg/s), $\boldsymbol{w}_{\text{black}}(t) = 60(1-\sin(6\pi t/T))$ (kg/s), $\mu_{\text{red}} = 1.0678$, $\underline{\mu}_{\text{yellow}} = 1.0140$, and $\underline{\mu}_{\text{purple}} = 1.0734$, where $T = 60$ (hr). The boundary condition that differs between the two solutions is $\boldsymbol{w}_{\text{cyan}}(t) = 110$ (kg/s) (solid lines) and $\boldsymbol{w}_{\text{cyan}}(t) = 130$ (kg/s) (dots). **(Right)** Same boundary conditions except for $(\boldsymbol{p}_s)_{\text{blue}} = 10$ (MPa).

overlap. However, a close examination shows that the density solutions do overlap at every node upstream from the point of hydrogen injection. The concentration solutions overlap at only the cyan node. The right side of Figure 6.3 injects gas at the supply node with double the pressure as that on the left side, but all other boundary conditions remain the same. This increase in supply pressure forces the pressure, density, and energy solutions to overlap at all of the non-slack nodes. The concentrations overlap at every node upstream the node of hydrogen injection. At nodes downstream the injection of hydrogen, the concentration of hydrogen is zero, as it ought to be. The solutions in Figure 6.3 may not be realistic in the current operation

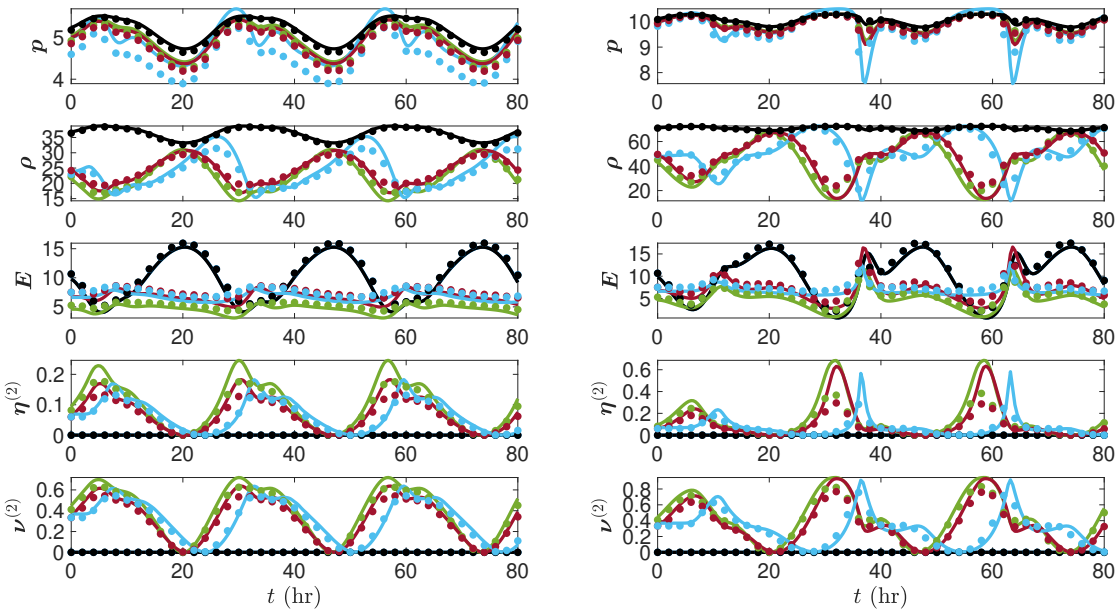

Figure 6.3: (Left) The boundary conditions for the two solutions are $(\boldsymbol{p}_s)_{\text{blue}} = 5$ (MPa), $\boldsymbol{\alpha}^{(2)}_{\text{blue}}(t) = 0$, $\boldsymbol{\beta}^{(2)}_{\text{green}}(t) = 1$, $\boldsymbol{q}_{\text{green}}(t) = 9(1 + \sin(6\pi t/T))$ (kg/s), $\boldsymbol{w}_{\text{black}}(t) = 100(1 - \sin(6\pi t/T))$ (kg/s), $\mu_{\text{red}} = 1.1096$, $\underline{\mu}_{\text{yellow}} = 1.0057$, and $\underline{\mu}_{\text{purple}} = 1.1301$, where $T = 80$ (hr). The other boundary condition is $\boldsymbol{w}_{\text{cyan}}(t) = 130$ (kg/s) (solid lines) and $\boldsymbol{w}_{\text{cyan}}(t) = 150$ (kg/s) (dots). **(Right)** Same boundary conditions except for $(\boldsymbol{p}_s)_{\text{blue}} = 10$ (MPa).

of natural gas pipelines because the concentration of hydrogen reaches very high levels. However, these figures indicate that the solutions may behave erratically if the pipelines are manufactured to deliver up to 20-30% of hydrogen by mass. In particular, the solution variables may have large gradient surges in small time intervals.

The five edges of the network are discretized into 240 refined edges with $\ell_k = 1$ (km) for all $k \in \hat{\mathcal{E}}$. Although one kilometer is sufficiently fine to demonstrate non-monotonicity for slowly-varying concentrations, a much smaller discretization size is required to accurately simulate rapidly-varying concentrations. We note that even the slowly-varying solutions in Figures 6.2-6.3 show noticeable convergence as the discretization size is decreased from 1 (km) to 100 (m). For small discretization

lengths ($\ell_k \leq 100$ (m)), the overlap between the solutions in these figures may be more pronounced.

6.3 Phase Interfaces

Proposition 3 shows that the total pressure and density system of ODEs is not monotone-ordered over the entire input region $\mathcal{D} = (\boldsymbol{p}_s, -\boldsymbol{q}, \boldsymbol{\alpha}^{(m)}, \boldsymbol{\beta}^{(m)})$. However, by Proposition 2, its Corollary, and the continuity of solutions with respect to initial conditions and inputs (Khalil (2002)), for a given set of plant parameters, the non-isolated total pressure and density system of ODEs is expected to be monotone-ordered over a certain sub-region $\mathcal{D}_0 \subset \mathcal{D}$ that consists of concentration vectors that are uniformly close to a constant concentration vector. Moreover, again by continuity, monotonicity is expected to hold for slow variations in concentration with large amplitudes. This suggests that there may be a nontrivial monotonic interface (MI) that partitions the concentration boundary conditions (hence $\mathcal{D}$) into monotonic and non-monotonic phase regions for each equivalent system variable. We analyze the MI numerically for a single pipeline. In the remainder of this section, we consider a single pipeline with concentration and pressure specified at the inlet of the pipeline (node 1) and with mass outflow specified at the outlet (node 2). The pipeline parameters and boundary conditions that do not change are $\ell = 50$ km, $D = 0.5$ m, $\lambda = 0.11$, and $\boldsymbol{p}_s = 7$ MPa. We denote the concentration of hydrogen at the inlet slack node by $\boldsymbol{\alpha}_1(t) = \boldsymbol{\alpha}_1^{(2)}(t)$ and specify it to be

$$\boldsymbol{\alpha}_1(t) = \alpha_1 \left(1 + \kappa \sin(2\pi\omega_* t)\right), \tag{6.8}$$

where κ is the amplitude factor of the sinusoid, ω_* is its frequency in cycles per hour, and α_1 is the mean concentration profile around which the sinusoid oscillates. Here, the subscript is with respect to the node number.

6.3.1 Monotonic Interface

We consider the following question.

> *What is the interface* (ω_*, κ_*) *in the* (ω_*, κ) *plane below and above which the solution is monotonic and non-monotonic, respectively?*

The MI is computed for each flow variable using numerical simulations. In addition to the boundary conditions that are specified at the beginning of this section, this subsection uses $\sigma_1 = 377$ (m/s), $\sigma_2 = 2.8\sigma_1$, and $\alpha_1 = 0.02$. For each (ω_*, κ) in (6.8), we compute three solutions corresponding to three monotone-ordered mass outflows $\boldsymbol{w}_2 = \overline{\varphi}\pi(D/2)^2$ (kg/s), where $\overline{\varphi} = 120$, 140, and 160 (kg/m^{2}s). The region in the (ω_*, κ) plane defined by $0 \leq \omega_* \leq 2$ and $0 \leq \kappa \leq 1$ is discretized into a 21×41 grid of discrete pairs. We numerically simulate the three solutions for each pair of boundary condition parameters on this grid. In particular, for each discrete ω_*, we compute the three solutions for each discrete κ with until we achieve the lower bound $\kappa = \kappa_*(\omega_*)$ at which at least two of the three solutions overlap. The MI curves for several equivalent system variables are depicted in Figure 6.4. The region below the MI curve is called the monotone operating region (MOR). Figure 6.4 shows that the MORs for hydrogen density, natural gas density, total density, energy, and pressure are nested increasing sets with the hydrogen density MOR being the smallest set and the pressure MOR being the largest. For time-varying concentration profiles, Figure 6.4 suggests that the pressure and energy equivalent system should be used if monotonicity properties are important to the formulation. This is the conclusion that we arrived at in Section 6.2. Of the five examples from Section 6.2, only Figure 6.2 considered time-variations in concentration. Figure 6.2 used two sinusoidal forcing frequencies, 0.1 (cyc/hr) and 0.033 (cyc/hr), each with unity amplitude factors $\kappa = 1$. Recall that in those figures, only the pressure and energy solutions did not overlap. This observation agrees with

the MIs in Figure 6.4, where the operating point $(\omega_* = 0.1, \kappa = 1)$ is above all of the MIs except for the pressure and energy MIs. For a more accurate comparison, the MIs ought to be recomputed with 5 and 10 (MPa) slack pressures instead of the 7 (MPa) that was used to compute the MIs in Figure 6.4.

As ω_* increases from $\omega_* = 0$ to $\omega_* = 2$ (cyc/hr), the MI curves qualitatively decrease from unity to a lower bound, flatten out, and then increase. The fact that the amplitude factor generally increases along the MI as ω_* increases beyond $\omega_* = 0.75$ is a robustness feature of monotonicity to high frequency uncertainty. This property appears to be a consequence of wave attenuation in gas pipelines that was covered in the previous chapter. In particular, the gas pipeline demonstrates low-pass filtering characteristics with which the amplitudes of high frequency travelling waves are significantly attenuated over short distances, and, therefore, the likelihood of the solutions overlapping decreases as the high frequency waves increase in frequency. If the concentration of hydrogen injected into the network contains a small variation of high frequency uncertainty, then the MIs suggest that this uncertainty typically will not cause an otherwise theoretically monotonic operation to become non-monotonic.

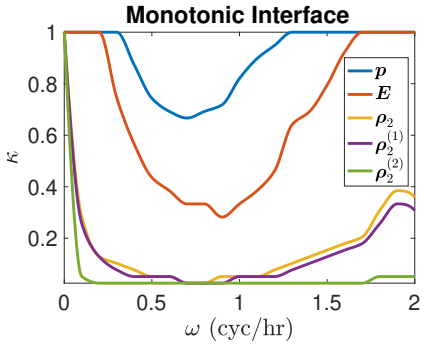

Figure 6.4: Monotonic interfaces.

6.3.2 Periodic Interface

In this section, we demonstrate that non-periodic solutions may emerge from sinusoidal concentration boundary conditions. To study periodic solutions, we must simulate solutions over large time intervals of up to 400 hours. In addition, we will consider large and fast variations in concentration. This requires an extremely fine

spatial discretization size for the simple endpoint discretization method. The large time interval and small discretization size is difficult to implement digitally. Therefore, in our study of periodic solutions, instead of using the endpoint discretization method, we discretize the pipeline at the (translated) nodes of Chebyshev polynomials for which exponential convergence properties are obtained (e.g., see Ascher and Greif (2011)). We briefly outline the method here. Consider a single pipeline of length ℓ, diameter D, and friction factor λ with axial variable $x \in [0, \ell]$. Discretize the interval $[0, \ell]$ with the $(N+1)$ discretization points $x_i = \ell/2(1 - \cos(i\pi/N))$ for $i = 0, \ldots, N$. Define the sampled variables $\boldsymbol{\rho}_i^{(m)}(t) = \rho^{(m)}(t, x_i)$ and $\boldsymbol{\varphi}_i(t) = \varphi(t, x_i)$. It follows from interpolating the values of $\boldsymbol{\rho}_i^{(m)}(t)$ at the points x_i using Lagrange polynomials of order N that (e.g., see Ascher and Greif (2011))

$$\partial_x \rho^{(m)}(t, x_i) \approx \boldsymbol{D}\boldsymbol{\rho}_i^{(m)}(t), \qquad \boldsymbol{D}_{ij} = \begin{cases} \sum\limits_{\substack{n=0 \\ n \neq j}}^{n} \frac{1}{x_j - x_n}, & i = j, \\ \frac{1}{x_j - x_i} \prod\limits_{\substack{n=0 \\ n \neq i,j}}^{n} \frac{x_i - x_n}{x_j - x_n} & i \neq j. \end{cases} \tag{6.9}$$

The discretized PDEs in (5.8)-(5.9) become

$$\dot{\boldsymbol{\rho}}^{(m)} + \boldsymbol{D}\left(\frac{\boldsymbol{\rho}^{(m)}}{\boldsymbol{\rho}^{(1)} + \boldsymbol{\rho}^{(2)}} \odot \boldsymbol{\varphi}\right) = 0, \tag{6.10}$$

$$\boldsymbol{D}\left(\sigma_1^2 \boldsymbol{\rho}^{(1)} + \sigma_2^2 \boldsymbol{\rho}^{(2)}\right) = -\frac{\lambda}{2D} \frac{\boldsymbol{\varphi} \odot |\boldsymbol{\varphi}|}{\boldsymbol{\rho}^{(1)} + \boldsymbol{\rho}^{(2)}}. \tag{6.11}$$

The boundary conditions are incorporated into the discretized equations by replacing $\boldsymbol{\rho}_0^{(m)}(t) = \boldsymbol{s}_0^{(m)}(t)$ and $\boldsymbol{\varphi}_N(t) = \boldsymbol{w}_N(t)/(0.25\pi D^2)$. This ODE system is implemented in Matlab using the function `ode15s`.

To introduce the transition to non-periodic phenomena, Figure 6.5 shows three examples that share the same boundary conditions with the exception of different frequencies ω_* and amplitude factors κ of the sinusoidal concentration profile in (6.8). The top of the three figures depict the pressure solutions at the outlet of the pipeline

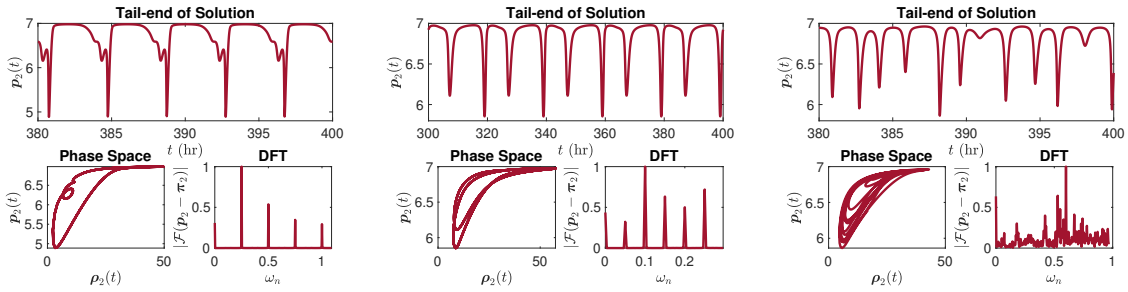

Figure 6.5: Pipeline solution with boundary conditions $\boldsymbol{w}_2(t) = 75\pi(D/2)^2$ (kg/s). **(Left)** $\omega_* = 0.25$ and $\kappa = 1.0$ with $\mathcal{P} = 0.12$. **(Middle)** $\omega_* = 0.1$ and $\kappa = 0.98$ with $\mathcal{P} = 0.1$. **(Right)** $\omega_* = 0.6$ and $\kappa = 0.9$ with $\mathcal{P} = 1.49$.

for $t \in [rT, T]$ with $0.7 \leq r \leq 0.95$, where $T = 400$ hr. The tail-ends of the solutions are used to bypass the initial transient responses that are not included here in the analysis of periodic orbits. We see that the solutions on the left and middle sides of the figure approach periodic orbits and that the solution on the right side does not appear to do so. The pressure on the left side has twice as many local minima than the inlet concentration over the time interval $[0.95T, T]$. The additional local minima correspond to the inner loop of the periodic orbit. The pressure in the middle solution has the same number of local minima as the inlet concentration over the interval $[0.75T, T]$, but has twice the period. These examples demonstrate that periodic solutions may even be incoherent in the following sense. From the laws of fluid dynamics, gas pressure should decrease with decreasing density under constant temperature and volume. However, the phase space diagrams in Figure 6.5 contain small time intervals and their periodic repetitions during which density decreases while pressure increases. The solutions in this section are computed with sound speeds $\sigma_1 = 338.38$ m/s, $\sigma_2 = 4\sigma_1$, and mean hydrogen mass concentration $\alpha_1 = 0.2$.

The frequency responses of each solution are also depicted in Figure 6.5 using the discrete Fourier transform (DFT) (Oppenheim *et al.* (2001)). The DFT is defined below in (6.12). The dominant frequency mode in the solution appears at the forcing

frequency $\omega_n = \omega_*$ in Figure 6.5. The generated frequency modes in the left, middle and right sides of Figure 6.5 appear, respectively, at integer multiples of ω_*, at half the values of the integer multiples of ω_*, and in a continuous distribution. These observations inspire a quantitative measure of periodicity in terms of the frequency response of the solution. This is the approach taken in (Tziperman *et al.* (1994)) for the transition to what they term "chaotic" responses in oceanic wind bursts. We define a sequence of evenly-spaced samples of the tail-end of the outlet pressure by $\boldsymbol{p}_2[k] = \boldsymbol{p}_2((0.8+k/N)T)$ for $k = 0, \ldots, 0.2N$, where N is equal to the number of time steps in the numerical solution over the interval $[0, T]$. For such a sampled sequence $\boldsymbol{\psi}[k]$ its normalized DFT is defined as

$$\{\mathcal{F}\boldsymbol{\psi}\}[\omega_n] = \frac{\sum_{k=0}^{0.2N} \boldsymbol{\psi}[k] e^{-\mathbf{j}2\pi\omega_n k}}{\max_{\omega_n} \left| \sum_{k=0}^{0.2N} \boldsymbol{\psi}[k] e^{-\mathbf{j}2\pi\omega_n k} \right|}, \tag{6.12}$$

where $\omega_n = n/(0.2T)$ (cyc/hr) are the sampling frequencies for $n = 0, \ldots, 0.2N$. The measure of periodicity is defined by the average power spectrum given by

$$\mathcal{P} = \frac{1}{0.2N+1} \sum_{n=0}^{0.2N} |\{\mathcal{F}(\boldsymbol{p}_2 - \boldsymbol{\pi}_2)\}[\omega_n]|^2 \times 100, \tag{6.13}$$

where $\boldsymbol{\pi}_2 = \boldsymbol{p}_2(0)$ is the initial steady-state value of pressure at the outlet of the pipeline. The shifted pressure in the power spectrum is used to suppress the zero frequency component of the initial state.

The power spectrum $\mathcal{P}$ is depicted in a color map as a function of (ω_*, κ) on the left side of Figure 6.6, where ω_* is the forcing frequency and κ is its amplitude factor given in (6.8). This figure has been obtained numerically as follows. Similarly to the way that we have computed the MIs, the region in the (ω_*, κ) plane defined by $0 \leq \omega_* \leq 2$ and $0.5 \leq \kappa \leq 1$ is discretized into a 31×15 grid of discrete pairs. For each frequency and amplitude factor of the forcing concentration on this grid, we numerically simulate the solution in the pipeline for 400 hours. We then compute

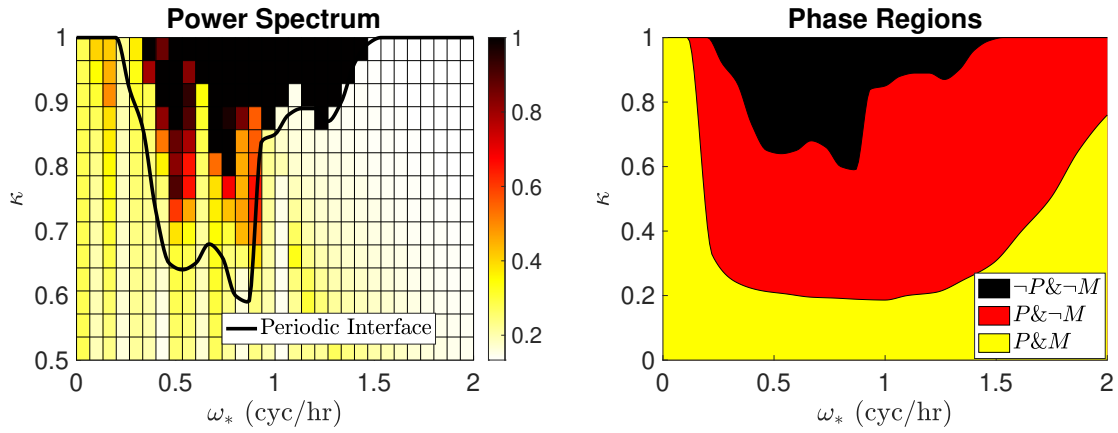

Figure 6.6: (Left) Color map of the power spectrum $\mathcal{P}$ in (6.13) as a function of (ω_*, κ) in (6.8). The boundary conditions are $\alpha_1 = 0.2$ and $\boldsymbol{w}_2(t) = 75$. The coloring depicts the minimum between 1 and $\mathcal{P}$ in (6.13). **(Right)** Phase operating regions that separate periodic and monotonic ($P\&M$), periodic and not monotonic ($P\&\neg M$), and neither periodic nor monotonic ($\neg P\&\neg M$).

the DFT and power spectrum of the sampled solution, as defined above. This gives the discrete set of quantified values depicted on the left side of Figure 6.6. The periodic interface (PI) in this figure is the set of operating points below or above which the solution does or does not visually approach a periodic orbit. For each ω_*, the parameter κ is increased from $\kappa = 0$ to $\kappa = \kappa^*(\omega_*)$, where $\kappa^*(\omega_*)$ is the upper bound on κ below which the tail-end of the solution $(\boldsymbol{p}_2(t), \boldsymbol{\rho}_2(t))$ traces a closed orbit. Figure 6.6 shows that the power spectrum measure and the visual periodic interface are in reasonable agreement.

We now compare the MI and the PI of the pressure variable with $\alpha_1 = 0.2$. These interfaces separate the phase regions from periodic and monotonic, to periodic and non-monotonic, to non-periodic and non-monotonic as shown on the right side of Figure 6.6. Note that the pressure MI in Figure 6.6 is different from the pressure MI in Figure 6.4 due to the different mean concentration α_1. Figure 6.6 shows that the interfaces are equal for $\omega_* < 0.2$. As the frequency increases from $\omega_* = 0.2$ to

$\omega_* = 0.5$, the value of κ on the MI decreases. As the frequency increases from $\omega_* = 0.3$ to $\omega_* = 0.5$, the value of κ on the PI decreases. The interfaces are roughly constant over the frequency range $0.5 < \omega_* < 0.9$. As frequency increases from $\omega_* = 1$, both of the interfaces generally increase. However, the PI shows a more significant increase in its accent over this frequency range than the MI. More importantly, the MI is never above the PI over the entire frequency range, so that the monotonic operating region is a subset of the periodic operating region. This suggests that monotonic solutions may eventually approach periodic orbits for certain plant parameters, which leads to some open questions. Can the MI, PI, or both be characterized or approximated analytically in terms of the set of plant parameters? Is the heterogeneous gas mixture system chaotic (Devaney (2021))? We present these questions here to inspire future work, but do not pursue them in this thesis.

Chapter 7

OPTIMAL CONTROL OF HETEROGENEOUS MIXTURES

This chapter uses the ODE control system from Chapter 5 as the constraints of an optimal control problem. The goal is to design control actions of compressor units to minimize the their expended energy during operation while satisfying the delivery and physical flow requirements. The OCP is formulated in Section 7.1 as an ODE-constrained optimization problem. The time interval is discretized into evenly-space sampling times in Section 7.2 and the derivative term in the ODE system constraints is approximated using Euler's method. This allows us to implement the nonlinear optimization program digitally in Matlab. We demonstrate the methodology on a small test network in Section 7.3. The optimal control problem has received significant attention by others for the case of natural gas flows (see, e.g. Zlotnik *et al.* (2015a); Sundar and Zlotnik (2018)). The key advancement of our work is the extension of the OCP from transient flows of natural gas in networks to transient flows of mixtures of natural gas and hydrogen in networks.

7.1 Formulation

The actions of compressors and regulators, defined by the function values $\underline{\mu}_k(t)$ and $\overline{\mu}_k(t)$, are designed to minimize the energy expended by their respective units. Because pressure down-regulation does not consume considerable energy, its proportion of total energy used for operating a pipeline may be neglected. The total energy required for compression is given by

$$J = \sum_{k\in\mathcal{E}} \int_0^T c_k |\underline{\varphi}_k(t)| \left((\underline{\mu}_k(t))^{(\nu-1)/\nu} - 1 \right) dt, \tag{7.1}$$

where c_k is related to the efficiency of the compressor $\underline{\mu}_k$ and ν is the isentropic exponent (Marić *et al.* (2005)) (which is assumed to be a weighted average of those of natural gas and hydrogen with weights equal to their respective mean concentration injections). Most compressors run using gas drawn from the pipeline itself, and the operational cost is the value of that gas. However, the flow model presented here does not include withdrawing from the pipeline at the compressor stations so that, effectively, the cost of operation may be considered as the equivalent cost of electrical or another type of energy that does not affect the pipeline flow. Gas network operators require pressure and compression to be within satisfactory limitations to ensure the safety of transportation and the quality of gas delivered to customers. These limitations are modeled for the discretized system in (5.23) for all $k \in \mathcal{E}$ with inequality constraints of the form

$$\boldsymbol{p}^{\min} \leq \sigma_1^2 \boldsymbol{\rho}^{(1)} + \sigma_2^2 \boldsymbol{\rho}^{(2)} \leq \boldsymbol{p}^{\max}, \quad 1 \leq \underline{\mu}_k, \overline{\mu}_k \leq 2, \tag{7.2}$$

where $\boldsymbol{p}^{\min}$ and $\boldsymbol{p}^{\max}$ are specified bounds on pressure (inequalities are taken componentwise). The optimal control problem is defined by

$$\begin{aligned} \min \quad & J \triangleq \text{compressor energy in (7.1)}, \\ \text{s.t.} \quad & \text{dynamic constraints: (5.23)}, \\ & \text{temporal constraints: (5.24)}, \\ & \text{inequality constraints: (7.2)}. \end{aligned} \tag{7.3}$$

The decision variables are partial densities, mass fluxes, compressor ratios, and regulator ratios throughout the network.

The OCP in (7.3) may be generally expressed as

$$\min_{x(t),u(t)} \quad \int_0^T \mathcal{J}(x(t),u(t))dt \tag{7.4a}$$

$$\text{s.t.} \quad R\frac{d}{dt}[R^{(m)}x(t)] = f^{(m)}(x(t),u(t),d(t)), \tag{7.4b}$$

$$x(0) = x_0 \quad \text{or} \quad x(0) = x(T), \tag{7.4c}$$

$$\text{l.b.} \leq (x(t),u(t)) \leq \text{u.b.}, \tag{7.4d}$$

where $x = (\boldsymbol{\rho}^{(1)}, \boldsymbol{\rho}^{(2)}, \underline{\varphi})^T$ is the state, $u = (\{\underline{\mu}_k, \overline{\mu}_k\})^T$ is the control, and $d = (\boldsymbol{s}^{(1)}, \boldsymbol{s}^{(2)}, \boldsymbol{w})^T$ is a fixed (potentially time-varying) vector of parameters. In the above problem, $R = (\overline{Q}_d^T X L \overline{M}_d)$ and $R^{(m)}$ is a row selector matrix that maps x into $\boldsymbol{\rho}^{(m)}$. The symbols l.b. and u.b. represent vector bounds that constrain the components of the state and input vectors, where the inequalities are applied componentwise. The nonlinear program is obtained by discretizing the time interval $[0,T]$ into N subintervals (t_n, t_{n+1}), for $n = 0,\ldots,(N-1)$, where the sampling times are defined by $t_n = nT/N$, in the case of the steady-state initial condition. In the case of periodic temporal constraints, the interval $[0,T)$ is discretized into N subintervals with equally-spaced collocation points $t_n = nT/N$ for $n = 0,\ldots,(N-1)$.

The vector-valued functions $x(t)$, $u(t)$, and $d(t)$ are sampled to form finite sequences of discrete vector-values $x[n] = x(t_n)$, $u[n] = u(t_n)$, and $d[n] = d(t_n)$, for $n = 0,\ldots,N$. The integral in the objective function is approximated using the left-endpoint integration method, resulting in

$$\int_0^T \mathcal{J}(x(t),u(t))dt \approx \sum_{n=0}^{N-1} \frac{T}{N}\mathcal{F}(x[n],u[n]).$$

The time derivative of $x(t)$, for $t \in (t_n, t_{n+1})$, is approximated with Euler's method

$$\dot{x}(t) \approx \frac{x[n+1]-x[n]}{T/N}.$$

The nonlinear and linear programs are then defined by

$$\min_{x[n],u[n]} \quad \sum_{n=0}^{N-1} \frac{T}{N} \mathcal{J}(x[n], u[n]) \tag{7.5a}$$

$$\text{s.t.} \quad RR^{(m)}(x[n+1] - x[n]) = \frac{T}{N} f^{(m)}(x[n], u[n], d[n]), \tag{7.5b}$$

$$x[0] = x_0 \quad \text{or} \quad x[0] = x[N], \tag{7.5c}$$

$$\text{l.b.} \leq (x[n], u[n]) \leq \text{u.b.}, \tag{7.5d}$$

where (7.5b) is defined for $n = 0, \ldots, (N-1)$ and (7.5d) is defined for $n = 1, \ldots, N$.

Solution of the NLP in (7.5) is implemented in Matlab with the interior-point algorithm using the function `fmincon`, and is evaluated on a MacBook Air 8-core CPU with 8GB of unified memory. The gradient of the objective and Jacobian of the constraints are supplied to the function for improved performance. The Hessian of the Lagrangian function is set to the default finite-difference approximation. Optimal control of compression and regulation is obtained from the optimal solution $U = U^*$. The optimized time-series for compressors and regulators, and any specified parameters, are linearly interpolated to provide control functions to the ODEs (5.23) The system is simulated in Matlab using the function `ode15s` for validation of the solution and an improved prediction of pressure and mass flux. The steady-state solution is used as the starting point for optimization, and the initial state of the optimal solution is used as the initial condition for simulation. In the following, we distinguish between the solution of the optimization problem (7.5) and the solution of the ODEs (5.23) that are driven by optimal compression and regulation. We consider this comparison an important validation of the presented optimal control scheme, because feasibility of the coarsly discretized physical system in the optimal solution of the NLP (7.5) does not necessarily guarantee that the control solution obtained by solving (7.5) results in that same physical solution in a simulation with controlled error. For the case studies in the next section, the two solutions are compared using

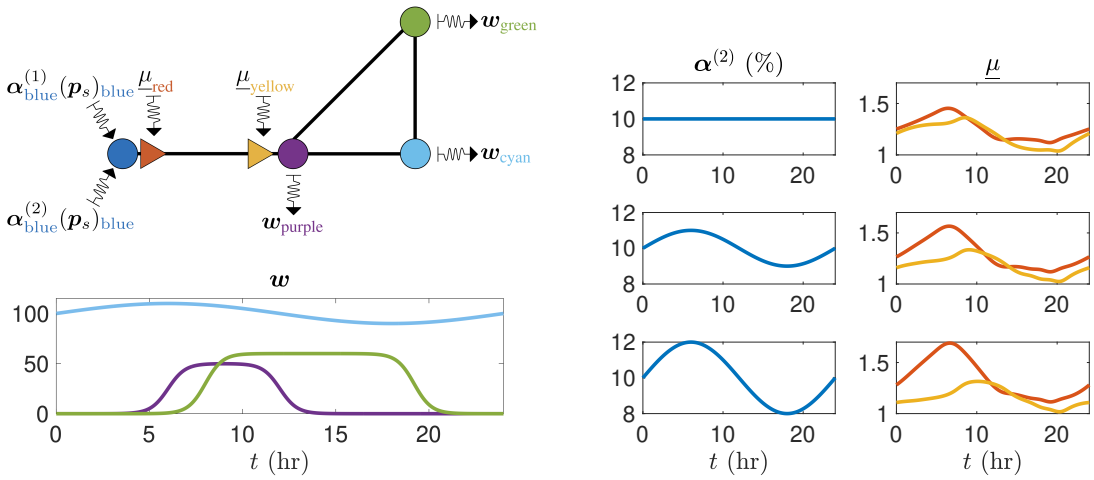

Figure 7.1: (Left) Top: Configuration of the network. Pipeline dimensions: blue to purple = 50 Km, purple to cyan = 30 Km, purple to green = 20 Km, and green to cyan Is 30 Km. Bottom: Withdrawal flow profiles, color-coded to correspond to associated nodes. The network has two compressors, indicated by triangles, located at the start and end of the pipe directed from blue to purple. **(Right)** Left column: Hydrogen concentration profiles at the supply node. Right column: Corresponding optimal compressor responses.

the average L^2 norm of the relative difference given by

$$\frac{1}{\hat{E}} \sum_{k \in \hat{\mathcal{E}}} \left(\frac{1}{T} \int_0^T \left(2 \frac{\underline{\varphi}_k(t) - \underline{\phi}_k(t)}{\underline{\varphi}_k(t) + \underline{\phi}_k(t)} \right)^2 dt \right)^{1/2} \times 100, \tag{7.6}$$

where $\underline{\varphi}_k$ is the optimized flux in edge $k \in \hat{\mathcal{E}}$, $\underline{\phi}_k$ is the simulated flux, and $\hat{E}$ is the number of refined edges in $\hat{\mathcal{E}}$. In addition, the maximum absolute relative difference is also documented as

$$\max_{k \in \hat{\mathcal{E}}} \left(\max_{t \in [0,T]} \left| 2 \frac{\underline{\varphi}_k(t) - \underline{\phi}_k(t)}{\underline{\varphi}_k(t) + \underline{\phi}_k(t)} \right| \right) \times 100. \tag{7.7}$$

Similar metrics are used for the difference between optimized and simulated pressure trajectories.

7.3 Example

The optimal control algorithm is demonstrated on a cyclic network whose configuration and dimensions are shown on the top left side of Figure 7.1. Optimization of gas flows in cyclic networks are typically more difficult to solve than non-cyclic networks (RIO (2006)). We create a refined network with a uniform discretization length of $\ell_k = 10$ km for all $k \in \hat{\mathcal{E}}$. The diameters and friction factors of the refined pipelines are uniform and equal to $D_k = 0.5$ m and $\lambda_k = 0.011$ for all $k \in \hat{\mathcal{E}}$. The speeds of sounds of the gases are $\sigma_1 = 338.38$ m/s and $\sigma_2 = 4\sigma_1$. We use $N = 20$ time steps with $\nu = 1.28$ and compressor efficiency values $c_1 = c_5 = D_k^4/T$ in (7.1). The minimum and maximum pressures in (7.2) are $\boldsymbol{p}_j^{\min} = 5$ MPa and $\boldsymbol{p}_j^{\max} = 12$ MPa for all $j \in \hat{\mathcal{V}}_w$. Discretization results in 780 optimization variables, 740 equality constraints, and 520 inequality constraints in the NLP (7.5).

The purple, green, and cyan nodes in the network graph on the left side of Figure 7.1 represent stations where gas is withdrawn with color-coordinated flow profiles depicted below. The red and yellow triangles represent two compressor stations whose time-dependent operations are optimized in a model-predictive manner. The blue node is the supply station for a mixture of natural gas and hydrogen with a fixed pressure of $(\boldsymbol{p}_s)_{\text{blue}} = 5$ MPa that is immediately boosted by the red compressor station. We demonstrate three solutions for this network, each of which are subject to the same above boundary conditions but differ in the injected concentration of hydrogen at the supply node. The left column on the right side of Figure 7.1 depicts the specified hydrogen concentration profiles at the supply node for the three solutions and the right column shows the associated results for optimal compression ratios of the two color-coordinated compressor stations. The total compressor energy values in as defined in equation (7.1) are $J = 0.787$, $J = 0.824$, and $J = 0.860$ (non-

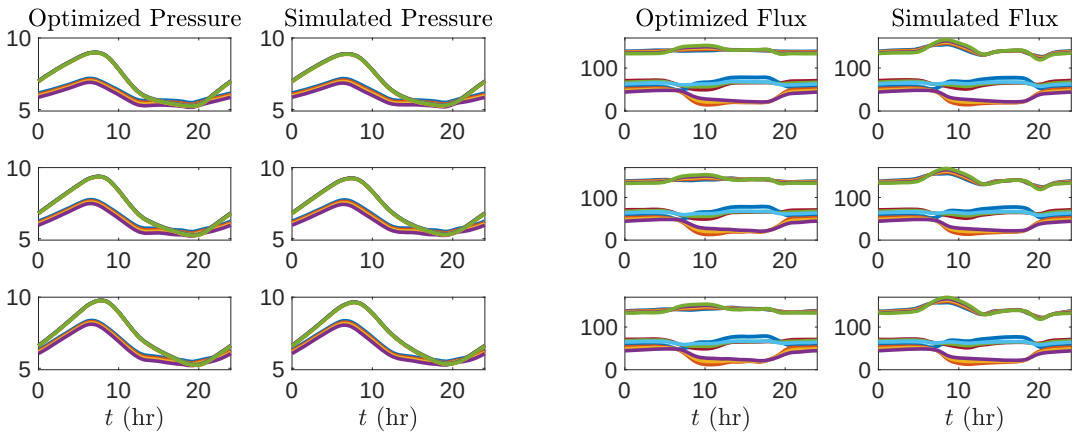

Figure 7.2: (Left) Left column: Optimized pressure at refined withdrawal nodes driven by the respective concentration profiles from Figure 7.1. Right column: Simulated pressure at refined withdrawal nodes driven by inlet concentration and optimal compression profiles from Figure 7.1. The average L^2 norm of the relative difference in pressures, using the metric (7.6), are approximately 0.769%, 0.770%, and 0.769% for the top, middle, and bottom Rows. The maximum relative difference in pressures, using the metric (7.7), are approximately 2.154%, 2.038%, and 1.971% for the top, middle, and bottom rows. The combined computational times for optimization and simulation are approximately 10.0 S, 8.0 S, and 7.7 S for the top, middle, and bottom rows, respectively. **(Right)** Left column: Optimized mass flux in refined edges driven by the respective concentration profiles from Figure 7.1. Right column: Simulated mass flux in refined edges driven by inlet concentration and optimal compression profiles from Figure 7.1. The L^2 relative difference metric values using (7.6) are approximately 3.994%, 4.608%, and 5.258% for the top, middle, and bottom rows. The maximum relative difference values using metric (7.7) are approximately 12.967%, 16.713%, and 21.509%, respectively.

dimensionalized units) corresponding to the optimal compression ratios given on the right side of Figure 7.1 from top to bottom, respectively. The left and right sides of Figure 7.2 depict pressure and mass flux solutions, respectively, where the left columns show the optimized solutions and the right columns show the validating simulation. The results demonstrate that minor variations in hydrogen concentration may have substantial effects on pressure and compressor activity. In particular, the pressure trajectories in Figure 7.2 increase by approximately 2 MPa from $t = 0$ to $t = 8$ hours for a fixed 10% hydrogen injection, while the change is approximately 3.5 MPa when

the hydrogen injection concentration slowly varies from 8% to 12% over the 24 hour time horizon. Observe that because this concentration is defined as the mass fraction, the volume fraction here is actually over 30%, and exhibits variations of up to 10%. A detailed analysis of how hydrogen blending impacts energy transport capacity of gas pipeline networks is outside the scope of this study, in which we focus on modeling flow dynamics and demonstrating our optimal control approach.

We now describe an open question. The monotone-ordering properties of equivalent systems from the previous chapter suggest that certain equivalent systems may have better behavior in the sense of monotone-ordering than others in certain operating regions. The question we ask is whether certain equivalent systems are better suited for optimization purposes of gas mixtures than others? We expect the answer to be affirmative, as this is true even for pure natural gas networks as well. In particular, pressure and velocity values have different orders of magnitude, so the variables are usually transformed into nondimensional variables (Zlotnik *et al.* (2015b)). This is an equivalent transformation.

Chapter 8

LINEAR CONTROL SYSTEM

This chapter combines some of the features from Chapters 3 and 7. Our central objective is to develop a linear time-invariant control system, primarily to improve the performance of optimizing gas flows in networks. The linear system is derived in a way that can be utilized for the design of feedback controllers and the investigation of asymptotic stability and transient responses. We touch upon each of these applications. This chapter considers only natural gas flows in networks, but we believe that the formulation can be extended to mixtures of gases. In Section 8.1, the isolated total density system of ODEs for a homogeneous mixture is reduced to an ODE system that models pure natural gas with zero hydrogen concentration. The linear system and linear program are derived in Section 8.2. In Section 8.3, the eigenvalues of the state matrix of the finite-dimensional linear control system are compared to the poles of the previously-studied irrational transfer matrix from Chapter 3 to gain insight into the transient behavior of the system. Section 8.4 demonstrates the performance of the nonlinear and linear programs for the test network that we used previously in Chapter 6. The error between the solutions of the two programs is analyzed computationally and analytically in Section 8.5. The analytical error bound is derived using a Lyapunov function associated with the asymptotically stable state matrix.

8.1 System Reduction to Natural Gas

In this chapter we change our notation slightly. Underlines and overlines are no longer used for the evaluations of flow variables at the inlets and outlets of pipelines. Instead, inlet and outlet edge variables are defined by attaching superscripts "0" and

"ℓ," respectively, to the associated edge variables. For example, $\varphi_k^0(t) = \varphi_k(t,0)$ and $\varphi_k^\ell(t) = \varphi_k(t,\ell_k)$. Correspondingly, the previous notation for the matrix $\overline{Q}_d$ is replaced with Q_d^ℓ. From here onward, overlines are used exclusively to denote the steady-state solution of (5.23). We also assume that the network does not contain any regulators. Compressor variables are now denoted by $\mu_k(t)$ for $k \in \mathcal{C}$, where $\mathcal{C} \subset \mathcal{E}$ is the set of edges that "contain" a compressor (at the inlet of the edge).

If the network contains only natural gas, then the input and state variables $\boldsymbol{\alpha}^{(2)}$, $\boldsymbol{\beta}^{(2)}$, $\boldsymbol{\eta}^{(2)}$, and $\boldsymbol{\rho}^{(2)}$ in (5.23) are equal to zero vectors. In this case, the system in (5.23) (or similarly in (5.31)) reduces to

$$(I^T X L I)\dot{\boldsymbol{\rho}}^{(1)} = \left(Q^T X \varphi - \boldsymbol{w}\right), \tag{8.1}$$

$$0 = -\sigma^2 L^{-1}\left(M\boldsymbol{\rho}^{(1)} + N\boldsymbol{s}^{(1)}\right) - K\frac{\varphi \odot |\varphi|}{I\boldsymbol{\rho}^{(1)}}, \tag{8.2}$$

where we use the notation $I = Q_d^\ell$, $M = M_d$, and $N = M_s$. The matrix K is diagonal with entries $K_{kk} = \lambda_k/(2D_k)$ for $k \in \mathcal{E}$. The above system consists of only one state equation corresponding to the one nonzero density state vector $\boldsymbol{\rho}^{(1)}$ and the one nonzero input vector $\boldsymbol{s}^{(1)}$. For simplicity, we denote these variables by $\boldsymbol{\rho}$ and $\boldsymbol{s}$. Lastly, to simplify the analysis, we include inertia in the momentum equation. Therefore, the system in (8.1)-(8.2) becomes (Himpe *et al.* (2021))

$$\dot{\boldsymbol{\rho}} = (I^T X L I)^{-1}\left(Q^T X \varphi - \boldsymbol{w}\right), \tag{8.3}$$

$$\dot{\varphi} = -\sigma^2 L^{-1}\left(M\boldsymbol{\rho} + N\boldsymbol{s}\right) - K\frac{\varphi \odot |\varphi|}{I\boldsymbol{\rho}}. \tag{8.4}$$

As previously discussed, the mass matrix $(I^T X L I)$ is diagonal with positive diagonal components given by $(I^T X L I)_{jj} = \sum_{k \in \mapsto j} \chi_k \ell_k$ for $j \in \mathcal{V}_w$. Therefore, the matrix $(I^T X L I)$ may be easily inverted to obtain the traditional control system presented above. The state variables are densities $\boldsymbol{\rho}$ at withdrawal nodes and fluxes φ at the inlets of the edges. The compressor actuators are contained in the matrices M and

N. The other matrices are known and constant. The steady-state initial condition in (5.24) is the solution of

$$Q^T X \overline{\varphi} = \overline{\boldsymbol{w}}, \qquad \sigma^2 \left(\overline{M} \overline{\boldsymbol{\rho}} + \overline{N} \overline{\boldsymbol{s}} \right) = -LK \frac{\overline{\varphi} \odot |\overline{\varphi}|}{I \overline{\boldsymbol{\rho}}}, \tag{8.5}$$

where $\overline{\boldsymbol{s}} = \boldsymbol{s}(0)$ and $\overline{\boldsymbol{w}} = \boldsymbol{w}(0)$. Overlines attached to state variables, actuation matrices, and parameters are used to denote a time-invariant steady-state solution. We assume that $\overline{M}$, $\overline{N}$, $\overline{\varphi}$, and $\overline{\boldsymbol{\rho}}$ are optimally determined to minimize compressor energy, as in (7.1), while satisfying flow requirements in (8.5) and inequality constraints, as in (7.2). The initial condition of the system in (8.3)-(8.4) is defined to be

$$\boldsymbol{\rho}(0) = \overline{\boldsymbol{\rho}}, \qquad \varphi(0) = \overline{\varphi}. \tag{8.6}$$

8.2 Linear System and Linear OCP

In this section, we use classical linearization techniques to derive a linear system that models the flow of gas in the network. Flow variables, compressor actuators, and time-varying supply and withdrawal profiles in (8.3)-(8.4) are first written in terms of variations around their steady-state counterparts. The system of variations is given by

$$\dot{\boldsymbol{\rho}} = (I^T X L I)^{-1} \left(Q^T X \varphi - \boldsymbol{w} \right), \tag{8.7}$$

$$\begin{aligned} \dot{\varphi} = & -\sigma^2 L^{-1} \left(M \boldsymbol{\rho} + \overline{M} \boldsymbol{\rho} + M \overline{\boldsymbol{\rho}} + N \boldsymbol{s} + \overline{N} \boldsymbol{s} + N \overline{\boldsymbol{s}} \right) \\ & + K \left(\frac{\overline{\varphi} \odot |\overline{\varphi}|}{I \overline{\boldsymbol{\rho}}} - \frac{(\overline{\varphi} + \varphi) \odot |\overline{\varphi} + \varphi|}{I \left(\overline{\boldsymbol{\rho}} + \boldsymbol{\rho} \right)} \right). \end{aligned} \tag{8.8}$$

The variation variables are expressed with the same symbols as their original counterparts. The system of variations in (8.7)-(8.8) is equivalent to the original system in (8.3)-(8.4), where the equivalence relation is represented as a translation of the equilibrium from the origin to the steady-state solution. A similar translation was performed in the continuous case for a single pipeline back in Chapter 3.

We first rewrite the control input products $M\overline{\boldsymbol{\rho}}$ and $N\overline{\boldsymbol{s}}$ in (8.8) into the standard form of a linear system. For $k \in i_{\mapsto} \cap \mathcal{C}$ with $i \in \mathcal{V}_s$, the only nonzero entries of N are $N_{ki} = -\mu_k$, where μ_k is the variation around the steady-state compressor $\overline{\mu}_k$. Likewise, for $k \in i_{\mapsto}$ with $i \in \mathcal{V}_w$, only the (k, i) entries of M are nonzero. Define the C-dimensional vector $\mu = (\{\mu_k\}_{k\in\mathcal{C}})$, where C is the cardinality of $\mathcal{C}$. Define the matrix $\overline{P}$ componentwise by

$$\overline{P}_{ki} = \begin{cases} \overline{\boldsymbol{s}}_i, & \text{if edge } k \in i_{\mapsto} \text{ leaves node } i \in \mathcal{V}_s, \\ \overline{\boldsymbol{\rho}}_i, & \text{if edge } k \in i_{\mapsto} \text{ leaves node } i \in \mathcal{V}_w, \\ 0, & \text{otherwise,} \end{cases}$$

and the $E \times C$ submatrix $\overline{B}$ of $\overline{P}$ by the removal of every column i of $\overline{P}$ for which $k \in i_{\mapsto}$ with $k \notin \mathcal{C}$. Then we have $-(M\overline{\boldsymbol{\rho}} + N\overline{\boldsymbol{s}}) = \overline{B}\mu$. Define the $E \times E$ diagonal matrices $\overline{\alpha}$ and $\overline{\beta}$ that result in linearizing the nonlinear frictional term in (8.8) by

$$\overline{\alpha} = K\mathrm{diag}\left(\frac{\overline{\varphi} \odot |\overline{\varphi}|}{I\overline{\boldsymbol{\rho}}^2}\right), \qquad \overline{\beta} = -2K\mathrm{diag}\left(\frac{|\overline{\varphi}|}{I\overline{\boldsymbol{\rho}}}\right). \tag{8.9}$$

These matrices are interpreted as the extensions of the scalars in (3.12) from the pipeline to the network. The difference is that this linearization does not perform the constant-coefficient approximation that was needed in Chapter 3 to derive an analytical solution of the PDEs. Instead, the diagonal components of the matrices $\overline{\alpha}$ and $\overline{\beta}$ are the samples of the spatially-dependent coefficients at the discretized nodes and edges of the refined network. Linearizing (8.7)-(8.8) in $\boldsymbol{\rho}$, φ, μ, $\boldsymbol{s}$, and $\boldsymbol{w}$ around the origin gives the linear time-invariant system

$$\begin{bmatrix} \dot{\boldsymbol{\rho}} \\ \varphi \end{bmatrix} = A \begin{bmatrix} \boldsymbol{\rho} \\ \varphi \end{bmatrix} + B\mu + W \begin{bmatrix} \boldsymbol{s} \\ \boldsymbol{w} \end{bmatrix}, \tag{8.10}$$

where the state, input, and disturbance matrices are given in block matrix form by

$$A = \begin{bmatrix} 0 & (I^T XLI)^{-1} Q^T X \\ \overline{\alpha} I - \sigma^2 L^{-1} \overline{M} & \overline{\beta} \end{bmatrix}$$

and

$$B = \sigma^2 L^{-1} \overline{B}, \quad W = \begin{bmatrix} 0 & -(I^T XLI)^{-1} \\ -\sigma^2 L^{-1} \overline{N} & 0 \end{bmatrix}.$$

The entries with zeros denote zero matrices of appropriate dimensions. The initial condition of (8.10) is given by

$$\boldsymbol{\rho}(0) = 0, \qquad \varphi(0) = 0. \tag{8.11}$$

The initial-value system in (8.10)-(8.11) describes the gas dynamics for all variations around the steady-state that are confined to a region in which linearization is applicable. In subsequent sections, we will analyze this applicable linearization region. Linearizing (7.1) around the steady-state gives the linear objective

$$J_{\text{lin}} = \sum_{k \in \mathcal{C}} c_k \int_0^T \varphi_k(t) \left((\overline{\mu}_k(t))^{(\nu-1)/\nu} - 1 \right) + \frac{\nu - 1}{\nu} |\overline{\varphi}_k| \overline{\mu}_k^{\nu} \mu_k(t) dt. \tag{8.12}$$

The inequality constraints in (7.2) are linear in the state and input. Translating these inequalities from the steady-state to the origin results in

$$\boldsymbol{p}_j^{\min} \leq \sigma^2 \left(\boldsymbol{\rho}_j + \overline{\boldsymbol{\rho}}_j \right) \leq \boldsymbol{p}_j^{\max}, \quad 1 \leq \mu_k + \overline{\mu}_k \leq 2. \tag{8.13}$$

The linear reduced optimal control model is given by

$$\begin{aligned} \min \quad & J_{\text{lin}} \triangleq \text{compressor energy in (8.12)}, \\ \text{s.t.} \quad & \text{dynamic constraints: (8.10)}, \\ & \text{temporal constraints: (8.11)}, \\ & \text{inequality constraints: (8.13)}. \end{aligned} \tag{8.14}$$

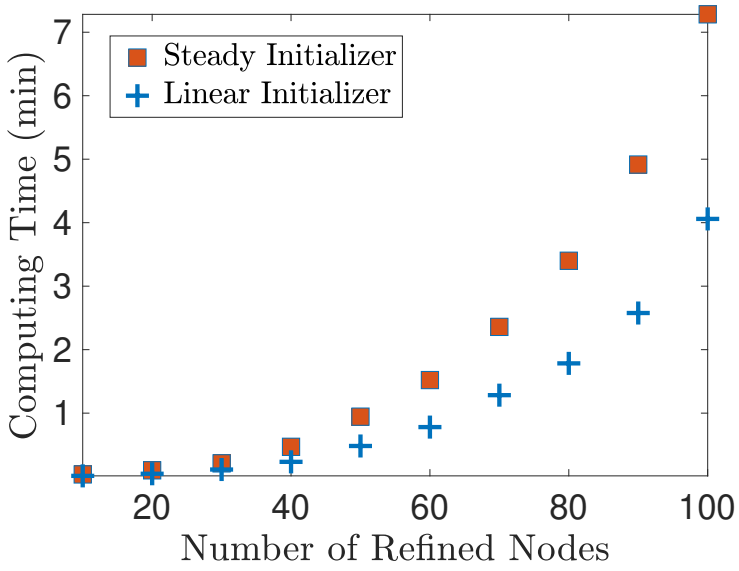

Figure 8.1: Computational time of the NLP as a function of the number of refined nodes of a single pipeline. The parameters are $\ell = 100$ (km), $D = 1$ (m), $\lambda = 0.01$, and $\sigma = 377$ (m/s).

This OCP is discretized in time at the same sampling times in exactly the same way we have done in Section 7.2. The nonlinear and linear optimization programs can both be initialized with the steady-state solution (translated to the origin) defined by $x[0] = 0$ and $u[0] = 0$. However, the performance of the nonlinear program is improved by first solving the linear program using the steady-state initializer and then using the optimal solution of the linear program as the initializer for the nonlinear program. Figure 8.1 depicts the optimization time of the nonlinear program as a function of the number of refined nodes of a pipeline. The computational time of the nonlinear program using the linearized solution as the initial point of optimization shows a reduction of about 50% for the pipeline that we consider here. It will be determined in future work whether this improvement holds in more general situations.

Although the linear program may be used to reduce the computational time of the nonlinear program, the computational time may still be too large for operators to timely determine intra-day adjustments. Instead of performing real-time calculations

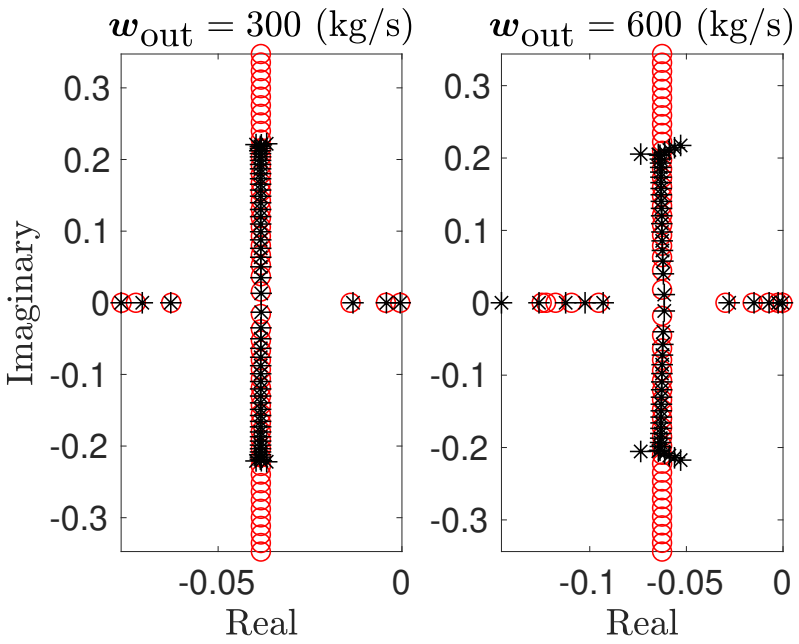

Figure 8.2: Eigenvalues ($*$) of A and poles ($\circ$) of $G(s)$ for a single pipeline with 30 refined edges. The pipeline parameters are $\ell = 100$ (km), $D = 0.75$ (m), $\lambda = 0.01$, and $\sigma = 377$ (m/s).

of compressor actions, numerous linear and nonlinear optimization routines may be performed offline in advance and the results may be stored for subsequent calculations. In particular, a bank of optimal controller actions may be stored depending on the particular withdrawal contract and used thereafter for the current operation planning.

8.3 Transient Response

Although the gas network is physically stable because of frictional effects that strongly dissipate kinetic energy, a quantitative analysis of the eigenvalues of the state matrix A is beneficial for the design of controllers and the analysis of transient and frequency responses. However, a closed-form representation of the eigenvalues may not exist for even the simplest of networks, such as a refined pipeline. We first provide a result that characterizes the "center of gravity" of the eigenvalues of A.

Proposition 4. Let $\{\zeta_m\}_{m=1}^{E+V_w}$ be the set of eigenvalues of A in (8.10), where E and V_w are the cardinalities of $\mathcal{E}$ and $\mathcal{V}_w$. Then

$$\sum_{m=1}^{E+V_w} \zeta_m = -\sum_{k=1}^{E} \frac{\lambda_k \overline{\varphi}_k}{D_k (I\overline{\boldsymbol{\rho}})_k}. \tag{8.15}$$

Proof. The trace formula for the sum of the eigenvalues of the matrix A gives

$$\sum_{m=1}^{E+V_w} \zeta_m = \sum_{k=1}^{E} \overline{\beta}_{kk}.$$

The result follows from (8.9). □

The center of gravity of the eigenvalues of A is the average value given by $c = \sum_{m=1}^{E+V_w} \zeta_m/(E+V_w)$. Proposition 1 shows that the center of gravity depends on $\overline{\beta}$, but not on $\overline{\alpha}$.

The left and right sides of Figure 8.2 depict the eigenvalues of A for a single pipeline with two different mass outflow boundary conditions. The figure also depicts a subset of poles of the irrational transfer matrix in (3.29), which we denote by $G(s)$. Although the eigenvalues of A and poles of $G(s)$ are, in general, not equal, the poles have a simple closed formula that can be used with caution to gain insight into the structure of the eigenvalues of A. The poles of $G(s)$ are given by

$$\zeta_m^{\pm} = \frac{\beta}{2} \pm \mathbf{j} \sqrt{\left(\frac{\pi\sigma}{2\ell}\right)^2 (2m+1)^2 - \left(\frac{\beta}{2}\right)^2} \tag{8.16}$$

for $m = 0, 1, \ldots$, where β is a scalar approximation of the diagonal elements of $\overline{\beta}$. The poles of $G(s)$ in Figure 8.2 are constructed using the average value $\beta = \sum_{k=1}^{E} \overline{\beta}_{kk}/E$ in (8.16). From Proposition 1, it can be shown that this average value of the diagonal elements of $\overline{\beta}$ results in $\beta = [(E+V_w)/E]c$. In the case of a single pipeline with one supply node, this result simplifies to $\beta = 2c$ (since $E = V_w$). Thus, the imaginary asymptote of the poles of $G(s)$ intersects the real axis at the center of gravity of the eigenvalues of A for this average choice of β. This is demonstrated in Figure 8.2, where the poles and eigenvalues gravitate toward the imaginary asymptote $c = \beta/2$.

All of the poles of $G(s)$ have negative real parts, irrespective of the pipeline parameters, because the diagonal elements of $\overline{\beta}$ are always negative. This observation agrees with the physical stability of the system. However, the time response may vary significantly for different parameter values. The settling time t_s is defined to be the time elapsed from the application of an ideal instantaneous step input to the time at which the system has entered and will remain within a specified percent error of the final state. The settling time of a transient input depends largely on the real parts of one or more of the eigenvalues of A. For our purpose, we approximate the settling time by $t_s = 1/\min|\mathrm{Re}(\lambda_m)|$. We investigate how the settling time changes as the parameters of the pipeline vary for two cases.

1. **Varying** ℓ. First, assume that $\ell < \pi\sigma/|\beta|$. In this case, all of the poles of $G(s)$ lie on the asymptote $c = \beta/2$ and the settling time is approximated with $t_s = 1/|c|$. Second, assume that $\ell > \pi\sigma/|\beta|$. In this case, there are at least two purely real poles, the largest of all of which is given by $\zeta_1^+ = [\beta/2 + \sqrt{(\beta/2)^2 - (\pi\sigma/2\ell)^2}]$. As ℓ increases without bound, the number of purely real poles of $G(s)$ increases without bound and ζ_1^+ increases toward the origin of the complex plane. This indicates that the settling time $t_s = 1/|\zeta_1^+|$ increases as ℓ increases, and that the system will never settle everywhere in the theoretical case of an infinitely long pipeline.

2. **Varying** $\overline{\varphi}$. For a single pipeline, the values $\overline{\varphi}_k$ for $k \in \mathcal{E}$ in (8.15) are all the same value, which we denote by $\overline{\varphi}$. The poles of $G(s)$ are given by

$$\zeta_m^{\pm} = -\frac{\lambda|\overline{\varphi}|}{2DE}\sum_{k=1}^{E}\frac{1}{(I\overline{\boldsymbol{\rho}})_k} \pm \mathbf{j}\sqrt{\left(\frac{\pi\sigma}{2\ell}\right)^2(2m+1)^2 - \left(\frac{\lambda|\overline{\varphi}|}{2DE}\sum_{k=1}^{E}\frac{1}{(I\overline{\boldsymbol{\rho}})_k}\right)^2}.$$

   As $|\overline{\varphi}| \to 0$, it is clear that all of the poles, hence the center of gravity, approach the imaginary axis of the complex plane. Thus, as $|\overline{\varphi}| \to 0$, the friction term in

the state equations goes to zero and the variations are undamped waves, leading to an infinite settling time. As $|\overline{\varphi}|$ theoretically increases without bound, the center of gravity c decreases without bound along the real axis of the complex plane. The decrease of the center of gravity as $|\boldsymbol{w}|$, hence $|\overline{\varphi}|$, increases is illustrated in Figure 8.2.

Figure 8.2 suggests that some of the eigenvalues and transient characteristics of the state matrix may be approximated using a subset of poles of the irrational transfer matrix. This approximation appears to be more applicable for single pipelines that have steady-state mass flow magnitudes of less than 300 (kg/s). We are currently looking into how the eigenvalues of the state matrix are affected by the topology of the network and whether a subset of poles of several transfer functions associated with several individual pipelines may be used to approximate the eigenvalues of the state matrix associated with a connected network structure. As an example, the eigenvalues of the state matrix associated with the network in Figure 8.3 appear to have multiple imaginary asymptotes. We are looking into whether the locations of these asymptotes and the number of eigenvalues gravitating along the asymptotes are related to average values of the parts of $\overline{\beta}$ associated with each of the five edges of the network.

8.4 Network Example

The solutions of the nonlinear and linear optimal control problems are examined for the test network that was used previously in Chapter 6 for the monotonicity experiments. We display the network again, along with the boundary conditions we now impose, here on the left side of Figure 8.3. The dark blue node is the only supply node, with pressure specified to be 5 (MPa). The five edges of the network are discretized into 48 refined edges, so that $\ell_k = 5$ (km) for all $k \in \hat{\mathcal{E}}$. The size of the

state matrix A is 95×95 and the size of the input matrix B is 95×3. The time interval $[0, T]$ is discretized into 24 subintervals using 25 evenly-spaced time samples. This results in 2,450 optimization variables for both the nonlinear and linearized programs.

The optimal solutions of the nonlinear and linearized programs are shown on the right side of Figure 8.3, where the solutions are translated back to non-variation variables by adding their associated steady-state components. Figure 8.3 shows that the linear program performs reasonably well at deciding the optimal solution for these boundary conditions. The percent relative error between the nonlinear and linearized solutions are 1.54% in pressure, 0.57% in mass flux, and 2.3% in compression, where the percent relative error of pressure between the nonlinear solution $\boldsymbol{p}_{\text{non}}$ and the linearized solution $\boldsymbol{p}_{\text{lin}}$ is defined by the expression

$$\max_{j \in \mathcal{V}_w, t \in [0,T]} \left(\frac{|(\boldsymbol{p}_{\text{non}})_j(t) - (\boldsymbol{p}_{\text{lin}})_j(t)|}{\overline{\boldsymbol{p}}_j} \right) \times 100. \tag{8.17}$$

The percent relative error in mass flux and compression are defined similarly.

8.5 Linearization Error Analysis

If $\boldsymbol{w}$, $\boldsymbol{s}$, and μ are time-invariant, then the initial-value systems in (8.7)-(8.8) and (8.10) are undisturbed and unforced, in the sense that the solutions of these systems remain at the origin for all time. Assuming that the eigenvalues of A have negative real parts, the origin of the linear and nonlinear systems is an asymptotically and a locally asymptotically stable equilibrium point, respectively. In this section, we assume that $\boldsymbol{s} = 0$ and $\mu = 0$, which is common for gas pipelines in practice.

Proposition 5. Suppose that the real parts of the eigenvalues of A are negative, that $\mu = 0$, $\boldsymbol{s} = 0$, and $\overline{\varphi}_k > 0$ for all $k \in \mathcal{E}$. If the solution of (8.7)-(8.8) satisfies $|\boldsymbol{\rho}_j| \leq \kappa \overline{\boldsymbol{\rho}}_j$ for all $j \in \mathcal{V}_w$ and $|\varphi_k| \leq \kappa \overline{\varphi}_k$ for all $k \in \mathcal{E}$ with $\kappa \in (0, \kappa_{\max})$ and $\kappa_{\max} < 1$

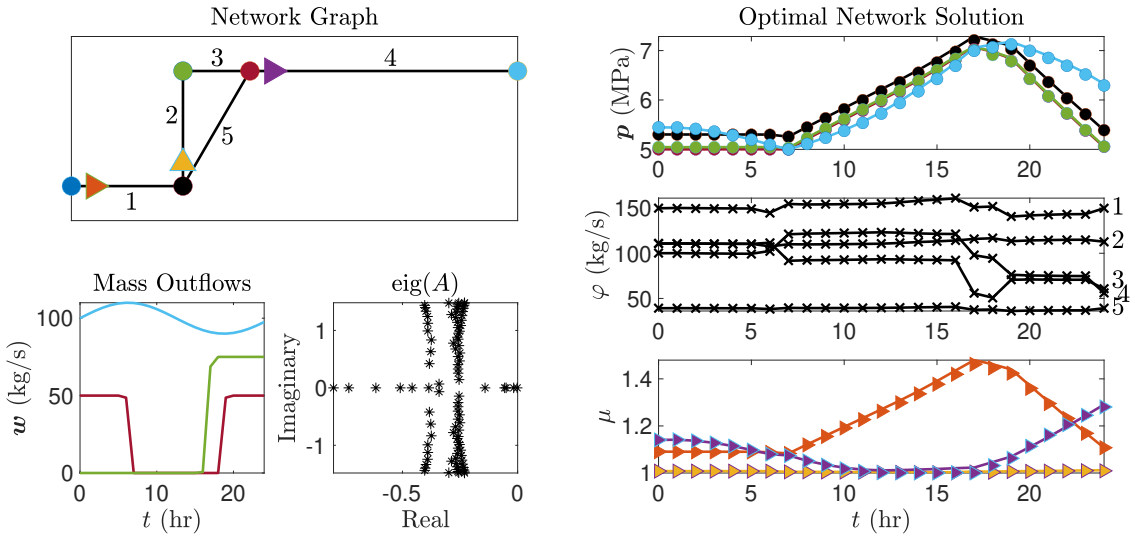

Figure 8.3: (Left) Top: Network configuration. Bottom left: Mass outflow profiles at the color-coordinated nodes. Bottom right: Eigenvalues of the state matrix A associated with the network. **(Right)** Optimal nodal pressures, mass flows at the inlets of the edges, and the compressor actions. Pressure and compressor actions are color-coordinated with the nodes and compressor stations of the network to the left. Solid lines represent the nonlinear solution and marker symbols represent the linearized solution.

sufficiently small, then there exists positive constants a, b, and r such that

$$\|\boldsymbol{e}\| \leq r\left(\frac{\kappa^3}{(1-\kappa)^2}a + \kappa^2 b\right), \tag{8.18}$$

where $\boldsymbol{e} = [(\boldsymbol{\rho}, \varphi) - (\boldsymbol{\rho}_{\text{lin}}, \varphi_{\text{lin}})]$ and $\|\boldsymbol{e}\|$ is the Euclidean norm of the vector $\boldsymbol{e}$. Here $(\boldsymbol{\rho}, \varphi)$ is the solution of (8.7)-(8.8) and $(\boldsymbol{\rho}_{\text{lin}}, \varphi_{\text{lin}})$ is the solution of (8.10).

Proof. The proof is based on standard Lyapunov arguments and we provide a brief outline here (see, e.g. Khalil (2002) for more examples). Assume that $(\boldsymbol{\rho}, \varphi)$ satisfies (8.7)-(8.8) and that $(\boldsymbol{\rho}_{\text{lin}}, \varphi_{\text{lin}})$ satisfies (8.10) under the conditions stated in Proposition 5. Define the error vector $\boldsymbol{e} = [(\boldsymbol{\rho}, \varphi) - (\boldsymbol{\rho}_{\text{lin}}, \varphi_{\text{lin}})]$.

Since $\mu = 0$, it follows that $M = 0$ and $N = 0$. The function $f(\boldsymbol{\rho}, \varphi, \boldsymbol{w})$ on the right-hand side of (8.7)-(8.8) may be uniquely written as $f(\boldsymbol{\rho}, \varphi, \boldsymbol{w}) = F(\boldsymbol{\rho}, \varphi) + \tilde{W}\boldsymbol{w}$,

where $\tilde{W}$ is defined to be the second block column of W as

$$\tilde{W} = \begin{bmatrix} -(I^T X L I)^{-1} \\ 0 \end{bmatrix}.$$

The error satisfies

$$\begin{aligned} \dot{\boldsymbol{e}} &= \left(\begin{bmatrix} \dot{\boldsymbol{\rho}} \\ \dot{\varphi} \end{bmatrix} - \begin{bmatrix} \dot{\boldsymbol{\rho}}_{\text{lin}} \\ \dot{\varphi}_{\text{lin}} \end{bmatrix} \right) \\ &= F(\boldsymbol{\rho}, \varphi) + \tilde{W}\boldsymbol{w} - A \begin{bmatrix} \boldsymbol{\rho}_{\text{lin}} \\ \varphi_{\text{lin}} \end{bmatrix} - \tilde{W}\boldsymbol{w} \\ &= A\boldsymbol{e} + F(\boldsymbol{\rho}, \varphi) - A \begin{bmatrix} \boldsymbol{\rho} \\ \varphi \end{bmatrix} \\ &= A\boldsymbol{e} + (\partial F(\boldsymbol{\rho}^*, \varphi^*) - A) \begin{bmatrix} \boldsymbol{\rho} \\ \varphi \end{bmatrix}, \end{aligned} \tag{8.19}$$

where we have used the mean-value theorem to replace F by

$$F(\boldsymbol{\rho}, \varphi) = F(0,0) + \partial F(\boldsymbol{\rho}^*, \varphi^*) \begin{bmatrix} \boldsymbol{\rho} \\ \varphi \end{bmatrix},$$

for some point $(\boldsymbol{\rho}^*, \varphi^*)$ on the line segment connecting $(\boldsymbol{\rho}, \varphi)$ to the origin. In the above equation, $F(0,0) = 0$ and the symbol $\partial F(\boldsymbol{\rho}^*, \varphi^*)$ represents the Jacobian matrix of the vector-valued function F evaluated at the point $(\boldsymbol{\rho}^*, \varphi^*)$. Therefore, the dynamics of $\boldsymbol{e}$ are represented as a perturbed linear system with a nonvanishing perturbation term.

The difference between the Jacobians in (8.19) is given by

$$\partial F(\boldsymbol{\rho}^*, \varphi^*) - A = \begin{bmatrix} 0 & 0 \\ (\alpha^* - \overline{\alpha})I & \beta^* - \overline{\beta} \end{bmatrix}$$

where $\overline{\alpha}$ and $\overline{\beta}$ are defined in (8.9) and

$$\alpha^* = K\mathrm{diag}\left(\frac{(\varphi^*+\overline{\varphi})\odot|\varphi^*+\overline{\varphi}|}{I\left(\boldsymbol{\rho}^*+\overline{\boldsymbol{\rho}}\right)^2}\right), \tag{8.20}$$

$$\beta^* = -2K\mathrm{diag}\left(\frac{|\varphi^*+\overline{\varphi}|}{I\left(\boldsymbol{\rho}^*+\overline{\boldsymbol{\rho}}\right)}\right). \tag{8.21}$$

The matrices K, α, α^*, β, and β^* are all diagonal. The k-th diagonal entries of the matrices $(\alpha^*-\overline{\alpha})$ and $(\beta^*-\overline{\beta})$ with $k: i \mapsto j$ are given by

$$\begin{aligned}(\alpha^*_{kk}-\overline{\alpha}_{kk}) &= K_{kk}\left(\frac{(\varphi^*_k+\overline{\varphi}_k)|\varphi^*_k+\overline{\varphi}_k|}{\left(\boldsymbol{\rho}^*_j+\overline{\boldsymbol{\rho}}_j\right)^2}-\frac{\overline{\varphi}_k|\overline{\varphi}_k|}{\overline{\boldsymbol{\rho}}_j^2}\right),\\ (\beta^*_{kk}-\overline{\beta}_{kk}) &= K_{kk}\left(-\frac{2|\varphi^*_k+\overline{\varphi}_k|}{\boldsymbol{\rho}^*_j+\overline{\boldsymbol{\rho}}_j}+\frac{2|\overline{\varphi}_k|}{\overline{\boldsymbol{\rho}}_j}\right).\end{aligned}$$

Since $|\boldsymbol{\rho}_j| \le \kappa\overline{\boldsymbol{\rho}}_j$ and $|\varphi_k| \le \kappa\overline{\varphi}_k$, it can be shown with elementary inequalities that

$$\|\alpha^*-\overline{\alpha}\| \le \frac{2\kappa^2}{(1-\kappa)^2}\|\overline{\alpha}\|, \qquad \|\beta^*-\overline{\beta}\| \le 2\kappa\|\overline{\beta}\|,$$

where the norm of a matrix is defined to be the induced Euclidean norm. It then follows from the inequality $\|(\boldsymbol{\rho},\varphi)\| \le \kappa(\|\overline{\boldsymbol{\rho}}\|+\|\overline{\varphi}\|)$ that

$$\begin{aligned}&\|(\partial F(\boldsymbol{\rho}^*,\varphi^*)-A)(\boldsymbol{\rho},\varphi)^T\|\\ &\quad\le \kappa\left(\|\alpha^*-\overline{\alpha}\|\|I\|+\|\beta^*-\overline{\beta}\|\right)(\|\overline{\boldsymbol{\rho}}\|+\|\overline{\varphi}\|)\\ &\quad\le \frac{\kappa^3}{(1-\kappa)^2}a+\kappa^2 b,\end{aligned}$$

where $a = 2\|\overline{\alpha}\|\|I\|(\|\overline{\boldsymbol{\rho}}\|+\|\overline{\varphi}\|)$ and $b = 2\|\overline{\beta}\|(\|\overline{\boldsymbol{\rho}}\|+\|\overline{\varphi}\|)$.

Since the eigenvalues of A have negative real parts, we may define the Lyapunov function $V(\boldsymbol{e}) = \boldsymbol{e}^T R\boldsymbol{e}$, where R is a positive definite and symmetric matrix that satisfies the Lyapunov equation $(A^TR+RA) = -I$. The time derivative of $V(\boldsymbol{e})$ along the trajectories of (8.19) is bounded by $\dot{V}(\boldsymbol{e}) \le (-\|\boldsymbol{e}\|^2 + L\|\boldsymbol{e}\|)$, where $L = 2\|R\|(a\kappa^3/(1-\kappa)^2 + b\kappa^2)$. Define $Z(\boldsymbol{e}) = \sqrt{V(\boldsymbol{e})}$. Since R is symmetric, it has real eigenvalues. It follows from Rayleigh's quotient that $\lambda_1\|\boldsymbol{e}\|^2 \le V(\boldsymbol{e}) \le \lambda_2\|\boldsymbol{e}\|^2$,

where λ_1 and λ_2 are the minimum and maximum eigenvalues of R. For $V(\boldsymbol{e}) > 0$, $\dot{Z}(\boldsymbol{e}) \leq (-\frac{1}{2\lambda_2} Z(\boldsymbol{e}) + \frac{L}{2\sqrt{\lambda_1}})$. By the comparison lemma,

$$Z(t) \leq \frac{L}{2\sqrt{\lambda_1}} \int_0^t e^{-(t-\tau)/2\lambda_2} d\tau \leq \frac{\lambda_2 L}{\sqrt{\lambda_1}}.$$

It can be shown that the above inequality also holds for $V = 0$ Khalil (2002). The proposition then follows from $\|\boldsymbol{e}\| \leq \sqrt{V/\lambda_1} \leq \lambda_2 L/\lambda_1$ with $r = 2\|R\|\lambda_2/\lambda_1$. Throughout this proof, we assume that $\kappa \leq \kappa_{\max}$ to ensure that the nonlinear solution is well-defined. □

The bound in (8.18) provides a rate by which the norm of the error changes in terms of the size of the variation around the steady-state. If $\kappa = 0$, then $\|e\| = 0$, as expected, since the solutions of the linear and nonlinear systems are undisturbed and remain in equilibrium at the origin. As κ increases from $\kappa = 0$ to $\kappa = \kappa_{\max}$, the norm of the error increases. Intuitively, if the variation in density $\boldsymbol{\rho}_j$ approaches the negative of $\overline{\boldsymbol{\rho}}_j$ for some $j \in \mathcal{V}_w$ (i.e., $\kappa \to 1$), then the magnitude of the nonlinear term in (8.8) increases without bound. This increase without bound is captured in the ratio on the right-hand-side of (8.18). However, the solution of the linear system is bounded due to the global asymptotic stability of the equilibrium of the linear system. Although the bound in (8.18) provides intuition about the size of the error, it is derived using conservative bounds, and, therefore, its quantitative bounds may be impractical for real gas systems.

To improve the error estimate, we use numerical optimization to analyze the error as a function of the size of the withdrawal variation. In particular, a series of optimization routines are performed on the single pipeline that was introduced in Section 8.3. The pipeline parameters are shown in Figure 8.2. The boundary conditions are constant 5 (MPa) pressure at the inlet of the pipeline and varying

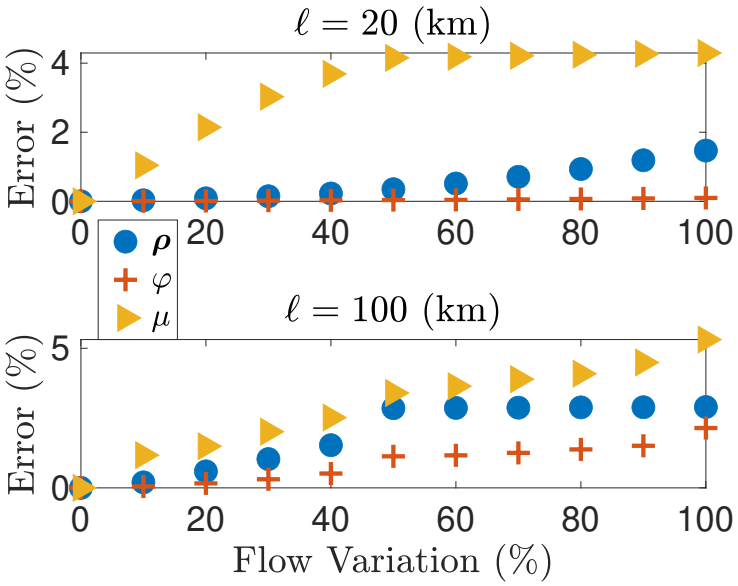

Figure 8.4: Percent relative error (as in (8.17)) as a function of percent flow variation (100κ) as defined in (8.22).

mass outflow profiles at the outlet given by

$$\boldsymbol{w}_{\text{out}}(t) = 200\,(1 + \kappa\,\text{step}(t - T/4) - \kappa\,\text{step}(t - 3T/4))\,, \tag{8.22}$$

where $0 \leq \kappa \leq 1$ and $\text{step}(t) = 0.5\tanh(7.2t)$. Here, $t \in [0, T]$ is in units of hours and $T = 24$ (hr). The percent relative error in pressure, mass flux, and compression between the solutions of the nonlinear and linearized optimal control problems are depicted in Figure 8.4 as a function of 100κ (percent flow variation).

Chapter 9

CONCLUSION

This thesis investigated several topics that may arise in the flow of natural gas in pipelines and networks of pipelines. We began our study with the attenuation of natural gas waves propagating through a pipe. The results enabled us to derive critical curves that partition the boundary condition parameters (frequency and amplitude of waves) into a practical operating region and its complement. We used numerical simulations to demonstrate that the level curves of the error between the linear and nonlinear solutions over the space of boundary parameters may be similar in geometrical shape to these practical critical curves. This observation allowed us to estimate the maximal region (in the space of boundary parameters) where the resulting linearization error is within a specified tolerance.

After studying natural gas flows in a single pipe, we moved to mixtures of natural gas and hydrogen in general networks of pipelines. We extended a control system model for natural gas networks to one that models heterogeneous mixtures of natural gas and hydrogen in pipeline networks. The motivation to develop such a control system originates from recent proposals to utilize the existing natural gas infrastructure to transport mixtures of natural gas and hydrogen with the intention of reducing harmful carbon dioxide emissions from end users (Raju *et al.* (2022)). Our control system is formulated for general networks so that it can be applied to real pipeline systems that operate time-variations of compressor and regulator units, supply stations that inject gas into the network with concentrated pressure, and flow stations that withdraw or inject concentrated mass flow from or into the network at nodes specified by the user. The nonlinear partial differential equation formulation is dis-

cretized using a popular finite volume method for natural gas systems to obtain a nonlinear control system of ODEs. The ODE system was proved to be monotonic for constant concentration vectors and to be non-monotonic, in general, for time-varying concentration vectors. The continuity of solutions with respect to initial conditions and inputs suggests that there is a nontrivial curve, called interface, in the space of boundary condition concentration parameters (frequency and amplitude) that partitions that space into a monotonic and non-monotonic operating regions. The monotonic interface was analyzed numerically and the results were illustrated on a test network.

While analyzing the transition across the monotonic interface, we observed with numerical simulations that a non-periodic solution may result from certain frequency and amplitude pairs of the concentration boundary condition profile. Similarly to the way we computed the monotonic interface, we used numerical simulations to compute the periodic interface that partitions the boundary parameter space into solutions that approach periodic orbits and solutions that do not. The numerical transition from periodic to non-periodic responses may be an indication that the gas mixture system is chaotic (Devaney (2021); Eckmann and Ruelle (1985)). As to whether the system is chaotic remains to be proven. An assertion may enable a gas pipeline system designer to determine limitations on operating the network to be able to reliably predict the future evolution of the operation. As our simulations suggest, operations outside even the monotone operating region may create surges with large pressure, energy, and concentration gradients. The monotonic interface analysis indicates that sufficiently slow variation in concentration about a small constant profile gives the operation a chance to maintain monotonicity and prevent large and rapid pressure transients from occurring. The relatively nice behavior of slow variations suggests that hydrogen should be gradually blended into natural gas pipeline networks. The

acceptable ramping rates depend on the structure of the network and should be determined through numerous simulations.

The ODE control system was used to model the distributed flow of mixtures of two gases with different physical properties through general pipeline networks with time-varying injections, withdrawals, and control actions of compressors. The discretized model is proved to be a consistent approximation of the original PDE system and is used as the dynamic constraints of an optimal control problem. The optimal solution tells us how the compressor activity profiles should be designed with respect to time to meet the requirements of time-varying delivery profiles and pressure limitations in such a way that the expended energy of compressors is minimized. The optimal control problem is implemented after time discretization using a nonlinear program and is validated by interpolating the optimal solution with respect to time and using the interpolated function to perform a numerical simulation of the ODE control system. The developed control system model and computational optimal control scheme may be used to solve a variety of problem formulations for gas transport networks. For example, the objective function could be modified to reflect the economic value of pipeline transport, in terms of natural gas and hydrogen flow provided by suppliers, and energy received by consumers. Including a price of carbon emissions mitigation, due to replacement of natural gas with hydrogen, could indicate optimal locations for integrating hydrogen supplies.

This thesis concluded with a study of pure natural gas operations in general pipeline networks that combined different aspects from linearization and optimal control. The nonlinear ODE control system for homogeneous gas mixtures was reduced to the natural gas system. The resulting ODE control system was linearized around its steady-state solution to obtain a traditional linear time-invariant control system. The eigenvalues of the linear state matrix for a single pipe were computed numer-

ically and compared to a subset of poles of the irrational transfer matrix that was previously used to study wave attenuation. The simple closed-form representation of the poles was used to analyze the transient behavior of the system, including the settling time associated with an instantaneous change in the input variables. Similarly to our development of the optimal control of gas mixture dynamics, we use the pure natural gas model as the dynamic constraints of the OCP. Although this has received significant attention in the literature, there has not been much work in comparing the linear and nonlinear OCPs. One motivation of our work is to reduce the computational cost of optimizing nonlinear gas dynamics in large networks to meet the unpredictable and highly variable demand from electric generators. The linear and corresponding nonlinear OCPs are compared for examples in a single pipeline and a small test network. Our numerical computations demonstrate approximately a 50% reduction in computation time of the nonlinear OCP if the solution of the linear OCP is used as the initialization point of the nonlinear OCP. This result was demonstrated on a single pipeline for specific time-varying boundary conditions. More work needs to be done to establish computational reduction time in more general settings. We also derived an analytical bound on the error between the solutions of the linear and nonlinear OCPs and verified the bound computationally by plotting the error against the size of the flow variation around the steady-state. In a pipeline with sufficiently slow variations, our numerical simulations demonstrate that the linear solution of the OCP is uniformly within 5% of the nonlinear solution for up to 100% variations in demand. Potential applications may include using the linear system to model the transient dynamics or using adaptive switching between the linear and nonlinear models to reduce the computational time of optimizing gas dynamics in the extension from small test networks to big infrastructures.

"Efficient operation of natural gas transmission systems: A network-based heuristic for cyclic structures", Computers Operations Research **33**, 8, 2323–2351 (2006).

Aalto, H., "Transfer functions for natural gas pipeline systems", IFAC Proceedings Volumes **41**, 2, 889–894 (2008).

Abbaspour, M. and K. S. Chapman, "Nonisothermal Transient Flow in Natural Gas Pipeline", Journal of Applied Mechanics **75**, 3 (2008).

Alamian, R., M. Behbahani-Nejad and A. Ghanbarzadeh, "A state space model for transient flow simulation in natural gas pipelines", Journal of Natural Gas Science and Engineering **9**, 51–59 (2012).

Angeli, D. and E. D. Sontag, "Monotone control systems", IEEE Transactions on automatic control **48**, 10, 1684–1698 (2003).

Ascher, U. M. and C. Greif, *A First Course in Numerical Methods* (Society for Industrial and Applied Mathematics, Philadelphia, PA, 2011).

Baker, L., D. Armbruster, A. Scaglione and R. B. Platte, "Analysis of a model of a natural gas pipeline—a transfer function approach", Transactions of Mathematics and Its Applications **5**, 1, tnab002 (2021).

Bales, P., O. Kolb and J. Lang, "Hierarchical modelling and model adaptivity for gas flow on networks", in "International Conference on Computational Science", pp. 337–346 (Springer, 2009).

Banagaaya, N., G. Alì, S. Grundel and P. Benner, "Index-aware model-order reduction for a special class of nonlinear differential-algebraic equations", Journal of Dynamics and Differential Equations **34**, 3, 2465–2489 (2022).

Behbahani-Nejad, M. and Y. Shekari, "The accuracy and efficiency of a reduced-order model for transient flow analysis in gas pipelines", Journal of Petroleum Science and Engineering **73**, 1-2, 13–19 (2010).

Bender, E., "Simulation of dynamic gas flows in networks including control loops", Computers Chemical Engineering **3**, 1, 611–613 (1979).

Benner, P., S. Grundel, C. Himpe, C. Huck, T. Streubel and C. Tischendorf, "Gas network benchmark models", in "Applications of Differential-Algebraic Equations: Examples and Benchmarks", pp. 171–197 (Springer, 2018).

Beylin, A., A. M. Rudkevich and A. Zlotnik, "Fast transient optimization of gas pipelines by analytic transformation to linear programs", in "PSIG annual meeting", (OnePetro, 2020).

Brouwer, J., I. Gasser and M. Herty, "Gas pipeline models revisited: model hierarchies, nonisothermal models, and simulations of networks", Multiscale Modeling & Simulation **9**, 2, 601–623 (2011).

Carter, R. G., "Pipeline optimization: Dynamic programming after 30 years", in "PSIG annual meeting", (OnePetro, 1998).

Chaczykowski, M., "Sensitivity of pipeline gas flow model to the selection of the equation of state", Chemical engineering research and design **87**, 12, 1596–1603 (2009).

Chaczykowski, M., F. Sund, P. Zarodkiewicz and S. M. Hope, "Gas composition tracking in transient pipeline flow", Journal of Natural Gas Science and Engineering **55**, 321–330 (2018).

Chen, C.-T., "Linear system theory and design", Saunders college publishing (1984).

Chertkov, M., S. Backhaus and V. Lebedev, "Cascading of fluctuations in interdependent energy infrastructures: Gas-grid coupling", Applied Energy **160**, 541–551 (2015).

Correa-Posada, C. M. and P. Sanchez-Martin, "Integrated power and natural gas model for energy adequacy in short-term operation", IEEE Transactions on Power Systems **30**, 6, 3347–3355 (2014).

De Wolf, D. and Y. Smeers, "The gas transmission problem solved by an extension of the simplex algorithm", Management Science **46**, 11, 1454–1465 (2000).

Devaney, R. L., *An introduction to chaotic dynamical systems* (CRC press, 2021).

Domschke, P., B. Geißler, O. Kolb, J. Lang, A. Martin and A. Morsi, "Combination of nonlinear and linear optimization of transient gas networks", INFORMS Journal on Computing **23**, 4, 605–617 (2011).

Eckmann, J.-P. and D. Ruelle, "Ergodic theory of chaos and strange attractors", Reviews of modern physics **57**, 3, 617 (1985).

Ehrhardt, K. and M. C. Steinbach, "Nonlinear optimization in gas networks", in "Modeling, simulation and optimization of complex processes", pp. 139–148 (Springer, 2005).

Fincham, A. and M. Goldwater, "Simulation models for gas transmission networks", Transactions of the Institute of Measurement and Control **1**, 1, 3–13 (1979).

Griepentrog, E. and R. März, *Differential-algebraic equations and their numerical treatment*, vol. 88 (Teubner, 1986).

Grundel, S. and M. Herty, "Hyperbolic discretization via Riemann invariants", preprint arXiv:2005.12158 (2020).

Grundel, S., N. Hornung, B. Klaassen, P. Benner and T. Clees, "Computing surrogates for gas network simulation using model order reduction", in "Surrogate-Based Modeling and Optimization", pp. 189–212 (Springer, 2013).

Grundel, S., L. Jansen, N. Hornung, T. Clees, C. Tischendorf and P. Benner, "Model order reduction of differential algebraic equations arising from the simulation of gas transport networks", in "Progress in Differential-Algebraic Equations: Deskriptor 2013", pp. 183–205 (Springer, 2014).

Gugat, M. and M. Herty, "Existence of classical solutions and feedback stabilization for the flow in gas networks", ESAIM: Control, Optimisation and Calculus of Variations **17**, 1, 28–51 (2011).

Gugat, M., M. Herty, A. Klar, G. Leugering and V. Schleper, "Well-posedness of networked hyperbolic systems of balance laws.", Constrained optimization and optimal control for partial differential equations **160**, 123–146 (2012).

Gugat, M., M. Herty and V. Schleper, "Flow control in gas networks: exact controllability to a given demand", Mathematical Methods in the Applied Sciences **34**, 7, 745–757 (2011).

Gugat, M., R. Schultz and D. Wintergerst, "Networks of pipelines for gas with nonconstant compressibility factor: stationary states", Computational and Applied Mathematics **37**, 2, 1066–1097 (2018).

Gugat, M. and S. Ulbrich, "The isothermal euler equations for ideal gas with source term: Product solutions, flow reversal and no blow up", Journal of Mathematical Analysis and Applications **454**, 1, 439–452 (2017).

Gugat, M. and D. Wintergerst, "Transient flow in gas networks: Traveling waves", International Journal of Applied Mathematics and Computer Science **28**, 2 (2018).

Gyrya, V. and A. Zlotnik, "An explicit staggered-grid method for numerical simulation of large-scale natural gas pipeline networks", Applied Mathematical Modelling **65**, 34–51 (2019).

Hall, K. C., W. S. Clark and C. B. Lorence, "A Linearized Euler Analysis of Unsteady Transonic Flows in Turbomachinery", Journal of Turbomachinery **116**, 3, 477–488 (1994).

Hall, K. C. and E. F. Crawley, "Calculation of unsteady flows in turbomachinery using the linearizedeuler equations", AIAA journal **27**, 6, 777–787 (1989).

Heath, M. and J. Blunt, *Dynamic simulation applied to the design and control of a pipeline network* (Gas Gouncil, 1968).

Hennings, F., "Benefits and limitations of simplified transient gas flow formulations", in "Operations research proceedings 2017", pp. 231–237 (Springer, 2018).

Herrán-González, A., J. M. De La Cruz, B. De Andrés-Toro and J. L. Risco-Martín, "Modeling and simulation of a gas distribution pipeline network", Applied Mathematical Modelling **33**, 3, 1584–1600 (2009).

Herty, M., "Modeling, simulation and optimization of gas networks with compressors", Networks & Heterogeneous Media **2**, 1, 81 (2007).

Herty, M., "Coupling conditions for networked systems of euler equations", SIAM Journal on Scientific Computing **30**, 3, 1596–1612 (2008).

Herty, M., J. Mohring and V. Sachers, "A new model for gas flow in pipe networks", Mathematical Methods in the Applied Sciences **33**, 7, 845–855 (2010).

Himpe, C., S. Grundel and P. Benner, "Model order reduction for gas and energy networks", Journal of Mathematics in Industry (2021).

Hirsch, M. W. and H. Smith, "Monotone dynamical systems", Handbook of differential equations: ordinary differential equations **2**, 239–357 (2006).

Issa, R. I. and D. B. Spalding, "Unsteady one-dimensional compressible frictional flow with heat transfer", Journal of Mechanical Engineering Science **14**, 6, 365–369 (1972).

Kazi, S. R., K. Sundar, S. Srinivasan and A. Zlotnik, "Modeling and optimization of steady flow of natural gas and hydrogen mixtures in pipeline networks", arXiv preprint arXiv:2212.00961 (2022).

Khalil, H. K., *Nonlinear systems; 3rd ed.* (Prentice-Hall, Upper Saddle River, NJ, 2002).

Králik, J., P. Stiegler, Z. Vostrú and J. Závorka, "Modeling the dynamics of flow in gas pipelines", IEEE Transactions on Systems, Man, and Cybernetics **SMC-14**, 4, 586–596 (1984).

Liu, C., M. Shahidehpour and J. Wang, "Coordinated scheduling of electricity and natural gas infrastructures with a transient model for natural gas flow", Chaos: An Interdisciplinary Journal of Nonlinear Science **21**, 2, 025102 (2011).

Luongo, C. A., "An efficient program for transient flow simulation in natural gas pipelines", in "PSIG Annual Meeting", (OnePetro, 1986).

Marić, I., A. Galović and T. Šmuc, "Calculation of natural gas isentropic exponent", Flow Measurement and Instrumentation **16**, 1, 13–20 (2005).

Melaina, M. W., O. Antonia and M. Penev, "Blending hydrogen into natural gas pipeline networks: a review of key issues", Tech. Rep. NREL/TP-5600-51995 (2013).

Misra, S., M. W. Fisher, S. Backhaus, R. Bent, M. Chertkov and F. Pan, "Optimal compression in natural gas networks: A geometric programming approach", IEEE Transactions on Control of Network Systems **2**, 1, 47–56 (2015).

Misra, S., M. Vuffray and A. Zlotnik, "Monotonicity properties of physical network flows and application to robust optimal allocation", Proceedings of the IEEE **108**, 9, 1558–1579 (2020).

Modisette, J. L., "Equation of state tutorial", in "PSIG Annual Meeting", (OnePetro, 2000).

Olds, R. and B. Sage, "Transient flow in gas transmission lines", Journal of Petroleum Technology **3**, 07, 217–222 (1951).

Oppenheim, A. V., J. R. Buck and R. W. Schafer, *Discrete-time signal processing. Vol. 2* (Upper Saddle River, NJ: Prentice Hall, 2001).

Oppenheim, A. V., A. S. Willsky, S. H. Nawab, G. M. Hernández *et al.*, *Signals & systems* (Pearson Educación, 1997).

Osiadacz, A., "Simulation of transient gas flows in networks", International journal for numerical methods in fluids **4**, 1, 13–24 (1984).

Osiadacz, A. J. and M. Chaczykowski, "Comparison of isothermal and non-isothermal pipeline gas flow models", Chemical Engineering Journal **81**, 1-3, 41–51 (2001).

Osiadacz, A. J. and M. GburzyĹska, "Selected mathematical models describing flow in gas pipelines", Energies **15**, 2 (2022).

Percell, P. B. and M. J. Ryan, "Steady state optimization of gas pipeline network operation", in "PSIG annual meeting", (OnePetro, 1987).

Poloni, M., D. Winterbone and J. Nichols, "Comparison of unsteady flow calculations in a pipe by the method of characteristics and the two-step differential lax-wendroff method", International Journal of Mechanical Sciences **29**, 5, 367–378 (1987).

Qiu, Y., S. Grundel, M. Stoll and P. Benner, "Efficient numerical methods for gas network modeling and simulation", Networks and Heterogeneous Media **15**, 4, 653–679 (2020).

Rachford, H. H. and R. G. Carter, "Optimizing pipeline control in transient gas flow", in "PSIG annual meeting", (OnePetro, 2000).

Raju, A. S. K., A. Martinez-Moralez, O. Lever and L. Asiedu-Akrofi, "Hydrogen blending impacts study", California Public Utilities Commission (2022).

Reddy, H. P., S. Narasimhan and S. M. Bhallamudi, "Simulation and state estimation of transient flow in gas pipeline networks using a transfer function model", Industrial & engineering chemistry research **45**, 11, 3853–3863 (2006).

Reddy, H. P., S. Narasimhan, S. M. Bhallamudi and S. Bairagi, "Leak detection in gas pipeline networks using an efficient state estimator. part-i: Theory and simulations", Computers & chemical engineering **35**, 4, 651–661 (2011).

Ríos-Mercado, R. Z. and C. Borraz-Sánchez, "Optimization problems in natural gas transportation systems: A state-of-the-art review", Applied Energy **147**, 536–555 (2015).

Ríos-Mercado, R. Z., S. Wu, L. R. Scott and E. A. Boyd, "A reduction technique for natural gas transmission network optimization problems", Annals of Operations Research **117**, 1, 217–234 (2002).

Ruths, J., A. Zlotnik and S. Li, "Convergence of a pseudospectral method for optimal control of complex dynamical systems", in "2011 50th IEEE Conference on Decision and Control and European Control Conference", pp. 5553–5558 (IEEE, 2011).

Sirvent, M., N. Kanelakis, B. Geißler and P. Biskas, "Linearized model for optimization of coupled electricity and natural gas systems", Journal of Modern Power Systems and Clean Energy **5**, 3, 364–374 (2017).

Srinivasan, S., K. Sundar, V. Gyrya and A. Zlotnik, "Numerical solution of the steady-state network flow equations for a non-ideal gas", IEEE Transactions on Control of Network Systems (2022).

Steinbach, M. C., "On pde solution in transient optimization of gas networks", Journal of computational and applied mathematics **203**, 2, 345–361 (2007).

Stolwijk, J. J. and V. Mehrmann, "Error analysis and model adaptivity for flows in gas networks", 10.14279/depositonce-7650 (2018).

Stoner, M. A., "Analysis and Control of Unsteady Flows in Natural Gas Piping Systems", Journal of Basic Engineering **91**, 3, 331–338 (1969).

Subani, N., N. Amin and B. G. Agaie, "Hydrogen-natural gas mixture leak detection using reduced order modelling", Applied and Computational Mathematics **4**, 3, 135–144 (2015).

Sundar, K. and A. Zlotnik, "State and parameter estimation for natural gas pipeline networks using transient state data", IEEE Transactions on Control Systems Technology **27**, 5, 2110–2124 (2018).

Thorley, A. and C. Tiley, "Unsteady and transient flow of compressible fluids in pipelines - a review of theoretical and some experimental studies", International journal of heat and fluid flow **8**, 1, 3–15 (1987).

Tziperman, E., L. Stone, M. A. Cane and H. Jarosh, "El niño chaos: Overlapping of resonances between the seasonal cycle and the pacific ocean-atmosphere oscillator", Science **264**, 5155, 72–74 (1994).

U.S. Energy Information Administration, N. G. D., Office of Oil Gas, "U.s. natural gas pipeline compressor stations illustration", Natural Gas Transportation Information System (2008).

van Deen, J. and S. Reintsema, "Modelling of high-pressure gas transmission lines", Applied Mathematical Modelling **7**, 4, 268–273 (1983).

Wang, P., B. Yu, Y. Deng and Y. Zhao, "Comparison study on the accuracy and efficiency of the four forms of hydraulic equation of a natural gas pipeline based on linearized solution", Journal of Natural Gas Science and Engineering **22**, 235–244 (2015).

Wong, P. and R. Larson, "Optimization of natural-gas pipeline systems via dynamic programming", IEEE Transactions on Automatic Control **13**, 5, 475–481 (1968a).

Wong, P. J. and R. E. Larson, "Optimization of tree-structured natural-gas transmission networks", Journal of Mathematical Analysis and Applications **24**, 3, 613–626 (1968b).

Wylie, E. B., V. L. Streeter and M. A. Stoner, "Unsteady-State Natural-Gas Calculations in Complex Pipe Systems", Society of Petroleum Engineers Journal **14**, 01, 35–43 (1974).

Zecchin, A. C., A. R. Simpson, M. F. Lambert, L. B. White and J. P. Vítkovskỳ, "Transient modeling of arbitrary pipe networks by a laplace-domain admittance matrix", Journal of Engineering Mechanics **135**, 6, 538–547 (2009).

Zlotnik, A., M. Chertkov and S. Backhaus, "Optimal control of transient flow in natural gas networks", in "2015 54th IEEE conference on decision and control (CDC)", pp. 4563–4570 (IEEE, 2015a).

Zlotnik, A., S. Dyachenko, S. Backhaus and M. Chertkov, "Model reduction and optimization of natural gas pipeline dynamics", in "Dynamic Systems and Control Conference", vol. 57267, p. V003T39A002 (American Society of Mechanical Engineers, 2015b).

Zlotnik, A., S. Misra, M. Vuffray and M. Chertkov, "Monotonicity of actuated flows on dissipative transport networks", in "2016 European Control Conference (ECC)", pp. 831–836 (IEEE, 2016a).

Zlotnik, A., L. Roald, S. Backhaus, M. Chertkov and G. Andersson, "Coordinated scheduling for interdependent electric power and natural gas infrastructures", IEEE Transactions on Power Systems **32**, 1, 600–610 (2016b).

Zlotnik, A., A. M. Rudkevich, E. Goldis, P. A. Ruiz, M. Caramanis, R. Carter, S. Backhaus, R. Tabors, R. Hornby and D. Baldwin, "Economic optimization of intra-day gas pipeline flow schedules using transient flow models", in "PSIG Annual Meeting", (OnePetro, 2017).

Zlotnik, A., K. Sundar, A. M. Rudkevich, A. Beylin and X. Li, "Optimal control for scheduling and pricing intra-day natural gas transport on pipeline networks", in "2019 IEEE 58th Conference on Decision and Control (CDC)", pp. 4887–4884 (IEEE, 2019).

APPENDIX A
PUBLISHED WORKS

This section fulfills the terms of Arizona State University's *Policy on using Previously Published or Publishable Work in a Culminating Experience Document*. Previously published or publishable work of the author included in this dissertation is labeled below. All co-authors have confirmed that these manuscripts may be included in this dissertation.

1. Baker, L., D. Armbruster, A. Scaglione and R. B. Platte, "Analysis of a model of a natural gas pipeline—a transfer function approach", Transactions of Mathematics and Its Applications 5, 1, tnab002 (2021) (Chapter 3)

2. Baker, L., S. R. Kazi, R. B. Platte and A. Zlotnik, "Optimal control of transient flows in pipeline networks with heterogeneous mixtures of hydrogen and natural gas", arXiv preprint arXiv:2210.06269 (2022) (Chapters 5 and 7)

3. Baker, L., S. R. Kazi and A. Zlotnik, "Transitions from monotonicity to chaos in gas mixture dynamics in pipeline networks", arXiv preprint arXiv:2303.17692 (2023) (Chapters 5-6)

Transactions of Mathematics and Its Applications (2021) **5**, 1–19
https://doi.org/10.1093/imatrm/tnab002

Analysis of a model of a natural gas pipeline—a transfer function approach

Luke Baker and Dieter Armbruster*
School of Mathematical and Statistical Sciences, Arizona State University, Tempe, AZ 85287, USA
*Corresponding author: armbruster@asu.edu

Anna Scaglione
School of Electrical, Computer and Energy Engineering, Arizona State University, Tempe, AZ 8527, USA

and

Rodrigo B. Platte
School of Mathematical and Statistical Sciences, Arizona State University, Tempe, AZ 85287, USA

[Received on 24 May 2021; revised on 9 September 2021; accepted on 1 October 2021]

A framework for natural gas pipelines is developed in a context similar to the theory of electric transmission lines. The system of semi-linear partial differential equations describing the time-dependent flow of natural gas is linearized around the steady-state flow. Additional approximations lead to a constant coefficient linear system that is equivalent to an electrical circuit that is analytically solvable and admits an ABCD matrix representation of input and output. The sinusoidal steady-state operation of natural gas pipelines is analysed including the distortion of waves. It is shown that the timing of the propagation of phases and other events is accurately represented in the approximation. The quantitative accuracy for flux and gas density of the approximation depending on different operating scenarios and depending on the frequency of the disturbances is documented.

Keywords: gas-pipeline, transfer function, Equivalent Circuit.

1. Introduction

Natural gas infrastructures are extremely complex operating systems composed of transmission pipelines that transmit natural gas hundreds of kilometers across state lines and sometimes even across the country. They include processing and supply stations, withdrawal stations and other essential components such as compressors, regulators and valves that are monitored and controlled by control station operators. Natural gas is purchased primarily through daily contracts between supplier and customer. Up until recent years, natural gas was almost entirely purchased by local distribution companies (LDCs) with the purpose of subsequent delivery to residences and businesses for their regular use. LDCs have their own set of distribution pipelines that distribute smaller volumes of natural gas over shorter distances and at much lower pressures than transmission pipelines. The withdrawal rate of natural gas by LDCs is steady and predictable on the daily market. Under steady supply and demand rates, the transmission of natural gas from supply to withdrawal stations is in a steady state independent of time (see Misra *et al.*, 2014; Wu *et al.*, 2000). Mathematically, the steady state flow is described by simple algebraic equations.

In the past 20 years, new emissions restrictions along with the increased supply of natural gas in the USA have further expanded the application of natural gas. In addition to LDCs, natural gas is now

the primary source of electric power generation in the USA. According to the US Energy Information Administration, natural gas currently accounts for 34% of total electricity generation and is expected to increase to 39% by 2050. The natural gas infrastructure is consequently faced with two major challenges. First, in addition to natural gas, the electric grid relies on other sources of energy for electric power generation, such as wind and solar. These secondary sources are unpredictable and highly variable and the variations have immediate impacts on daily natural gas withdrawal. To analyse the time-dependent pipeline operation, the transmission of natural gas should be modeled with a system of nonlinear partial differential equations (PDEs) that depend on both time and location along the pipe. Second, as has become evident in the Texas winter storm of February 2021, the natural gas and electric power infrastructures are incredibly reliant on one another and both need increasingly close communication and coordination.

Since most gas-powered generators have little or no associated gas storage facility, changes in the electric grid lead to gas withdrawal rates that change with time presenting a new challenge for both system operators and the research community. Much of the current literature focuses on the optimization of compressor settings with which potential objectives are minimizing market costs or load shedding (see Wong & Larson, 1968; Zlotnik *et al.*, 2015). Compounding this problem is one of particular interest in which the electric power operations are included in the optimization problem (as in Li *et al.*, 2008; Zlotnik *et al.*, 2016). The exact solutions of these large-scale optimization problems are impossible to obtain since the flow of gas in each pipe is modeled with a system of nonlinear PDEs and the flow through each node connecting two or more pipes is incorporated with mass conservation laws.

Although numerical solutions to the flow equations are able to serve many meaningful objectives, there is a limit into the depth of the analysis. To gain insight into natural gas operations and to provide a warm startup for the optimization problem, approximate analytical solutions in the time domain have been developed. One approach involves a simplification of the nonlinear PDEs, followed by asymptotic analysis of the natural gas variables (Herty *et al.*, 2010). Another approach is to linearize the nonlinear PDEs, apply the Laplace transform and approximate the resulting transfer functions so that the inverse Laplace transforms exist in standard Laplace transform tables (e.g. Alamian *et al.*, 2012; Reddy *et al.*, 2006). The accuracy of the approximation of the transfer function was investigated in Králik *et al.* (1984). The accuracy of the linearization of nonlinear gas flow equations was investigated in Luongo *et al.* (1986) and Wang *et al.* (2015).

In light of the close coordination between natural gas and electric power infrastructures, we represent the gas pipeline as an equivalent electric circuit leading to an ABCD matrix representation of gas flow between input and output (see Ke & Ti, 2000, for an electrical analogy). The ABCD matrix representation is obtained by linearizing the nonlinear terms in the PDE around the steady-state flow and applying the Fourier transform to the resulting linear PDEs. The primary intention of this paper is analysing distortion of sinusoidal waves in gas pipelines using the ABCD matrix. We also analyse the accuracy of the linearized PDEs for sinusoidal and step boundary conditions.

The rest of this paper is organized in the following way. Section 2 introduces the PDEs that drive the flow of natural gas in a pipeline. Constant coefficient linearized gas flow equations are derived in Section 3 and these equations are solved in the frequency domain in Section 4. The ABCD matrix relation between supply and withdrawal rates is derived in Section 5. It will be shown that wave distortion and optimal gas operations depend on the ABCD matrix coefficients; these are analysed in Section 6. Section 7 analyses the distortion of waves composed of low- and high-frequency components. Section 8 illustrates the accuracy of the linearized PDEs with a variety of different boundary conditions. Throughout the paper, several examples are provided which serve to demonstrate additional properties of natural gas pipelines. A conclusion and an appendix are provided in Sections 9 and Appendix A.

2. Natural gas flow equations in a pipeline

The transmission of natural gas in a pipeline is described mathematically with the one-dimensional isothermal Euler equations with friction. A common simplification is given by the semi-linear PDEs (see Herty *et al.*, 2010; Thorley & Tiley, 1987; Zlotnik *et al.*, 2015)

$$\partial_t \rho + \partial_x \varphi = 0, \tag{2.1}$$

$$\partial_t \varphi + \sigma^2 \partial_x \rho = -\frac{\lambda}{2D}\frac{\varphi|\varphi|}{\rho} - g\sin\theta\rho. \tag{2.2}$$

The time and space variables are $t \in [0, T]$ and $x \in [0, L]$ and the flow variables are mass flux $\varphi(t, x)$ and density $\rho(t, x)$, where T is the time horizon and L is the length of the pipe. The parameters are diameter D, inclination angle θ, friction factor λ and gravitational acceleration g. It is assumed that $p = \sigma^2\rho$ and $\sigma^2 = ZR\mathrm{T}$, where $p(t, x)$ is the pressure and σ is the speed of sound. Here, Z, R, and T are gas compressibility factor, ideal gas constant and constant temperature, respectively. The linear proportionality between density and pressure is known as the equation of state. The variables and parameters are measured in SI units and these units are generally suppressed in our exposition.

The initial state of the natural gas pipeline is determined by the final state of the previous operating day, which will be described shortly. Until stated otherwise, the boundary conditions are assumed to be specified at the sending end of the pipeline. The initial and boundary conditions associated with (2.1) and (2.2) are given by

$$\rho(0, x) = \rho_0(x), \qquad \varphi(0, x) = \varphi_0(x), \qquad x \in [0, L], \tag{2.3}$$

$$\rho(t, 0) = \rho_s(t), \qquad \varphi(t, 0) = \varphi_s(t), \qquad t \in [0, T], \tag{2.4}$$

where ρ_s and φ_s are known functions that dictate the rates of density and mass flux at the sending end of the pipeline. The solution, ρ and φ, of (2.1)–(2.4) is generally dependent on time due to the boundary conditions in (2.4). We assume that the solution is unique and exists for all $t \in [0, T]$ and $x \in [0, L]$. We refer the reader to Barbu & Korman (1993) for a general method of existence and uniqueness of solutions of PDEs and to Gugat & Herty (2011) for results for gas pipelines.

The initial condition in (2.3) is assumed to be the steady-state solution ρ_0 and φ_0, defined by the set of ordinary differential equations

$$\frac{d\varphi_0}{dx} = 0, \qquad \sigma^2\frac{d\rho_0}{dx} = -\frac{\lambda}{2D}\frac{\varphi_0|\varphi_0|}{\rho_0} - g\sin\theta\rho_0, \tag{2.5}$$

with boundary conditions

$$\rho_0(0) = \overline{\rho}, \qquad \varphi_0(0) = \overline{\varphi}, \tag{2.6}$$

where $\overline{\rho}$ and $\overline{\varphi}$ are constants. For a horizontal pipe ($\theta = 0$) the steady-state solution is

$$\varphi_0(x) = \overline{\varphi}, \qquad \rho_0^2(x) = \overline{\rho}^2 - \frac{\lambda\overline{\varphi}|\overline{\varphi}|}{\sigma^2 D}x. \tag{2.7}$$

For inclined and declined pipes ($\theta \neq 0$) mass flux remains the same and density is given by

$$\rho_0^2(x) = \overline{\rho}^2 e^{-\frac{2g\sin\theta}{\sigma^2}x} + \frac{\lambda\overline{\varphi}|\overline{\varphi}|}{2Dg\sin\theta}\left(e^{-\frac{2g\sin\theta}{\sigma^2}x} - 1\right). \tag{2.8}$$

In fact, (2.8) reduces to (2.7) in the limit $\theta \to 0$ using l'Hopital's rule and writing $\left(e^{-\frac{2g\sin\theta}{\sigma^2}x} - 1\right) \approx -\frac{2g\sin\theta}{\sigma^2}x$. The steady-state solution explicitly shows the drop in density in the direction of flow in non-decreasing pipes due to friction and gravity.

3. Linearized equations of natural gas flow

Our objective is to analyse the transmission of natural gas that is initially in steady-state for time-dependent boundary conditions. It is convenient to write density and flux as steady state and perturbation components of the form

$$\begin{aligned} \rho(t,x) &= \rho_0(x) + \rho_e(t,x), \\ \varphi(t,x) &= \varphi_0(x) + \varphi_e(t,x). \end{aligned} \tag{3.1}$$

We substitute (3.1) into (2.1) and (2.2) and use (2.5) to get the governing equations of the perturbation variables. The resulting nonlinearity on the right-hand side of (2.2) is given by

$$f(\rho_e, \varphi_e) = \frac{\lambda}{2D}\left(\frac{\varphi_0|\varphi_0|}{\rho_0} - \frac{(\varphi_0+\varphi_e)|\varphi_0+\varphi_e|}{\rho_0+\rho_e}\right). \tag{3.2}$$

Making the following two approximations: (i) the function f in (3.2) is approximated with its linearization around the origin and (ii) the coefficients of the linearization are approximated using $1/\rho_0 \simeq 1/\overline{\rho}$, we obtain the constant coefficient linear system of PDEs

$$\partial_t \rho_e + \partial_x \varphi_e = 0, \tag{3.3}$$

$$\partial_t \varphi_e + \sigma^2 \partial_x \rho_e = \alpha\rho_e + \beta\varphi_e, \tag{3.4}$$

with initial and boundary conditions

$$\begin{aligned} \rho_e(0,x) &= 0, && x \in [0,L], \\ \varphi_e(0,x) &= 0, && x \in [0,L], \\ \rho_e(t,0) &= \rho_s(t) - \overline{\rho}, && t \in [0,T], \\ \varphi_e(t,0) &= \varphi_s(t) - \overline{\varphi}, && t \in [0,T], \end{aligned} \tag{3.5}$$

where α and β are constant coefficients given by

$$\alpha = \frac{\lambda\overline{\varphi}|\overline{\varphi}|}{2D\overline{\rho}^2} - g\sin\theta, \qquad \beta = -\frac{\lambda|\overline{\varphi}|}{D\overline{\rho}}. \tag{3.6}$$

Here, we label the linearized perturbation variables with the same symbols as the nonlinear perturbation variables. From here onward, these symbols will always represent the perturbation variables of the linear system. Therefore, we have the approximation

$$\begin{aligned} \rho(t,x) &\simeq \rho_0(x) + \rho_e(t,x), \\ \varphi(t,x) &\simeq \varphi_0(x) + \varphi_e(t,x). \end{aligned} \tag{3.7}$$

Note that for constant boundary conditions given by $\rho_s(t) = \overline{\rho}$ and $\varphi_s(t) = \overline{\varphi}$, the steady state of ρ_e and φ_e is zero. Thus, ρ_e can become negative and the requirement of $\rho > 0$ transforms to $\rho_e > -\rho_0$.

In Section 8, the accuracy of the approximation in (3.7) is illustrated with numerical examples. We do not pursue analytical results on the accuracy of the approximation. Instead, we discuss how the error of the approximation depends on the two assumptions made above. We note how the accuracy may be improved by removing approximation (ii), which leads to the constant coefficients in the linear PDE. However, this mild improvement in the accuracy comes at the expense of an unsolvable system of PDEs. The coefficients must be constant to derive an analytical solution.

In Appendix A, we demonstrate that the term involving α in (3.4) can typically be omitted for the *dimensionless* equations describing the flow of natural gas in horizontal pipelines. While this is not necessarily true for the dimensional equations, setting $\alpha = 0$ allows comparisons with electrical power lines and simplifies the algebra. This observation leads to the following definitions. The class of linear systems in (3.3)–(3.5) is called *amplified* if α in (3.4) is defined by (3.6). It is called *unamplified* if α in (3.4) is defined to be zero. Until stated otherwise, the systems are assumed to be amplified.

4. Natural gas pipelines in the sinusoidal steady state

The perturbation variables can be further decomposed into transient and sinusoidal responses. In this section, we investigate the sinusoidal response of the perturbation, which is governed by the linear PDEs and the boundary conditions. The initial conditions in (3.5) effect the transient response but not the sinusoidal response and are therefore disregarded in this section. This approach is analogous to the sinusoidal steady-state operation of voltage and current in electric transmission lines (see, e.g. Glover *et al.*, 2012). The continuous-time Fourier transform of a function $f(t,x)$ and its inverse are defined by

$$F(\omega,x) = \int_{-\infty}^{\infty} f(t,x) e^{-j\omega t}\,\mathrm{d}t, \quad f(t,x) = \frac{1}{2\pi}\int_{-\infty}^{\infty} F(\omega,x) e^{j\omega t}\,\mathrm{d}\omega,$$

where ω is the frequency. Occasionally, we will use operator notation $F(\omega,x) = (\mathfrak{F}f)(\omega,x)$ and $f(t,x) = (\mathfrak{F}^{-1}F)(t,x)$ to denote the analysis and synthesis pair.

We define the Fourier transforms of the perturbation variables by $P(\omega,x) = (\mathfrak{F}\,\rho_e)(\omega,x)$ and $\Phi(\omega,x) = (\mathfrak{F}\,\varphi_e)(\omega,x)$. In this definition, the time interval $[0,T]$ is extended to the entire real line and the perturbation variables are extended in time by periodic repetition with period T. We abuse notation and use the same symbols for the extended functions. Applying the Fourier transform to the driving equations in (3.3) and (3.4) and using Fourier transform properties, we obtain the spatial dynamics in the frequency domain given by

$$\begin{aligned} j\omega P + \partial_x \Phi &= 0, \\ j\omega \Phi + \sigma^2 \partial_x P &= \alpha P + \beta \Phi. \end{aligned} \tag{4.1}$$

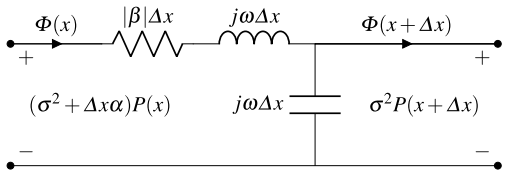

FIG. 1. Circuit representation of a section of pipeline.

The boundary conditions associated with (4.1) are given by

$$P(\omega,0)=P_s(\omega), \qquad \Phi(\omega,0)=\Phi_s(\omega), \tag{4.2}$$

where $P_s(\omega) = \mathfrak{F}(\rho_s(t)-\overline{\rho})(\omega)$ and $\Phi_s(\omega) = \mathfrak{F}(\varphi_s(t)-\overline{\varphi})(\omega)$. The equations in (4.1) and (4.2) characterize the sinusoidal response in the frequency domain. Since the coefficients in (4.1) are constant, we can derive a solution. Before proceeding in this quest, it is instructive to represent a section of pipeline as an electric circuit with linear circuit elements and use the circuit to draw insightful comparisons between gas systems and electric transmission lines. This is the subject of the following example.

EXAMPLE 4.1 Suppose that a small section of pipe with a length of Δx is represented by the two-port network shown in Fig. 1. The equations in (4.1) are obtained by applying Kirchhoff's circuit laws. The drop in density along the pipeline is considered to be comparable to the voltage drop induced by the impedance of the circuit. The conservation of current through a node in a power system is identical to the conservation of flux through a node in a gas system. In this way, voltage and current in electric transmission lines are thought to play similar roles to density and mass flux in natural gas pipelines. It is seen in Fig. 1 that $|\beta|$ represents *resistance* and α represents *amplification* of density. The amplification of density explains the previous terminology.

We define shunt admittance, series impedance and characteristic impedance for the gas pipeline, respectively, by

$$y=j\omega, \qquad z=j\omega-\beta, \qquad z_c=\sqrt{z/y}. \tag{4.3}$$

Two of these quantities depend on β but none depend on α.

The driving equations in (4.1) are weakly coupled and can be decoupled by introducing second-order derivatives

$$\begin{aligned} \sigma^2\partial_{xx}P-\alpha\partial_x P-yzP &= 0,\\ \sigma^2\partial_{xx}\Phi-\alpha\partial_x\Phi-yz\Phi &= 0. \end{aligned} \tag{4.4}$$

A solution of (4.4) is given by

$$P(\omega,x) = \Psi_+ e^{\mu_+ x}+\Psi_- e^{\mu_- x}, \tag{4.5}$$

$$\Phi(\omega, x) = \frac{\sigma^2}{z}\left(\mu_- \Psi_+ e^{\mu_+ x} + \mu_+ \Psi_- e^{\mu_- x}\right), \tag{4.6}$$

where $\mu_\pm = \alpha/(2\sigma^2) \pm \mu/\sigma^2$ and $\mu = \sqrt{\alpha^2/4 + \sigma^2 yz}$. The complex exponential terms $e^{\mu_\pm x}$ represent traveling waves that propagate in opposite directions along the length of the pipe. The waves travel along the pipe with distortion depending upon $\mu_\pm$ and the set of frequencies with which P_s and Φ_s in (4.2) are composed. We emphasize that both of the traveling waves $e^{\mu_\pm x}$ are physically relevant since the pipe has finite length and, therefore, the waves are bounded. In general, it follows that Ψ_+ and Ψ_- are both nonzero.

The coefficients $\Psi_\pm$ are uniquely determined by the boundary conditions. Evaluating (4.5) and (4.6) at $x = 0$ and using (4.2), we obtain

$$\Psi_\pm = \pm\frac{\mu_\pm}{\mu_+ - \mu_-} P_s \mp \frac{z\sigma^{-2}}{\mu_+ - \mu_-}\Phi_s.$$

Substituting these coefficients into (4.5) and (4.6) gives an expression for P and Φ explicitly in terms of P_s and Φ_s of the form

$$P = \frac{\mu_+ e^{\mu_+ x} - \mu_- e^{\mu_- x}}{\mu_+ - \mu_-} P_s - \frac{z}{\sigma^2}\frac{e^{\mu_+ x} - e^{\mu_- x}}{\mu_+ - \mu_-}\Phi_s, \tag{4.7}$$

$$\Phi = -y\frac{e^{\mu_+ x} - e^{\mu_- x}}{\mu_+ - \mu_-} P_s - \frac{\mu_- e^{\mu_+ x} - \mu_+ e^{\mu_- x}}{\mu_+ - \mu_-}\Phi_s. \tag{4.8}$$

These expressions define the solution of (4.1) for each $x \in [0, L]$.

EXAMPLE 4.2 Suppose that the periodic extensions of the boundary conditions of the perturbation variables given by (3.5) are continuous and periodic with period T. In this case, they can be expanded into Fourier series representations of the form

$$\rho_e(t, 0) = \sum_{k=-\infty}^{\infty} \overline{\rho}_k e^{j\omega_k t}, \quad \varphi_e(t, 0) = \sum_{k=-\infty}^{\infty} \overline{\varphi}_k e^{j\omega_k t}, \tag{4.9}$$

where $\omega_k = 2\pi k/T$ for each integer k. The Fourier coefficients are constants defined in the usual way. Let $\delta(\omega)$ be the Dirac delta function or impulse at $\omega = 0$. The Fourier transforms of the representations in (4.9) are the trains of impulses

$$P_s(\omega) = \sum_{k=-\infty}^{\infty} 2\pi\overline{\rho}_k \delta(\omega - \omega_k), \tag{4.10}$$

$$\Phi_s(\omega) = \sum_{k=-\infty}^{\infty} 2\pi\overline{\varphi}_k \delta(\omega - \omega_k), \tag{4.11}$$

where the area of each impulse is proportional to the Fourier series coefficients of the boundary conditions. Define

$$a = \frac{\mu_+ e^{\mu_+ x} - \mu_- e^{\mu_- x}}{\mu_+ - \mu_-}, \qquad b = -\frac{z}{\sigma^2}\frac{e^{\mu_+ x} - e^{\mu_- x}}{\mu_+ - \mu_-}, \tag{4.12}$$

$$c = -y\frac{e^{\mu_+ x} - e^{\mu_- x}}{\mu_+ - \mu_-}, \qquad d = -\frac{\mu_- e^{\mu_+ x} - \mu_+ e^{\mu_- x}}{\mu_+ - \mu_-}. \tag{4.13}$$

Taking inverse Fourier transforms in (4.7) and (4.8) and using the definition of the impulse, we obtain the solution expression in the time domain given by

$$\begin{aligned} \rho_e(t,x) &= \textstyle\sum_{k=-\infty}^{\infty}[a(\omega_k,x)\overline{\rho}_k + b(\omega_k,x)\overline{\varphi}_k]e^{j\omega_k t}, \\ \varphi_e(t,x) &= \textstyle\sum_{k=-\infty}^{\infty}[c(\omega_k,x)\overline{\rho}_k + d(\omega_k,x)\overline{\varphi}_k]e^{j\omega_k t}. \end{aligned} \tag{4.14}$$

The Fourier series coefficients of the solution in (4.14) are weighted sums of the Fourier series coefficients in (4.9), where the weights are equal to samples of the coefficients in (4.7) and (4.8) at equally spaced frequencies $\omega = \omega_k$.

The harmonic component $e^{j\omega_n t}$ is present in (4.14) if and only if it is present in at least one of the Fourier series representations in (4.9). This is the principle of superposition in linear systems. We interpret this result as follows. A given frequency component is present in density and mass flux along the entire pipe if and only if it is present in either density or mass flux at the boundary of the pipe. It is evident from (4.14) that the magnitudes of the harmonic components are altered according to the magnitudes of the corresponding coefficients. This is known as amplitude distortion.

5. ABCD matrix representation

The sending and receiving ends of a natural gas pipeline are assumed to represent the locations of supply and withdrawal stations. A linear relation between density and mass flux at these stations provides immediate information on wave distortion, whether the supply rate can meet the required demand, and operation settings with which optimal gas delivery is achieved. This linear relation is called the ABCD matrix representation. The ABCD matrix has as its input flows at the sending end, P_{s} and Φ_{s}, and as its output flows at the receiving end, P_{r} and Φ_{r}, where $P_{\mathrm{r}}(\omega) = P(\omega, L)$ and $\Phi_{\mathrm{r}}(\omega) = \Phi(\omega, L)$. Evaluating $P(\omega, x)$ and $\Phi(\omega, x)$ in (4.7) and (4.8) at $x = L$, we obtain the desired representation

$$\begin{bmatrix} P_{\mathrm{r}} \\ \Phi_{\mathrm{r}} \end{bmatrix} = \begin{bmatrix} A & B \\ C & D \end{bmatrix} \begin{bmatrix} P_{\mathrm{s}} \\ \Phi_{\mathrm{s}} \end{bmatrix}, \tag{5.1}$$

where the ABCD matrix is given by

$$\begin{bmatrix} A & B \\ C & D \end{bmatrix} = \begin{bmatrix} \frac{\mu_+ e^{\mu_+ L} - \mu_- e^{\mu_- L}}{\mu_+ - \mu_-} & -\frac{z}{\sigma^2}\frac{e^{\mu_+ L} - e^{\mu_- L}}{\mu_+ - \mu_-} \\ -y\frac{e^{\mu_+ L} - e^{\mu_- L}}{\mu_+ - \mu_-} & -\frac{\mu_- e^{\mu_+ L} - \mu_+ e^{\mu_- L}}{\mu_+ - \mu_-} \end{bmatrix}. \tag{5.2}$$

A simpler expression of the ABCD matrix is obtained by assuming that the gas pipeline is unamplified. With the assumption $\alpha = 0$, we find $\mu_{\pm} = \pm\gamma/\sigma$ and

$$\begin{bmatrix} A & B \\ C & D \end{bmatrix} = \begin{bmatrix} \cosh\left(\gamma\frac{L}{\sigma}\right) & -\frac{z_c}{\sigma}\sinh\left(\gamma\frac{L}{\sigma}\right) \\ -\frac{\sigma}{z_c}\sinh\left(\gamma\frac{L}{\sigma}\right) & \cosh\left(\gamma\frac{L}{\sigma}\right) \end{bmatrix}, \tag{5.3}$$

where we have defined the propagation factor $\gamma = \sqrt{yz}$.

Note: The ABCD matrix of an unamplified natural gas pipeline is fundamentally identical to the ABCD matrix corresponding to an electric transmission line Glover *et al.* (2012). This is not surprising since, for $\alpha = 0$ as discussed in Fig. 1 the unamplified gas pipeline is identical to a transmission line.

6. Magnitudes of the ABCD matrix coefficients for the unamplified pipeline

We assume that the natural gas system is unamplified and study the coefficients in (5.3). We write a complex-valued function H in polar coordinates as $H(\omega) = |H(\omega)|e^{j\theta_H(\omega)}$, where $|H|$ is the magnitude and θ_H is the phase of H.

It can be shown that the real and imaginary parts of the ABCD matrix coefficients are either odd or even with respect to ω. We restrict our attention to $\omega \geqslant 0$ and derive expressions for the magnitudes of each ABCD coefficient in (5.3) separately. Since $A = D$ for an unamplified pipeline, we consider only the components of A, B and C.

Defining $\gamma = \gamma_+ + j\gamma_-$, where

$$\gamma_{\pm} = \frac{1}{\sqrt{2}}\left[\sqrt{\omega^4 + \beta^2\omega^2} \mp \omega^2\right]^{\frac{1}{2}} \tag{6.1}$$

and using hyperbolic trigonometric identities, we get

$$\begin{aligned} |A|^2 &= \cosh^2(\gamma_+\tfrac{L}{\sigma}) - \sin^2(\gamma_-\tfrac{L}{\sigma}), \\ |B|^2 &= \tfrac{\sqrt{1+\beta^2/\omega^2}}{\sigma^2}(\sinh^2(\gamma_+\tfrac{L}{\sigma}) + \sin^2(\gamma_-\tfrac{L}{\sigma})), \\ |C|^2 &= \tfrac{\sigma^2}{\sqrt{1+\beta^2/\omega^2}}(\sinh^2(\gamma_+\tfrac{L}{\sigma}) + \sin^2(\gamma_-\tfrac{L}{\sigma})). \end{aligned} \tag{6.2}$$

The properties of the ABCD coefficients can be understood by taking the limits $L \to 0$, $L \gg 1$ and $\omega \to 0$, $\omega \gg 1$ in (6.2). For instance, as $L \to 0$ the ABCD matrix becomes the identity matrix as it should. For large ω, $\gamma_+ \to |\beta|/2$ and $\gamma_- \to \omega$. If, in addition, $|\beta|L/(2\sigma) \gg 1$ then $|\cosh(|\beta|L/2\sigma)| \approx |\sinh(|\beta|L/2\sigma)| = K(L) \gg 1$ and therefore

$$|A|^2 \approx K(L), \quad |B|^2 \approx \frac{1}{\sigma^2}K(L), \quad |C|^2 \approx \sigma^2 K(L). \tag{6.3}$$

For small ω with large and finite L, we get

$$|A|^2 \approx 1 + \frac{\beta^2 L^4}{6\sigma}\omega^2 + O(\omega^3), \quad |B|^2 \approx \frac{|\beta|L^2}{\sigma^4} + O(\omega), \quad |C|^2 \approx L^2\omega^2 + O(\omega^3). \tag{6.4}$$

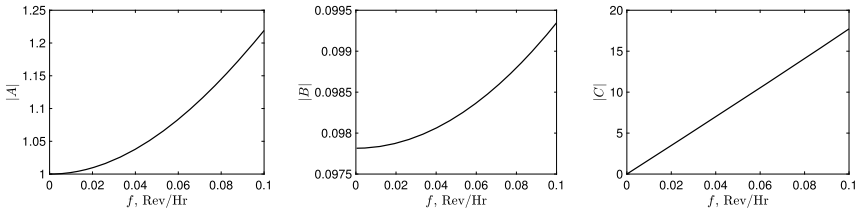

(a) small ω, large L

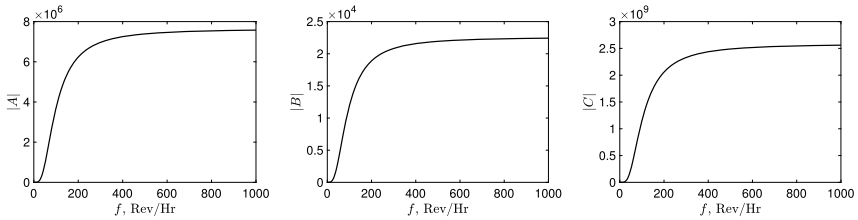

(b) large ω, large L

FIG. 2. Magnitudes of the ABCD matrix in limiting cases as a function of the forcing frequency f in revolutions per hour, i.e. $\omega = 2\pi f/3600$. (a) shows the limit $\omega \to 0$ for large and finite L, Equation (6.4). Here, $|A| \to 1$, $|B|$ approaches a nonzero constant and C approaches zero linearly with ω; (b) shows the limits for large ω and large L, Equation (6.3). Note that $\sigma \approx 3 \cdot 10^2$ and $|B| \approx \frac{|A|}{\sigma}$, $|C| \approx \sigma|A|$ for large ω.

The magnitudes of the ABCD coefficients are depicted in Fig. 2 for a pipe with a length of 100 kilometers confirming the above limits. The other pipeline parameters are associated with Example 8.1 of Section 8.

7. Distortion in natural gas pipelines

Transmission of natural gas from a supply station located at the sending end of the pipe to a withdrawal station located at the receiving end suggests that boundary conditions should be split in the sense that density is specified at the sending end and mass flux is specified at the receiving end. Thus, we replace the boundary condition (2.4) by

$$\rho(t,0) = \rho_{\mathrm{s}}(t), \qquad \varphi(t,L) = \varphi_{\mathrm{r}}(t), \qquad t \in [0,T], \tag{7.1}$$

where $\rho_{\mathrm{s}}(t)$ and $\varphi_{\mathrm{r}}(t)$ are the specified time-dependent rates of supply and demand. The boundary conditions of the linear systems in (3.3)–(3.5) are adjusted accordingly. This reflects the fact that the linear operator in (3.3)–(3.5) corresponds to a second-order wave equation that has forwards and backwards characteristics requiring boundary conditions at both ends (see, e.g. Grundel & Herty, 2020, and the references therein). We note that α and β in (3.6) remain unchanged. From here onward, it is assumed that natural gas operations are governed by (2.1)–(2.3) and (7.1).

A direct representation of input and output is obtained by rearranging (5.1) in the form

$$\begin{bmatrix} P_{\mathrm{r}} \\ \Phi_{\mathrm{s}} \end{bmatrix} = \begin{bmatrix} \operatorname{sech}\left(\gamma \frac{L}{\sigma}\right) & -\frac{z_c}{\sigma}\tanh\left(\gamma \frac{L}{\sigma}\right) \\ \frac{\sigma}{z_c}\tanh\left(\gamma \frac{L}{\sigma}\right) & \operatorname{sech}\left(\gamma \frac{L}{\sigma}\right) \end{bmatrix} \begin{bmatrix} P_{\mathrm{s}} \\ \Phi_{\mathrm{r}} \end{bmatrix}, \tag{7.2}$$

where we have used the fact that $AD - BC = \cosh^2(\gamma \frac{L}{\sigma}) - \sinh^2(\gamma \frac{L}{\sigma}) = 1$.

In this section, we discuss the distortion of waves in natural gas pipelines, i.e. we determine the changes of the magnitudes of the input P_{s} and Φ_{r} as they transmit along the pipe. Specifically, we are interested in the magnitudes of the output P_{r} and Φ_{s} as a function of the input. We observe that if the boundary conditions in (7.1) are given by the steady-state solution, i.e. $\rho_{\mathrm{s}}(t) = \overline{\rho}$ and $\varphi_{\mathrm{r}}(t) = \overline{\varphi}$, there is no perturbation at the boundaries and therefore there is zero distortion for constant supply and demand rates.

EXAMPLE 7.1 The most natural mode of operation for natural gas pipelines is constant supply and temporally varying demand. Since we again focus on the linearized equation, we decompose the time varying demand into its Fourier components and choose sinusoidal boundary conditions. The pipeline parameters are $L = 100$ km, $D = 0.5$m, $\lambda = 0.011$ and $\theta = 0$. Boundary conditions in (7.1) are given by

$$\rho_{\mathrm{s}}(t) = \overline{\rho}, \quad \varphi_{\mathrm{r}}(t) = \overline{\varphi}[1 + 0.1\sin(\omega_k t)], \tag{7.3}$$

where $\omega_k = 2\pi k/T$ with the time scale $T = 12$ hrs, leading to boundary conditions for the linearized equations of the form

$$\rho_e(t, 0) = 0, \quad \varphi_e(t, L) = 0.1\overline{\varphi}\sin(\omega_k t). \tag{7.4}$$

By linearity of the Fourier transform and the definition of the impulse, the Fourier transforms of the boundary conditions in (7.4) are given by $P_{\mathrm{s}} = 0$, $\Phi_{\mathrm{r}} = 0.1\overline{\varphi}\frac{\pi}{j}[\delta(\omega - \omega_k) - \delta(\omega + \omega_k)]$. Substituting these into (7.2), we obtain

$$P_{\mathrm{r}} = -\frac{z_c}{\sigma}\tanh(\gamma \tfrac{L}{\sigma})]\Phi_{\mathrm{r}}, \qquad \Phi_{\mathrm{s}} = \operatorname{sech}(\gamma \tfrac{L}{\sigma})\Phi_{\mathrm{r}}. \tag{7.5}$$

Taking limits of the magnitudes of these expressions as $\omega_k \to \infty$ gives

$$|P_{\mathrm{r}}| \to \frac{1}{\sigma}|\Phi_{\mathrm{r}}|, \qquad |\Phi_{\mathrm{s}}| \to O(e^{-|\beta|L/(2\sigma)}) \approx 0. \tag{7.6}$$

The limiting expressions in (7.6) show that, as the oscillation frequency of $\varphi_e(t, L)$ increases, the amplitude of $\varphi_e(t, 0)$ approaches zero and the amplitude of $\rho_e(t, L)$ approaches the amplitude of $\varphi_e(t, L)$ divided by the speed of sound σ. We conclude that if mass flux withdrawal at the receiving end is characterized by high frequency oscillations, the resultant oscillatory wave at the sending end of the pipe has been damped out. In pipeline operations, this is an important feature. In particular, high frequency demand oscillations are averaged out and there is no need to adjust supply rates at the sending end of the pipe to match them. This is illustrated in Fig. 3 where we observe that for high frequency demand, the amplitude of mass flux at the sending end approaches zero and the amplitude of density at the receiving end approaches the amplitude of mass flux at the receiving end divided by the speed of sound.

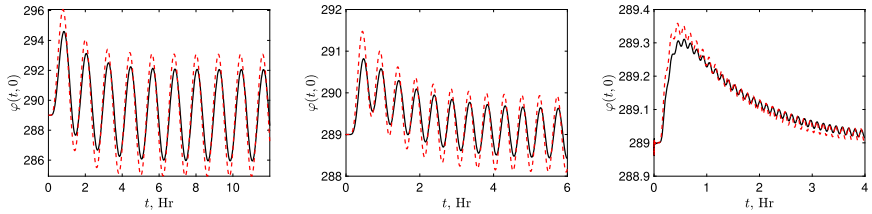

(a) sending flux for $\omega_k = 20\frac{\pi}{12}, 50\frac{\pi}{12}$ and $200\frac{\pi}{12}$, respectively.

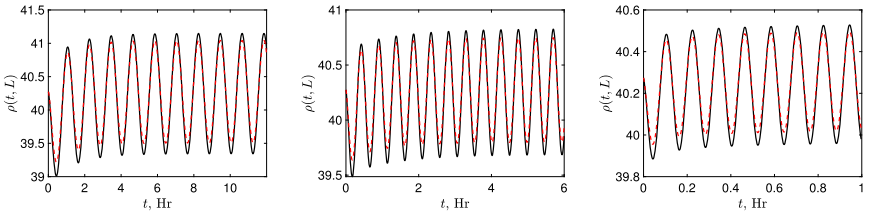

(b) receiving density for $\omega_k = 20\frac{\pi}{12}, 50\frac{\pi}{12}$ and $200\frac{\pi}{12}$, respectively.

FIG. 3. Top row: sending flux for the full nonlinear equation ($\varphi(t,0)$, black solid line) and the linearized approximation ($\varphi_l(t,0;\alpha = 0)$, red dashed line). Bottom row: the corresponding receiving densities ($\rho(t,L)$, black solid line) and the linearized approximation ($\rho_l(t,L;\alpha = 0)$, red dashed line) for different frequencies. The boundary conditions are $\rho_s = \overline{\rho}$ and $\varphi_r = \overline{\varphi}[1 + 0.1\sin(\omega_k t)]$, where ω_k is indicated in the subfigures. This figure is associated with Example 7.1 that corresponds to variable demand in a very large pipeline ($L = 100\ km$).

EXAMPLE 7.2 An alternate mode of pipeline operation is sinusoidally varying supply and constant withdrawal. This corresponds, e.g. to the spectral decomposition of supply perturbations caused from time-dependent withdrawal in neighboring segments of the pipeline. Hence, boundary conditions in (7.1) are given by

$$\rho_s(t) = \overline{\rho}[1 + 0.1\sin(\omega_k t)], \quad \varphi_r(t) = \overline{\varphi}, \tag{7.7}$$

Following the calculations that lead to (7.5), we arrive at

$$P_r = \operatorname{sech}(\gamma\tfrac{L}{\sigma})P_s, \qquad \Phi_s = \frac{\sigma}{z_c}\tanh(\gamma\tfrac{L}{\sigma})]P_s. \tag{7.8}$$

Taking again the high frequency limits, we find

$$|P_r| \to O(e^{-|\beta|L/(2\sigma)}) \approx 0, \qquad |\Phi_s| \to \sigma|P_s|. \tag{7.9}$$

The limiting expressions in (7.9) show that as the frequency of $\rho(t,0)$ increases, the amplitude of $\rho(t,L)$ approaches zero and the amplitude of the resulting oscillation in $\varphi(t,0)$ approaches the amplitude of $\rho(t,0)$ multiplied by the speed of sound σ. At high frequency, the resulting sending flux oscillations

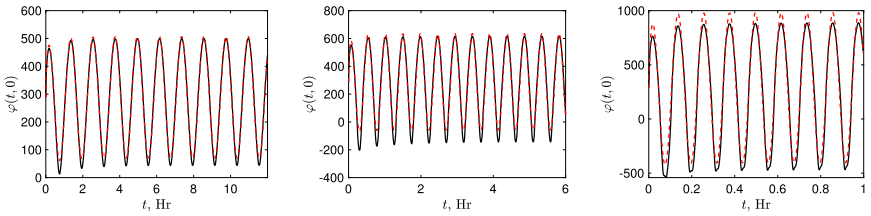

(a) sending flux for $\omega_k = 20\frac{\pi}{12}, 50\frac{\pi}{12}$ and $200\frac{\pi}{12}$, respectively.

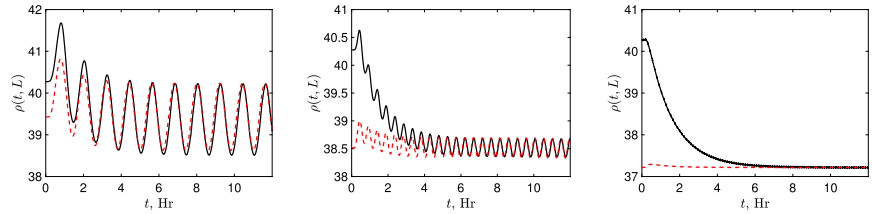

(b) receiving density for $\omega_k = 20\frac{\pi}{12}, 50\frac{\pi}{12}$ and $200\frac{\pi}{12}$ respectively.

FIG. 4. Depicted are sending flux $\varphi(t,0)$, $\varphi_l(t,0;\alpha=0)$ (solid, dashed) and receiving density $[\rho(t,L)+d]$, $\rho_l(t,L;\alpha=0)$ (solid, dashed). The boundary conditions are $\rho_s = \overline{\rho}[1+0.1\sin(\omega_k t)]$ and $\varphi_r = \overline{\varphi}$, where ω_k is indicated in the subfigures. This figure is associated with Example 7.2 that corresponds to variable supply in a very large pipeline ($L = 100$ *km*).

have amplitudes large enough to drive gas into the negative flow direction, as the factor $\sigma \approx 3 \cdot 10^2$ in (7.9) is large. This conclusion is confirmed by the simulations in Fig. 4. In Fig. 4, the amplitude of the sending flux approaches the amplitude of the sending density times the speed of sound and the amplitude of the receiving density approaches zero as ω_k increases.

8. Accuracy of amplified and unamplified pipelines

The linear constant coefficient system in (7.2) allows us to determine distortion of waves with a relatively simple theory of ABCD matrix coefficients. It is based on two approximations: we linearize the nonlinear source terms in (2.1) and (2.2) and we approximate the spatially dependent steady-state profile (2.8) by a constant. An additional approximation is made when we consider the unamplified pipeline and set $\alpha = 0$ in the linearized equation. In this section, we discuss the resulting errors. Define

$$\begin{aligned} \rho_l(t,x;\alpha) &= \rho_0(x) + \rho_e(t,x;\alpha), \\ \varphi_l(t,x;\alpha) &= \varphi_0(x) + \varphi_e(t,x;\alpha), \end{aligned}$$

where α is specified or set equal to zero to distinguish between an amplified or unamplified pipeline, respectively. The accuracy of the approximation in (3.7) is analysed numerically by solving the fully nonlinear equations (2.1) and (2.2) comparing ρ with ρ_l and φ with φ_l for different pipeline parameters and operational conditions.

TABLE 1 *Maximal pointwise relative error between the simulation of the nonlinear system and the linearized and unamplified system for Experiment 7.1 displayed in Fig. 3*

Errors	Transient flux	Steady-state flux	Transient density	Steady-state density
$\omega_k = 20\pi/12$	0.0062	0.0046	0.0046	0.0033
$\omega_k = 50\pi/12$	0.0028	0.0014	0.0027	0.0020
$\omega_k = 200\pi/12$	4.2192e-04	5.1695e-05	0.0012	9.4740e-04

TABLE 2 *Maximal pointwise relative error between the simulation of the nonlinear system and the linearized and unamplified system for Experiment 7.2 displayed in Fig. 4*

Errors	Transient flux	Steady-state flux	Transient density	Steady-state density
$\omega_k = 20\pi/12$	0.1689	0.0960	0.0207	0.0058
$\omega_k = 50\pi/12$	0.4673	0.2943	0.0322	0.0013
$\omega_k = 200\pi/12$	0.6540	0.4087	0.0543	4.9123e-04

We begin by studying the errors from Example 7.1 that has a constant supply and a variable demand. Figure 3 shows a comparison of the transients for the nonlinear solution and the linearized unamplified solution. The top row shows the transient time evolution of the sending flux $\varphi(t, 0)$ while the bottom row shows the same for the receiving density $\rho(t, L)$ for low, medium and high frequency demand variations, respectively.

We observe two important facts: since the hyperbolic equations with the linear and the nonlinear source terms have the same characteristics, the wave speed is the same for both equations and hence their phases are identical. In particular, the linear equation correctly predicts the arrival times of maxima and minima of the perturbations at the other end of the pipeline. Secondly, while the ABCD analysis is valid only for the steady-state operation, the transient behavior of both simulations is very close. Table 1 shows the maximal relative error for the transient determined via these simulations (first column for the sending flux and third column for the receiving density) and for the steady-state part (second column for the sending flux and fourth column for the receiving density) determined by comparisons of the nonlinear simulation and the analytic results due to the ABCD matrix analysis. They are of order $O(10^{-3})$ or smaller.

The dual Experiment 7.2 has a constant demand (flux) and a variable sending density. Figure 4 top row shows $\varphi(t, 0)$ while Fig. 4 bottom row shows $\rho(t, L)$ for low, medium and high frequency demand variations, respectively.

We observe two qualitative issues for the comparison of the transient simulations: (i) the linearized model matches the nonlinear simulation much better for the sending flux (top row) than for the receiving density (bottom row); (ii) for middle- and high-frequency perturbations the flux becomes negative indicating flow reversals. Table 2 displays the transient and steady-state error analysis as in Table 1 for the sending flux and the receiving density. It is interesting to note that while the density errors are still small, order $O(10^{-3})$ for the steady state and $O(10^{-2})$ for the transients, the errors for the flux are of order $O(10^{-1})$.

Switching from steady-state Fourier analysis to time-dependent boundary conditions we study four cases. Some of these experiments can be found in Gyrya & Zlotnik (2019) and are described here.

EXAMPLE 8.1 The common parameters of all the cases are $\lambda = 0.011$, $\theta = 0$ and $\sigma = 338.23$ m/s. All examples refer to the typical model for pipeline operation, i.e. a variable density at the supply side

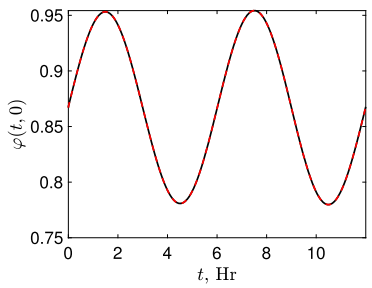

(a) Sending flux for Example 8.1.1 (short pipeline)

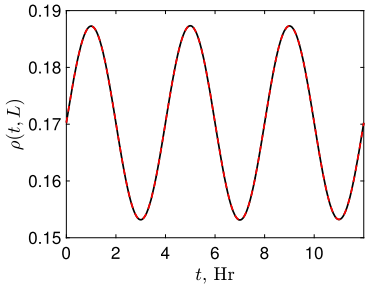

(b) Receiving density for Example 8.1.1 (short pipeline).

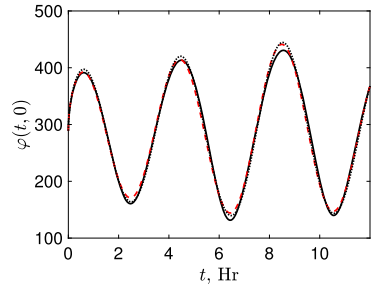

(c) Sending flux for Example 8.1.2 (very large pipeline).

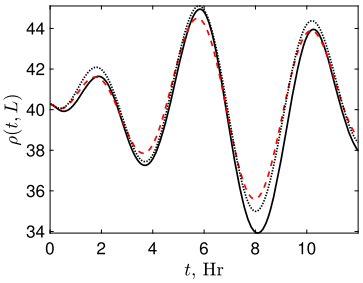

(d) Receiving density for Example 8.1.2 (very large pipeline).

FIG. 5. Depicted are sending flux $\varphi(t,0)$, $\varphi_l(t,0)$, $\varphi_l(t,0;\alpha=0)$ (solid, dotted, dashed) and receiving density $\rho(t,L)$, $\rho_l(t,L)$, $\rho_l(t,L;\alpha=0)$ (solid, dotted, dashed). The associated examples are indicated in the subfigures.

$\rho_s(t)$ and a variable demand given by $\varphi_r(t)$ at the end of the pipeline. The experiments differ in the time horizon, the length of the pipeline, and the type of time-dependent boundary conditions.

1. We set $L = 100$ m and $D = 0.1$ m and consider the steady-state values $\overline{\rho} = 0.003 \times 56.817$ kg/m^3 and $\overline{\varphi} = 0.003 \times 289$ kg/sm^2. For the following boundary conditions with a 12-hr time evolution

$$\rho_s(t) = \overline{\rho}[1 + 0.1\sin(\pi/2t)], \quad \varphi_r(t) = \overline{\varphi}[1 + 0.1\sin(\pi/3t)], \tag{8.1}$$

the rates of density supply and flux demand vary slowly with a period of 4 hrs and 6 hrs, respectively. Figure 5(a) shows that the sending flux has period $T = 6$, while Fig. 5b shows that the receiving density has period $T = 4$ corresponding to the forcing frequencies of flux and density, respectively. This is consistent with the realization that the ABCD matrix becomes the identity for small L, indicating that the pipeline is too short to allow for perturbations of flux and density to mix.

2. The second experiment changes the diameter to $D = 0.5$ m, the length to $L = 100$ km and the steady-state values to $\overline{\rho} = 56.817$ kg/m^3 and $\overline{\varphi} = 289$ kg/sm^2. The time-dependent boundary

conditions are the same as before but with the new steady-state constants. Figure 5(c,d) shows that flux and density perturbations superimpose the frequency components of both boundary terms.

3. We now consider a medium length pipe with $L = 20$ km, $D = 0.9144$ m and steady-state values $\overline{\rho} = 56.812$ kg/m^3 and $\overline{\varphi} = 1200$ kg/sm^2. The boundary condition models a partial closing and opening of a valve. To this end, we define the 'box' function $\text{box}(t) = [u(t-0.33) - u(t-0.66)]$, where $t \in [0, 1]$ is measured in hours and u is the unit step defined by $u(t) = 0$ for $t < 0$ and $u(t) = 1$ for $t \geqslant 0$. Specifically, the boundary conditions are given by

$$\rho_{\text{s}}(t) = \overline{\rho} \qquad \varphi_{\text{r}}(t) = \overline{\varphi}[1 - 0.5\text{box}(t)]. \tag{8.2}$$

4. For the same pipeline, we change the time-dependent boundary conditions to

$$\rho_{\text{s}}(t) \;=\; \overline{\rho}[1 + 0.1\sin(\pi/3t)], \tag{8.3}$$

$$\varphi_{\text{r}}(t) \;=\; 0.1\overline{\varphi}\sin(\pi/2t) + \overline{\varphi}[1 - 0.5\text{box}(t)]. \tag{8.4}$$

For Examples 8.1.1 to 8.1.4, Figs 5 and 6 show the sending flux $\varphi(0, t)$ and the receiving density $\rho(L, t)$ for the fully nonlinear simulations (solid black line), the linearized simulation (dotted black line) and the unamplified model (red dashed line), respectively. As discussed previously, the time of specific events (maxima, minima, perturbations) is resolved exactly by both linear approximations, since the characteristics of all three hyperbolic equations are the same. The relative error of these simulations are typically of the order $O(10^{-3})$ for Example 8.1.2 but rise to $O(10^{-1})$ for the large boundary variations of Example 8.1.3.

9. Conclusion

Starting from the standard equations for gas pipeline flows, we derived approximations based on three steps: we linearize the equations around their steady state, leading to a linear PDE with space-dependent coefficients and source terms in density and flux. We approximate the coefficients by constants and show that the density-dependent source term can be neglected for typical gas pipeline flows. The resulting constant coefficient linear PDE is equivalent to an electrical circuit and can be analysed by Fourier decompositions leading to an input–output relationship between flows and densities at the start and end of the pipeline. This allows us to analytically solve the typical gas pipeline problem that determines the density at the end of the pipeline and the flow at the beginning of the pipeline, given the density at the beginning of the pipeline and the required flow at the end. The analytic formulation allows us insight that is not available through simulation experiments of the nonlinear pipeline equations. Specifically, since the hyperbolic wave equations for the nonlinear and the linear source terms have the same differential operator, they share identical characteristics. Thus, the timing of any event, e.g. demand reductions or other perturbations of the system propagates along the characteristics in the same way for both models and can hence most easily be followed with the linear wave equation.

We show via simulations that the error between the full nonlinear simulation and the approximate linear models is in most cases small. We also find that the constant coefficient linear model has low error for the case of temporarily varying demand and constant supply representing the important case of fluctuating demand due to changes of renewable power generation. Specifically, for long pipelines

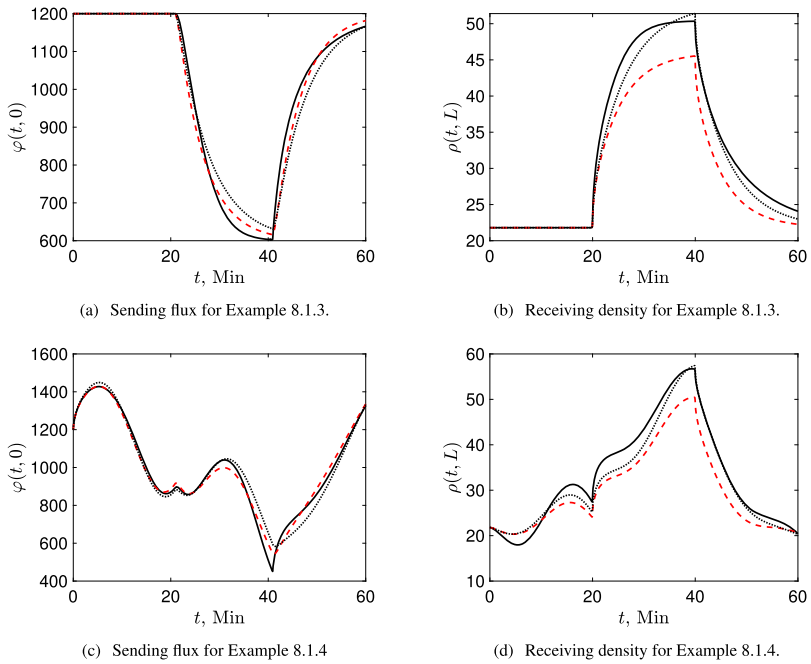

(a) Sending flux for Example 8.1.3.

(b) Receiving density for Example 8.1.3.

(c) Sending flux for Example 8.1.4

(d) Receiving density for Example 8.1.4.

FIG. 6. Depicted are sending flux $\varphi(t,0)$, $\varphi_l(t,0)$, $\varphi_l(t,0;\alpha=0)$ (solid, dotted, dashed) and receiving density $\rho(t,L)$, $\rho_l(t,L)$, $\rho_l(t,L;\alpha=0)$ (solid, dotted, dashed). Experiment 8.1.3 corresponds to constant sending density and time-varying receiving flow, whereas Experiment 8.1.4 has time-dependent boundary conditions at both ends of the pipeline. Both experiments are for the same, large pipeline.

and large frequencies the perturbations are damped by a factor $1/\sigma$, with σ the speed of sound. In contrast, experiments with constant withdrawal and temporarily varying supply is qualitatively still modeled correctly by the linear model but quantitatively has larger errors due to two factors: (i) flow reversals for larger frequencies and (ii) the fact that perturbations are multiplied by σ and hence the oscillations in the flux become of order $O(10^2)$.

Frequency based error analysis shows that in particular *high frequency perturbations of the demand are damped along the pipeline and hence may be neglected at the supply end for longer pipelines.* We show that for short pipelines, perturbations in the flow and in the density will not mix significantly. Depending on the frequency of the perturbations, mixing will exceed a threshold at a critical length. Similarly, based on the analytical understanding of the linearized equations, we can determine the approximate position of flow reversals along a pipeline, given the size and frequency of the perturbations. In a subsequent paper, we will discuss the safe operating limits of a pipeline that avoids flow reversals based on these understandings in more detail (Baker *et al.*, 2021).

As an additional next step, we will extend this analysis to network flows. Having a good understanding of the error behavior will allow us in future work to use the tools of linear control and systems theory to develop robust control algorithms to optimally operate pipeline networks.

Acknowledgements

The authors would like to thank Ignacio Carreno and Michael Herty for useful discussions. Any opinions, and findings expressed in this material are those of the authors and do not necessarily reflect those of the sponsors.

Funding

National Science Foundation (DMS-1502640 to R.P.); Director, Office of Electricity Delivery and Energy Reliability, Cybersecurity for Energy Delivery Systems program, of the US Department of Energy (DE-AC02-05CH11231 and DEOE0000780).

References

Alamian, R., Behbahani-Nejad, M. & Ghanbarzadeh, A. (2012) A state space model for transient flow simulation in natural gas pipelines. *J. Nat. Gas Sci. Eng.*, **9**, 51–59.

Baker, L., Armbruster, D., Platte, R. & Herty, M. (2021) Safe operation and flow reversal in natural gas pipelines. In preparation.

Barbu, V. & Korman, P. (1993) *Analysis and Control of Nonlinear Infinite Dimensional Systems*, vol. 190. Boston: Academic Press.

Glover, J. D., Sarma, M. S. & Overbye, T. (2012) *Power System Analysis & Design, SI Version*. Cengage Learning.

Grundel, S. & Herty, M. (2020) Hyperbolic discretization via Riemann invariants. Preprint arXiv:2005.12158.

Gugat, M. & Herty, M. (2011) Existence of classical solutions and feedback stabilization for the flow in gas networks. *ESAIM Control Optim. Calc. Var.*, **17**, 28–51.

Gyrya, V. & Zlotnik, A. (2019) An explicit staggered-grid method for numerical simulation of large-scale natural gas pipeline networks. *Appl. Math. Model.*, **65**, 34–51.

Herty, M., Mohring, J. & Sachers, V. (2010) A new model for gas flow in pipe networks. *Math. Methods Appl. Sci.*, **33**, 845–855.

Ke, S. & Ti, H. (2000) Transient analysis of isothermal gas flow in pipeline network. *Chem. Eng. J.*, **76**, 169–177.

Králik, J., Stiegler, P., Vostrú, Z. & Závorka, J. (1984) Modeling the dynamics of flow in gas pipelines. *IEEE Trans. Syst. Man Cybern.*, **14**, 586–596.

Li, T., Eremia, M. & Shahidehpour, M. (2008) Interdependency of natural gas network and power system security. *IEEE Trans. Power Syst.*, **23**, 1817–1824.

Luongo, C. A., et al. (1986) An efficient program for transient flow simulation in natural gas pipelines. *Pipeline Simulation Interest Group* PSIG Annual Meeting. New Orleans, Louisiana.

Misra, S., Fisher, M. W., Backhaus, S., Bent, R., Chertkov, M. & Pan, F. (2014) Optimal compression in natural gas networks: a geometric programming approach. *IEEE Trans. Control Netw. Syst.*, **2**, 47–56.

Reddy, H. P., Narasimhan, S. & Bhallamudi, S. M. (2006) Simulation and state estimation of transient flow in gas pipeline networks using a transfer function model. *Ind. Eng. Chem. Res.*, **45**, 3853–3863.

Thorley, A. & Tiley, C. (1987) Unsteady and transient flow of compressible fluids in pipelines—a review of theoretical and some experimental studies. *Int. J. Heat Fluid Flow*, **8**, 3–15.

Wang, P., Yu, B., Deng, Y. & Zhao, Y. (2015) Comparison study on the accuracy and efficiency of the four forms of hydraulic equation of a natural gas pipeline based on linearized solution. *J. Nat. Gas Sci. Eng.*, **22**, 235–244.

Wong, P. & Larson, R. (1968) Optimization of natural-gas pipeline systems via dynamic programming. *IEEE Trans. Automat. Control*, **13**, 475–481.

Wu, S., Rios-Mercado, R. Z., Boyd, E. A. & Scott, L. R. (2000) Model relaxations for the fuel cost minimization of steady-state gas pipeline networks. *Math. Comput. Model.*, **31**, 197–220.

Zlotnik, A., Chertkov, M. & Backhaus, S. (2015) Optimal control of transient flow in natural gas networks. *2015 54th IEEE Conference on Decision and Control (CDC)*. IEEE, pp. 4563–4570.

Zlotnik, A., Roald, L., Backhaus, S., Chertkov, M. & Andersson, G. (2016) Coordinated scheduling for interdependent electric power and natural gas infrastructures. *IEEE Trans. Power Syst.*, **32**, 600–610.

A. Appendix

To get a dimensionless form of the pipeline equations, we perform the following transformations $\hat{t} = t/(\ell/\sigma)$, $\hat{x} = x/\ell$, $\hat{\rho} = \rho/\varrho$, $\hat{\varphi} = \varphi/(\sigma\varrho)$, where ℓ and ϱ are nominal length and density resulting in

$$\partial_{\hat{t}}\hat{\rho} + \partial_{\hat{x}}\hat{\varphi} = 0 \tag{A.1}$$

$$\partial_{\hat{t}}\hat{\varphi} + \partial_{\hat{x}}\hat{\rho} = -\frac{\lambda\ell}{2D}\frac{\hat{\varphi}|\hat{\varphi}|}{\hat{\rho}} - \frac{g\ell\sin\theta}{\sigma^2}\hat{\rho} \tag{A.2}$$

with corresponding initial and boundary conditions. As a result, for a horizontal pipeline, the source terms in the linearized equations become

$$\hat{\alpha} = \frac{\lambda\ell}{2D}\frac{\bar{\hat{\varphi}}|\bar{\hat{\varphi}}|}{\bar{\hat{\rho}}^2}, \quad \hat{\beta} = -\frac{\lambda\ell}{D}\frac{|\bar{\hat{\varphi}}|}{\bar{\hat{\rho}}},$$

where $\bar{\hat{\rho}}$ and $\bar{\hat{\varphi}}$ are the boundary conditions for the steady-state solutions of (A.1) and (A.2). Thus, $\hat{\alpha}/\hat{\beta} = (1/\sigma)(\alpha/\beta) = -\overline{\varphi}/(2\sigma\overline{\rho})$. This ratio is independent of the length, diameter and friction content of the pipe. In Experiments 1 and 3 from Example 8.1, we have $\hat{\alpha}/\hat{\beta} = 0.0075$ and $\hat{\alpha}/\hat{\beta} = 0.0312$, respectively. Since $\sigma = 338$ we get that $\hat{\alpha}/\hat{\beta} = O(10^{-2})$ and thus $\hat{\alpha}$ can mostly be ignored for horizontal pipes.

Optimal Control of Transient Flows in Pipeline Networks with Heterogeneous Mixtures of Hydrogen and Natural Gas

Luke Baker[1], Saif R. Kazi[2], Rodrigo B. Platte[1], and Anatoly Zlotnik[2]

***Abstract*— We formulate a control system model for the distributed flow of mixtures of highly heterogeneous gases through large-scale pipeline networks with time-varying injections of constituents, withdrawals, and control actions of compressors. This study is motivated by the proposed blending of clean hydrogen into natural gas pipelines as an interim means to reducing end use carbon emissions while utilizing existing infrastructure for its planned lifetime. We reformulate the partial differential equations for gas dynamics on pipelines and balance conditions at junctions using lumped elements to a sparse nonlinear differential algebraic equation system. Our key advance is modeling the mixing of constituents in time throughout the network, which requires doubling the state space needed for a single gas and increases numerical ill-conditioning. The reduced model is shown to be a consistent approximation of the original system, which we use as the dynamic constraints in a model-predictive optimal control problem for minimizing the energy expended by applying time-varying compressor operating profiles to guarantee time-varying delivery profiles subject to system pressure limits. The optimal control problem is implemented after time discretization using a nonlinear program, with validation of the results done using a transient simulation. We demonstrate the methodology for a small test network, and discuss scalability and potential applications.**

I. Introduction

Transportation of natural gas through networks of large-scale transmission pipelines has been studied in steady-state [1], [2], [3], [4], [5] and transient [6], [7], [8] operations with applications to the optimal control of compressor actuators. In steady-state, the flow of gas in the network is balanced, so that inflows from processing plants and supply stations and outflows from withdrawal stations sum to zero. Steady-state pipeline flows are described using simple time-invariant algebraic equations that relate pressure drop in the direction of flow to mass flow along each pipeline. In the transient regime, computational complexity increases significantly because the flow in each pipeline cannot be modeled with simple algebraic equations but rather requires a system of nonlinear partial differential equations (PDEs) [9], [10]. Model reduction methods have been proposed to reduce the complexity of optimizing gas flows in networks [11], [12]. Although natural gas is projected to be a primary fuel source through the year 2050 [13], worldwide economies have invested in transitioning from fossil fuels such as natural gas to more sustainable resources. Hydrogen is a potential candidate, which, because it does not produce carbon dioxide when burned, is considered to have the potential to address climate change [14]. Natural gas pipeline operation and management protocols may be modified to transport mixtures of natural gas and hydrogen. Recent studies indicate that natural gas pipelines can safely and effectively transport mixtures of up to 20% hydrogen [15], [16]. However, the complexity of modeling steady-state and transient flows, and thus designing and operating pipelines, is compounded with the injection of hydrogen [17], [18].

Natural gas and hydrogen have significantly different physical and chemical properties. Hydrogen is less dense than natural gas, and the speed of sound through hydrogen is roughly four times as large as that of natural gas. Viscosity, velocity, density, pressure, and energy of the gas mixture all vary with varying hydrogen concentration [19], [20], and these directly affect the transportation of the mixture [21]. Numerical simulations have been performed to demonstrate various effects on steady-state and transient-state flows of mixtures of hydrogen and natural gas in pipeline networks [22], [23], [24], [25], [26], [27], [28]. The method of characteristics was used in the numerical simulation of transient flows on cycle networks with homogeneous flow mixtures [25]. Another recent study investigates gas composition tracking using a moving grid method and an implicit backward difference method [23]. It was shown that both methods of tracking perform well, but the implicit difference method may lose some finer detail in the response due to numerical diffusion. A finite element method using COMSOL Multiphysics was also developed [26]. This study considers the effects of hydrogen concentration on the compressibility factor of the mixture and its relation with pressure. Moreover, there the authors demonstrate that pressure may exceed pipeline limitations in the transient evolution of flow and that the likelihood of this happening increases proportionally with increasing hydrogen concentration.

In contrast to pure natural gas, few studies have examined optimization of steady-state and transient operations of mixtures of hydrogen and natural gas in networks. To our knowledge, there are no results on the optimal control of transient flows of heterogeneous mixtures of gases in pipelines or networks of pipelines. Optimal control of compressor actuators for transport of pure natural gas typically seeks to minimize the cost of running compressors while

*This study was supported by the U.S. Department of Energy's Advanced Grid Modeling (AGM) project "Dynamical Modeling, Estimation, and Optimal Control of Electrical Grid-Natural Gas Transmission Systems". Research conducted at Los Alamos National Laboratory is done under the auspices of the National Nuclear Security Administration of the U.S. Department of Energy under Contract No. 89233218CNA000001.

[1]Luke Baker and Rodrigo Platte are with the School of Mathematical and Statistical Sciences at Arizona State University, Tempe, Arizona, 85281; {lsbaker1,rplatte}@asu.edu.

[2]Saif Kazi and Anatoly Zlotnik are in the Applied Mathematics & Plasma Physics Group at Los Alamos National Laboratory, Los Alamos, New Mexico, 87545; {skazi,azlotnik}@lanl.gov.

being subjected to PDE flow dynamics, nodal pressure and nodal flow balance constraints, and inequality box constraints that limit the pressure throughout the network [29]. Other formulations may use an objective function that maximizes economic value [30]. When transients are sufficiently slow, a friction-dominated approximation may be made [31], and this was shown to be valid in the regime of normal pipeline operations [32]. We use friction-dominated modeling to simplify the reduced modeling in the heterogeneous gas setting.

In this study, we formulate a control system model for transporting heterogeneous mixtures of gases through pipeline networks of general form, and extend optimal control problems for gas pipeline flow to this setting. Our key advance is modeling the mixing of constituents in time throughout the network, which requires doubling the state space needed for a single gas and increases numerical ill-conditioning. This enables the formulation and solution of optimal control problems in which constituent gases may be injected at different points in the network at varying concentrations, e.g., the addition of 100% hydrogen at certain nodes. An algorithm is implemented to obtain solutions, and the results are demonstrated on a small test network that includes a cycle.

The remainder of the manuscript is organized as follows. The governing equations for the flow of mixtures of gases in a network are presented in Section II. In Section III, an endpoint discretization method is employed to reduce the system of PDEs to a system of ordinary differential equations (ODEs). There, we show that the discretization method is consistent and results in the equations for natural gas only in the case of zero hydrogen injection, and yields the steady-state equations when supply and withdrawal are held constant. Section IV describes time-discretization of the optimal control problem that yields a nonlinear program (NLP). The NLP is solved for a test network in Section V, and we discuss applications in Section VI.

II. Network Flow Control Formulation

We begin by defining notation that will be used in the study. A gas network is modeled as a connected and directed graph $(\mathcal{E}, \mathcal{V})$ consisting of edges (pipelines) $\mathcal{E} = \{1, \ldots, E\}$ and nodes (junctions) $\mathcal{V} = \{1, 2, \ldots, V\}$, where E and V denote the cardinalities of the sets. It is assumed that the nodes and edges are ordered within their sets according to their integer labels. The symbol k is conserved for identifying edges in $\mathcal{E}$ and the symbols i and j are conserved for identifying nodes in $\mathcal{V}$. Supply nodes $\mathcal{V}_s \subset \mathcal{V}$ and withdrawal nodes $\mathcal{V}_w \subset \mathcal{V}$ are assumed to be disjoint sets that partition $\mathcal{V}$, i.e., $\mathcal{V}_s \cup \mathcal{V}_w = \mathcal{V}$ and $\mathcal{V}_s \cap \mathcal{V}_w = \emptyset$. It is assumed that supply nodes are ordered in $\mathcal{V}$ before withdrawal nodes so that $i < j$ for all $i \in \mathcal{V}_s$ and $j \in \mathcal{V}_w$. The graph is directed by judiciously assigning a positive flow direction along each edge. It is assumed that gas physically flows in only the direction of positive flow so that the mass flux and velocity of the gas are positive quantities. The notation $k : i \mapsto j$ means that edge $k \in \mathcal{E}$ is directed from node $i \in \mathcal{V}$ to node $j \in \mathcal{V}$. For each node $j \in \mathcal{V}$, we define (potentially empty) incoming and outgoing sets of pipelines by $_{\mapsto}j = \{k \in \mathcal{E} | k : i \mapsto j\}$ and $j_{\mapsto} = \{k \in \mathcal{E} | k : j \mapsto i\}$, respectively.

The transportation of the mixture of hydrogen and natural gas is modeled as a simplification of the isothermal Euler equations. For each pipe $k \in \mathcal{E}$, the flow variables are natural gas density $\rho_k^{(1)}(t,x)$, hydrogen density $\rho_k^{(2)}(t,x)$, and mass flux $\varphi_k(t,x)$ of the mixture, with $t \in [0,T]$ and $x \in [0, \ell_k]$, where T denotes the time horizon and ℓ_k denotes the length of the pipe. Assuming zero inclination and sufficiently slow transients, the flow through edge k is governed by the friction-dominated PDEs

$$\partial_t \rho_k^{(m)} + \partial_x \left(\frac{\rho_k^{(m)}}{\rho_k^{(1)} + \rho_k^{(2)}} \varphi_k \right) = 0, \tag{1}$$

$$\partial_x \left(\sigma_1^2 \rho_k^{(1)} + \sigma_2^2 \rho_k^{(2)} \right) = -\frac{\lambda_k}{2D_k} \frac{\varphi_k |\varphi_k|}{\rho_k^{(1)} + \rho_k^{(2)}}, \tag{2}$$

where (1) is defined for each component $m = 1, 2$. The parameters are diameter D_k, friction factor λ_k, speed of sound through natural gas σ_1, and speed of sound through hydrogen gas σ_2. In the above dynamic equations, the compressibility factors of the gasses are assumed to be constants so that the equations of states are ideally given by $p_k^{(m)} = \sigma_m^2 \rho_k^{(m)}$, where $p_k^{(m)}$ is the partial pressure. The summation of partial pressures results in the equation of state $p_k = (\sigma_1^2 \eta_k^{(1)} + \sigma_2^2 \eta_k^{(2)}) \rho_k$, where $p_k = (p_k^{(1)} + p_k^{(2)})$ is the total pressure, $\rho_k = (\rho_k^{(1)} + \rho_k^{(2)})$ is the total density, $\eta_k^{(1)} = \rho_k^{(1)} / \rho_k$ is the concentration of natural gas, and $\eta_k^{(2)} = \rho_k^{(2)} / \rho_k$ is the concentration of hydrogen. Superscripts 1 and 2 on a gas variable are conserved for identifying natural gas and hydrogen variables, respectively.

Friction forces between the interior wall of a pipe and gas flowing through it cause pressure to decrease in the direction of flow, as reflected in the momentum equation (2). Compressor stations receive gas at low pressure and reduce its volume to increase its pressure to levels required for transportation and customer contracts. In addition to compressors, regulators are installed to reduce the pressure of the received gas to within limits that are compatible with lower pressure distribution systems. For convenience, we assume that a compressor is located at the inlet and a regulator is located at the outlet of each pipeline with respect to the prescribed positive flow direction. For each pipeline $k \in \mathcal{E}$, compression and regulation are modeled with time-varying multiplicative compressor ratio $\underline{\mu}_k(t) \geq 1$ and regulator ratio $\overline{\mu}_k(t) \geq 1$.

Natural gas and hydrogen are injected into the network at each supply node $i \in \mathcal{V}_s$ with specified time-varying profiles of natural gas density $\boldsymbol{s}_i^{(1)}(t)$ and hydrogen density $\boldsymbol{s}_i^{(2)}(t)$. The concentration of gases $m = 1, 2$ at supply nodes are denoted by $\boldsymbol{\gamma}_i^{(m)}(t) = \boldsymbol{s}_i^{(m)} / (\boldsymbol{s}_i^{(1)} + \boldsymbol{s}_i^{(2)})$. Gas is withdrawn downstream at each withdrawal node $j \in \mathcal{V}_w$ with specified time-varying mass flux $\boldsymbol{w}_j(t)$. For $m = 1, 2$ and all $j \in \mathcal{V}_w$, define nodal density variables $\boldsymbol{\rho}_j^{(m)}(t)$ and nodal concentration variables $\boldsymbol{\eta}_j^{(m)}(t)$. All of the nodal quantities in this work are identified with bold symbols. Inlet and outlet

edge variables are defined by attaching underlines below and overlines above the associated edge variables, respectively. For example, $\underline{\varphi}_k(t) = \varphi_k(t,0)$ and $\overline{\varphi}_k(t) = \varphi_k(t,\ell_k)$. The boundary conditions for the flow of the mixture are defined for $m = 1, 2$ by

$$\underline{\rho}_k^{(m)} = \underline{\mu}_k \boldsymbol{s}_i^{(m)}, \qquad \overline{\rho}_k^{(m)} = \overline{\mu}_k \boldsymbol{\rho}_j^{(m)}, \tag{3}$$

$$\underline{\rho}_k^{(m)} = \underline{\mu}_k \boldsymbol{\rho}_i^{(m)}, \qquad \overline{\rho}_k^{(m)} = \overline{\mu}_k \boldsymbol{\rho}_j^{(m)}, \tag{4}$$

$$\boldsymbol{\eta}_j^{(m)} \boldsymbol{w}_j = \sum_{k \in \mapsto j} \overline{\eta}_k^{(m)} \overline{\varphi}_k - \sum_{k \in j \mapsto} \underline{\eta}_k^{(m)} \underline{\varphi}_k, \tag{5}$$

where (3) is defined for $k : i \mapsto j$ with $i \in \mathcal{V}_s$, (4) is defined for $k : i \mapsto j$ with $i \in \mathcal{V}_w$, and (5) is defined for $j \in \mathcal{V}_w$. The conditions in (3)-(4) represent the effects of compression and regulation, and the conditions in (5) represent the conservation of mass flow of each constituent through withdrawal nodes. It is assumed that the final operating state returns to its initial state, resulting in periodic temporal constraints

$$\rho_k^{(m)}(0,x) = \rho_k^{(m)}(T,x) \tag{6}$$

for all $k \in \mathcal{E}$ and $x \in [0, \ell_k]$. Periodicity in time requires the parameters $\boldsymbol{s}_i^{(m)}(t)$, $\boldsymbol{w}_j(t)$, $\underline{\mu}_k(t)$, and $\overline{\mu}_k(t)$ to be periodic with period T. We assume that the boundary conditions are smooth, slowly-varying, and ly bounded in their respective domains to ensure the existence of a smooth, slowly-varying, bounded solution. The flow of the mixture of gases in the network is defined by the initial-boundary value system of PDEs (1)-(6).

Gas network operators require pressure, compression, and regulation to be within satisfactory limitations to ensure the safety of transportation and the quality of gas delivered to customers. These limitations are modeled for all $k \in \mathcal{E}$ with inequality constraints of the form

$$p_k^{\min} \le \sigma_1^2 \rho_k^{(1)} + \sigma_2^2 \rho_k^{(2)} \le p_k^{\max}, \quad 1 \le \underline{\mu}_k, \overline{\mu}_k \le 2, \tag{7}$$

where $p_k^{\min}$ and $p_k^{\max}$ are specified bounds on pressure for each pipeline $k \in \mathcal{E}$. Compression $\underline{\mu}_k$ and regulation $\overline{\mu}_k$ are the control actuators in the network that are designed to minimize total consumption. Since regulation does not consume considerable energy, its contribution may be omitted. The total energy required for compression is given by

$$J = \sum_{k \in \mathcal{E}} \int_0^T c_k |\underline{\varphi}_k(t)| \left((\underline{\mu}_k(t))^{(\nu-1)/\nu} - 1 \right) dt, \tag{8}$$

where c_k is related to the efficiency of the compressor $\underline{\mu}_k$ and ν is the isentropic exponent [33] (which is assumed to be a weighted average of those of natural gas and hydrogen with weights equal to their respective mean concentration injections). The continuous optimal control problem is

$$\begin{array}{ll} \min & J \triangleq \text{compressor energy in (8)}, \\ \text{s.t.} & \text{dynamic constraints: (1)-(2)}, \\ & \text{boundary conditions: (3)-(5)}, \\ & \text{temporal constraints: (6)}, \\ & \text{inequality constraints: (7)}. \end{array} \tag{9}$$

The decision variables are partial densities, mass fluxes, compressor ratios, and regulator ratios.

III. Network Flow Control Discretization

The intial-boundary value system of PDEs from the previous section will be discretized in space to obtain an initial-value system of ODEs. Discretization will be formalized by refining the graph of the gas network. A graph refinement $(\hat{\mathcal{E}}, \hat{\mathcal{V}})$ of the graph $(\mathcal{E}, \mathcal{V})$ is made by adding auxiliary nodes to $\mathcal{V}$ that subdivide the edges of $\mathcal{E}$ so that $\ell_k \le \ell$ for all $k \in \hat{\mathcal{E}}$, where ℓ is sufficiently small, i.e., $\sim$ 2-10 km [12]. The refined graph inherits the prescribed direction of the parent graph. For sufficiently fine network refinement, the relative difference of the flow variables between adjacent nodes is small in magnitude by continuity of the flow variables. We assume that the graph has been sufficiently refined and that the hats may be omitted moving forward.

The system of ODEs is obtained by integrating the dynamic equations in (1)-(2) along the length of each refined pipeline segment so that

$$\int_0^\ell \partial_t \rho^{(m)} dx = -\int_0^\ell \partial_x \left(\frac{\rho^{(m)}}{\rho^{(1)} + \rho^{(2)}} \varphi \right) dx,$$

$$\int_0^\ell \partial_x \left(\sigma_1^2 \rho^{(1)} + \sigma_2^2 \rho^{(2)} \right) dx = -\frac{\lambda}{2D} \int_0^\ell \frac{\varphi|\varphi|}{\rho^{(1)} + \rho^{(2)}} dx,$$

where edge subscripts have been removed for readability. The above integrals of space derivatives are evaluated using the fundamental theorem of calculus. The remaining integrals are evaluated by approximating pipeline density with outlet density and pipeline flux with inlet flux. These approximations are independent of x and may be factored out of the integrals. The above equations become

$$\ell \dot{\overline{\rho}}^{(m)} = \underline{\eta}^{(m)} \underline{\varphi} - \overline{\eta}^{(m)} \overline{\varphi}, \tag{10}$$

$$\sum_{n=1}^{2} \sigma_n^2 \left(\overline{\rho}^{(n)} - \underline{\rho}^{(n)} \right) = -\frac{\lambda \ell}{2D} \frac{\varphi \, |\varphi|}{\overline{\rho}^{(1)} + \overline{\rho}^{(2)}}, \tag{11}$$

where a dot above a variable represents the time-derivative of the variable. We now write the discretized system in matrix form. Define the $E \times E$ diagonal matrices L and K with diagonal entries $L_{kk} = \ell_k$ and $K_{kk} = \lambda_k/(2D_k)$. Define the time-varying (transposed) incidence matrix M of size $E \times V$ componentwise by

$$M_{ki} = \begin{cases} \overline{\mu}_k(t), & \text{edge } k \in_{\mapsto} i \text{ enters node } i, \\ -\underline{\mu}_k(t), & \text{edge } k \in i_{\mapsto} \text{ leaves node } i, \\ 0, & \text{else.} \end{cases} \tag{12}$$

Define the $E \times r$ submatrix M_s of M by the removal of columns $i \in \mathcal{V}_w$, the $E \times (V - r)$ submatrix M_w of M by the removal of columns $i \in \mathcal{V}_s$, and the positive and negative parts of M_w by $\overline{M}_w$ and $\underline{M}_w$ so that $M_w = (\overline{M}_w + \underline{M}_w)/2$ and $|M_w| = (\overline{M}_w - \underline{M}_w)/2$, where r denotes the number of supply nodes and $|A|$ denotes the componentwise absolute value of a matrix A. Define the signed matrices $Q_w = \text{sign}(M_w)$, $\overline{Q}_w = \text{sign}(\overline{M}_w)$, $\underline{Q}_w = \text{sign}(\underline{M}_w)$, and similarly for M_s. These signed matrices are well-defined by the inequalities in (7).

Define inlet and outlet edge mass flux vectors by $\underline{\varphi} = (\underline{\varphi}_1, \ldots, \underline{\varphi}_E)^T$ and $\overline{\varphi} = (\overline{\varphi}_1, \ldots, \overline{\varphi}_E)^T$, and similarly for inlet and outlet edge concentrations. Moreover, define the vectors $\boldsymbol{\rho}^{(m)} = (\boldsymbol{\rho}_{r+1}^{(m)}, \ldots, \boldsymbol{\rho}_V^{(m)})^T$, $\boldsymbol{\eta}^{(m)} = (\boldsymbol{\eta}_{r+1}^{(m)}, \ldots, \boldsymbol{\eta}_V^{(m)})^T$, and $\boldsymbol{\gamma}^{(m)} = (\boldsymbol{\gamma}_1^{(m)}, \ldots, \boldsymbol{\gamma}_r^{(m)})^T$, where the subscripts of the entries are indexed according to the node labels in $\mathcal{V}$. Applying the above matrix definitions, the discretized equations in (10)-(11) together with the boundary conditions in (3)-(5) become

$$L\overline{M}_w \dot{\boldsymbol{\rho}}^{(m)} = \underline{\eta}^{(m)} \odot \underline{\varphi} - \overline{\eta}^{(m)} \odot \overline{\varphi}, \quad (13)$$

$$\sum_{m=1}^{2} \sigma_m^2 \left(M_w \boldsymbol{\rho}^{(m)} + M_s \boldsymbol{s}^{(m)} \right) = -\frac{LK(\underline{\varphi} \odot |\underline{\varphi}|)}{\overline{M}_w (\boldsymbol{\rho}^{(1)} + \boldsymbol{\rho}^{(2)})}, \quad (14)$$

$$\boldsymbol{\eta}^{(m)} \odot \boldsymbol{w} = \overline{Q}_w^T \left(\overline{\eta}^{(m)} \odot \overline{\varphi} \right) + \underline{Q}_w^T \left(\underline{\eta}^{(m)} \odot \underline{\varphi} \right), \quad (15)$$

where $\odot$ is the Hadamard product, and the ratio of vectors on the right-hand-side of (14) is understood to be componentwise. It is assumed that regulators vary slowly so that the time derivative of $\overline{M}_w$ is insignificant, justifying its removal from (13). Multiplying both sides of (13) on the left by $\overline{Q}_w^T$ and using (15), we may combine (13) and (15) to form the equation $\overline{Q}_w^T L \overline{M}_w \dot{\boldsymbol{\rho}}^{(m)} = [\underline{Q}_w^T (\underline{\eta}^{(m)} \odot \underline{\varphi}) - \boldsymbol{\eta}^{(m)} \odot \boldsymbol{w}]$, where we have used $Q_w = (\underline{Q}_w + \overline{Q}_w)$. By the definitions of supply and withdrawal concentrations, the above equations become

$$\overline{Q}_w^T L \overline{M}_w \dot{\boldsymbol{\rho}}^{(m)} = Q_w^T [(|\underline{Q}_w| \boldsymbol{\eta}^{(m)} + |\underline{Q}_s| \boldsymbol{\gamma}^{(m)}) \odot \underline{\varphi}] - \boldsymbol{\eta}^{(m)} \odot \boldsymbol{w}, \quad (16)$$

$$\sum_{m=1}^{2} \sigma_m^2 \left(M_w \boldsymbol{\rho}^{(m)} + M_s \boldsymbol{s}^{(m)} \right) = -\frac{LK(\underline{\varphi} \odot |\underline{\varphi}|)}{\overline{M}_w (\boldsymbol{\rho}^{(1)} + \boldsymbol{\rho}^{(2)})}. \quad (17)$$

Periodic temporal constraints in (6) reduce to

$$\boldsymbol{\rho}^{(m)}(0) = \boldsymbol{\rho}^{(m)}(T). \quad (18)$$

Pressure, compression, and regulation inequality constraints in (7) reduce to

$$\boldsymbol{p}_j^{\min} \le \sigma_1^2 \boldsymbol{\rho}_j^{(1)} + \sigma_2^2 \boldsymbol{\rho}_j^{(2)} \le \boldsymbol{p}_j^{\max}, \quad 1 \le \underline{\mu}_k, \overline{\mu}_k \le 2, \quad (19)$$

where $\boldsymbol{p}_j^{\min}$ and $\boldsymbol{p}_j^{\max}$ are specified bounds for each node $j \in \mathcal{V}_w$. The reduced-model optimal control problem is formulated as

$$\begin{array}{ll} \min & J \triangleq \text{compressor energy in (8),} \\ \text{s.t.} & \text{dynamic constraints: (16)-(17),} \\ & \text{temporal constraints: (18),} \\ & \text{inequality constraints: (19).} \end{array} \quad (20)$$

We now present several results on the discretization method. Proposition 1 below shows that the discretized system in (16)-(17) approaches the continuous system in (1)-(2) in a single pipeline as the distance between adjacent nodes of the refined pipeline approaches zero. Proposition 2 shows that the number of density variables in (16)-(17) reduces to half this number for homogeneous mixtures. Moreover, there we show that the discretized system reduces to the steady-state equations in the time-invariant setting.

Proposition 1. Consider a single pipeline of length ℓ, and refine its graph as a chain connection of E segments of uniform length $\Delta\ell = \ell/E$, diameter D, and friction factor λ. Suppose the gas mixture is supplied to the pipeline at the inlet $\mathcal{V}_s = \{1\}$ with boundary conditions as in (3) and withdrawn from only the outlet so that $\boldsymbol{w}_j = 0$ for $j \neq E+1$. Suppose for simplicity that there are no compressors or regulators. Then the resulting system in (16)-(17) is a consistent spatial discretization of (1)-(5).

Proof. The matrix $\overline{M}_w$ is the $E \times E$ identity matrix, $\underline{M}_w$ is the $E \times E$ lower off-diagonal matrix with nonzero entries $(\underline{M}_w)_{n+1,n} = -1$, and $\underline{Q}_s$ is an $E \times 1$ unit vector with one nonzero entry given by $(\underline{Q}_s)_1 = -1$. For the intermediate segment $n : n \mapsto (n+1)$ with $2 \le n \le E-1$, the associated dynamics in (16)-(17) are given by

$$\dot{\boldsymbol{\rho}}_{n+1}^{(m)} + \frac{1}{\Delta\ell} \left(\boldsymbol{\eta}_{n+1}^{(m)} \underline{\varphi}_{n+1} - \boldsymbol{\eta}_n^{(m)} \underline{\varphi}_n \right) = 0$$

$$\frac{1}{\Delta\ell} \sum_{m=1}^{2} \sigma_m^2 \left(\boldsymbol{\rho}_{n+1}^{(m)} - \boldsymbol{\rho}_n^{(m)} \right) = -\frac{\lambda}{2D} \frac{\underline{\varphi}_n |\underline{\varphi}_n|}{\boldsymbol{\rho}_{n+1}^{(1)} + \boldsymbol{\rho}_{n+1}^{(2)}}.$$

Taking the limit $\Delta\ell \to 0$, the above equations approach the dynamics in (1)-(2). Similarly, as $\Delta\ell \to 0$, it can be shown that the first and last segments of the pipe reduce to the dynamics (1)-(2) with boundary conditions (3)-(5). □

Proposition 2. The network system in (16)-(17) reduces to a system with total density as the only density variable if the concentration of hydrogen at supply nodes is time-invariant. If the concentration of hydrogen is zero at supply nodes, then the system reduces further to the pure natural gas equations. If supply concentration, supply pressure, and withdrawal flux are time-invariant, yielding a time-invariant solution, then the system in (16)-(17) reduces to the steady-state balance laws.

Proof. If $\boldsymbol{\gamma}^{(m)}$ is constant, then $\boldsymbol{\eta}^{(m)}$ is constant as well. Define $\boldsymbol{\gamma}^{(2)} = \boldsymbol{\gamma}$ and $\boldsymbol{\eta}^{(2)} = \boldsymbol{\eta}$, where $\boldsymbol{\gamma}$ and $\boldsymbol{\eta}$ are constant vectors. For constant concentration injection, the relation $(\sigma_1^2 \boldsymbol{\rho}^{(1)} + \sigma_2^2 \boldsymbol{\rho}^{(2)}) = \boldsymbol{a}^2 \odot \boldsymbol{\rho}$ holds, where $\boldsymbol{\rho} = (\boldsymbol{\rho}^{(1)} + \boldsymbol{\rho}^{(2)})$ is total density, $\boldsymbol{a} = (\sigma_1^2(1-\boldsymbol{\eta}) + \sigma_2^2 \boldsymbol{\eta})^{1/2}$ is a constant vector, and the square-root is understood to be componentwise. Moreover, $(\sigma_1^2 \boldsymbol{s}^{(1)} + \sigma_2^2 \boldsymbol{s}^{(2)}) = \boldsymbol{b}^2 \odot \boldsymbol{s}$, where $\boldsymbol{s} = (\boldsymbol{s}^{(1)} + \boldsymbol{s}^{(2)})$ and $\boldsymbol{b} = (\sigma_1^2(1-\boldsymbol{\gamma}) + \sigma_2^2 \boldsymbol{\gamma})^{1/2}$. Superimposing (16) for $m = 1, 2$ results in

$$\overline{Q}_w^T L \overline{M}_w \dot{\boldsymbol{\rho}} = Q_w^T \underline{\varphi} - \boldsymbol{w}, \quad (21)$$

$$M_w \left(\boldsymbol{a}^2 \odot \boldsymbol{\rho} \right) + M_s \left(\boldsymbol{b}^2 \odot \boldsymbol{s} \right) = -\frac{LK(\underline{\varphi} \odot |\underline{\varphi}|)}{\overline{M}_w \boldsymbol{\rho}}. \quad (22)$$

If $\boldsymbol{\gamma} = 0$, then $\boldsymbol{\eta} = 0$ and the above equations reduce to the single gas endpoint discretization method with $\boldsymbol{a} = \boldsymbol{b} = \sigma_1$ [34]. If $\boldsymbol{w}$, $\boldsymbol{\gamma}^{(2)}$, $\boldsymbol{s}$, and $\boldsymbol{\rho}$ are constant, then the system (21)-(22) reduces to the Weymouth equations for a mixture of gases [5]. □

IV. Implementation

The optimal control problem in (20) may be expressed as

$$\min \quad \int_0^T \mathcal{F}(x(t), u(t))dt \tag{23a}$$

$$\text{s.t.} \quad F\frac{d}{dt}[R^{(m)}x(t)] = f^{(m)}(x(t), u(t), p(t)), \tag{23b}$$

$$e(x(T), x(0), u(T), u(0)) = 0, \tag{23c}$$

$$q(x(t), u(t)) \geq 0, \tag{23d}$$

where $x = (\boldsymbol{\rho}^{(1)}, \boldsymbol{\rho}^{(2)}, \underline{\varphi})^T$ is the state, $u = (\{\underline{\mu}_k, \overline{\mu}_k\})^T$ is the control, and $p = (\boldsymbol{s}^{(1)}, \boldsymbol{s}^{(2)}, \boldsymbol{w})^T$ is a fixed (potentially time-varying) vector of parameters. The function e represents temporal periodic constraints, q represents inequality constraints, $R^{(m)}$ is a row selector matrix that maps x into $\boldsymbol{\rho}^{(m)}$, and $F = \overline{Q}_w^T L \overline{M}_w$. A nonlinear program is obtained by discretizing the time interval $[0, T)$ into N subintervals with equally-spaced collocation points $t_n = (n-1)T/N$ for $n = 1, \ldots, N$.

The vector-valued functions $x(t)$, $u(t)$, and $p(t)$ are interpolated with piecewise-linear vector-valued functions $\hat{x}(t)$, $\hat{u}(t)$, and $\hat{p}(t)$, respectively. For $n = 1, \ldots, N$, the function $\hat{x}(t)$ is defined for $t \in [t_n, t_{n+1})$ by

$$\hat{x}(t) = x(t_n) + \frac{x(t_{n+1}) - x(t_n)}{T/N}(t - t_n),$$

where $x(t_{N+1}) = x(t_1)$ by the assumption of periodicity. The functions $\hat{u}(t)$ and $\hat{p}(t)$ are defined similarly. The integral in the objective function is approximated using the trapezoidal rule, resulting in

$$\int_0^T \mathcal{F}(x(t), u(t))dt \approx \sum_{n=1}^{N} \frac{T}{N} \mathcal{F}(\hat{x}(t_n), \hat{u}(t_n)).$$

The time derivative of $R^{(m)}x(t)$ is approximated using the finite difference $d/dt[R^{(m)}x(t)] \approx N/T(R^{(m)}x(t_{n+1}) - R^{(m)}x(t_n))$. Define the $N \times N$ differentiation matrix D componentwise by $D_{n,n} = -T/N$, $D_{n,n+1} = T/N$, and $D_{N,1} = T/N$. The differentiation matrix includes a periodic constraint to the vector on which it operates. Define the stacked state vector $X = (\hat{x}(t_1), \ldots, \hat{x}(t_N))^T$, input $U = (\hat{u}(t_1), \ldots, \hat{u}(t_N))^T$, parameter $P = (\hat{p}(t_1), \ldots, \hat{p}(t_N))^T$, and extend D, F, $R^{(m)}$, and all of the other matrices using Kronecker products with identity matrices of appropriate dimensions. Then the nonlinear program may be written as

$$\min \quad \sum_{n=1}^{N} \frac{T}{N} \mathcal{F}(X_n X, U_n U) \tag{24a}$$

$$\text{s.t.} \quad FDR^{(m)}X_n X = f^{(m)}(X_n X, U_n U, P_n P),$$

$$m = 1, 2, \; n = 1, \ldots, N, \tag{24b}$$

$$q(X_n X, U_n U) \geq 0, \; n = 1, \ldots, N, \tag{24c}$$

where X_n, U_n, and P_n are row selector matrices that satisfy $X_n X = \hat{x}(t_n)$, $U_n U = \hat{u}(t_n)$, and $P_n P = \hat{p}(t_n)$ for $n = 1, \ldots, N$.

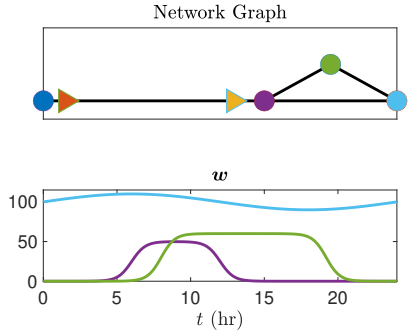

Fig. 1. Top: Configuration of the network. Pipeline dimensions: dark blue to purple = 50 km, purple to light blue = 30 km, purple to green = 20 km, and green to light blue is 30 km. Bottom: Withdrawal flow profiles.

The NLP in (24) is performed on a MacBook Air 8-core CPU with 8GB of unified memory, and is implemented in Matlab with the interior-point algorithm using the function fmincon. The gradient of the objective and Jacobian of the constraints are supplied to the function for improved performance. The Hessian of the Lagrangian function is set to the default finite-difference approximation. Optimal control of compression and regulation is obtained from the optimal solution $U = U^*$. Optimal compressors, regulators, and specified parameters are supplied to the ODEs (16)-(17) and simulated in Matlab using the function ode15s for validation of the solution and an improved prediction of pressure and mass flux. The steady-state solution is used as the starting point for optimization, and the initial state of the optimal solution is used as the initial condition for simulation. In the following, we distinguish between the solution of the optimization problem (24) and the solution of the ODEs (16)-(17) that are driven by optimal compression and regulation. The two solutions are compared using the average L^2 norm of the relative difference given by

$$\frac{1}{\hat{E}} \sum_{k \in \hat{\mathcal{E}}} \left(\frac{1}{T} \int_0^T \left(2\frac{\underline{\varphi}_k(t) - \underline{\phi}_k(t)}{\underline{\varphi}_k(t) + \underline{\phi}_k(t)} \right)^2 dt \right)^{1/2} \times 100, \tag{25}$$

where $\underline{\varphi}_k$ is the optimized flux in edge $k \in \hat{\mathcal{E}}$, $\underline{\phi}_k$ is the simulated flux, and $\hat{E}$ is the cardinality of $\hat{\mathcal{E}}$. In addition, the maximum absolute relative difference is also documented as

$$\max_{k \in \hat{\mathcal{E}}} \max_{t \in [0,T]} \left| 2\frac{\underline{\varphi}_k(t) - \underline{\phi}_k(t)}{\underline{\varphi}_k(t) + \underline{\phi}_k(t)} \right| \times 100. \tag{26}$$

Similar metrics are used for the difference between optimized and simulated pressure trajectories.

V. Case Study

The optimal control algorithm is demonstrated on a cyclic network whose configuration and dimensions are shown on the top of Fig. 1. The refined network has a uniform discretization length of $\ell_k = 10$ km for all $k \in \hat{\mathcal{E}}$. The

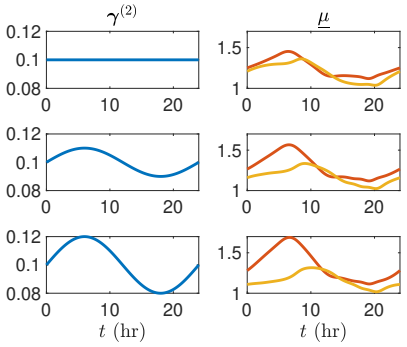

Fig. 2. Left column: Hydrogen concentration profiles at the supply node. Right column: Corresponding optimal compressor responses.

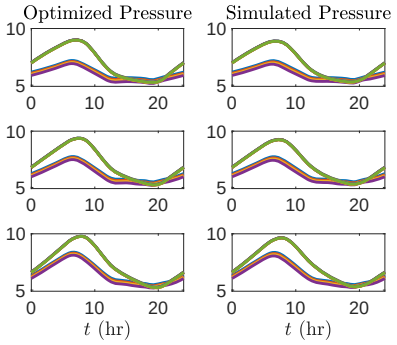

Fig. 3. Left column: Optimized pressure at refined withdrawal nodes driven by the respective concentration profiles from Fig. 2. Right column: Simulated pressure at refined withdrawal nodes driven by inlet concentration and optimal compression profiles from Fig. 2. The average L^2 norm of the relative difference in pressures, using the metric (25), are approximately 0.769%, 0.770%, and 0.769% for the top, middle, and bottom rows. The maximum relative difference in pressures, using the metric (26), are approximately 2.154%, 2.038%, and 1.971% for the top, middle, and bottom rows. The combined computational times for optimization and simulation are approximately 10.0 s, 8.0 s, and 7.7 s for the top, middle, and bottom rows, respectively.

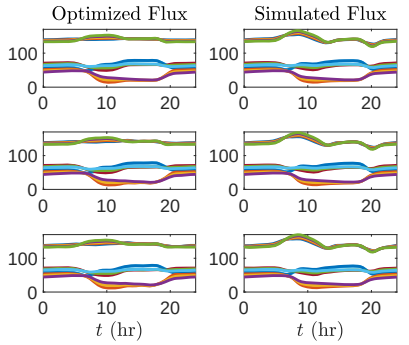

Fig. 4. Left column: Optimized mass flux in refined edges driven by the respective concentration profiles from Fig. 2. Right column: Simulated mass flux in refined edges driven by inlet concentration and optimal compression profiles from Fig. 2. The L^2 relative difference metric values using (25) are approximately 3.994%, 4.608%, and 5.258% for the top, middle, and bottom rows. The maximum relative difference values using metric (26) are approximately 12.967%, 16.713%, and 21.509%, respectively.

diameters and friction factors of the refined pipelines are uniform and equal to $D_k = 0.5$ m and $\lambda_k = 0.011$ for all $k \in \hat{\mathcal{E}}$. The speeds of sounds of the gases are $\sigma_1 = 338.38$ m/s and $\sigma_2 = 4\sigma_1$. We use $N = 20$ time steps with $\nu = 1.28$ and $c_1 = c_5 = D_k^4/T$ in (8). The minimum and maximum pressures in (19) are $\boldsymbol{p}_j^{\min} = 5$ MPa and $\boldsymbol{p}_j^{\max} = 12$ MPa for all $j \in \hat{\mathcal{V}}_w$. Discretization results in 780 optimization variables, 740 equality constraints, and 520 inequality constraints in the NLP (24).

The purple, green, and light blue nodes in the network graph in Figure 1 represent stations where gas is withdrawn with color-coordinated flow profiles depicted on the bottom of Fig. 1. The red and yellow objects represent two compressor stations whose time-dependent operations are optimized in a model-predictive setting. The dark blue node is the supply station for a mixture of natural gas and hydrogen with a fixed pressure of 5 MPa that is immediately boosted by the red compressor station. We demonstrate three solutions for this network, each of which are subject to the same above boundary conditions but differ in the injected concentration of hydrogen at the supply node. The left column of Fig. 2 depicts the specified hydrogen concentration profiles at the supply node for the three solutions and the right column shows the associated results for optimal compression of the two color-coordinated compressor stations. The total compressor energy values in (8) for the optimal compressors in Fig. 2 are $J = 0.787$, $J = 0.824$, and $J = 0.860$ (non-dimensionalized units) from top to bottom. Figs. 3 and 4 depict pressure and mass flux solutions, respectively, where the left-hand-side columns depict the optimized solutions and the right-hand-side columns depict the validating simulation. The results demonstrate that slight increases in hydrogen concentration may have substantial effects on pressure and compressor activity. In particular, the pressure gradients in Fig. 3 from $t = 0$ to $t = 8$ hr are approximately 2 MPa for a fixed 10% hydrogen injection and approximately 3.5 MPa for a slowly-varying hydrogen injection from 10% to 12% hydrogen.

VI. Conclusions

We synthesized a control system model for the distributed flow of mixtures of two gases with different physical properties through large-scale pipeline networks with time-varying injections, withdrawals, and control actions of compressors. The motivation is to develop analysis methods to evaluate recent proposals for blending of clean hydrogen into natural gas pipelines as an interim means for carbon emissions reduction that allows utilization of existing infrastructure

for its planned lifetime. The partial differential equations for gas dynamics on pipelines and balance conditions at junctions are approximated using lumped elements to a sparse nonlinear differential algebraic equation system. In contrast to previously published results, we model the mixing of constituents in time throughout the network. The optimal control technique we develop is able to rapidly produce validated solutions, even though representing dynamics of the gas mixture requires doubling the state space with respect to models for a single gas, and worsens numerical conditioning. We show that the reduced model is a consistent approximation of the original system, use it as the dynamic constraints in a model-predictive optimal control method for minimizing the energy expended by applying time-varying compressor operating profiles to guarantee time-varying delivery profiles subject to system pressure limits. The optimal control problem is implemented after time discretization using a nonlinear program, with validation of the results done using a transient simulation.

The developed control system model and computational optimal control scheme can be used to solve a variety of problem formulations for gas transport networks. The objective function could be modified to reflect the economic value of pipeline transport, in terms of natural gas and hydrogen flow provided by suppliers, and energy received by consumers. Including a price of carbon emissions mitigation due to replacement of natural gas with hydrogen could indicate optimal locations for integrating hydrogen supplies.

REFERENCES

[1] P. L. Wong and R. Larson, "Optimization of natural-gas pipeline systems via dynamic programming," *IEEE Transactions on Automatic Control*, vol. 13, no. 5, pp. 475–481, 1968.

[2] P. B. Percell and M. J. Ryan, "Steady state optimization of gas pipeline network operation," in *PSIG annual meeting*. OnePetro, 1987.

[3] S. Wu, R. Z. Rios-Mercado, E. A. Boyd, and L. R. Scott, "Model relaxations for the fuel cost minimization of steady-state gas pipeline networks," *Mathematical and Computer Modelling*, vol. 31, no. 2-3, pp. 197–220, 2000.

[4] D. De Wolf and Y. Smeers, "The gas transmission problem solved by an extension of the simplex algorithm," *Management Science*, vol. 46, no. 11, pp. 1454–1465, 2000.

[5] S. Misra, M. W. Fisher, S. Backhaus, R. Bent, M. Chertkov, and F. Pan, "Optimal compression in natural gas networks: A geometric programming approach," *IEEE Transactions on Control of Network Systems*, vol. 2, no. 1, pp. 47–56, 2014.

[6] M. Abbaspour and K. S. Chapman, "Nonisothermal Transient Flow in Natural Gas Pipeline," *Journal of Applied Mechanics*, vol. 75, no. 3, 05 2008, 031018. [Online]. Available: https://doi.org/10.1115/1.2840046

[7] A. Osiadacz, "Simulation of transient gas flows in networks," *International Journal for Numerical Methods in Fluids*, vol. 4, no. 1, pp. 13–24, 1984.

[8] A. Zlotnik, M. Chertkov, and S. Backhaus, "Optimal control of transient flow in natural gas networks," in *54th IEEE Conference on Decision and Control*. IEEE, 2015, pp. 4563–4570.

[9] A. J. Osiadacz and M. Chaczykowski, "Comparison of isothermal and non-isothermal pipeline gas flow models," *Chemical Engineering Journal*, vol. 81, no. 1-3, pp. 41–51, 2001.

[10] A. R. D. Thorley and C. H. Tiley, "Unsteady and transient flow of compressible fluids in pipelines—a review of theoretical and some experimental studies," *International journal of heat and fluid flow*, vol. 8, no. 1, pp. 3–15, 1987.

[11] R. Z. Ríos-Mercado *et al.*, "A reduction technique for natural gas transmission network optimization problems," *Annals of Operations Research*, vol. 117, no. 1, pp. 217–234, 2002.

[12] S. Grundel, N. Hornung, B. Klaassen, P. Benner, and T. Clees, "Computing surrogates for gas network simulation using model order reduction," in *Surrogate-Based Modeling and Optimization*. Springer, 2013, pp. 189–212.

[13] S. Nalley and A. LaRose, "Annual energy outlook 2022," *U.S. Energy Information Agency*, 2022.

[14] B. L. Salvi and K. A. Subramanian, "Sustainable development of road transportation sector using hydrogen energy system," *Renewable and Sustainable Energy Reviews*, vol. 51, pp. 1132–1155, 2015.

[15] M. Götz, J. Lefebvre, F. Mörs, A. M. Koch, F. Graf, S. Bajohr, R. Reimert, and T. Kolb, "Renewable power-to-gas: A technological and economic review," *Renewable energy*, vol. 85, pp. 1371–1390, 2016.

[16] M. Ozturk and I. Dincer, "A comprehensive review on power-to-gas with hydrogen options for cleaner applications," *International Journal of Hydrogen Energy*, vol. 46, no. 62, pp. 31 511–31 522, 2021.

[17] T. van der Hoeven, *Math in gas and the art of linearization*. Energy Delta Institute Groningen, The Netherlands, 2004.

[18] M. W. Melaina, O. Antonia, and M. Penev, "Blending hydrogen into natural gas pipeline networks: A review of key issues," *National Renewable Energy Laboratory*, 2013.

[19] A. A. Abd, S. Z. Naji, T. C. Thian, and M. R. Othman, "Evaluation of hydrogen concentration effect on the natural gas properties and flow performance," *International Journal of Hydrogen Energy*, vol. 46, no. 1, pp. 974–983, 2021.

[20] T. Blacharski *et al.*, "The effect of hydrogen transported through gas pipelines on the performance of natural gas grid," *AGH Drilling, Oil, Gas*, vol. 33, no. 2, 2016.

[21] Ł. Zabrzeski, P. Janusz, K. Liszka, M. Łaciak, and A. Szurlej, "Hydrogen-natural gas mixture compression in case of transporting through high-pressure gas pipelines," *IOP Conference Series: Earth and Environmental Science*, vol. 214, p. 012137, 2019. [Online]. Available: https://doi.org/10.1088/1755-1315/214/1/012137

[22] F. E. Uilhoorn, "Dynamic behaviour of non-isothermal compressible natural gases mixed with hydrogen in pipelines," *International journal of hydrogen energy*, vol. 34, no. 16, pp. 6722–6729, 2009.

[23] M. Chaczykowski, F. Sund, P. Zarodkiewicz, and S. M. Hope, "Gas composition tracking in transient pipeline flow," *Journal of Natural Gas Science and Engineering*, vol. 55, pp. 321–330, 2018.

[24] G. Guandalini *et al.*, "Dynamic modeling of natural gas quality within transport pipelines in presence of hydrogen injections," *Applied Energy*, vol. 185, pp. 1712–1723, 2017.

[25] S. Elaoud, Z. Hafsi, and L. Hadj-Taieb, "Numerical modelling of hydrogen-natural gas mixtures flows in looped networks," *Journal of Petroleum Science and Engineering*, vol. 159, pp. 532–541, 2017.

[26] Z. Hafsi, S. Elaoud, and M. Mishra, "A computational modelling of natural gas flow in looped network: Effect of upstream hydrogen injection on the structural integrity of gas pipelines," *Journal of Natural Gas Science and Engineering*, vol. 64, pp. 107–117, 2019.

[27] D. Fan, J. Gong, S. Zhang, G. Shi, Q. Kang, Y. Xiao, and C. Wu, "A transient composition tracking method for natural gas pipe networks," *Energy*, vol. 215, p. 119131, 2021.

[28] B. G. Agaie *et al.*, "Reduced-order modelling for high-pressure transient flow of hydrogen-natural gas mixture," *The European Physical Journal Plus*, vol. 132, no. 5, pp. 1–16, 2017.

[29] H. H. Rachford and R. G. Carter, "Optimizing pipeline control in transient gas flow," in *PSIG annual meeting*. OnePetro, 2000.

[30] A. Zlotnik, K. Sundar, A. M. Rudkevich, A. Beylin, and X. Li, "Optimal control for scheduling and pricing intra-day natural gas transport on pipeline networks," in *58th Conference on Decision and Control*. IEEE, 2019, pp. 4887–4884.

[31] K. Sundar and A. Zlotnik, "State and parameter estimation for natural gas pipeline networks using transient state data," *IEEE Transactions on Control Systems Technology*, vol. 27, no. 5, pp. 2110–2124, 2019.

[32] S. Misra, M. Vuffray, and A. Zlotnik, "Monotonicity properties of physical network flows and application to robust optimal allocation," *Proceedings of the IEEE*, vol. 108, no. 9, pp. 1558–1579, 2020.

[33] I. Marić, A. Galovic, and T. Smuc, "Calculation of natural gas isentropic exponent," *Flow Measurement and Instrumentation*, vol. 16, pp. 13–20, 03 2005.

[34] C. Himpe, S. Grundel, and P. Benner, "Model order reduction for gas and energy networks," *Journal of Mathematics in Industry*, vol. 11, no. 1, pp. 1–46, 2021.

Transitions from Monotonicity to Chaos in Gas Mixture Dynamics in Pipeline Networks

Luke S. Baker,[1,2] Saif R. Kazi,[2,3] and Anatoly Zlotnik[2]

[1] *School of Mathematical and Statistical Sciences, Arizona State University, Tempe, AZ*
[2] *Applied Mathematics and Plasma Physics, Los Alamos National Laboratory, Los Alamos, NM**
[3] *Center for Nonlinear Studies, Los Alamos National Laboratory, Los Alamos, NM*

(Dated: April 3, 2023)

The blending of hydrogen generated using clean energy into natural gas pipeline networks is proposed in order to utilize existing energy systems for their planned lifetime while reducing their reliance on fossil fuels. We formulate a system of partial differential equations (PDEs) that govern the flow dynamics of mixtures of gases in pipeline networks under the influence of time-varying compressor and regulator control actions. The formulation is derived for general gas networks that can inject or withdraw arbitrary time-varying mixtures of gases into or from the network at arbitrarily specified nodes. The PDE formulation is discretized in space to form a nonlinear control system which is used to prove that homogeneous mixtures are well-behaved and heterogeneous mixtures may be ill-behaved in the sense of monotone-ordering of solutions. We use numerical simulations to compute interfaces that delimit periodic and monotone system responses and show that any solution in the monotonic operating region eventually approaches a periodic orbit. Our results are demonstrated for examples of a single pipeline and a small test network.

I. INTRODUCTION

Although natural gas is projected to be a primary fuel source through the year 2050 [1], societies worldwide are investing intensively to transition from fossil fuels such as natural gas and coal to more sustainable and cleaner resources. In particular, hydrogen is an energy carrier that can be cleanly produced [2] and can address climate change because it does not produce carbon dioxide or other harmful emissions when it is burned. Several qualities of hydrogen make it an attractive fuel option for a variety of applications that include transportation and high temperature manufacturing. Hydrogen can also be used to power turbines, which can potentially be used for aviation and electric power production. Hydrogen can be produced directly from fossil fuels, biomass, or direct electrolysis, by splitting water into its constituent components of hydrogen and oxygen. After hydrogen is produced, it can be transported to end users economically by dedicated pipeline systems.

Recent studies have proposed that natural gas pipelines can safely transport mixtures of up to 20% hydrogen or more by volume [3, 4]. Thus, hydrogen could be transported through the existing infrastructure and then separated, or the mixture could be used directly as an end-use fuel. Because the physical and chemical properties of hydrogen and natural gas (primarily methane) differ significantly, the mass and energy transport dynamics of inhomogeneous mixtures of these constituent gases are considerably more complex than for a homogeneous gas [5]. The mathematical modeling of such mixtures is also considerably more challenging than what has traditionally been done for gas pipelines [6]. The introduction of substantial proportions of much lighter hydrogen into natural gas pipelines requires much closer spacing of gas compressors, and this relationship has been characterized in an empirical study [7]. Additionally, the pressure and flow dynamics in gas networks have been proven to satisfy certain physically intuitive and conceptually valuable monotonicity properties [8], which must be re-examined in the presence of inhomogeneous gas mixing.

The physical complexities of blending hydrogen in natural gas pipelines present several mathematical challenges. First, additional state variables are needed to account for changes in mass fraction, which affect total density, energy content, and flow dynamics. Modeling the flow of a homogeneous gas on a network requires partial differential equations (PDEs) for mass and momentum conservation on each pipe, and a linear mass flow balance equation at each network junction. Adding a second gas requires the addition of another PDE on each pipe and a bilinear nodal balance equation at each junction to account for conservation of composition. This more than doubles the state space of the continuous model. Moreover, the faster wave speed corresponding to the lower density of hydrogen worsens the numerical ill-conditioning of the dynamic model. Such issues have been highlighted by the numerical simulations of hydrogen and natural gas flows in pipelines [7, 9–16].

One recent study has demonstrated conditions under which pipeline pressures may exceed allowable upper limits, and that the likelihood of this occurrence increases proportionally with increasing hydrogen concentration [13]. Another study examined the effects of hydrogen blending on the detection and estimation of leaks [16], and demonstrated that the amount of leak discharge increases as the concentration of hydrogen increases. A moving grid method and an implicit backward difference method for tracking gas concentration were both shown to perform well but the implicit difference method may

* Electronic address: {lsbaker,skazi,azlotnik}@lanl.gov

lose some finer detail due to numerical diffusion [10]. The method of characteristics was also applied for the numerical simulation of transient flows on cyclic networks with homogeneous flow mixtures [12]. Modeling networks of pipelines with composition tracking was the focus of another recent study [7], although this model does not include control actions of compressor units. In general, these models demonstrate a simulation capability or sensitivity study for a specific network. Addressing challenging design, operational, and economic issues in the pipeline transport of gas mixtures will require minimal and generalizable mathematical models that adequately describe the relevant physics, as well as comprehensive characterizations of their properties.

The scope of the present study is threefold. First, we extend general control system models for gas pipeline networks [17] to account for heterogeneous mixtures of hydrogen and natural gas. The state variables are flows, partial densities, and pressures throughout the network, and the control variables are the actions of compressor and regulator units. Control actions may be designed to minimize fuel consumption [18–20] or maximize economic value [21]. The PDE control system of the mixture is discretized in space using an endpoint lumped-element method [22] and written in matrix form as a finite-dimensional control system of nonlinear ordinary differential equations (ODEs). Second, we prove that solutions to initial boundary value problems (IBVPs) of a gas mixture have certain monotone ordering properties if the concentration is homogeneous but, in general, do not have these properties if the concentration is heterogeneous. The homogeneous monotonicity result generalizes the pure natural gas monotonicity result for obtaining control formulations that are robust to uncertainty in pressure and withdrawal profiles [8, 23]. Third, we demonstrate that an IBVP solution may be chaotic, in the sense that a time-periodic boundary condition can generate a non-periodic solution composed of a continuous distribution of frequency modes. Numerical simulations are used to characterize flow solution behavior in a phase space of periodic forcing functions and identify boundaries between the regions of periodic and monotonic, periodic and non-monotonic, and non-periodic and non-monotonic solution behavior. Transitions through such fluid mixing phase regions were observed in oceanic wind bursts [24, 25] and in flame combustion of hydrogen and air mixtures [26, 27]. The nested transition through phase regions shows that every solution in the monotonic phase region eventually approaches a periodic orbit, which can be used to reliably estimate the dynamics of mixtures. Simulation-based analysis such as that presented here could be used to evaluate appropriate limitations on blending of hydrogen into existing natural gas pipeline networks.

The rest of this paper is organized as follows. The PDEs that govern heterogeneous mixtures of hydrogen and natural gas are presented in Section II. In Section III, the PDE system is discretized in space to obtain a system of ODEs. Section IV presents the derivation of equivalent ODE systems in terms of other state variables of interest. Section V contains a proof that each of the equivalent systems have monotonic solutions if the concentration is homogeneous, as well as a proof that the solutions are, in general, non-monotonic if the concentration is heterogeneous. Section VI illustrates the non-monotonic results using numerical simulations of flows through a small test network that contains a loop, and which was examined in a previous study [28]. Moreover, that section illustrates that certain types of equivalent systems may have more desirable monotone system behavior than others in certain operating regimes. Sections VIII and IX compute the monotonic and periodic interfaces for flow in a single pipeline, and Section X provides concluding remarks and an outlook for future work.

II. GAS NETWORK MODELING

A gas transport network is modeled as a connected and directed graph $(\mathcal{E}, \mathcal{V})$ consisting of edges $\mathcal{E} = \{1, \ldots, E\}$ and nodes $\mathcal{V} = \{1, \ldots, V\}$, where E and V denote the numbers of edges and nodes, respectively. It is assumed that the elements of these sets are ordered according to their integer labels. The edges represent pipelines and the nodes represent junctions or stations where gas can be injected into or withdrawn from the network. The symbol k is reserved for identifying edges in $\mathcal{E}$ and the symbols i and j are reserved for identifying nodes in $\mathcal{V}$. The graph is directed by assigning a positive flow direction along each edge. It is assumed that gas physically flows in only the direction of positive flow, so that the mass flow and velocity values of the gas are positive quantities everywhere in the network. The notation $k : i \mapsto j$ means that edge $k \in \mathcal{E}$ is directed from node $i \in \mathcal{V}$ to node $j \in \mathcal{V}$. For each node $j \in \mathcal{V}$, we define (potentially empty) incoming and outgoing sets of pipelines by ${}_{\mapsto}j = \{k \in \mathcal{E} | k : i \mapsto j\}$ and $j_{\mapsto} = \{k \in \mathcal{E} | k : j \mapsto i\}$, respectively.

A. Modeling Physical Flow in a Pipe

Compressible flow of a homogeneous ideal gas through a pipe is described using the one-dimensional isothermal Euler equations [29],

$$\partial_t \rho + \partial_x(\rho u) = 0, \tag{1a}$$

$$\partial_t(\rho u) + \partial_x(p + \rho u^2) = -\frac{\lambda}{2D}\rho u|u| - \rho g \frac{\partial h}{\partial x}, \tag{1b}$$

$$p = \rho Z R \mathbf{T} = \sigma^2 \rho, \tag{1c}$$

where $u(t,x)$, $p(t,x)$, and $\rho(t,x)$ are gas velocity, pressure, and density variables, respectively. Here, $t \in [0,T]$ and $x \in [0,\ell]$, where T denotes the time horizon and ℓ denotes the length of the pipe. The symbols ∂_t and ∂_x denote the differential operators with respect to time

t and location x, respectively. The above system describes mass conservation (1a), momentum conservation (1b), and the gas equation of state (1c). The variable h represents the elevation of the pipe. The dominant term in the momentum equation (1b) is the phenomenological Darcy-Weisbach term that models momentum loss caused by turbulent friction, and is scaled by a dimensionless parameter λ called the friction factor. The remaining parameters are the internal pipe diameter D, the wave (sound) speed $\sigma = \sqrt{ZR\mathbf{T}}$ in the gas, and the gravitational acceleration g, where Z, R, and $\mathbf{T}$ are the gas compressibility factor, specific gas constant, and absolute temperature, respectively. Here, we assume that gas pressure p and gas density ρ satisfy the ideal gas equation of state (1c) with constant wave speed σ. While non-ideal modeling is necessary in practice to correctly quantify flows at pressures used in large gas transport pipelines, ideal gas modeling still qualitatively captures the flow phenomenology, so we use it for simplicity of exposition. Extension to non-ideal gas modeling can be made by applying appropriate nonlinear transforms [28].

It is standard to use the per area mass flux $\varphi = \rho u$, and assume that gas flow is an isothermal process, that flow is turbulent and has high Reynolds number, and that the flow is adiabatic, i.e. there is no heat exchange with ground [30]. For slowly varying boundary conditions, the kinetic energy term $\partial_x(\rho u^2)$ and the inertia term $\partial_t(\rho u)$ in equation (1b) may be omitted [29]. With these assumptions, and given no elevation changes, the equations (1) can be reduced to

$$\partial_t \rho + \partial_x \varphi = 0, \tag{2a}$$

$$\sigma^2 \partial_x \rho = -\frac{\lambda}{2D}\frac{\varphi|\varphi|}{\rho}. \tag{2b}$$

where ρ and φ denote density and mass flux (in per-area units). The above equations have been used in several previous studies [8, 31], and we refer the reader there for further justifications. Here, we extend these equations to the case of a mixture of two constituent gases, whose partial densities, partial flows, and mass fractions are denoted by $\rho^{(1)}$ and $\rho^{(2)}$, $\varphi^{(1)}$ and $\varphi^{(2)}$, and $\eta^{(1)}$ and $\eta^{(2)}$, respectively, where $\eta^{(m)} \equiv \rho^{(m)}/(\rho^{(1)} + \rho^{(2)}) = \rho^{(m)}/\rho$. From here onward, we use the terms mass fraction and concentration interchangeably, and specifically refer to *volumetric* concentration where that quantity is examined. The propagation of either concentration quantity $\eta^{(m)}$ can then be modeled by the convection-diffusion equation with diffusion terms omitted [10], i.e.,

$$\partial_t \eta^{(m)} + \frac{\varphi}{\rho}\partial_x \eta^{(m)} = 0. \tag{2c}$$

The local wave speed of the mixture will then depend on the local concentration according to $\sigma^2 = \eta^{(1)}\sigma_1^2 + \eta^{(2)}\sigma_2^2$, which is equivalent to $\sigma^2\rho = \sigma_1^2\rho^{(1)} + \sigma_2^2\rho^{(2)}$. Henceforth, superscripts "(1)" and "(2)" identify correspondence of variables to natural gas and hydrogen, respectively. Next, we reformulate equations (2a)-(2c) into a more convenient form, and add nodal compatibility conditions to define the dynamics of the flow mixture on a network.

B. Gas Mixture Dynamics on a Network

With the above assumptions, the flow dynamics through the level pipeline $k \in \mathcal{E}$ is modeled with the friction-dominated PDEs

$$\partial_t \rho_k^{(m)} + \partial_x\left(\frac{\rho_k^{(m)}}{\rho_k^{(1)} + \rho_k^{(2)}}\varphi_k\right) = 0, \tag{3}$$

$$\partial_x\left(\sigma_1^2\rho_k^{(1)} + \sigma_2^2\rho_k^{(2)}\right) = -\frac{\lambda_k}{2D_k}\frac{\varphi_k|\varphi_k|}{\rho_k^{(1)} + \rho_k^{(2)}}, \tag{4}$$

where Eq. (3) is defined for both $m = 1$ and $m = 2$. We leave it as an exercise for the reader to verify that Eqs. (3)-(4) defined in terms of partial densities $\rho^{(1)}$ and $\rho^{(2)}$ and total flow φ are equivalent to Eq. (2) defined in terms of total density ρ, total flow φ, and one concentration variable $\eta^{(2)}$. The parameters are wave speeds σ_1 and σ_2 in natural gas and hydrogen, respectively, and diameter D_k, length ℓ_k, and friction factor λ_k corresponding to the pipeline $k \in \mathcal{E}$.

Compressor and regulator stations are critical components that actuate the flow of gas throughout the network and reduce pressure in the direction of flow, respectively. For convenience, we assume that a compressor is located at the inlet and a regulator is located at the outlet of each pipeline, where inlet and outlet are defined with respect to the oriented positive flow direction. For each pipeline $k \in \mathcal{E}$, compression and regulation are modeled with multiplicative control variables $\underline{\mu}_k(t) \geq 1$ and $\overline{\mu}_k(t) \geq 1$, respectively. For example, the pressure of gas leaving a compressor unit is $\underline{\mu}_k(t)$ times larger than the pressure of gas entering the unit.

The boundary conditions for a mixture of gases allow for more degrees of freedom than those for a single gas, and are formulated here to enable definition of a range of potential scenarios. All of the flow quantities defined in this paragraph are, in general, time-varying, but we omit time-dependence for readability. The network nodes are partitioned into slack nodes $\mathcal{V}_s \subset \mathcal{V}$ and non-slack nodes $\mathcal{V}_d \subset \mathcal{V}$. Slack nodes are assumed to be ordered in $\mathcal{V}$ before non-slack nodes, so that $i < j$ for all $i \in \mathcal{V}_s$ and $j \in \mathcal{V}_d$. A mixture of gas is injected into the network at each slack node $i \in \mathcal{V}_s$. The boundary conditions at the slack nodes $i \in \mathcal{V}_s$ are defined by specifying individual densities $\boldsymbol{s}_i^{(1)}$ and $\boldsymbol{s}_i^{(2)}$. Alternatively, pressure $(\boldsymbol{p}_s)_i$ and concentration $\boldsymbol{\alpha}_i^{(m)}$ may be specified at slack nodes $i \in \mathcal{V}_s$. The relations $(\boldsymbol{p}_s)_i = (\sigma_1^2\boldsymbol{s}_i^{(1)} + \sigma_2^2\boldsymbol{s}_i^{(2)})$ and $\boldsymbol{\alpha}_i^{(m)} = \boldsymbol{s}_i^{(m)}/(\boldsymbol{s}_i^{(1)} + \boldsymbol{s}_i^{(2)})$ can then be used to determine the corresponding densities that will achieve the specified pressures and concentrations. Non-slack nodes are partitioned into injection nodes $\mathcal{V}_q \subset \mathcal{V}_d$ and withdrawal nodes $\mathcal{V}_w \subset \mathcal{V}_d$. We order the non-slack nodes

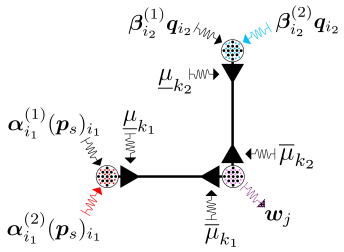

Figure 1. Configuration of the boundary conditions. Here, $j \in \mathcal{V}_w$, $k_1 : i_1 \mapsto j$ with $i_1 \in \mathcal{V}_s$, and $k_2 : i_2 \mapsto j$ with $i_2 \in \mathcal{V}_q$.

$\mathcal{V}_d$ with injection nodes enumerated before withdrawal nodes, so that $i < j$ for all $i \in \mathcal{V}_q$ and $j \in \mathcal{V}_w$. A mixture is withdrawn from the network at each withdrawal node $j \in \mathcal{V}_w$ with boundary conditions specified by mass outflow $\boldsymbol{w}_j \geq 0$. At each injection node $j \in \mathcal{V}_q$, a mixture is injected into the network with boundary conditions specified by both the mass inflow $\boldsymbol{q}_j$, with $\boldsymbol{q}_j \geq 0$, and the concentration $\boldsymbol{\beta}_j^{(m)}$. Although a mass inflow is specified at each injection node $j \in \mathcal{V}_q$ with concentration $\boldsymbol{\beta}_j^{(m)}$, this does not, in general, imply that the concentration flowing from node j into outgoing edges is equal to $\boldsymbol{\beta}_j^{(m)}$, because the nodal concentration is a mixture of flows entering node j either by injection or from incoming pipelines. Boundary condition designations are illustrated for a small example network in Fig. 1.

Individual density and concentration variables are unknown at non-slack nodes and are denoted by $\boldsymbol{\rho}_j^{(m)}$ and $\boldsymbol{\eta}_j^{(m)} = \boldsymbol{\rho}_j^{(m)}/(\boldsymbol{\rho}_j^{(1)} + \boldsymbol{\rho}_j^{(2)})$, respectively, for each $j \in \mathcal{V}_d$. All of the nodal quantities in this study are identified with bold symbols. Inlet and outlet edge variables are defined by attaching underlines below and overlines above the associated edge variables, respectively. For example, $\underline{\varphi}_k(t) = \varphi_k(t, 0)$ and $\overline{\varphi}_k(t) = \varphi_k(t, \ell_k)$. Define the cross-sectional area of edge $k \in \mathcal{E}$ by $\chi_k = \pi D_k^2/4$. The boundary conditions for the flow of the mixture are defined for $m = 1$ and $m = 2$ by

$$\underline{\varrho}_k^{(m)} = \underline{\mu}_k \boldsymbol{s}_i^{(m)}, \qquad \overline{\rho}_k^{(m)} = \overline{\mu}_k \boldsymbol{\rho}_j^{(m)}, \tag{5}$$

$$\underline{\rho}_k^{(m)} = \underline{\mu}_k \boldsymbol{\rho}_i^{(m)}, \qquad \overline{\rho}_k^{(m)} = \overline{\mu}_k \boldsymbol{\rho}_j^{(m)}, \tag{6}$$

$$\boldsymbol{\gamma}_j^{(m)} \boldsymbol{d}_j = \sum_{k \in_{\mapsto} j} \chi_k \overline{\eta}_k^{(m)} \overline{\varphi}_k - \sum_{k \in j_{\mapsto}} \chi_k \underline{\eta}_k^{(m)} \underline{\varphi}_k, \tag{7}$$

where Eq. (5) is defined for $k : i \mapsto j$ with $i \in \mathcal{V}_s$, Eq. (6) is defined for $k : i \mapsto j$ with $i, j \in \mathcal{V}_d$, and Eq. (7) is defined for $j \in \mathcal{V}_d$ with the condition that $\boldsymbol{\gamma}_j^{(m)} \boldsymbol{d}_j = \boldsymbol{\eta}_j^{(m)} \boldsymbol{w}_j$ if $j \in \mathcal{V}_w$ and $\boldsymbol{\gamma}_j^{(m)} \boldsymbol{d}_j = -\boldsymbol{\beta}_j^{(m)} \boldsymbol{q}_j$ if $j \in \mathcal{V}_q$. The initial condition of partial density is assumed to be a steady-state solution given for all $k \in \mathcal{E}$ and $x \in [0, \ell_k]$ by

$$\rho_k^{(m)}(0, x) = \varrho_k^{(m)}(x). \tag{8}$$

The steady-state solution is defined to be the time-invariant solution of the system in Eqs. (3)-(7) when the boundary condition profiles are time-invariant (i.e. equal to the initial values of the time-varying boundary profiles). More details on the initial condition for the discretized system are provided in the following section. Mass flux is not initially specified because it is uniquely determined from the density. We assume standard conditions for well-posedness [32], and specifically that the boundary conditions are smooth, slowly-varying, bounded in their respective domains, and compatible with the initial conditions to ensure the existence of a smooth, slowly-varying, bounded solution. The flow of the mixture of gases in the network is defined by the initial-boundary value system of PDEs defined by equations (3)-(8).

III. SPATIAL DISCRETIZATION

To analyze the system of PDEs (3)-(8) on the graph $(\mathcal{E}, \mathcal{V})$, we have developed a process of discretization, which includes a *refinement* of the graph, *approximation* of the PDE system by an ODE system using a finite volume approach, and a *reformulation* in terms of variable vectors and parameter matrices. The vectors include variables that represent the states and boundary parameters, and the matrices incorporate network model parameters, the incidence structure of the graph, and the control values.

Graph Refinement: A refinement $(\hat{\mathcal{E}}, \hat{\mathcal{V}})$ of the graph $(\mathcal{E}, \mathcal{V})$ is created by adding auxiliary nodes to $\mathcal{V}$ in order to subdivide the edges of $\mathcal{E}$ so that $\ell_k \leq \ell$ for all $k \in \hat{\mathcal{E}}$, where ℓ is sufficiently small [33]. Henceforth we assume that $\ell \leq 1$ km, and will use that threshold for computational studies as well. The refined graph inherits the prescribed orientation of the parent graph. Assuming sufficiently fine network refinement, the relative difference of the density variables of adjacent nodes in the solution to the IBVP (3)-(8) can be made arbitrarily small in magnitude because of continuity of the solution to the system given well-posed conditions [32]. We assume for all $k \in \hat{\mathcal{E}}$ that

$$\frac{\left|\overline{\rho}_k^{(m)} - \underline{\rho}_k^{(m)}\right|}{\underline{\rho}_k^{(m)}} < \epsilon, \qquad \frac{\left|\overline{\rho}_k^{(m)} - \underline{\rho}_k^{(m)}\right|}{\overline{\rho}_k^{(m)}} < \epsilon, \tag{9}$$

where $0 \leq \epsilon \ll 1$. The proofs that follow only require $\epsilon \leq 1$. We assume that the graph has been sufficiently refined to satisfy Eq. (9) and that the hats may be omitted moving forward.

Finite Volume Approximation: The system of ODEs is obtained by integrating the dynamic equations

in (3)-(4) along the length of each refined pipeline segment so that

$$\int_0^\ell \partial_t \rho^{(m)} dx = -\int_0^\ell \partial_x \left(\frac{\rho^{(m)}}{\rho^{(1)}+\rho^{(2)}} \varphi \right) dx,$$

$$\int_0^\ell \partial_x \left(\sigma_1^2 \rho^{(1)} + \sigma_2^2 \rho^{(2)} \right) dx = -\frac{\lambda}{2D} \int_0^\ell \frac{\varphi|\varphi|}{\rho^{(1)}+\rho^{(2)}} dx,$$

where edge subscripts have been removed for readability. The above integrals of space derivatives are evaluated using the fundamental theorem of calculus. The remaining integrals are evaluated by approximating pipeline density with outlet density and pipeline flux with inlet flux. These approximations are independent of x and may be factored out of the integrals. The above equations become

$$\ell \dot{\overline{\rho}}^{(m)} = \underline{\eta}^{(m)} \underline{\varphi} - \overline{\eta}^{(m)} \overline{\varphi}, \tag{10}$$

$$\sum_{n=1}^{2} \sigma_n^2 \left(\overline{\rho}^{(n)} - \underline{\rho}^{(n)} \right) = -\frac{\lambda \ell}{2D} \frac{\underline{\varphi} \left| \underline{\varphi} \right|}{\overline{\rho}^{(1)} + \overline{\rho}^{(2)}}, \tag{11}$$

where a dot above a variable represents the time-derivative of the variable.

Matrix Form: We now write the discretized system in matrix-vector form. Define $E \times E$ diagonal matrices L and X with diagonal entries $L_{kk} = \ell_k$ and $X_{kk} = \chi_k$. Define the time-varying (transposed) incidence matrix M of size $E \times V$ componentwise by

$$M_{kj} = \begin{cases} \overline{\mu}_k(t), & \text{edge } k \in_{\mapsto} j \text{ enters node } j, \\ -\underline{\mu}_k(t), & \text{edge } k \in j_{\mapsto} \text{ leaves node } j, \\ 0, & \text{else.} \end{cases} \tag{12}$$

Define the $E \times V_s$ submatrix M_s of M by the removal of columns $i \in \mathcal{V}_d$, the $E \times (V - V_s)$ submatrix M_d of M by the removal of columns $i \in \mathcal{V}_s$, and the positive and negative parts of M_d by $\overline{M}_d$ and $\underline{M}_d$ so that $M_d = (\overline{M}_d + \underline{M}_d)/2$ and $|M_d| = (\overline{M}_d - \underline{M}_d)/2$, where V_s denotes the number of slack nodes and $|A|$ denotes the componentwise absolute value of a matrix A. Define the signed matrices Q_d =sign(M_d), $\overline{Q}_d$ =sign($\overline{M}_d$), $\underline{Q}_d$ =sign($\underline{M}_d$), and similarly for M_s. These signed matrices are well-defined by the lower-bound constraints on compression and regulation. Define the $V_d \times V_d$ identity matrix I, the $V_d \times V_q$ submatrix I_q of I by the removal of columns $j \in \mathcal{V}_w$, and the $V_d \times V_d$ matrix I_w by replacing columns $j \in \mathcal{V}_q$ of I with the zero vector. Here, V_d and V_q denote the numbers of non-slack nodes and non-slack injection nodes, respectively.

Define inlet and outlet edge mass flux vectors by $\underline{\varphi} = (\underline{\varphi}_1, \ldots, \underline{\varphi}_E)^T$ and $\overline{\varphi} = (\overline{\varphi}_1, \ldots, \overline{\varphi}_E)^T$, and similarly for inlet and outlet edge concentrations $\underline{\eta}$ and $\overline{\eta}$. Moreover, define the vectors $\boldsymbol{\rho}^{(m)} = (\boldsymbol{\rho}^{(m)}_{V_s+1}, \ldots, \boldsymbol{\rho}^{(m)}_{V_d})^T$, $\boldsymbol{\alpha}^{(m)} = (\boldsymbol{\alpha}^{(m)}_1, \ldots, \boldsymbol{\alpha}^{(m)}_{V_s})^T$, and $\boldsymbol{\beta}^{(m)} = (\boldsymbol{\beta}^{(m)}_{V_s+1}, \ldots, \boldsymbol{\beta}^{(m)}_{V_q})^T$, where the subscripts of the vector components are indexed according to the node labels in $\mathcal{V}$. Similarly, define the vectors $\boldsymbol{\eta}^{(m)} = (\boldsymbol{\eta}^{(m)}_{V_s+1}, \ldots, \boldsymbol{\eta}^{(m)}_{V_d})^T$ and $\boldsymbol{d} = (\boldsymbol{d}_{V_s+1}, \ldots, \boldsymbol{d}_{V_d})^T$. Recall that the components of $\boldsymbol{d}$ are positive for those corresponding to non-slack withdrawal nodes and negative for non-slack injection nodes. Define the function $f : \mathbb{R}^E \times \mathbb{R}^E \to \mathbb{R}^E$ component-wise for $k \in \mathcal{E}$ by

$$f_k(y, z) = -\text{sign}(z_k) \Lambda_k \left| y_k z_k \right|^{1/2}, \tag{13}$$

where $\Lambda_k = \sqrt{2D_k/(\lambda_k \ell_k)}$. This function is used to express $\underline{\varphi}$ in Eq. (11) in terms of density and its spatial derivative so that we may eliminate flux from the dynamic equations. Using the function in Eq. (13), the discretized flow in Eqs. (10)-(11) together with the boundary conditions in Eqs. (5)-(7) may be expressed in matrix-vector form as

$$L \overline{M}_d \dot{\boldsymbol{\rho}}^{(m)} = \underline{\eta}^{(m)} \odot F - \overline{\eta}^{(m)} \odot \overline{\varphi}, \tag{14}$$

$$\boldsymbol{\gamma}^{(m)} \odot \boldsymbol{d} = \overline{Q}_d^T X \left(\overline{\eta}^{(m)} \odot \overline{\varphi} \right) + \underline{Q}_d^T X \left(\underline{\eta}^{(m)} \odot F \right), \tag{15}$$

where $\odot$ is the Hadamard product and

$$F = f\ \left(\overline{M}_d (\boldsymbol{\rho}^{(1)} + \boldsymbol{\rho}^{(2)}), \sum_m \sigma_m^2 (M_s \boldsymbol{s}^{(m)} + M_d \boldsymbol{\rho}^{(m)}) \right). \tag{16}$$

It is assumed that regulators vary slowly so that the time derivative of $\overline{M}_d$ is insignificant, justifying its removal from Eq. (10). Multiplying both sides of Eq. (10) on the left by $\overline{Q}_d^T X$ and using Eq. (11), we may combine Eq. (10) and Eq. (11) to form the equation $\overline{Q}_d^T X L \overline{M}_d \dot{\boldsymbol{\rho}}^{(m)} = [Q_d^T X (\underline{\eta}^{(m)} \odot F) - \boldsymbol{\gamma}^{(m)} \odot \boldsymbol{d}]$, where we have used $Q_d = (\underline{Q}_d + \overline{Q}_d)$. By writing edge concentrations in terms of nodal concentrations, and nodal concentrations in terms of concentrations of flows into the nodes, the system in Eqs. (10)-(11) may be written for $m = 1, 2$ as

$$R \dot{\boldsymbol{\rho}}^{(m)} = Q_d^T X \left(\left(|\underline{Q}_s| \boldsymbol{\alpha}^{(m)} + |\underline{Q}_d| \boldsymbol{\eta}^{(m)} \right) \odot F \right) - \left(I_q \boldsymbol{\beta}^{(m)} + I_w \boldsymbol{\eta}^{(m)} \right) \odot \boldsymbol{d}, \tag{17}$$

where $R = \overline{Q}_d^T X L \overline{M}_d$. The system in Eq. (17) will be called the partial density system of ODEs. Each row k of $\overline{M}_d$ contains exactly one nonzero component given by $\overline{M}_{kj} = \overline{\mu}_k$ for $k \in_{\mapsto} j$. Using the additional fact that X and L are diagonal, it can be shown that the mass matrix R on the left-hand-side of Eq. (17) is diagonal with positive diagonal components given by $\boldsymbol{r}_j = \sum_{k \in_{\mapsto} j} \chi_k \ell_k \overline{\mu}_k$ for $j \in \mathcal{V}_d$. Therefore, the matrix R may readily be inverted to obtain a nonlinear control system in the usual, although complicated, ODE form. The initial condition in Eq. (8), sampled at the refined nodes of the network, is the time-invariant solution of the system in Eq. (17) with $\boldsymbol{d} = \boldsymbol{d}(0)$, $\boldsymbol{\alpha}^{(m)} = \boldsymbol{\alpha}^{(m)}(0)$, and $\boldsymbol{\beta}^{(m)} = \boldsymbol{\beta}^{(m)}(0)$. We assume that this steady-state solution is the initial condition of the partial density system.

IV. EQUIVALENT SYSTEMS

The system in Eq. (17) is expressed in terms of partial densities at non-slack nodes. Equivalent systems expressed in terms of other variables of interest may be derived from Eq. (17) using appropriate transformations. One such transformation has been performed in the continuous case going from Eqs. (2a)-(2c) to Eqs. (3)-(4). In fact, such transformations exist even for pure natural gas systems. For example, the equations of natural gas flow may be expressed in terms of pressure and velocity, in terms of density and mass flux, or in terms of their dimensionless quantities. Define vectors $\boldsymbol{\rho}$, $\boldsymbol{p}$, $\boldsymbol{\nu}^{(m)}$, and $\boldsymbol{E}$ of nodal values for density, pressure, volumetric concentration, and energy, respectively, at non-slack nodes by

$$\boldsymbol{\rho} = \boldsymbol{\rho}^{(1)} + \boldsymbol{\rho}^{(2)}, \tag{18}$$

$$\boldsymbol{p} = \sigma_1^2 \boldsymbol{\rho}^{(1)} + \sigma_2^2 \boldsymbol{\rho}^{(2)}, \tag{19}$$

$$\boldsymbol{\nu}^{(m)} = \frac{\sigma_m^2 \boldsymbol{\rho}^{(m)}}{\sigma_1^2 \boldsymbol{\rho}^{(1)} + \sigma_2^2 \boldsymbol{\rho}^{(2)}}, \tag{20}$$

$$\boldsymbol{E} = (|\overline{Q}_d^T| X \underline{\varphi}) \odot \left(r^{(1)} \boldsymbol{\eta}^{(1)} + r^{(2)} \boldsymbol{\eta}^{(2)} \right), \tag{21}$$

where $r^{(1)} = 44.2$ (MJ/kg) and $r^{(2)} = 141.8$ (MJ/kg). Equivalent systems may be expressed in terms of any two vector variables from the set $\{\boldsymbol{\rho}^{(m)}, \boldsymbol{\eta}^{(m)}, \boldsymbol{\nu}^{(m)}, \boldsymbol{\rho}, \boldsymbol{p}, \boldsymbol{E}\}$, excluding pairs from the subset $\{\boldsymbol{\eta}^{(1)}, \boldsymbol{\eta}^{(2)}, \boldsymbol{\nu}^{(1)}, \boldsymbol{\nu}^{(2)}\}$ because variables in the latter subset would reduce to constant vectors in the case of homogeneous mixtures. The choice of which equivalent system to use may depend on the sought application, although some systems have better conditioning with fewer nonlinear operations than others. Define (potentially time-varying) generalized sound speeds $\boldsymbol{a} = (\sigma_1^2 \boldsymbol{\alpha}^{(1)} + \alpha_2^2 \boldsymbol{\alpha}^{(2)})^{1/2}$ and $\boldsymbol{b} = (\sigma_1^2 \boldsymbol{\beta}^{(1)} + \sigma_2^2 \boldsymbol{\beta}^{(2)})^{1/2}$, where the square-root is applied component-wise. The transformation from partial densities to *total density and pressure* is obtained by superimposing Eq. (17) for $m = 1, 2$ to obtain an equation for $\dot{\boldsymbol{\rho}}$ and linearly combining Eq. (17) for $m = 1, 2$ with coefficients σ_1^2 and σ_2^2 to obtain an equation for $\dot{\boldsymbol{p}}$. This transformation is linear, invertible, and produces the equations

$$R\dot{\boldsymbol{\rho}} = Q_d^T X F - \boldsymbol{d}, \tag{22}$$

$$R\dot{\boldsymbol{p}} = Q_d^T X \left(\left(|\underline{Q}_s| \boldsymbol{a}^2 + |\underline{Q}_d| \frac{\boldsymbol{p}}{\boldsymbol{\rho}} \right) \odot F \right) - \left(I_q \boldsymbol{b}^2 + I_w \frac{\boldsymbol{p}}{\boldsymbol{\rho}} \right) \odot \boldsymbol{d}, \tag{23}$$

where $F = f(\overline{M}_d \boldsymbol{\rho}, M_s \boldsymbol{p}_s + M_d \boldsymbol{p})$. The system in Eqs. (22)-(23) will be called the total density and pressure system of ODEs. We do not derive other equivalent systems. Instead, we compute the solution of the partial density system of ODEs numerically, and, thereafter, obtain the other variables of interest by subsequently applying the appropriate transformations.

If $\boldsymbol{\eta}^{(m)}$ is a constant vector, then the system of total density and pressure decouples into two isolated subsystems that are equivalent to one another because, for constant concentration, $\boldsymbol{p} = \boldsymbol{c}^2 \odot \boldsymbol{\rho}$, where $\boldsymbol{c} = (\sigma_1^2 \boldsymbol{\eta}^{(1)} + \sigma_2^2 \boldsymbol{\eta}^{(2)})^{1/2}$ is a constant vector. In particular, the total density and pressure system in Eqs. (22)-(23) reduces by half its dimension to the isolated system

$$R\dot{\boldsymbol{p}} = Q_d^T X \left(\left(|\underline{Q}_s| \boldsymbol{a}^2 + |\underline{Q}_d| \boldsymbol{c}^2 \right) \odot f\left(\overline{M}_d \frac{\boldsymbol{p}}{\boldsymbol{c}^2}, M_s \boldsymbol{p}_s + M_d \boldsymbol{p} \right) \right) - \left(I_q \boldsymbol{b}^2 + I_w \boldsymbol{c}^2 \right) \odot \boldsymbol{d}. \tag{24}$$

The system in Eq. (24) is called the isolated total pressure system of ODEs. Equivalent isolated subsystems expressed in terms of one vector variable from the set $\{\boldsymbol{\rho}^{(m)}, \boldsymbol{\rho}, \boldsymbol{E}\}$ may be derived. Each isolated subsystem is applicable if and only if the concentration vector $\boldsymbol{\eta}^{(m)}$ is constant. Rigorous definitions and proofs of conditions on $\boldsymbol{\alpha}^{(m)}$, $\boldsymbol{\beta}^{(m)}$, $\boldsymbol{q}$, and $\boldsymbol{w}$ that would result in $\boldsymbol{\eta}^{(m)}$ being constant are outside the scope of this study.

V. MONOTONICITY

The monotonicity of solutions to flows of a homogeneous gas through an actuated transport network was examined as a means to reduce the complexity of optimization and optimal control of natural gas networks in the presence of uncertainty [8]. Here, we examine how such concepts can be extended to the transport of inhomogeneous gas mixtures, and specifically to characterize the extent and variability of hydrogen blending into a natural gas pipeline that is acceptable. We first present some analytical results before proceeding with numerical simulations in the next section.

A nonlinear input-to-state initial-value system of ODEs may be generally expressed as

$$\dot{x} = g(x, u, d), \qquad x(0) = y, \tag{25}$$

where $x(t) \in \mathcal{X} \subset \mathbb{R}^n$ is the state vector, $u(t) \in \mathcal{U} \subset \mathbb{R}^m$ is the control input vector, and $d(t) \in \mathcal{D} \subset \mathbb{R}^r$ is the parameter input vector defined for $t \in [0, T]$. It is assumed that the subsets $\mathcal{X}$, $\mathcal{U}$, and $\mathcal{D}$ are compact and convex and that the function $g : \mathcal{X} \times \mathcal{U} \times \mathcal{D} \to \mathcal{X}$ is Lipschitz in $\mathcal{X} \times \mathcal{U} \times \mathcal{D}$.

Definitions: Suppose that two independent state solutions $\{x_1(t), x_2(t)\} \subset \mathcal{X}$ exist (and are thus unique because g is Lipschitz) with initial conditions $\{y_1, y_2\} \subset \mathcal{X}$, and which correspond to the piecewise-continuous control inputs $\{u_1(t), u_2(t)\} \subset \mathcal{U}$ and piecewise-continuous parameter inputs $\{d_1(t), d_2(t)\} \subset \mathcal{D}$ for $t \in [0, T]$. For the given set of control inputs, the system (25) is said to be *monotone-ordered* with respect to $d(t)$ if $x_1(t) \leq x_2(t)$ for $t \in [0, T]$ whenever $y_1 \leq y_2$ and $d_1(t) \leq d_2(t)$, where inequalities for vectors are taken componentwise. In this case, the solution states x_1 and x_2 are said to

be *monotone-ordered*. For simplicity, we say that a monotone-ordered system and a set of monotone-ordered solutions are *monotone*, *monotonic*, and have the property of *monotonicity*. An $n \times n$ matrix A is called *Metzler* if all of its off-diagonal elements are non-negative, i.e. $A_{ij} \geq 0$ for all $i \neq j$. An $n \times m$ matrix is called *non-negative* if all of its entries are non-negative.

Theorem 1 (Monotonicity) [34, 35]: The nonlinear system in Eq. (25) is monotone if and only if the Jacobian matrices $\partial g/\partial x$ and $\partial g/\partial d$ are, respectively, Metzler and non-negative almost everywhere in $\mathcal{X} \times \mathcal{U} \times \mathcal{D}$.

A. Homogeneous Concentration

The equivalent systems described in Section IV are first reformulated in terms of the monotone system definitions above. In steady-state [8], the pressure $\boldsymbol{p}$ increases componentwise with *decreasing* withdrawal $\boldsymbol{w} \geq 0$ and with *increasing* injection $-\boldsymbol{q} \leq 0$. In reference to Eq. (25), we assume that all non-slack nodes are injection nodes and define the input parameter by $d = \{\boldsymbol{p}_s, \boldsymbol{d}\} = \{\boldsymbol{p}_s, -\boldsymbol{q}\}$.

Proposition 1 (Monotonicity of Total Pressure and Density): Assume that i) all non-slack nodes are injection nodes; ii) gas flows only in the positive direction through each edge according to its orientation in the network graph; iii) pressure is positive in each node; and iv) Eq. (9) is satisfied. Suppose that the concentration vector $\boldsymbol{\eta}^{(2)}$ is constant and that there exist two state solutions $\boldsymbol{p}_1$, $\boldsymbol{p}_2$ of the system in Eq. (24) with respective initial conditions $\boldsymbol{\pi}_1$, $\boldsymbol{\pi}_2$, slack pressures $(\boldsymbol{p}_s)_1$, $(\boldsymbol{p}_s)_2$, and non-slack injection flows $\boldsymbol{q}_1$, $\boldsymbol{q}_2$ for a given fixed set of control inputs $\{\underline{\mu}, \overline{\mu}\}$. Here, the vector subscripts denote the first and second solutions and not the refined nodes. If $\boldsymbol{\pi}_1 \leq \boldsymbol{\pi}_2$, $(\boldsymbol{p}_s)_1(t) \leq (\boldsymbol{p}_s)_2(t)$, and $\boldsymbol{q}_1(t) \geq \boldsymbol{q}_2(t)$ componentwise for all $t \in [0, T]$, then $\boldsymbol{p}_1(t) \leq \boldsymbol{p}_2(t)$. Consequently, $\boldsymbol{\rho}_1(t) \leq \boldsymbol{\rho}_2(t)$, where $\boldsymbol{\rho}_1$ and $\boldsymbol{\rho}_2$ are the total densities of the two solutions.

Proof: Throughout this proof, the state and input subscripts correspond to the nodes of the refined graph. Because flow is in the positive oriented direction, it follows from Eq. (4) that $\underline{\mu}_k \boldsymbol{p}_i(t) > \overline{\mu}_k \boldsymbol{p}_j(t)$ for all $i, j \in \mathcal{V}$ with $k : i \mapsto j$. Thus, the sign and absolute value operations in Eq. (13) are unnecessary. The j-th state dynamics in Eq. (24) for $j \in \mathcal{V}_d$ may be written as

$$\begin{aligned} \boldsymbol{r}_j \dot{\boldsymbol{p}}_j = &\sum_{k:i\mapsto j} \frac{\boldsymbol{\sigma}_i^2 \chi_k \Lambda_k}{\boldsymbol{c}_j} \left(\overline{\mu}_k \boldsymbol{p}_j \left(\underline{\mu}_k \boldsymbol{p}_i - \overline{\mu}_k \boldsymbol{p}_j\right)\right)^{1/2} \\ &- \sum_{k:j\mapsto i} \frac{\boldsymbol{c}_j^2 \chi_k \Lambda_k}{\boldsymbol{c}_i} \left(\overline{\mu}_k \boldsymbol{p}_i \left(\underline{\mu}_k \boldsymbol{p}_j - \overline{\mu}_k \boldsymbol{p}_i\right)\right)^{1/2} \\ &+ \boldsymbol{b}_j^2 \boldsymbol{q}_j, \end{aligned} \tag{26}$$

where $\boldsymbol{p}_i = (\boldsymbol{p}_s)_i$ and $\boldsymbol{\sigma}_i^2 = \boldsymbol{a}_i^2$ if $i \in \mathcal{V}_s$, whereas $\boldsymbol{\sigma}_i^2 = \boldsymbol{c}_i^2$ if $i \in \mathcal{V}_d$. It is clear from this expanded form that the function on the right-hand-side of Eq. (24) is continuously differentiable (hence Lipschitz) in the state and input variables over the domain of positive flow and pressure. In reference to Theorem 1, we first show that the state Jacobian matrix is Metzler, i.e., $\partial \dot{\boldsymbol{p}}_j / \partial \boldsymbol{p}_i$ is non-negative for all $i, j \in \mathcal{V}_d$ with $i \neq j$. If i and j are non-adjacent with $i \neq j$, then clearly $\partial \dot{\boldsymbol{p}}_j / \partial \boldsymbol{p}_i = 0$. Suppose that i and j are adjacent with $k : j \mapsto i$. Substituting Eqs. (5)-(6) into Eq. (9) and using the relation between pressure and partial densities, it can be shown that $(\overline{\mu}_k \boldsymbol{p}_i - \underline{\mu}_k \boldsymbol{p}_j) > -\overline{\mu}_k \boldsymbol{p}_i$. Thus, the Jacobian component

$$\frac{\partial \dot{\boldsymbol{p}}_j}{\partial \boldsymbol{p}_i} = \frac{\boldsymbol{c}_j^2 \chi_k \Lambda_k \overline{\mu}_k (2\overline{\mu}_k \boldsymbol{p}_i - \underline{\mu}_k \boldsymbol{p}_j)}{2\boldsymbol{r}_j \boldsymbol{c}_i (\overline{\mu}_k \boldsymbol{p}_i (\underline{\mu}_k \boldsymbol{p}_j - \overline{\mu}_k \boldsymbol{p}_i))^{1/2}} \tag{27}$$

is positive. Suppose that i and j are adjacent with $k : i \mapsto j$. Then

$$\frac{\partial \dot{\boldsymbol{p}}_j}{\partial \boldsymbol{p}_i} = \frac{\boldsymbol{\sigma}_i^2 \chi_k \Lambda_k \underline{\mu}_k \overline{\mu}_k \boldsymbol{p}_j}{2\boldsymbol{r}_j \boldsymbol{c}_j (\overline{\mu}_k \boldsymbol{p}_j (\underline{\mu}_k \boldsymbol{p}_i - \overline{\mu}_k \boldsymbol{p}_j))^{1/2}} > 0. \tag{28}$$

Because $j \in \mathcal{V}_d$ is arbitrary, it follows that the state Jacobian matrix is Metzler. We now show that the parameter Jacobian matrix is non-negative. The above computation can be extended to show that $\partial \dot{\boldsymbol{p}}_j / \partial (\boldsymbol{p}_s)_i$ is non-negative for $i \in \mathcal{V}_s$. With respect to mass inflow parameters, the Jacobian components $\partial \dot{\boldsymbol{p}}_j / \partial \boldsymbol{q}_i = \boldsymbol{b}_j^2 / \boldsymbol{r}_j \delta_{i,j}$ are non-negative ($\delta_{i,j}$ is the Kronecker delta). We conclude from Theorem 1 that the system in Eq. (24) is monotone. Because $\boldsymbol{p}_j = \boldsymbol{c}_j^2 \boldsymbol{\rho}_j$ for $j \in \mathcal{V}_d$, it follows that the isolated total density system is monotone as well. □

Corollary 1 (Monotonicity of Equivalent Systems): Assume that the conditions hold from Proposition 1. Then $\boldsymbol{\rho}_1^{(m)}(t) \leq \boldsymbol{\rho}_2^{(m)}(t)$ componentwise for all $t \in [0, T]$, where $\boldsymbol{\rho}_1^{(m)}$ and $\boldsymbol{\rho}_2^{(m)}$ are the partial densities of the two solutions.

Proof: The mass fraction $\boldsymbol{\eta}^{(m)}$ is constant, therefore it follows from Proposition 1 that $\boldsymbol{\rho}_1^{(m)} = \boldsymbol{\eta}^{(m)} \odot \boldsymbol{\rho}_1 \leq \boldsymbol{\eta}^{(m)} \odot \boldsymbol{\rho}_2 = \boldsymbol{\rho}_2^{(m)}$. □

B. Heterogeneous Concentration

Proposition 2 (Non-Monotonicity of Total Pressure and Density): Assume that i) all non-slack nodes are injection nodes; ii) gas flows only in the positive direction through each edge according to its orientation in the network graph; and iii) pressure and density are positive in each node. Suppose that, for a given fixed set of control inputs $\{\underline{\mu}, \overline{\mu}\}$, there exist two state solutions $(\boldsymbol{\rho}, \boldsymbol{p})_1$, $(\boldsymbol{\rho}, \boldsymbol{p})_2$ of the system in Eqs. (22)-(23) with respective initial conditions $(\boldsymbol{\varrho}, \boldsymbol{\pi})_1$, $(\boldsymbol{\varrho}, \boldsymbol{\pi})_2$, slack inputs $(\boldsymbol{\rho}_s, \boldsymbol{p}_s)_1$, $(\boldsymbol{\rho}_s, \boldsymbol{p}_s)_2$, and non-slack mass inflows $\boldsymbol{q}_1$, $\boldsymbol{q}_2$ that satisfy $(\boldsymbol{\varrho}, \boldsymbol{\pi})_1 \leq (\boldsymbol{\varrho}, \boldsymbol{\pi})_2$, $(\boldsymbol{\rho}_s(t), \boldsymbol{p}_s(t))_1 \leq (\boldsymbol{\rho}_s(t), \boldsymbol{p}_s(t))_2$, and $\boldsymbol{q}_1(t) \geq \boldsymbol{q}_2(t)$ componentwise for all $t \in [0, T]$. If $\boldsymbol{\eta}^{(m)}(t)$ is time-varying, then, in general, $(\boldsymbol{\rho}(t), \boldsymbol{p}(t))_1 \not\leq (\boldsymbol{\rho}(t), \boldsymbol{p}(t))_2$ component-wise for all $t \in [0, T]$.

Proof: Throughout this proof, the state and input subscripts correspond to the nodes of the refined graph.

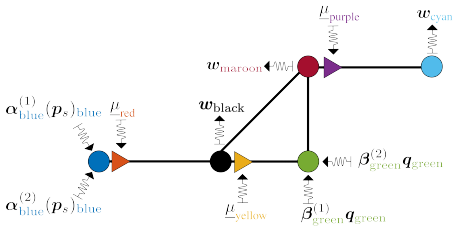

Figure 2. Network configuration (not to scale). The triangles represent compressor stations. Pipeline dimensions between nodes: blue to black (20 km), black to green (70 km), green to maroon (10 km), black to maroon (60 km), maroon to cyan (80 km). The pipelines have uniform diameter (0.9144 m) and friction factor (0.01), except for the black to maroon pipeline that has diameter (0.635 m) and friction factor (0.015).

From Theorem 1, it suffices to show that one component of the state Jacobian matrix is negative. The j-th nodal pressure dynamics in Eq. (23) may be written as

$$\begin{aligned}\boldsymbol{r}_j\dot{\boldsymbol{p}}_j = &\sum_{k:i\mapsto j}\boldsymbol{\sigma}_i^2\chi_k\Lambda_k\left(\overline{\mu}_k\boldsymbol{\rho}_j\left(\underline{\mu}_k\boldsymbol{p}_i-\overline{\mu}_k\boldsymbol{p}_j\right)\right)^{1/2}\\ &-\sum_{k:j\mapsto i}\frac{\boldsymbol{p}_j}{\boldsymbol{\rho}_j}\chi_k\Lambda_k\left(\overline{\mu}_k\boldsymbol{\rho}_i\left(\underline{\mu}_k\boldsymbol{p}_j-\overline{\mu}_k\boldsymbol{p}_i\right)\right)^{1/2}\\ &+\boldsymbol{b}_j^2\boldsymbol{q}_j,\end{aligned}\tag{29}$$

where $\boldsymbol{p}_i = (\boldsymbol{p}_s)_i$, $\boldsymbol{\rho}_i = (\boldsymbol{\rho}_s)_i$, and $\boldsymbol{\sigma}_i^2 = \boldsymbol{a}_i^2$ if $i \in \mathcal{V}_s$, and $\boldsymbol{\sigma}_i^2 = \boldsymbol{p}_i/\boldsymbol{\rho}_i$ if $i \in \mathcal{V}_d$. By adding a refined edge to the graph if necessary, we assume that there is an edge $k' : i' \mapsto j$ with $i' \in \mathcal{V}_d$. The Jacobian component corresponding to $\boldsymbol{\rho}_{i'}$ is given by

$$\frac{\partial\dot{\boldsymbol{p}}_j}{\partial\boldsymbol{\rho}_{i'}} = -\frac{\chi_{k'}\Lambda_{k'}}{\boldsymbol{r}_j}\frac{\boldsymbol{p}_{i'}}{\boldsymbol{\rho}_{i'}^2}\left(\overline{\mu}_{k'}\boldsymbol{\rho}_j\left(\underline{\mu}_{k'}\boldsymbol{p}_{i'}-\overline{\mu}_{k'}\boldsymbol{p}_j\right)\right)^{1/2},$$

which is negative. It follows from Theorem 1 that the system in Eqs. (22)-(23) is not monotone, regardlesss of Eq. (9). □

VI. NETWORK CASE STUDY

We use numerical simulations to examine how time-varying heterogeneity of a transported mixture affects flow dynamics throughout a network and compare equivalent system variables. The simulations are performed for a test network that was used in a previous study [28], in which the authors presented a staggered grid discretization method for the numerical solution of homogeneous natural gas pipeline flow. We refer the reader to the Appendix in which we show the results of our implementation of the IBVP posed in the former study in order to verify that we obtain the same solution when no hydrogen is present. The configuration and dimensions of the network are shown in Fig. 2. The dark blue node is a slack node at which pressure and concentration are specified, the black, maroon, and cyan nodes are non-slack withdrawal nodes, and the green node is a non-slack injection node. The sound speeds are chosen to be $\sigma_1 = 377$ (m/s) and $\sigma_2 = 2.8\sigma_1$. We simulate several examples to illustrate that some physical quantities may exhibit fewer crossings than others in certain operating regimes, given ordered boundary parameters. These examples provide insight into which equivalent system may be more useful for a particular operating regime. Figs. 3-7 show the solutions of five different examples. Two solutions corresponding to monotone-ordered boundary conditions are simulated for each example. We now describe the simulation results for each example.

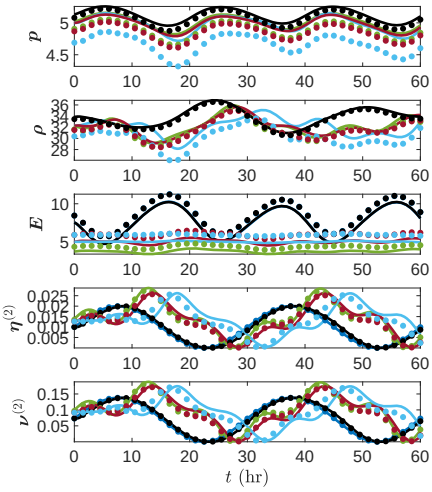

Figure 3. Two solutions (solid lines vs. dots) at the color-coordinated network nodes in Fig. 2. From top to bottom, the depicted nodal solutions are total pressure (MPa), total density (kg/m^3), total energy (GJ/s), concentration by mass, and concentration by volume. The boundary conditions for both solutions are $(\boldsymbol{p}_s)_{\text{blue}} = 5$ MPa, $\boldsymbol{\alpha}^{(2)}_{\text{blue}}(t) = 0.01(1 + \sin(4\pi t/T))$, $\boldsymbol{\beta}^{(2)}_{\text{green}}(t) = 0.125(1+\sin(12\pi t/T))$, $\boldsymbol{q}_{\text{green}}(t) = 3$ (kg/s), $\boldsymbol{w}_{\text{black}}(t) = 60(1 - \sin(6\pi t/T))$ (kg/s), $\mu_{\text{red}} = 1.0678$, $\underline{\mu}_{\text{yellow}} = 1.0140$, and $\underline{\mu}_{\text{purple}} = 1.0734$, where $T = 60$ hrs. The boundary condition that differs between the two solutions is $\boldsymbol{w}_{\text{cyan}}(t) = 110$ (kg/s) (solid lines) and $\boldsymbol{w}_{\text{cyan}}(t) = 130$ (kg/s) (dots).

In Fig. 3, total pressure, density, and energy solutions at the non-slack nodes do not overlap, but the mass and volumetric concentrations do overlap. The solutions in Fig. 4 have the same boundary conditions as those in

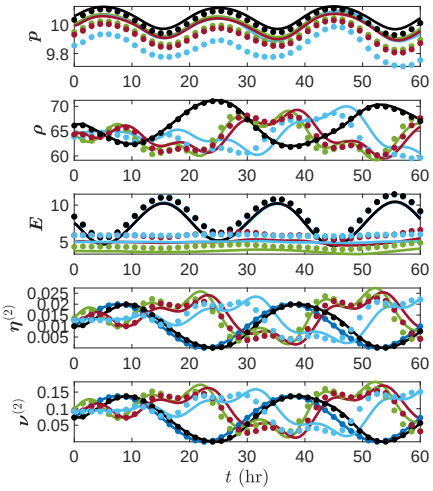

Figure 4. Same boundary conditions as in Fig. 3 except for $(\boldsymbol{p}_s)_{\text{blue}} = 10$ (MPa).

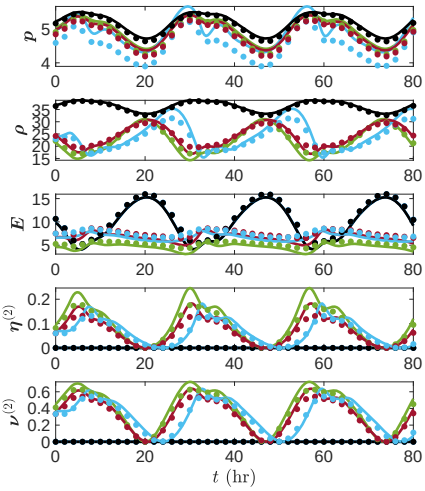

Figure 5. The boundary conditions for the two solutions are $(\boldsymbol{p}_s)_{\text{blue}} = 5$ (MPa), $\boldsymbol{\alpha}^{(2)}_{\text{blue}}(t) = 0$, $\boldsymbol{\beta}^{(2)}_{\text{green}}(t) = 1$, $\boldsymbol{q}_{\text{green}}(t) = 9(1 + \sin(6\pi t/T))$ (kg/s), $\boldsymbol{w}_{\text{black}}(t) = 100(1 - \sin(6\pi t/T))$ (kg/s), $\mu_{\text{red}} = 1.1096$, $\mu_{\text{yellow}} = 1.0057$, and $\mu_{\text{purple}} = 1.1301$, where $T = 80$ hrs. The other boundary condition is $\boldsymbol{w}_{\text{cyan}}(t) = 130$ (kg/s) (solid lines) and $\boldsymbol{w}_{\text{cyan}}(t) = 150$ (kg/s) (dots).

Fig. 3 except for the supply pressure. By doubling the supply pressure, the total density now overlaps at each non-slack node but the pressure and energy still do not overlap. In Figs. 5 and 6, the blue node injects pure natural gas and the green node injects pure hydrogen with a varying mass inflow profile. As seen in Fig. 5, the pressure and energy solutions at each node do not overlap. However, a close examination shows that the density solutions do overlap at every node upstream from the point of hydrogen injection. The concentration solutions overlap at only the cyan node. In Fig. 6, the supply pressure is increased to double the supply pressure in Fig. 5, but all other boundary conditions remain the same. This increase in supply pressure forces the pressure, density, and energy solutions to overlap at all of the non-slack nodes. The concentrations overlap at every node upstream the node of hydrogen injection. At nodes downstream the injection of hydrogen, the concentration of hydrogen is zero, as it ought to be. The solutions in Figs. 5 and 6 may not be realistic in the current operation of natural gas pipelines because the concentration of hydrogen reaches very high levels. However, these figures indicate that the solutions may behave erratically if the pipelines are manufactured to deliver significant amounts of hydrogen. In particular, all of the solution variables show large gradient surges in small time intervals.

The simulation in Fig. 7 demonstrates that pressure, density, and energy solutions may overlap even if the concentration solutions do not, where density overlaps only upstream the point of hydrogen injection. The difference between the solid line and dotted solutions in Fig. 7 is that the solid line represents the solution of pure natural gas and the other solution has a small injection of hydrogen at the green non-slack node. The concentration variables between the two solutions cannot overlap in this case because one of the examples corresponds to zero hydrogen concentration.

The five edges of the network are discretized into 240 refined edges with $\ell_k = 1$ (km) for all $k \in \hat{\mathcal{E}}$. Although one kilometer is sufficiently fine to demonstrate non-monotonicity for slowly-varying concentrations, a much smaller discretization size is required to accurately simulate rapidly-varying concentrations. We note that even the slowly-varying solutions in Figs. 3-7 show noticeable convergence as the discretization size is decreased from 1 (km) to 100 (m). For small discretization lengths ($\ell_k \leq 100$ (m)), the overlap between the solutions in Figs. 3-7 may be more pronounced.

VII. PHASE INTERFACES

Proposition 2 shows that the total pressure and density system of ODEs is not monotone-ordered over the

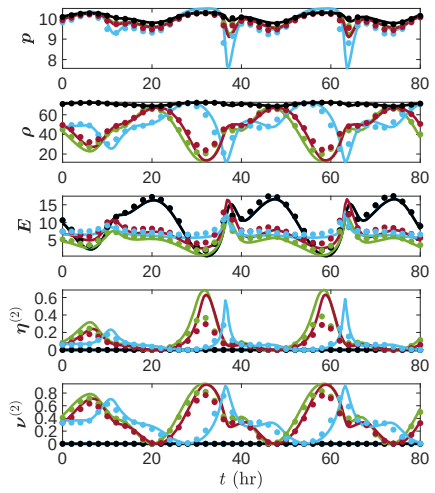

Figure 6. Same boundary conditions as in Fig. 5 except for $(\boldsymbol{p}_s)_{\text{blue}} = 10$ (MPa).

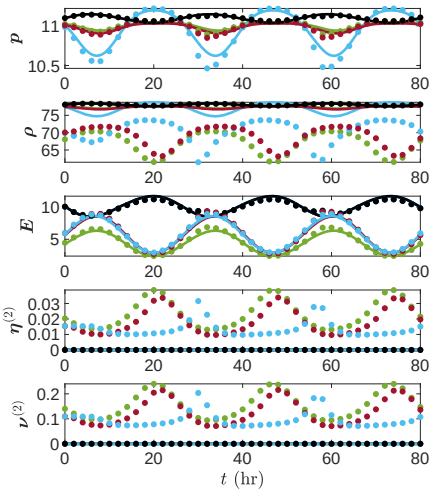

Figure 7. The boundary conditions for the two solutions are $(\boldsymbol{p}_s)_{\text{blue}} = 11$ (MPa), $\boldsymbol{\alpha}^{(2)}_{\text{blue}}(t) = 0$, $\boldsymbol{\beta}^{(2)}_{\text{green}}(t) = 1$, $\boldsymbol{w}_{\text{black}}(t) = 100(1-\sin(6\pi t/T))$ (kg/s), $\boldsymbol{w}_{\text{cyan}}(t) = 130(1+0.5\sin(6\pi t/T))$ (kg/s), $\mu_{\text{red}} = 1.0240$, $\underline{\mu}_{\text{yellow}} = 1.0029$, and $\underline{\mu}_{\text{purple}} = 1.0199$, where $T = 80$ hrs. The other boundary condition is $\boldsymbol{q}_{\text{green}}(t) = 0$ (kg/s) (solid lines) and $\boldsymbol{q}_{\text{green}}(t) = 2$ (kg/s) (dots).

entire input region $\mathcal{D} = (\boldsymbol{p}_s, -\boldsymbol{q}, \boldsymbol{\alpha}^{(m)}, \boldsymbol{\beta}^{(m)})$. However, by Proposition 1, its Corollary, and the continuity of solutions with respect to initial conditions and inputs [36], for a given set of plant parameters, the non-isolated total pressure and density system of ODEs is expected to be monotone-ordered over a certain sub-region $\mathcal{D}_0 \subset \mathcal{D}$ that consists of concentration vectors that are uniformly close to a constant concentration vector. Moreover, again by continuity, monotonicity is expected to hold for slow variations in concentration with large amplitudes. This suggests that there may be a nontrivial monotonic interface (MI) that partitions the concentration boundary conditions (hence $\mathcal{D}$) into monotonic and non-monotonic phase regions for each equivalent system variable. We analyze the MI numerically for a single pipeline. The interface analysis presented in the following sections considers a single pipeline with concentration and pressure specified at the inlet of the pipeline (node 1) and with mass outflow specified at the outlet (node 2). The pipeline parameters and boundary conditions that do not change are $\ell = 50$ km, $D = 0.5$ m, $\lambda = 0.11$, and $\boldsymbol{p}_s = 7$ MPa. We denote the concentration of hydrogen at the inlet slack node by $\boldsymbol{\alpha}_1(t) = \boldsymbol{\alpha}^{(2)}_1(t)$ and specify it to be

$$\boldsymbol{\alpha}_1(t) = \alpha_1 \left(1 + \kappa \sin(2\pi\omega_* t)\right), \tag{30}$$

where κ is the amplitude factor of the sinusoid, ω_* is its frequency in cycles per hour, and α_1 is the mean concentration profile around which the sinusoid oscillates. Here, the subscript is with respect to the node number.

VIII. MONOTONIC INTERFACE

We consider the following question.

> *What is the interface (ω_*, κ_*) in the (ω_*, κ) plane below and above which the solution is monotonic and non-monotonic, respectively?*

The MI is computed for each flow variable using numerical simulations. In addition to the boundary conditions that are specified at the beginning of this section, this subsection uses $\sigma_1 = 377$ (m/s), $\sigma_2 = 2.8\sigma_1$, and $\alpha_1 = 0.02$. For each (ω_*, κ) in Eq. (30), we compute three solutions corresponding to three monotone-ordered mass outflows $\boldsymbol{w}_2 = \overline{\varphi}\pi(D/2)^2$ (kg/s), where $\overline{\varphi} = 120$, 140, and 160 (kg/m^{2}s). The region in the (ω_*, κ) plane defined by $0 \le \omega_* \le 2$ and $0 \le \kappa \le 1$ is discretized into a 21×41 grid of discrete pairs. We numerically simulate the three solutions for each pair of boundary condition parameters on this grid. In particular, for each discrete ω_*, we compute the three solutions for each discrete κ with until we achieve the lower bound $\kappa = \kappa_*(\omega_*)$ at which at least two of the three solutions overlap. The interpolated MI curves for several equivalent system variables are depicted in Fig. 8. The region below the MI

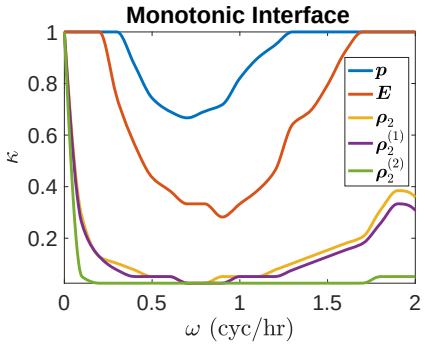

Figure 8. Monotonic interfaces (ω_*, κ_*) in the (ω_*, κ) plane.

curve is called the monotone operating region (MOR). Fig. 8 shows that the MORs for hydrogen density, natural gas density, total density, energy, and pressure are nested increasing sets with the hydrogen density MOR being the smallest set and the pressure MOR being the largest. For time-varying concentration profiles, Fig. 8 suggests that the pressure and energy equivalent system should be used if monotonicity properties are important to the formulation. This is the conclusion that we arrived at in Section VI. Of the five examples from Section VI, only Figs. 3-4 consider time-variations in concentration. Figs. 3-4 used two sinusoidal forcing frequencies, 0.1 (cyc/hr) and 0.033 (cyc/hr), each with unity amplitude factors $\kappa = 1$. Recall that in those figures, only the pressure and energy solutions did not overlap. This observation agrees with the MIs in Fig. 8, where the operating point $(\omega_* = 0.1, \kappa = 1)$ is above all of the MIs except for the pressure and energy MIs. For a more accurate comparison, the MIs ought to be recomputed with 5 and 10 (MPa) slack pressures instead of the 7 (MPa) that was used to compute the MIs in Fig. 8.

As ω_* increases from $\omega_* = 0$ to $\omega_* = 2$ (cyc/hr), the MI curves qualitatively decrease from unity to a lower bound, flatten out, and then increase. The fact that the amplitude factor generally increases along the MI as ω_* increases beyond $\omega_* = 0.75$ is a robustness feature of monotonicity to high frequency uncertainty. This property appears to be a consequence of wave attenuation in gas pipelines [37]. In particular, the gas pipeline demonstrates low-pass filtering characteristics with which the amplitudes of high frequency travelling waves are significantly attenuated over short distances, and, therefore, the likelihood of the solutions overlapping decreases as the high frequency waves increase in frequency. If the concentration of hydrogen injected into the network contains a small variation of high frequency uncertainty, then the MIs demonstrate that this uncertainty typically will not cause an otherwise theoretically monotonic operation to become non-monotonic.

IX. PERIODIC INTERFACE

In this section, we demonstrate that non-periodic solutions may emerge from sinusoidal concentration boundary conditions. To study periodic solutions numerically, we must simulate solutions over large time intervals of up to 400 hours. In addition, we will consider large and fast variations in concentration. This requires an extremely fine spatial discretization size for the simple endpoint discretization method. The large time interval and small spatial discretization size is difficult to implement digitally. Therefore, in our study of periodic solutions, instead of using the endpoint discretization method, we discretize the pipeline at the (translated) nodes of Chebyshev polynomials for which exponential convergence properties are obtained (e.g., see [38]). We briefly outline the method in the Appendix. The results in this section are performed in the single 50 km pipeline that was used previously to study the MI. However, the parameters that change are $\sigma_1 = 338.38$ (m/s), $\sigma_2 = 4\sigma_1$, and $\alpha_1 = 0.2$ in Eq. (30).

To introduce the transition to non-periodic phenomena, Figs. 9-11 show three examples that share the same boundary conditions with the exception of different frequencies ω_* and amplitude factors κ of the sinusoidal concentration profile in Eq. (30). The top of the three figures depict the pressure solutions at the outlet of the pipeline for $t \in [rT, T]$ with $0.7 \leq r \leq 0.95$, where $T = 400$ hr. The tail-ends of the solutions are used to bypass the initial transient responses that are not included here in the analysis of periodic orbits. The bottom left-hand-sides of Figures 9-11 show the phase space diagrams of outlet density and outlet pressure during the tail-ends of the operations. We see that the solutions in Figs. 9 and 10 approach periodic orbits and that the solution in Fig. 11 does not appear to do so. The pressure in Fig. 9 has twice as many local minima than the inlet concentration over the time interval $[0.95T, T]$. The additional local minima correspond to the inner loop of the periodic orbit. The pressure in Fig. 10 has the same number of local minima as the inlet concentration over the interval $[0.75T, T]$, but has twice the period. These examples demonstrate that periodic solutions may even be incoherent in the following sense. From the laws of fluid dynamics, gas pressure should decrease with decreasing density under constant temperature and volume. However, the phase space diagram in Fig. 9 contains three small time intervals and their periodic repetitions during which density decreases while pressure increases, and the phase space diagram in Fig. 10 contains two such time intervals. The solutions in this section are computed with sound speeds $\sigma_1 = 338.38$ m/s, $\sigma_2 = 4\sigma_1$, and mean hydrogen mass concentration $\alpha_1 = 0.2$.

The frequency responses of the outlet pressures are depicted on the bottom right-hand-sides of Figs. 9-11 using the discrete Fourier transform (DFT) [39]. The DFT is defined below in Eq. (31). The dominant frequency mode in the solution appears at the forcing frequency

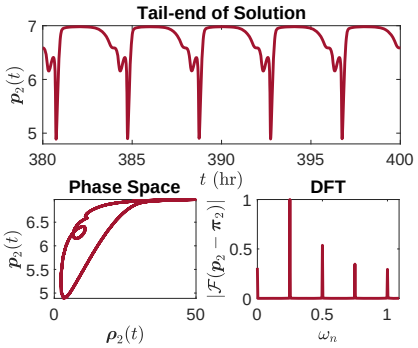

Figure 9. Pipeline solution with boundary conditions $q_2(t) = 75\pi(D/2)^2$ (kg/s), $\omega_* = 0.25$, and $\kappa = 1.0$. The periodicity measure is $\mathcal{P} = 0.12$.

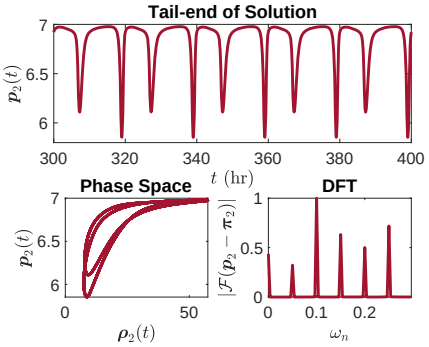

Figure 10. Pipeline solution with boundary conditions $q_2(t) = 75\pi(D/2)^2$ (kg/s), $\omega_* = 0.1$, and $\kappa = 0.98$. The periodicity measure is $\mathcal{P} = 0.1$.

$\omega_n = \omega_*$ in Figs. 9-11. The generated frequency modes in Fig. 9 appear at integer multiples of ω_*. This behavior is the most familiar to pure natural gas operations [37]. The generated frequency modes in Fig. 10 appear at half the values of the integer multiples of ω_*. This behavior is indicative of period-doubling bifurcations [40] at the forcing frequency $\omega_* = 0.1$ as the amplitude factor κ increases. We note that this period-doubling behavior is more easily seen with greater pressure. The pressure in Fig. 11 appears to form a continuous distribution of generated frequency modes. These observations inspire a quantitative measure of periodicity in terms of the frequency response of the solution. This is the approach taken in [24] for the transition to chaotic responses in oceanic wind bursts. We define a sequence of evenly-spaced samples of the tail-end of the outlet pressure by $\boldsymbol{p}_2[k] = \boldsymbol{p}_2((0.8+k/N)T)$ for $k = 0, \ldots, 0.2N$, where N is

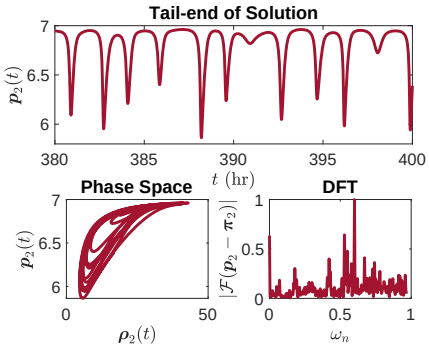

Figure 11. Pipeline solution with boundary conditions $q_2(t) = 75\pi(D/2)^2$ (kg/s), $\omega_* = 0.6$, and $\kappa = 0.9$. The periodicity measure is $\mathcal{P} = 1.49$.

equal to the number of time steps in the numerical solution over the interval $[0, T]$. For such a sampled sequence $[k]$ its normalized DFT is defined as

$$\{\mathcal{F}\boldsymbol{\psi}\}[\omega_n] = \frac{\sum_{k=0}^{0.2N} [k] e^{-\boldsymbol{j} 2\pi \omega_n k}}{\max_{\omega_n} \left| \sum_{k=0}^{0.2N} [k] e^{-\boldsymbol{j} 2\pi \omega_n k} \right|}, \quad (31)$$

where $\boldsymbol{j}$ is the imaginary unit and $\omega_n = n/(0.2T)$ (cyc/hr) are the sampling frequencies for $n = 0, \ldots, 0.2N$. The measure of periodicity is defined by the average power spectrum given by

$$\mathcal{P} = \frac{1}{0.2N+1} \sum_{n=0}^{0.2N} |\{\mathcal{F}(\boldsymbol{p}_2 - \boldsymbol{\pi}_2)\}[\omega_n]|^2 \times 100, \quad (32)$$

where $\boldsymbol{\pi}_2 = \boldsymbol{p}_2(0)$ is the initial steady-state value of pressure at the outlet of the pipeline. The shifted pressure in the power spectrum is used to suppress the zero frequency component of the initial state.

The power spectrum $\mathcal{P}$ is depicted in a color map as a function of (ω_*, κ) in Fig. 12, where ω_* is the forcing frequency and κ is its amplitude factor given in (30). This figure has been obtained numerically as follows. Similarly to the way that we have computed the MIs, the region in the (ω_*, κ) plane defined by $0 \leq \omega_* \leq 2$ and $0.5 \leq \kappa \leq 1$ is discretized into a 31×15 grid of discrete pairs. For each frequency and amplitude factor of the forcing concentration on this grid, we numerically simulate the solution in the pipeline for 400 hours. We then compute the DFT and power spectrum of the sampled solution, as defined above. This gives the discrete set of quantified values depicted in Figure 12. The periodic interface (PI) in Fig. 12 is the set of operating points below or above which the solution does or does not visually approach a periodic orbit. For each ω_*, the parameter κ is increased from $\kappa = 0$ to $\kappa = \kappa^*(\omega_*)$, where $\kappa^*(\omega_*)$ is the upper bound on κ below which the tail-end of the solution $(\boldsymbol{p}_2(t), \boldsymbol{\rho}_2(t))$ traces a closed orbit. Fig. 12 shows

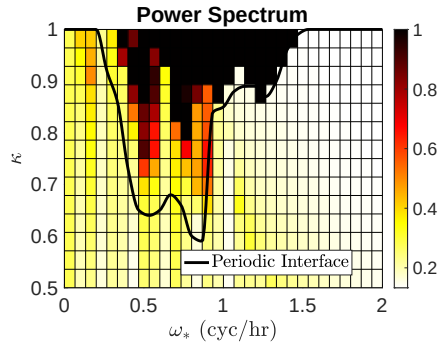

Figure 12. Color map of the power spectrum $\mathcal{P}$ in (32) as a function of (ω_*, κ) in (30). The boundary conditions are $\alpha_1 = 0.2$ and $\boldsymbol{q_2}(t) = 75$. In this figure, we plot the minimum between 1 and $\mathcal{P}$ in Eq. (32).

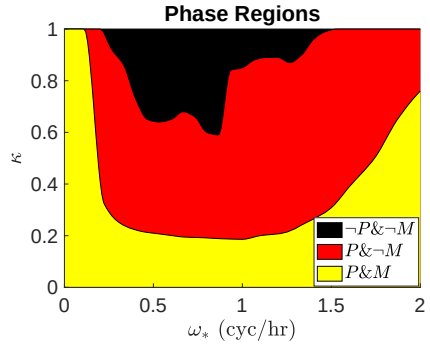

Figure 13. Phase operating regions that separate periodic and monotonic ($P\&M$), periodic and not monotonic ($P\&\neg M$), and neither periodic nor monotonic ($\neg P\&\neg M$). Same boundary conditions as those in Fig. 12.

that the power spectrum measure and the visual periodic interface are in reasonable agreement.

We now compare the MI and the PI of the pressure variable with $\alpha_1 = 0.2$. These interfaces separate the phase regions from periodic and monotonic, to periodic and non-monotonic, to non-periodic and non-monotonic as shown in Fig. 13. Note that the pressure MI in Fig. 13 is different from the pressure MI in Fig. 8 due to the different mean concentration α_1. Fig. 13 shows that the interfaces are equal for $\omega_* < 0.2$. As the frequency increases from $\omega_* = 0.2$ to $\omega_* = 0.5$, the value of κ on the MI decreases. As the frequency increases from $\omega_* = 0.3$ to $\omega_* = 0.5$, the value of κ on the PI decreases. The interfaces are roughly constant over the frequency range $0.5 < \omega_* < 0.9$. As frequency increases from $\omega_* = 1$, both of the interfaces generally increase. However, the PI shows a more significant increase in its accent over this frequency range than the MI. More importantly, the MI is never above the PI over the entire frequency range, so that the monotonic operating region is a subset of the periodic operating region. This suggests that monotonic solutions may eventually approach periodic orbits.

X. CONCLUSIONS

We developed a model for transporting heterogeneous mixtures of natural gas and hydrogen through pipeline networks. The formulation may be applied to real pipeline systems that operate time-variations of compressor and regulator units, supply stations that inject gas into the network with concentrated pressure, and flow stations that withdraw or inject concentrated mass flow from or into the network. The nonlinear partial differential equation formulation is discretized using a lumped element method to obtain a nonlinear input-to-state system which was proved to be monotonic for constant concentration vectors and to be non-monotonic, in general, for time-varying concentration vectors. The interface of the transition from monotonic to non-monotonic response to sinusoidal variation of concentration, called the monotonic interface, was analyzed numerically and the results were illustrated on a test network.

This paper also demonstrates that a non-periodic solution may emerge from a sinusoidal variation in concentration at the boundary. The periodic interface was analyzed numerically and compared with the monotonic interface. Characterizing the monotonic interface and periodic interface may enable a gas pipeline system designer to determine limitations on operating the network safely and predictably given blending of heterogeneous gases. Operations outside the monotone operating region may create surges with large pressure, energy, and concentration gradients, which do not occur in flows of a homogeneous gas. The monotonic interface analysis indicates that sufficiently slow variation in concentration about a constant profile will likely maintain monotonicity of ordered solutions in overall system pressures, and prevent large, rapid pressure transients. Such conditions are critical to maintain a physical flow regime with behavior that is intuitive for pipeline control room operators. This suggests that hydrogen may be blended into a natural gas pipeline network as long as injection rates are changed only gradually. The acceptable ramping rates depend significantly on the structure of the network, and would have to be determined through numerous simulations.

ACKNOWLEDGEMENTS

The authors are grateful to Vitaliy Gyrya, Rodrigo Platte, Dieter Armbruster, and Yan Brodskyi for numerous helpful discussions. This study was supported by the U.S. Department of Energy's Advanced Grid Modeling (AGM) project "Dynamical Modeling, Estimation, and Optimal Control of Electrical Grid-Natural Gas Transmission Systems", as well as LANL Laboratory Directed R&D project "Efficient Multi-scale Modeling of Clean Hydrogen Blending in Large Natural Gas Pipelines to Reduce Carbon Emissions". Research conducted at Los Alamos National Laboratory is done under the auspices of the National Nuclear Security Administration of the U.S. Department of Energy under Contract No. 89233218CNA000001.

[1] Stephen Nalley and Angelina LaRose. Annual energy outlook 2022 (AEO2022). *U.S. Energy Information Agency*, 2022.

[2] B. L. Salvi and K. A. Subramanian. Sustainable development of road transportation sector using hydrogen energy system. *Renewable and Sustainable Energy Reviews*, 51: 1132–1155, 2015.

[3] Manuel Götz, Jonathan Lefebvre, Friedemann Mörs, Amy McDaniel Koch, Frank Graf, Siegfried Bajohr, Rainer Reimert, and Thomas Kolb. Renewable power-to-gas: A technological and economic review. *Renewable energy*, 85:1371–1390, 2016.

[4] Merve Ozturk and Ibrahim Dincer. A comprehensive review on power-to-gas with hydrogen options for cleaner applications. *International Journal of Hydrogen Energy*, 46(62):31511–31522, 2021.

[5] Tom van der Hoeven. *Math in gas and the art of linearization*. Energy Delta Institute Groningen, The Netherlands, 2004.

[6] Marc W. Melaina, Olga Antonia, and Michael Penev. Blending hydrogen into natural gas pipeline networks: a review of key issues, 2013.

[7] Andrzej Witkowski, Andrzej Rusin, Mirosław Majkut, and Katarzyna Stolecka. Comprehensive analysis of hydrogen compression and pipeline transportation from thermodynamics and safety aspects. *Energy*, 141:2508–2518, 2017. ISSN 0360-5442.

[8] Sidhant Misra, Marc Vuffray, and Anatoly Zlotnik. Monotonicity properties of physical network flows and application to robust optimal allocation. *Proceedings of the IEEE*, 108(9):1558–1579, 2020.

[9] F. E. Uilhoorn. Dynamic behaviour of non-isothermal compressible natural gases mixed with hydrogen in pipelines. *International journal of hydrogen energy*, 34 (16):6722–6729, 2009.

[10] Maciej Chaczykowski, Filip Sund, Paweł Zarodkiewicz, and Sigmund Mongstad Hope. Gas composition tracking in transient pipeline flow. *Journal of Natural Gas Science and Engineering*, 55:321–330, 2018.

[11] Giulio Guandalini, Paolo Colbertaldo, and Stefano Campanari. Dynamic modeling of natural gas quality within transport pipelines in presence of hydrogen injections. *Applied energy*, 185:1712–1723, 2017.

[12] Sami Elaoud, Zahreddine Hafsi, and Lamjed Hadj-Taieb. Numerical modelling of hydrogen-natural gas mixtures flows in looped networks. *Journal of Petroleum Science and Engineering*, 159:532–541, 2017.

[13] Zahreddine Hafsi, Sami Elaoud, and Manoranjan Mishra. A computational modelling of natural gas flow in looped network: Effect of upstream hydrogen injection on the structural integrity of gas pipelines. *Journal of Natural Gas Science and Engineering*, 64:107–117, 2019.

[14] Di Fan, Jing Gong, Shengnan Zhang, Guoyun Shi, Qi Kang, Yaqi Xiao, and Changchun Wu. A transient composition tracking method for natural gas pipe networks. *Energy*, 215:119131, 2021.

[15] Baba G. Agaie, Ilyas Khan, Ali Saleh Alshomrani, and Aisha M. Alqahtani. Reduced-order modelling for high-pressure transient flow of hydrogen-natural gas mixture. *The European Physical Journal Plus*, 132(5):1–16, 2017.

[16] Norazlina Subani, Norsarahaida Amin, and Baba Galadima Agaie. Leak detection of non-isothermal transient flow of hydrogen-natural gas mixture. *Journal of Loss Prevention in the Process Industries*, 48:244–253, 2017. ISSN 0950-4230.

[17] Anatoly Zlotnik, Michael Chertkov, and Scott Backhaus. Optimal control of transient flow in natural gas networks. In *54th IEEE Conference on Decision and Control (CDC)*, pages 4563–4570. IEEE, 2015.

[18] P. Wong and R. Larson. Optimization of natural-gas pipeline systems via dynamic programming. *IEEE Transactions on Automatic Control*, 13(5):475–481, 1968.

[19] Peter B. Percell and Michael J. Ryan. Steady state optimization of gas pipeline network operation. In *PSIG annual meeting*. OnePetro, 1987.

[20] Henry H. Rachford and Richard G. Carter. Optimizing pipeline control in transient gas flow. In *PSIG annual meeting*. OnePetro, 2000.

[21] Anatoly Zlotnik, Kaarthik Sundar, Aleksandr M Rudkevich, Aleksandr Beylin, and Xindi Li. Optimal control for scheduling and pricing intra-day natural gas transport on pipeline networks. In *58th Conference on Decision and Control*, pages 4887–4884. IEEE, 2019.

[22] Christian Himpe, Sara Grundel, and Peter Benner. Model order reduction for gas and energy networks. *Journal of Mathematics in Industry*, 11(1):1–46, 2021.

[23] Anatoly Zlotnik, Sidhant Misra, Marc Vuffray, and Michael Chertkov. Monotonicity of actuated flows on dissipative transport networks. In *2016 European Control Conference (ECC)*, pages 831–836. IEEE, 2016.

[24] Eli Tziperman, Lewi Stone, Mark A. Cane, and Hans Jarosh. El Niño chaos: Overlapping of resonances between the seasonal cycle and the pacific ocean-atmosphere oscillator. *Science*, 264(5155):72–74, 1994.

[25] Ian Eisenman, Lisan Yu, and Eli Tziperman. Westerly wind bursts: Enso's tail rather than the dog? *Journal of Climate*, 18(24):5224–5238, 2005.

[26] Gianmarco Pizza, Christos E. Frouzakis, John Mantzaras, Ananias G. Tomboulides, and Konstantinos Boulouchos. Dynamics of premixed hydrogen/air flames

in microchannels. *Combustion and Flame*, 152(3): 433–450, 2008.
[27] Alireza Alipoor and Kiumars Mazaheri. Combustion characteristics and flame bifurcation in repetitive extinction-ignition dynamics for premixed hydrogen-air combustion in a heated micro channel. *Energy*, 109:650–663, 2016.
[28] Vitaliy Gyrya and Anatoly Zlotnik. An explicit staggered-grid method for numerical simulation of large-scale natural gas pipeline networks. *Applied Mathematical Modelling*, 65:34–51, 2019.
[29] Andrzej Osiadacz. Simulation of transient gas flows in networks. *International Journal for Numerical Methods in Fluids*, 4(1):13–24, 1984.
[30] Michael Herty, Jan Mohring, and Veronika Sachers. A new model for gas flow in pipe networks. *Mathematical Methods in the Applied Sciences*, 33(7):845–855, 2010.
[31] Kaarthik Sundar and Anatoly Zlotnik. State and parameter estimation for natural gas pipeline networks using transient state data. *IEEE Transactions on Control Systems Technology*, 27(5):2110–2124, 2019.
[32] Martin Gugat, Michael Herty, Axel Klar, Günter Leugering, and Veronika Schleper. Well-posedness of networked hyperbolic systems of balance laws. In *Constrained optimization and optimal control for partial differential equations*, volume 160, pages 123–146. Springer, 2012.
[33] Sara Grundel, Nils Hornung, Bernhard Klaassen, Peter Benner, and Tanja Clees. Computing surrogates for gas network simulation using model order reduction. In *Surrogate-Based Modeling and Optimization*, pages 189–212. Springer, 2013.
[34] David Angeli and Eduardo D. Sontag. Monotone control systems. *IEEE Transactions on automatic control*, 48 (10):1684–1698, 2003.
[35] Morris W. Hirsch and Hal Smith. Monotone dynamical systems. *Handbook of differential equations: ordinary differential equations*, 2:239–357, 2006.
[36] Hassan K. Khalil. *Nonlinear Systems*. Pearson Education. Prentice Hall, 2002.
[37] Luke Baker, Dieter Armbruster, Anna Scaglione, and Rodrigo B. Platte. Analysis of a model of a natural gas pipeline—a transfer function approach. *Transactions of Mathematics and Its Applications*, 5(1):tnab002, 2021.
[38] Uri M. Ascher and Chen Greif. *A first course on numerical methods*. SIAM, 2011.
[39] Alan V. Oppenheim, John R. Buck, and Ronald W. Schafer. *Discrete-time signal processing. Vol. 2*. Upper Saddle River, NJ: Prentice Hall, 2001.
[40] Jie Zhang, Nan-Sheng Liu, and Xi-Yun Lu. Route to a chaotic state in fluid flow past an inclined flat plate. *Phys. Rev. E*, 79:045306, Apr 2009.

Appendix A: Model Comparison

The interested reader is referred to [28] for a model comparison of homogeneous gas flow in the network shown in Fig. 2. Using the same initial and boundary conditions as used in the previous study, we recover the same solution, up to machine precision, with our mixed gas model. Our solution is shown in Fig. 14.

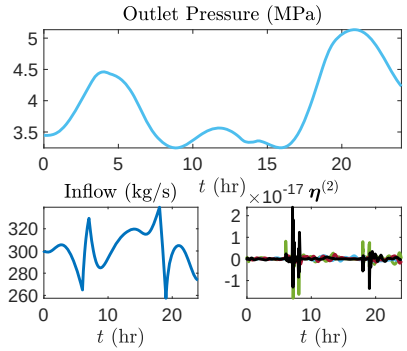

Figure 14. Model comparison (see Fig. 11 in [28]).

Appendix B: Chebyshev Spectral Differentiation

Consider a single pipeline of length ℓ, diameter D, and friction factor λ with axial variable $x \in [0, \ell]$. Discretize the interval $[0, \ell]$ with the $(N+1)$ discretization points $x_i = \ell/2(1-\cos(i\pi/N))$ for $i = 0, \ldots, N$. Define the sampled variables $\boldsymbol{\rho}_i^{(m)}(t) = \rho^{(m)}(t, x_i)$ and $\boldsymbol{\varphi}_i(t) = \varphi(t, x_i)$. It follows from interpolating the values of $\boldsymbol{\rho}_i^{(m)}(t)$ at the points x_i using Lagrange polynomials of order N that (e.g., see [38])

$$\partial_x \rho^{(m)}(t, x_i) \approx \boldsymbol{D}\boldsymbol{\rho}_i^{(m)}(t), \tag{B1}$$

where

$$\boldsymbol{D}_{ij} = \begin{cases} \sum\limits_{\substack{n=0 \\ n\neq j}}^{n} \frac{1}{x_j - x_n}, & i = j, \\ \frac{1}{x_j - x_i} \prod\limits_{\substack{n=0 \\ n\neq i,j}}^{n} \frac{x_i - x_n}{x_j - x_n} & i \neq j. \end{cases} \tag{B2}$$

The discretized PDEs in (3)-(4) become

$$\dot{\boldsymbol{\rho}}^{(m)} + \boldsymbol{D}\left(\frac{\boldsymbol{\rho}^{(m)}}{\boldsymbol{\rho}^{(1)} + \boldsymbol{\rho}^{(2)}} \odot \boldsymbol{\varphi}\right) = 0, \tag{B3}$$

$$\boldsymbol{D}\left(\sigma_1^2 \boldsymbol{\rho}^{(1)} + \sigma_2^2 \boldsymbol{\rho}^{(2)}\right) = -\frac{\lambda}{2D} \frac{\boldsymbol{\varphi} \odot |\boldsymbol{\varphi}|}{\boldsymbol{\rho}^{(1)} + \boldsymbol{\rho}^{(2)}}. \tag{B4}$$

The boundary conditions are incorporated into the discretized equations by replacing $\boldsymbol{\rho}_0^{(m)}(t) = \boldsymbol{s}_0^{(m)}(t)$ and $\boldsymbol{\varphi}_N(t) = \boldsymbol{w}_N(t)/(0.25\pi D^2)$.